Uncovering the Physics of Frustrated Quantum Magnets using the Correlation Density Matrix Approach

THÈSE N^{O} 4852 (2010)

PRÉSENTÉE LE 26 OCTOBRE 2010

À LA FACULTÉ SCIENCES DE BASE

CHAIRE DE THÉORIE DE LA MATIÈRE CONDENSÉE

PROGRAMME DOCTORAL EN PHYSIQUE

ÉCOLE POLYTECHNIQUE FÉDÉRALE DE LAUSANNE

POUR L'OBTENTION DU GRADE DE DOCTEUR ÈS SCIENCES

PAR

Julien SUDAN

acceptée sur proposition du jury:

Prof. O. Schneider, président du jury
Prof. F. Mila, Dr A. M. Läuchli Herzig, directeurs de thèse
Prof. S. Capponi, rapporteur
Prof. D. Ivanov, rapporteur
Dr G. Misguich, rapporteur

ÉCOLE POLYTECHNIQUE
FÉDÉRALE DE LAUSANNE

Suisse
2010

Résumé

Ce travail est consacré à l'étude, au développement, et à l'application d'une nouvelle méthode systématique livrant de manière non-biaisée les corrélations dominantes d'un état quantique à plusieurs corps. Les corrélations dominantes entre une paire arbitraire de blocs disjoints dans le système sont extraites de la *matrice densité de corrélation* (MDC) entre ces mêmes blocs au moyen d'une *décomposition en valeurs singulières* de celle-ci. Nous déterminons différentes propriétés mathématiques et caractéristiques de cette méthode, en particulier les conséquences des symétries du réseau ou de celles intrinsèques à l'état étudié sur le spectre de valeurs singulières. Nous étudions la relation entre la norme de la MDC – qui fournit une mesure naturelle de la corrélation totale entre les deux blocs – et la quantité appelée *information mutuelle*, originellement utilisée en théorie de l'information quantique.

Cet outil novateur est utilisé dans le but de faire la lumière sur la physique à température nulle de la chaîne J_1–J_2 de Heisenberg ferromagnétique frustrée de spin 1/2 plongée dans un champ magnétique, et la physique de basse énergie de l'antiferroaimant de Heisenberg frustré de spin 1/2 sur le réseau bidimensionnel kagomé. Les états sont obtenus par diagonalisation exacte et par la procédure du groupe de renormalisation par la matrice densité dans le premier cas, et par diagonalisation exacte uniquement dans le deuxième cas. Après une introduction de ce travail donnée dans le chapitre 1, le premier de ces modèles est traité dans le chapitre 2. Le chapitre 3 présente la méthode MDC, et le chapitre 4 est consacré à l'étude de l'antiferroaimant sur réseau kagomé.

Dans la chaîne J_1–J_2, nous faisons état de l'existence d'une phase chirale vectorielle à bas champ et d'une suite de phases liquides de Luttinger multipolaires à haut champ. Nous montrons explicitement que ces phases multipolaires sont le fruit de la destabilisation –

via un mécanisme de blocage – de l'état spiral, qui est état fondamental classique en l'absence de champ. Cette manière de voir les choses est complètement nouvelle: s'il était bien connu que les phases multipolaires pouvaient naître de la destabilisation de phases ferromagnétiques, il était en revanche ignoré qu'elles puissent naître également de la destabilisation de spirales.

Quant à l'antiferroaimant sur réseau kagomé, nous nous intéressons pour la première fois à la nature des états singulets qui composent son spectre singulet très dense au-dessus de son état fondamental. Nous montrons que certains de ces états singulets de basse énergie ont des corrélations de dimères importantes, qui ne semblent pas decroître significativement avec la distance; nos résultats MDC confirment par ailleurs que les corrélations dominantes dans ces états singulets sont du type dimère-dimère. Des calculs d'entropies de bloc de Von Neumann révèlent une très petite longueur de corrélation d'une part, et des entropies qui sont plus ou moins indépendantes de l'énergie de l'état considéré d'autre part. Le scénario d'une phase cristal de dimères est examiné, et l'aptitude de différents types de cristaux (tirés de la littérature ou ad hoc) à reproduire les corrélations de dimères dans l'échantillon de 36 sites est analysée.

Mots clefs: matrice densité de corrélation, modèle de Heisenberg, système frustré, liquide de Luttinger, chaîne de spin frustrée, antiferroaimant sur réseau kagomé, spirale, phase multipolaire, cristal de liens de valence, entropie de Von Neumann, intrication.

Abstract

This work is devoted to the study, the development, and the application of a new systematic method yielding the dominant correlations that govern a quantum many-body state in an unbiased way. The dominant correlations between any two disjoint blocks of a system are extracted by performing a *singular value decomposition* of the *correlation density matrix* (CDM) between those blocks. We determine several mathematical properties and features of this method, in particular the consequences of the lattice symmetries or the symmetries intrinsic to the studied state on the singular values spectrum. We investigate the relation between the norm of the CDM – providing a natural measure of the total correlation between the two blocks – and the so-called *mutual information*, a quantity originally introduced in quantum information theory.

This novel tool is utilized for sheding new light on the zero temperature physics of the spin-1/2 frustrated ferromagnetic J_1–J_2 Heisenberg chain in a magnetic field as well as on the low-energy physics of the spin-1/2 antiferromagnetic Heisenberg model on the two-dimensional kagomé lattice. The states are computed using exact diagonalization and the density matrix renormalization group procedure in the first case, and exact diagonalization only in the second case. This work is introduced in Chapter 1. The first model is then presented in Chapter 2. Chapter 3 introduces the CDM method, and Chapter 4 is devoted to the study of the kagomé antiferromagnet.

In the J_1–J_2 chain, we reveal a vector chiral phase at low magnetic field and a sequence of multipolar Luttinger liquid phases at high field. We explicitly show that these multipolar phases result from the destabilization – driven by a locking mechanism – of the classical spiral ground state in the absence of magnetic field. This point of view is completely new:

multipolar phases were known to be a possible destabilization of ferromagnetic phases, but they have never been reported as a destabilization of spiral states yet.

Regarding the kagomé antiferromagnet, we address for the first time the question of the nature of the singlet states forming its quite dense singlet spectrum above the ground state. We show that some of these low-lying singlet states have large dimer correlations which do not seem to significantly decrease with the distance, moreover our CDM studies confirm that the dominant correlations in those singlet states are of the dimer-dimer type. Studies of Von Neumann block entropies reveal a very short correlation length on the one hand, and entropies that are roughly independent on the energy of the state under consideration on the other hand. The scenario of a valence bond crystal phase is investigated and the relevance of different kinds of crystals (from the literature or ad hoc) for reproducing the dimer correlations in the 36-site sample is probed.

Keywords: correlation density matrix, Heisenberg model, frustrated system, Luttinger liquid, frustrated spin chain, kagomé antiferromagnet, spiral, multipolar phase, valence bond crystal phase, Von Neumann entropy, entanglement.

Remerciements

Je tiens en premier lieu à remercier chaleureusement Andreas Läuchli et Frédéric Mila d'avoir cru en moi en me donnant la possibilité de mener une thèse à l'IRRMA. Des remerciements tout particuliers à Andreas qui a guidé et encadré ma thèse pour le temps énorme qu'il m'a consacré et tout ce que j'ai pu apprendre grâce à lui, qu'il trouve ici l'expression de ma profonde gratitude.

Je remercie mes collègues et anciens collègues de groupe: Andreas Lüscher, avec qui j'ai partagé mon bureau pendant un peu moins de deux ans dans le bâtiment PPH avant de migrer vers le cubotron, pour son aide précieuse en début de thèse; Ioannis Rousochatzakis, récemment parti à Dresden, pour m'avoir familiarisé avec la méthode de diagonalisation exacte, pour sa disponibilité, ses explications toujours très pédagogiques, et son énorme gentillesse; Jean-David Picon pour son aide précieuse et sa disponibilité lorsque j'avais des problèmes d'informatique et toutes les discussions intéressantes que nous avons pu avoir; Tamás Tóth qui a commencé et va terminer ses études doctorales en même temps que moi, pour toutes les discussions "géniales" que nous avons eues, et avec qui j'ai eu un grand plaisir à enseigner, je pense que nous formions une bien belle "paire de Cooper"; Salvatore Manmana pour l'aide qu'il a pu m'apporter suite à toutes sortes de questions et pour sa gentillesse; Julien Dorier pour les sympathiques moments passés en sa compagnie; ainsi que les nouveaux arrivés dans le groupe Sandro Wenzel, Tommaso Coletta, et Frédéric Michaud, pour l'ambiance sympathique et propice à la discussion qui régnait au sein de notre groupe. Je remercie aussi Nicolas Dorsaz qui n'est pas un collègue de groupe à proprement parler, mais avec qui j'ai partagé mon bureau du cubotron, pour l'ambiance agréable qui y régnait. A tous, je souhaite un parcours plein de réussite et de bonheur.

Je remercie Florence Hagen et Noémi Porta, respectivement informaticienne et secrétaire de l'IRRMA, pour leur grande efficacité et gentillesse.

Je remercie l'Institut Max-Planck de Dresden pour son hospitalité lors de mes différentes visites.

Je remercie le Prof. Christopher L. Henley de l'Université de Cornell à New York, qui a été le premier à imaginer et à mettre en avant l'approche utilisée dans ma thèse, pour les discussions intéressantes que nous avons eues ainsi que pour ses bonnes idées et suggestions.

Je remercie le Prof. Olivier Schneider d'avoir bien voulu présider le jury de thèse, ainsi que le Prof. Dmitri Ivanov, le Dr. Grégoire Misguich, et le Prof. Sylvain Capponi d'avoir accepté la tâche de rapporteurs de cette thèse.

Mon dernier remerciement, mais pas le moindre, s'adresse à ma femme Chimène pour son soutien durant mes années de thèse. Il n'est pas tous les jours facile de partager la vie d'un doctorant.

Julien Sudan

À Sylviane

Contents

CHAPTER 1

General introduction

Condensed matter theorists aim to determine the magnetic properties of materials from mathematical models capturing the dominant interactions between the electronic magnetic moments (spins) of the atoms or molecules forming those materials. Descriptions of macroscopic phenomena based on the understanding of mechanisms occurring at the microscopic level can thus be provided. Some of these models are analytically and exactly solvable [1] but in most of the cases the research of approximate analytical solutions is already a complicated task. Numerical simulation has therefore become a natural and powerful tool in condensed matter physics as well as in other fields. The results presented in this thesis are obtained by simulations based on Exact Diagonalization and on the Density Matrix Renormalization Group algorithm (those algorithms are described in details in Appendix A).

Let us first explain the origin and the essence of the type of quantum model we consider in this work. In 1926, Heisenberg and Dirac independently explained the splitting between the singlet and the triplet levels in the spectrum of helium by an exchange given by the scalar product between the electronic spins (Heisenberg exchange) [2]. Later on, it was found that this type of exchange actually describes the magnetism of several insulators whose physics is governed by the Heisenberg hamiltonian whose most general form reads

$$H = \sum_{(i,j),\alpha=x,y,z} J_{i,j}^{\alpha} S_i^{\alpha} S_j^{\alpha}, \tag{1.1}$$

where the symbol (i,j) means that the sum runs over spin pairs, $\mathbf{S}_i = (S_i^x, S_i^y, S_i^z)$ is a spin operator located at site i, and $J_{i,j}^{\alpha}$ are the coupling parameters. Positive values of the coupling $J_{i,j}^{\alpha}$ favor an antiparallel alignment of the spins located at sites i and j in direction α [antiferromagnetic (AF) case], whereas negative values of $J_{i,j}^{\alpha}$ favor a parallel alignment of the spins located at sites i and j in direction α [ferromagnetic (F) case]. Note that the Heisenberg hamiltonian Eq. (1.1) implicitly assumes that all the degrees of freedom different from the electronic spin are frozen, which is justified in plethora of magnetic insulators. It nevertheless happens that charge, orbital, or lattice degrees of freedom have to be taken into account as well. If charge degrees of freedom are taken into account for instance, more complicated types of exchanges appear (like multiple-spin exchange). Hamiltonian Eq. (1.1) consists of interactions of arbitrary range, in the three directions $\alpha = x, y, z$ of the spin space, but it is often sufficient to restrict oneself to the isotropic case with interactions between nearest and next nearest neighbors (nn and nnn) only.

If the energy contributions of the different interactions in hamiltonian Eq. (1.1) can be independently classically minimized[1], the model is said to be *non-frustrated*. It has been observed that the $S = 1/2$ Heisenberg model with non-frustrated nn interactions on any 2D Bravais lattice (e.g. square) has magnetic order at zero temperature. If the energy contributions of the different interactions cannot be independently classically minimized the model is *frustrated*. By tuning the frustration (i.e. varying the coupling parameter ratios) one generally observes that magnetic order survives at low frustration but it is destroyed around the point of maximal frustration[2] often giving rise to intriguing exotic types of orderings, this is the reason why highly frustrated systems are very good candidates for displaying exciting and unexpected phases.

In this thesis, we shall mostly focus on the ground state (i.e. zero-temperature) properties of low-dimensional (1D and 2D) spin $S = 1/2$ systems. For this value of spin, quantum fluctuations are very strong, and a large and rich variety of phases may emerge, each of which breaking specific symmetries and being characterized by a particular behavior of elementary excitations (see Refs. [4; 5] for a good overview). Let us briefly review and describe some of these types of phases. Among the phases we list below, those breaking a continuous symmetry[3] are marked with an asterisk (*); a direct consequence of the

[1]The classical version of a spin model is obtained by replacing the spin operators by classical vectors of fixed length S. The physics of a model becomes classical in the limit $S \to \infty$ since the commutator between two spin components is much smaller than the square of the spin variables in that limit: $[S^{\alpha}, S^{\beta}] = i\epsilon^{\alpha,\beta,\gamma} S^{\gamma} = \mathcal{O}(S) \ll \mathcal{O}(S^2)$.

[2]For instance, if nnn AF $J_2 = J_1/2$ interactions are added to the magnetically ordered model with nn AF J_1 interactions on the square lattice, the magnetic order is destroyed [3].

[3]In 1D at zero temperature, the breaking of a continuous symmetry is prohibited by the Mermin-Wagner theorem (see Appendix B). Phases breaking a continuous symmetry can therefore not have any finite order

breaking of a continuous symmetry is the existence of a Goldstone gapless excitation mode (see Appendix B).

- The magnetically ordered phase we have pointed out above to be stabilized in non-frustrated models is also called **semi-classical Néel ordered phase***. It sustains long-range order (LRO) in the spin correlations, i.e. the spin structure factor (which can be measured by neutron or X-ray diffraction for instance)

$$S(\mathbf{q}) := \lim_{N\to\infty} \frac{1}{N} \left\langle \left| \sum_j e^{i\mathbf{q}\cdot\mathbf{x}_j} \mathbf{S}_j \right|^2 \right\rangle \tag{1.2}$$

  (the sum runs over the N spins of the sample, $\mathbf{x}_j$ is the location of spin $\mathbf{S}_j$) diverges with the size of the sample for at least one wave vector, say $\tilde{\mathbf{q}}$; the suitable order parameter is then given by the staggered magnetization

$$m_{\tilde{\mathbf{q}}} := \lim_{N\to\infty} \frac{1}{N} \left\langle \sum_j e^{i\tilde{\mathbf{q}}\cdot\mathbf{x}_j} S_j^z \right\rangle .$$

  A Néel phase breaks the $SU(2)$, the space group, and the time reversal $t \mapsto -t$ (resulting in $\mathbf{S}_j \mapsto -\mathbf{S}_j \; \forall j$) symmetries[4]. Its elementary excitations are gapless magnons (spin waves). For the sake of illustration, Fig. 1.1 displays the wave vector dependence of the spin wave intensity (yielding the structure factor Eq. (1.2)) as a function of the wave vector for the high-T_c parent compound La_2CuO_4 at $T = 295K$. The measures are performed by inelastic neutron scattering. The peak at $(h, k) = (1/2, 1/2)$ (wave vector (π, π)) characterizing an AF ordering is well visible.

- A **valence bond crystal phase** (VBC) has LRO in the dimer arrangements or in more complex $S = 0$ (total spin singlet) plaquettes, and breaks the space group symmetries. The suitable order parameter for this phase is thus the dimer-dimer LRO, or $S = 0$ plaquettes LRO. In a VBC phase, the spin structure factor Eq. (1.2) never diverges, whatever the wave vector. All excitations are gapped, and elementary excitations in a VBC can be created by the promotion of a dimer (or a $S = 0$ plaquette) to a triplet (or excited $S = 0$, or other total spin) state. The two spins $1/2$ forming the triplet state can nevertheless not separate far apart: such a process would create a string of misaligned dimer bonds, with an energy penalty increasing with the length of that string, see Fig. 1.2. This is energetically unfavorable, and

parameter in this case. They are characterized by a *quasi-long-range order* decaying algebraically with the distance instead of a true long-range order.

[4]Notice that the space group symmetries live in the real space whereas the others live in the spin space.

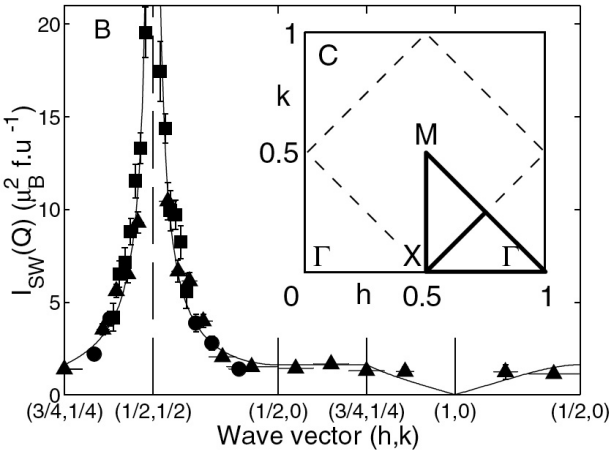

Figure 1.1: Wave vector dependence of the spin wave intensity in La_2CuO_4 at $T = 295K$ (obtained by inelastic neutron scattering), from Ref. [6].

these spins 1/2 (spinons) are thus confined. The ground state of the Heisenberg model with nn AF interactions on the checkerboard lattice (see Fig. F.1) is an example of VBC [7], and VBC also naturally emerge as typical ground states of quantum dimer models [8].

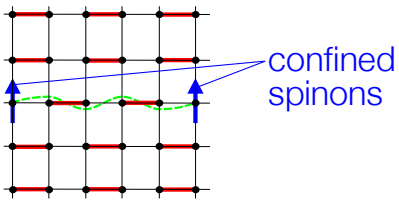

Figure 1.2: Confined spinons (blue arrows) in a VBC, the red lines denote dimer bonds.

- A **short-range resonating valence bond spin liquid** *(Anderson, 1973 [9])* (SRRVB) denotes a wave function that has the following properties:

  1. it is a linear superposition of an exponential number of disordered valence bond configurations of short-ranged dimers (in contrast to the VBC where only a finite number of ordered configurations dominate the ground state wave function),
  2. it does not break any symmetry, has no local order parameter, and is short-ranged in any kind of correlation function[5].

[5](1) does not imply (2). A wave function can satisfy (1) and nonetheless have critical dimer correlations [10], or even magnetic order [11].

In a SRRVB, the dimer LRO that was existing in the VBC has been "molten" because of frustration and quantum resonances. As in the VBC the spin structure factor Eq. (1.2) never diverges, whatever the wave vector, and as in a VBC, excitations in a SRRVB can be created by the promotion of a dimer (or a $S = 0$ plaquette) to a triplet (or excited $S = 0$, or other total spin) state. But in contrast to a VBC, two spins 1/2 (spinons) of a triplet are not confined. They can separate far apart without any energy cost since any disordered configuration does contribute in a SRRVB, see Fig. 1.3: excitations in a SRRVB thus appear as *continua* and not as well separated modes as in a VBC, and are not necessarily gapped. Note that topological degeneracy can appear in a SRRVB phase[6]. This phase is realized for instance in the multi-spin exchange model on the triangular lattice [13], or in the J_1-J_2 Heisenberg model on the hexagonal lattice ($J_1 < 0$, $J_2 > 0$) at $J_2/J_1 \approx 0.25$ [14].

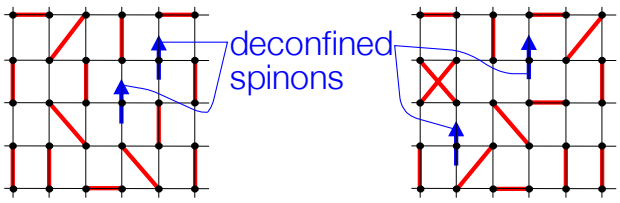

Figure 1.3: Deconfined spinons (blue arrows) in a SRRVB, the red lines denote dimer bonds.

- The definition of a SRRVB excludes any long-range order. However, a state with broken time reversal symmetry and LRO in the scalar chirality $\mathbf{S}_i \cdot (\mathbf{S}_j \times \mathbf{S}_k)$ could accommodate with all the properties of the spin liquid described as SRRVB. Such a state is called **chiral spin liquid** *(Wen, 1989 [15])* and – as for the SRRVB – has deconfined spinons as elementary excitations. It breaks two discrete symmetries: the time reversal and the parity. All its excitations are gapped, and its spin structure factor Eq. (1.2) never diverges, whatever the wave vector. Finding a parent hamiltonian for this phase has long remained an open problem, which was finally solved by Schroeter and collaborators [16] three years ago.

- **Nematic phases*** *(Andreev & Grishchuk, 1984 [17])* break the continuous $SU(2)$ spin symmetry (the elementary excitations are thus gapless) but in contrast to Néel

[6]The underlying order of a *topological ordered phase* cannot be described by any order parameter (see Ref. [12] for studies of quantum Hall systems). One of the signatures of topological local order is the dependence of the ground state degeneracy on the topology of the manifold on which the system is defined. Such a ground state degeneracy is called *topological degeneracy* to distinguish it from the case of ordinary spontaneous symmetry breaking with a local order parameter, where the ground state degeneracy is determined by the pattern of the symmetry breaking and thus does not depend on the topology.

phases, the time reversal symmetry is preserved and there is no sublattice magnetization. A nematic state is characterized by a LRO in the rank-2 tensor

$$S_i^\alpha S_j^\beta = \delta_{\alpha,\beta} A(i,j) + \epsilon^{\alpha,\beta,\gamma} B^\gamma(i,j) + Q^{\alpha,\beta}(i,j),$$

where $A(i,j)$ is a scalar function, $B^\gamma(i,j) = \mathbf{S}_i \times \mathbf{S}_j$ is an antisymmetric pseudovector, and

$$Q^{\alpha,\beta}(i,j) = \frac{1}{2}\left(\mathbf{S}_i^\alpha \mathbf{S}_j^\beta + \mathbf{S}_i^\beta \mathbf{S}_j^\alpha\right) - \frac{\delta_{\alpha,\beta}}{3}\mathbf{S}_i \cdot \mathbf{S}_j$$

is a traceless symmetric rank-2 tensor. One usually distinguishes between spin nematics that are long-ranged in $B(i,j)$ (p-type spin nematics) and those that are long-ranged in $Q(i,j)$ (n-type spin nematics). A simple picture of a spin nematic is that the spins – albeit disordered – remain correlated within a preferred plane that is spontaneously selected. This plane is oriented for p-type nematics and nonoriented for n-type nematics. A spin nematic phase was reported for the first time in the case of spins $S = 1/2$ by Läuchli and collaborators five years ago [18], and other examples have been reported since [19].

It is interesting to draw a parallel with the nematic phase arising in *liquid crystals*, and characterized by a directional LRO of the liquid crystal molecules (their long axes are roughly parallel, like spins selecting a preferred plane) but no positional order as shown in Fig. 1.4. The properties of liquid crystals in this phase are extremely useful in *liquid crystal displays* (LCD).

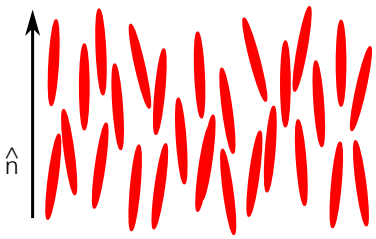

Figure 1.4: Liquid crystal molecules in the nematic phase. They are roughly parallel to the preferred direction (director) denoted by $\hat{n}$.

- In case of a LRO in tensors of rank higher than 2, one speaks of **multipolar phases*** [20; 21]. The continuous $SU(2)$ spin symmetry is broken as in the nematic phase, elementary excitations are therefore gapless as well. The time reversal symmetry is broken only if the tensor rank of the order parameter is odd.

The enumeration we have done here only aims to familiarize the reader with the main phases he may encounter in this thesis. It is not an exhaustive list, and does not reflect

the incredible richness of the physics of low-dimensional systems. The existence of important phases like for instance the superconducting, the superfluid, and the supersolid ones – which are currently at the heart of intense researches – have been omitted. In the supersolid phase, the particles that must supply the rigidity to form a crystal, at the same time provide for superfluid nonviscous flow. Such a state of matter was conjectured 40 years ago [22] and some experimental evidences are searched in solid ^{4}He, but interpretations of these researches are still under active debate [23]. It combines complicated and fascinating phenomena, and corresponds to a superfluid phase with a broken translational symmetry. Supersolid phases may arise in certain antiferromagnets above low-magnetization plateaux: at low magnetic field, bosonic triplet $S = 1$ excitations of those antiferromagnets called *triplons* appear and are spread uniformly throughout the lattice. They Bose-Einstein condense, leading to a superfluid phase. If the field is increased and the triplon density becomes commensurate with the lattice periodicity, the triplons crystallize (breaking the translation symmetry in the lattice space) and form a superstructure; the magnetization plateau is entered at this stage. If the field is increased further, those triplons which were crystallized keep a crystallized configuration (the translation symmetry is thus not restored) while additional triplons appear, are spread throughout the lattice and Bose-Einstein condense, restoring the superfluidity. The supersolid phase is then entered. Ref. [24] reviews the phenomenon in a very nice and pedagogical way.

A phase is characterized by a specific type of dominant correlation displaying LRO (or quasi-LRO in 1D). In frustrated systems – where exotic and unpredictable types of correlations may dominate – the candidates for displaying LRO can be very difficult to find out, and necessarily demand an a priori suspicion about the phase that might be stabilized. In order to overcome this kind of obstacle, Cheong and Henley put forward four years ago the idea that the dominant correlation between two disjoint blocks of a quantum spin (or more generally many-body) system can be extracted in an unbiased way from the *correlation density matrix* (CDM) object, see Ref. [25]. Roughly at the same time, Furukawa, Misguich, and Oshikawa [26] proposed a very similar method consisting in determining the order parameter of a symmetry breaking (unknown) phase by comparing the reduced density matrices of the different nearly degenerate ground states of a finite system. This thesis is based on the approach by Cheong and Henley. In contrast to the previous one, the CDM from which the dominant correlation is extracted is computed in *one specific* state.

This thesis is devoted to the development of a framework for using the CDM tool and to the determination of the features and properties of this new tool on the one hand, as well as to the application of this tool in order to solve – or at least to shed some new light – on the physics of low-dimensional spin $S = 1/2$ systems on the other hand. The first model we consider, namely the chain with F interactions between nn and AF interactions between

nnn, is realized in several compounds like the cuprates $LiCuVO_4$ [27], Li_2ZrCuO_4 [28], and $Rb_2Cu_2Mo_3O_{12}$ [29]. We start with this topic in Chapter 2. Chapter 3 is then devoted to the CDM tool and its properties, and Chapter 4 utilizes it in order to study the Heisenberg model on the 2D kagomé lattice. We clarify the low-energy physics of this model which – although studied since the early nineties – remains theoretically poorly understood. Even from the experimental side, it is really challenging to find realizations of this second model in nature. A lot of hopes have been put in the recently synthesized organometallic hybrid compound Cu(1,3-benzenedicarboxylate) [30] consisting of structurally perfect spin-1/2 copper kagomé planes. Many research groups are currently working on theoretical or experimental aspects of the spin-1/2 kagomé antiferromagnet. The final conclusion and the future perspectives are finally given in Chapter 5.

CHAPTER 2

Frustrated ferromagnetic spin-1/2 Heisenberg chain in a magnetic field

2.1 Introduction

The first explanation for spiral states was proposed fifty years ago by Villain, Kaplan, and Yoshimori [31]. It is based on magnetic frustration, where geometric constraints and competing interactions make it impossible to select a single lowest-energy configuration of collinear spins, spiral ordering then emerges as a compromise[1]. Several materials are successfully described by theories based on spiral states [33]. For low spin and dimensionality however, quantum fluctuations become important and might destabilize the spirals.

A prominent instability of spiral states is their intrinsic twist $\langle \mathbf{S}_i \times \mathbf{S}_j \rangle$ [34]. It has been recognized that finite temperature [35] or quantum [36] fluctuations can disorder the spin moment $\langle \mathbf{S}_i \rangle$ of the spiral, while the twist remains finite. Such a state is called p-type spin nematic [17]. In the context of quantum fluctuations such a scenario has been confirmed recently in a ring-exchange model [18], while possible experimental evidence for the thermal scenario has been presented in Ref. [37]. The twist also gained attention in multiferroics, since it couples directly to the ferroelectricity [38].

[1] Later on, Dzyaloshinskii-Moriya interactions were shown to favor non-collinear spins in certain cases as well [32].

This chapter is devoted to the study of the ferromagnetic frustrated spin-1/2 Heisenberg chain in a magnetic field in which we have revealed the existence of a novel instability of spiral states towards *spin-multipolar phases*. The basic idea is that many spin-multipolar order parameters are finite in the magnetically ordered spiral state, but that under a suitable amount of fluctuations the primary spin order is lost, while a spin-multipolar order parameter survives. The frustrated ferromagnetic spin-1/2 Heisenberg chain is defined by the hamiltonian

$$H = J_1 \sum_i \mathbf{S}_i \cdot \mathbf{S}_{i+1} + J_2 \sum_i \mathbf{S}_i \cdot \mathbf{S}_{i+2} - h \sum_i S_i^z \tag{2.1}$$

where $\mathbf{S}_i$ is a spin-1/2 operator at site i, $J_1 < 0$ (we set $J_1 := -1$) and $J_2 > 0$ (free parameter) are respectively ferromagnetic and antiferromagnetic coupling parameters, and h (free parameter) denotes a uniform magnetic field.

The classical ground state of hamiltonian (2.1) is ferromagnetic for $J_2 < 1/4$, and a spiral with monotonically increasing pitch angle with J_2 otherwise. The Lifshitz point[2] is located at $J_2 = 1/4$. In a magnetic field the spins develop a uniform component along the field, while the pitch angle in the plane transverse to the field axis is unaltered.

The zero field quantum mechanical phase diagram for $S = 1/2$ is still unsettled. Field theoretical work predicts a finite, but tiny gap accompanied by dimerization [40; 41] for $J_2 > 1/4$, which present numerical approaches are unable to resolve. The classical Lifshitz point $J_2 = 1/4$ is not renormalized for $S = 1/2$, and the transition point manifests itself on finite systems as a level crossing between the ferromagnetic multiplet and an exactly known singlet state [42]. The theoretical phase diagram at finite field has recently received considerable attention [43–45], triggered by experiments on quasi-1D cuprate helimagnets, like $LiCuVO_4$ ($J_2 = 2.2$) [27][3], Li_2ZrCuO_4 ($J_2 = 0.3$) [28], and $Rb_2Cu_2Mo_3O_{12}$ ($J_2 = 0.37$) [29]. As shown in Fig. 2.1, exchange interactions between the Cu^{2+} ions in CuO_2 chains building those compounds are well approximated by Eq. (2.1), assuming that the couplings beyond next nearest neighbors are neglected. One of the most peculiar features of the finite size magnetization process is the appearance of elementary magnetization steps of $\Delta S^z = 2, 3, 4$ in certain J_2 and h regions. This has been attributed to the formation of bound states of spin flips, leading to dominant spin-multipolar correlations close to saturation. A detailed phase diagram was however still lacking.

In this chapter, we first present the overall phase diagram of hamiltonian Eq. (2.1) and

[2] In a magnetic system, the Lifshitz point is a triple point where paramagnetic, ferromagnetic, and helicoidal phases meet [39]. The paramagnetic phase shows up if the phase diagram is extended to the finite temperature region, it meets the two other phases in the limit $T \searrow 0$.

[3] The values $J_1 = -1.6$ meV and $J_2 = 3.56$ meV from [27] are controversial: Ref. [46] claims that $J_2/J_1 > -1$, in agreement with the neutron scattering data and findings of independent theoretical studies.

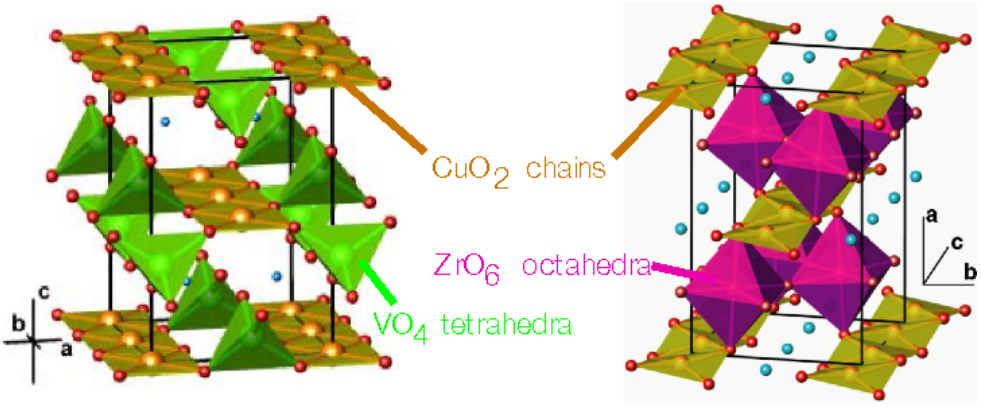

Figure 2.1: Structure of $LiCuVO_4$ from Ref. [27] (left) and Li_2ZrCuO_4 from Ref. [28] (right). In both compounds, interactions between the Cu^{2+} ions in the brown CuO_2 chains are described by hamiltonian Eq. (2.1).

characterize in details the multipolar Luttinger liquid (high field) and vector chiral phases (low field) we have obtained. We show that the multipolar and chiral correlations in the analytically known singlet ground state at the Lifshitz point agree qualitatively and even quantitatively well with a classical spiral, and put forward the novel point of view that the multipolar Luttinger liquid phases arising at high field are due to the destabilization of a spiral state. We provide evidences by revealing the mechanism driving this destabilization, and by showing that from the zero field physics of the model, this mechanism allows to predict the kind of multipolar phase that is realized at higher field. We finally show that this result sheds new light on previously discovered [19; 20] spin-multipolar phases in two-dimensional $S = 1/2$ quantum magnets in a magnetic field.

2.2 Phase diagram

In Fig. 2.2, we present the overall numerical phase diagram [21; 47] of hamiltonian Eq. (2.1) as a function of J_2/J_1 and the magnetization m (normalized by the saturation magnetization m_{sat}). It was obtained by Exact Diagonalization (ED) on systems with up to $L = 64$ sites, complemented by Density Matrix Renormalization Group (DMRG) simulations on open systems with maximally 384 sites, retaining up to 800 basis states (refer to Appendix A for details about these numerical methods). On these finite systems, the magnetization is defined as $m := (1/L)\sum_i S_i^z$.

The phase diagram shows five different phases. The low magnetization region consists of a single vector chiral (or p-type spin nematic, see description in Chapter 1) phase (gray) with broken parity symmetry, long-range vector chiral order, and incommensurate spin

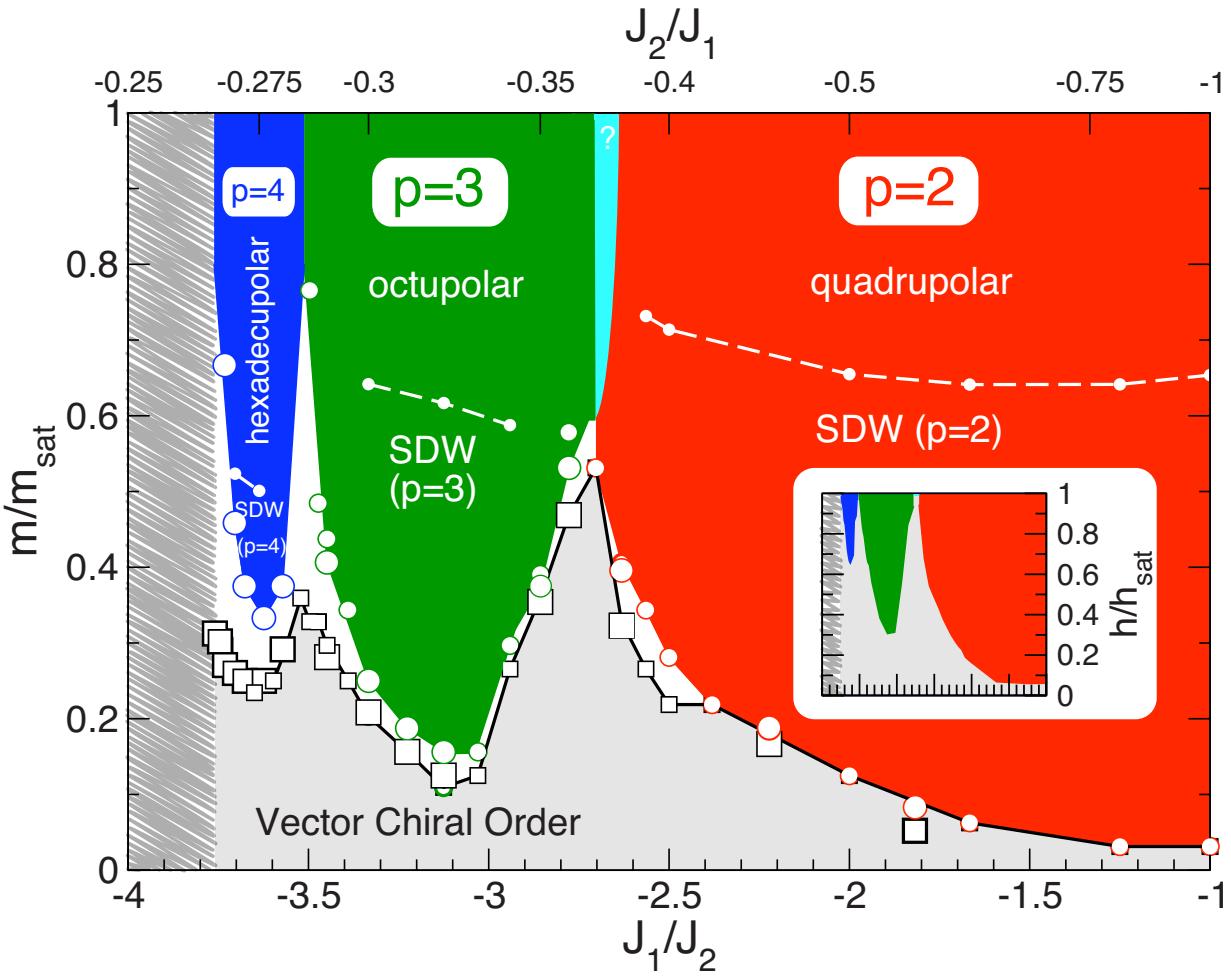

Figure 2.2: Phase diagram of the frustrated ferromagnetic chain [Eq. (2.1)] in the J_1/J_2 vs. $m/m_{\rm sat}$ plane. The gray low-m region exhibits vector chiral long-range order. The colored regions denote spin-multipolar Luttinger liquids of bound states of $p = 2, 3, 4$ spin flips. Close to saturation the dominant correlations are multipolar, while below the dashed crossover lines, the dominant correlations are of SDW(p)-type. The tiny cyan colored region corresponds to an incommensurate $p = 2$ phase. The white region denotes a metamagnetic jump. Finally the scribbled region close to the transition $J_2/|J_1| \searrow 1/4$ has not been studied here, but consists most likely of a low field vector chiral phase, followed by a metamagnetic region extending up to saturation magnetization. The inset shows the same diagram in the J_1/J_2 vs. $h/h_{\rm sat}$ plane.

correlations. Below the saturation magnetization we confirm the presence of three different multipolar Luttinger liquid phases (red, green and blue, see description in Chapter 1). The red phase extends up to $J_2 \to \infty$ [44], and its lower border approaches $m = 0^+$ in that limit.

All three multipolar liquids present a crossover as a function of m, where the dominant correlations change from spin-multipolar close to saturation to spin density wave (SDW)[4] character at lower magnetization. One also expects a tiny incommensurate $p = 2$ phase close to the $p = 3$ phase [45]. Finally, the multipolar Luttinger liquids are separated from the vector chiral phase by a metamagnetic transition, which occupies a larger and larger fraction of m as $J_2 \searrow 1/4$, leading to an absence of multipolar liquids with $p \geq 5$.

2.2.1 Vector chiral phase

For $m > 0$ we reveal a contiguous phase sustaining long-range vector chiral order [48] breaking discrete parity symmetry[5], similar to phases recently discovered for $J_1, J_2 > 0$ [49; 50]. The chiral correlator

$$\kappa^2(r, d) := \langle [\mathbf{S}_0 \times \mathbf{S}_d]^z [\mathbf{S}_r \times \mathbf{S}_{r+d}]^z \rangle \tag{2.2}$$

obtained by DMRG on a $L = 192$ system is displayed in the left panel of Fig. 2.3 for long distance correlations ($r = L/2$) between J_1 bonds ($d = 1$, black symbols) and J_2 bonds ($d = 2$, red symbols). It is an order parameter for this phase, and thus provides direct evidence of vector chiral order in the low magnetization region. The three chosen values of J_2 reflect positions underneath each of the three spin-multipolar Luttinger liquids shown in Fig. 2.2. The non-monotonic behavior of the correlations at very small m is probably a finite size artifact or convergence issue. Beyond the long-range order in the vector chirality, the system behaves as a single channel Luttinger liquid (with central charge $c = 1$)[6] with critical incommensurate transverse spin correlation functions [49]. The transition to the spin-multipolar phases at larger m seems to occur via metamagnetic behavior.

[4]SDW is a low-energy ordered state of solids consisting of a spatial modulation of collinear spins. It occurs at low temperature in anisotropic, low-dimensional materials or in metals that have high densities of states at the Fermi level. While in conventional antiferromagnets the magnetic moments have opposite orientation and are located at two crystallographic sublattices, the SDW is a many-particle phenomenon of an itinerant magnetism which is not fixed to the crystal lattice.

[5]Classically, states with chiral order emerge only together with a helical long-range order and simply distinguish left and right spirals. In 1D systems however, existence of a true helical order is prohibited by the Mermin-Wagner theorem (see Appendix B). In contrast to the helical spin order, the chiral order breaks only a discrete symmetry between left and right (parity), and can thus survive even in 1D. So, one can view the chiral order as a remnant of the classical helical order in a 1D spin system.

[6]The central charge c of a model characterizes its universality class. Roughly speaking, the central charge counts the number of gapless degrees of freedom, and $c = 1$ means that we deal with Luttinger liquids having a single component.

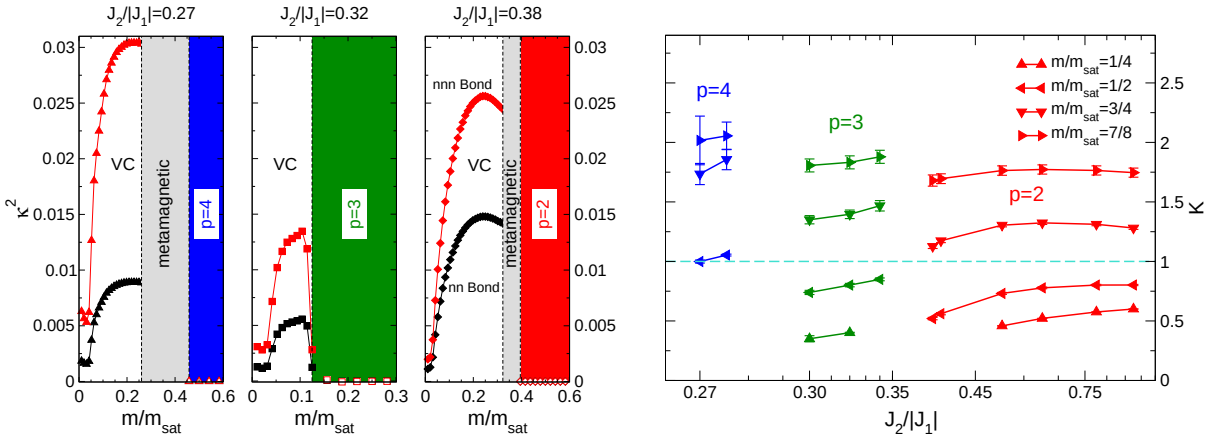

Figure 2.3: (Left panel) chiral order parameter $\kappa^2(r = L/2, d)$ [Eq. (2.2)] obtained from DMRG calculations on a 192-site system. Black and red symbols correspond to $d = 1, 2$ respectively. The three chosen values of J_2 reflect positions underneath each of the three spin-multipolar Luttinger liquids shown in Fig. 2.2. (Right panel) Luttinger parameters K for several magnetizations. At $K = 1$, along the dashed turquoise line, multipolar correlations of order p [Eq. (2.3)] and longitudinal spin correlations [Eq. (2.4)] decay with the same exponent.

2.2.2 Multipolar Luttinger liquid phases

Hamiltonian Eq. (2.1) presents unusual elementary step sizes $\Delta S^z > 1$ in some extended J_2 and m domains, where ΔS^z is independent on the system size [43]. This phenomenon has been explained based on the formation of bound states of $p = \Delta S^z$ magnons in the completely saturated state, and at finite m a description in terms of a single component Luttinger liquid of bound states has been put forward [44; 45]. We have determined the extension of the $\Delta S^z = 2, 3, 4$ regions in Fig. 2.2, based on ED simulations on systems sizes up to 32 sites and DMRG simulations on systems up to 192 sites. The boundaries are in very good agreement with previous results [43] where available. The $\Delta S^z = 3$ and 4 domains form lobes which are widest at $m = m_{\rm sat}$ and whose tips do not extend down to zero magnetization. The higher lobes are successively narrower in the J_2 direction. We have also searched for $\Delta S^z = 5$ and higher regions, but found them to be unstable against a direct metamagnetic transition from the vector chiral phase to full saturation[7]. Individual

[7] After the publication of our results, Heidrich-Meisner, McCulloch, and Kolezhuk [51] have shown that the length (in the m direction in Fig. 2.2) of the multipolar lobes can actually be tuned by considering an anisotropy Δ in the z-direction, which is the same for the J_1 and J_2 couplings (i.e. the new couplings in the z-direction are $\Delta J_1 S^z_i S^z_{i+1}$ and $\Delta J_2 S^z_i S^z_{i+2}$). $\Delta < 1$ moves the tip of the lobes upwards, while $\Delta > 1$ moves them downwards. We have tried (by ED on systems up to size $L = 30$) to make the $p = 5$ lobe appear with a small $\Delta > 1$ anisotropy but did not succeed, the $p = 5$ lobe is – as in the isotropic $\Delta = 1$ case – covered by the metamagnetic transition.

bound states of $p \geq 5$ magnons do exist (see Fig. 2.5), but they experience a too strong mutual attraction to be thermodynamically stable.

An exciting property of the Luttinger liquids of p bound magnon states [45] is that the transverse spin correlations are exponentially decaying as a function of distance due to the binding, while p-multipolar spin correlations

$$M_p(r) := \left\langle \prod_{n=0}^{p-1} S^+_{0+n} \prod_{n=0}^{p-1} S^-_{r+n} \right\rangle \sim (-1)^r \left(\frac{1}{r}\right)^{1/K} \tag{2.3}$$

(K is the Luttinger parameter) are critical with propagation vector π (multipolar correlations with $p' < p$ also decay exponentially). $p = 2, 3, 4$ correspond to quadrupolar, octupolar, and hexadecupolar correlations respectively. Therefore they can be considered as 1D analogues of spin-multipolar ordered phases found in higher dimensions. Another important correlation function is the longitudinal spin correlator, which is also critical [45]

$$\langle S^z_0 S^z_r \rangle - m^2 \sim \cos\left[\frac{(1 - m/m_{\rm sat})\pi r}{p}\right] \left(\frac{1}{r}\right)^K . \tag{2.4}$$

We verified numerically $c = 1$ and determined the Luttinger parameter K as a function of m and J_2 by fits to the local S^z profile (Friedel oscillations) in DMRG simulations.

An important information is contained in the crossover line $K = 1$ where p-multipolar and longitudinal spin correlations decay with the same exponent. This crossover line is shown for the three lobes in Fig. 2.2. Close to saturation the spin-multipolar correlations dominate while towards the tip of the lobes the longitudinal spin correlations decay more slowly, characterizing a spin density wave [SDW(p) phase]. The analogy with a Luttinger liquid of hardcore bosons of bound states is useful: the Luttinger parameter is $K = 2$ at $m = m_{\rm sat}$ and decreases with the concentration of hardcore bosons of bound states. For a fixed J_2 value for instance, this concentration decreases with the magnetization, K is thus increasing with m. On the contrary, the Luttinger liquid of hardcore bosons of bound states becomes more dilute when increasing p at constant m (the number of magnons in the bound states increases, hence the number of bound states decreases). One can therefore understand why the crossover line $K = 1$ is rather flat in the J_2 direction, but drops to lower m values when going from $p = 2$ to 3 and 4.

Very recently, Zhitomirsky and Tsunetsugu [52] have developed an analytical approach to study the zero-temperature properties as well as the low-energy magnetic excitations of a condensate of two-magnon bound states ($p = 2$), exploiting the analogy with bound electron pairs in a BCS superconductor.

2.2.3 Experimental relevance

If probed by neutron scattering experiments, the phases we point out are in principle distinguishable. The following responses are expected:

- a transverse Bragg peak in the vector chiral phase (low field) due to the criticality of the transverse spin correlations,
- no transverse peak, but a longitudinal peak at wave vector $(\pi/p)(1 - m/m_{\mathrm{sat}})$ in SDW(p) phases (intermediate field) due to the criticality of the longitudinal spin correlations (transverse correlations are gapped),
- no peak in the nematic-like p-multipolar phases (high field).

Recently, Sato, Momoi, and Furusaki [53; 54] showed that multipolar Luttinger liquids are also detectable by nuclear magnetic resonance (NMR) experiments. The relaxation rate in a multipolar Luttinger liquid decreases with lowering temperature (due to the gapped nature of transverse spin correlations), while it diverges in a more conventional Luttinger liquid (e.g. the spin-1/2 antiferromagnetic chain and ladder in a magnetic field).

One must keep in mind that in quasi-1D compounds the single spin chains Eq. (2.1) still experience a weak – but nonetheless non-vanishing – interchain coupling (IC) between them, which we neglect. However, this IC can have important consequences on the physics of multipolar phases we have described above: using DMRG combined with other techniques, Nishimoto and collaborators [55] showed that an (even weak) IC can readily eliminate them, especially for $p \geq 3$. In fact, they predict that for most CuO_2 chain systems studied so far, except probably $LiCuVO_4$, the IC is too strong to allow for multipolar phases. These predictions agree with experimental data available so far: strong signals of the stabilization of a quadrupolar phase in $LiCuVO_4$ were indeed reported by Svistov and collaborators [56] very recently[8], whereas evidences of the stabilization of multipolar phases in other kinds of CuO_2 chains have never been reported yet.

[8]Ref. [56] actually determines the magnetic field h_{quad} above which the quadrupolar phase is believed to be entered (SDW to quadrupolar crossover). h_{quad} is defined as the field at which the magnetic susceptibility (measured on $LiCuVO_4$ with a pulse field technique) exhibits a peak, the magnetization increases very fast upon approaching h_{quad} and reaches 95% of the saturation value at h_{quad}. The field difference $h_{\mathrm{sat}} - h_{\mathrm{quad}}$ they obtain agrees with the theoretical estimations of Ref. [52], which strengthens the opinion of the authors that the new phase between h_{quad} and h_{sat} they point out may indeed be identified with a quadrupolar phase.

2.3 Comparison between classical and quantum correlations in a spiral state

In order to understand how a classical spiral can be destabilized towards quantum multipolar phases, it is in a first step necessary to realize that remnants of the classical spiral survive to the quantum fluctuations. This is the aim of this section.

2.3.1 Chiral & multipolar correlators in a classical spiral

We consider a classical spiral with spins of length S, parametrized by

$$\mathbf{S}_j = S \begin{pmatrix} \cos(qj)\cos(\vartheta) \\ \sin(qj)\cos(\vartheta) \\ \sin(\vartheta) \end{pmatrix} \tag{2.5}$$

with propagation vector q and canting angle ϑ due to the magnetic field. The ground state of hamiltonian Eq. (2.1) is a ferromagnet for $J_2 < 1/4$. Otherwise, the energy is minimized for

$$q = \arccos\left(\frac{1}{4J_2}\right) \in [0, \pi/2] \qquad \text{and} \qquad \vartheta = \arcsin\left[\frac{4hJ_2}{S(4J_2-1)^2}\right] \in [0, \pi/2].$$

Using the substitution $S_j^{\pm} \to S_j^x \pm i S_j^y$, the classical spiral displays vector chiral correlations of the form

$$\langle [\mathbf{S}_0 \times \mathbf{S}_d]^z [\mathbf{S}_r \times \mathbf{S}_{d+r}]^z \rangle \to S^4 \cos^4(\vartheta) \sin^2(qd), \tag{2.6}$$

and multipolar correlations of order $p = 1$ (spin, dipolar), $p = 2$ (quadrupolar), $p = 3$ (octupolar), and $p = 4$ (hexadecupolar)

$$\begin{aligned}
&\langle S_0^+ S_r^- + h.c. \rangle = 2\langle S_0^x S_r^x \rangle + 2\langle S_0^y S_r^y \rangle \to 2S^2 \cos^2(\vartheta)\cos(qr) \\
&\langle S_0^+ S_1^+ S_r^- S_{r+1}^- + h.c. \rangle \to 2S^4 \cos^4(\vartheta)\cos(2qr) \\
&\langle S_0^+ S_1^+ S_2^+ S_r^- S_{r+1}^- S_{r+2}^- + h.c. \rangle \to 2S^6 \cos^6(\vartheta)\cos(3qr) \\
&\langle S_0^+ S_1^+ S_2^+ S_3^+ S_r^- S_{r+1}^- S_{r+2}^- S_{r+3}^- + h.c. \rangle \to 2S^8 \cos^8(\vartheta)\cos(4qr)
\end{aligned} \tag{2.7}$$

Note that if the in-plane spin correlations have propagation vector q, then the in-plane multipolar correlations of order p propagate with vector $q_p = pq$.

2.3.2 A quantum spiral: the uniformly distributed resonating valence bond (UDRVB) state

Let us now consider the effect of quantum fluctuations. At the Lifshitz point $J_2 = 1/4$, the singlet ground state (that is degenerate with the ferromagnetic one) is analytically

explicitly known [42] to be the uniformly distributed resonating valence bond (UDRVB) state given by

$$|\mathrm{UDRVB}\rangle := \frac{1}{\mathcal{N}} \sum [i,j][k,l][m,n]\cdots$$

where $[i,j]$ denotes two sites i and j that are paired up in a singlet state. The summation runs over all combinations of ordered pairs of spins $i<j, k<l, m<n, \cdots$, and $\mathcal{N}$ is some normalizing factor such that $\langle \mathrm{UDRVB}|\mathrm{UDRVB}\rangle = 1$. The spin correlations of the UDRVB state have been obtained analytically [42] in the thermodynamic limit

$$\lim_{L\to\infty} \langle \mathrm{UDRVB}|S_i^+ S_{i+r}^-|\mathrm{UDRVB}\rangle = \frac{1}{6}\cos\left(\frac{2\pi}{L}r\right), \tag{2.8}$$

suggesting that this state should be considered as a quantum analog of a long wavelength spiral with an L-dependent propagation vector $q = 2\pi/L$. To study this analogy in more details, we have numerically computed the vector chiral correlations $\kappa^2(r,d)$ Eq. (2.2) and the spin-multipolar correlations $M_p(r)$ Eq. (2.3) up to order $p=4$ in the UDRVB state. These results are presented in the left panel of Fig. 2.4. For comparison, the exact result

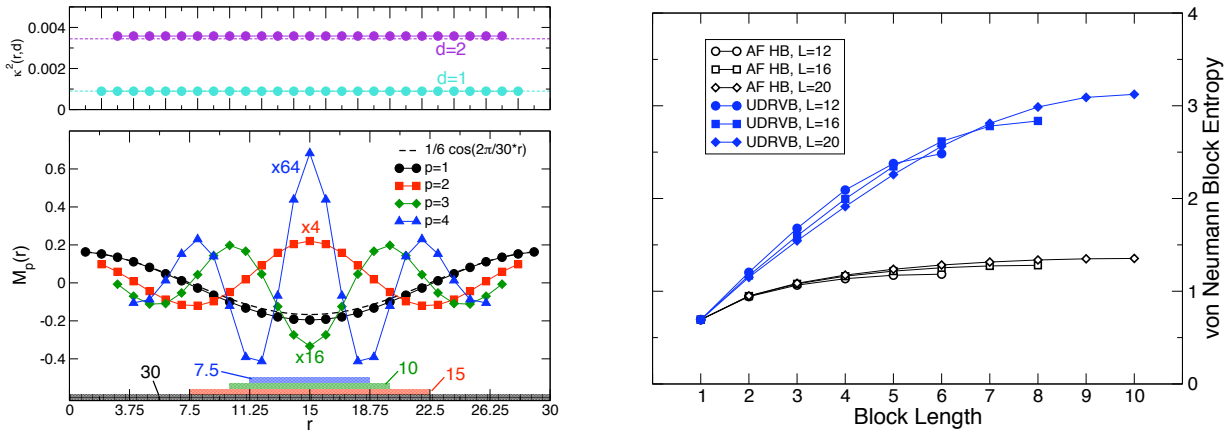

Figure 2.4: (Left) Vector chiral (upper panel) and spin-multipolar (lower panel) correlators of the UDRVB state for $L=30$ from ED (full symbols). They behave qualitatively as those of the classical spiral Eqs. (2.6) and (2.7). The multipolar correlator of order p has a propagation vector $q_p = pq$ (periods are given on the bottom), q being the propagation vector of the UDRVB spiral. (Right) Comparison of the von Neumann entropy of a block of l ($1 \le l \le L/2$) consecutive spins for the unfrustrated antiferromagnetic Heisenberg chain and the UDRVB state.

Eq. (2.8) for $p=1$ is drawn as well. We aim to stress that the simple relations between the propagation vectors of multipolar correlation functions in a classical spiral are also obeyed in the quantum analog, i.e. in the UDRVB state.

We first notice that vector chiral correlations (Fig. 2.4, left plot, upper panel) of the UDRVB state are small and independent on the distance r, which – as shown by Eq. (2.6) – is in complete agreement with a spiral. Furthermore, the multipolar correlations (Fig. 2.4, left plot, lower panel) indeed follow the phenomenology of the classical spiral, where the p-multipolar correlations have a propagation vector pq for a spiral with propagation vector q. A quantitative comparison is more involved due to the sizable finite size effects at distance $\sim L/2$, and the fact that the UDRVB state is a singlet, which requires a contraction of all components of the $SU(2)$ multipolar operators of rank p. Such a comparison is performed in Appendix C, which shows that the spin-multipolar correlations in the UDRVB state are in good quantitative agreement with the spin-multipolar correlations in a classical spiral with propagation vector $q = 2\pi/L$.

We close this section by presenting the peculiar entanglement entropy of the UDRVB state in comparison to the well studied unfrustrated antiferromagnetic Heisenberg chain (right plot of Fig. 2.4) for periodic systems. First of all, the UDRVB state has a much larger entanglement entropy for large blocks than the Heisenberg chain for the same block length [57]. Secondly, the finite size behavior of the entanglement entropy for a given block size is not monotonous in the UDRVB state, again in contrast to the pure Heisenberg chain. This might be due to the fact that its propagation vector $q = 2\pi/L$ depends on the system size, so that the local structure of the spiral changes as L is increased.

2.4 Interpretation: a locking rule driving spiral states towards multipolar phases

Let us first investigate how the longitudinal and transverse equal-time spin structure factors $S^{zz}(q)$ and $S^{xx}(q)$ evolve as a function of the magnetization m. In the left plot of Fig. 2.5 we display the location of the maximum of $S^{zz}(q)$ and $S^{xx}(q)$ (disregarding the $q = 0$ peak in $S^{zz}(q)$ due to the total magnetization) for three representative values of J_2. At $m = 0$, it is known that $S(q)$ has a maximum at an incommensurate position $q_{\max}(J_2)$, which is strongly renormalized compared to the classical expectation $q_{\max}^{\text{class}}(J_2) = \arccos[1/(4J_2)]$, see also lower right panel of Fig. 2.5. In the low magnetization region, corresponding to the vector chiral phase, the location of the maxima of both structure factors are only weakly dependent on m, and in a first approximation remains the same as for $m = 0$. However as m is increased, the $q_{\max}$ of $S^{zz}(q)$ locks onto a straight line with slope $-\pi/p$. It seems that if $q_{\max}(J_2)/\pi > 1/3$ at $m = 0$, the magnetization process enters the $(p = 2)$-multipolar phase at larger m. If instead $1/3 > q_{\max}(J_2)/\pi > 1/4$ at $m = 0$, the system will enter the $(p = 3)$-multipolar phase. Based on an extended analysis including many J_2, we are led to

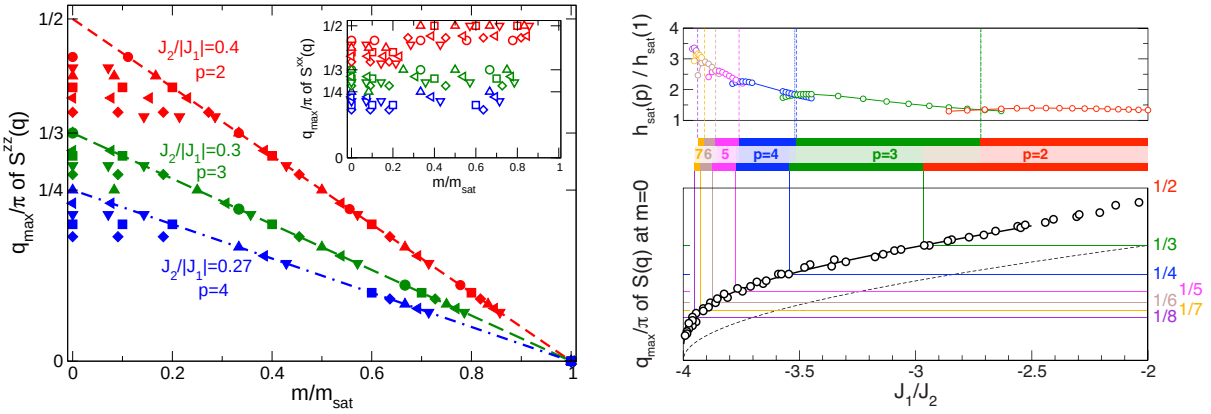

Figure 2.5: (Left) Propagating vector $q_{\rm max}$ maximizing the longitudinal (inset: transverse) spin structure factor as a function of the magnetization m for selected values of J_2, each one belonging to a different p sector at high m. The straight lines are guides to the eye and show $(\pi/p)(1-m/m_{\rm sat})$. The different symbols denote ED results on system sizes ranging from 18 up to 28 sites. (Right) Upper panel: ED results for the domain of stability of bound states of p spin flips above the saturated ferromagnetic state. Lower panel: Location $q_{\rm max}$ of the maximum of the zero field spin structure factor $S(q)$ as a function of J_2. The colored lines indicate the construction of the domain boundaries from the zero field physics, based on the locking rule Eq. (2.9). The thin dashed line displays $q_{\rm max}^{\rm class}$ for the classical model.

conjecture that if

$$1/p > q_{\rm max}(J_2)/\pi > 1/(p+1) \quad \text{at } m=0, \tag{2.9}$$

then $q_{\rm max}$ locks onto the line with slope $-\pi/p$ at higher magnetizations. According to the behavior of the longitudinal spin correlations in multipolar Luttinger liquids Eq. (2.4), the multipolar liquid of order p leads precisely to a slope of $-\pi/p$. Regarding the transverse spin correlations, Eqs. (2.3) and (2.9) now show that while $q_{\rm max}(J_2)$ of $S^{xx}(q)$ approximately equals π/p, the spin-multipolar correlations of order p are accurately *locked* to π, i.e. to a propagation vector p times as large as the propagation vector of transverse spin correlations, as in the spiral. Note that while the above considerations devoted to the classical spiral showed that many multipolar correlations are finite without actually selecting a specific one, in the frustrated ferromagnetic chain in a field, it is the additional locking mechanism $pq_{\rm max}(J_2)=\pi$, which is responsible for the selection of p.

Despite the fact that there are no stable multipolar Luttinger liquids with $p>4$, it is possible to examine the process of individual bound state formation by pushing previous calculations from $p\leq 4$ in Ref. [45] to $p=8$. We have performed ED without truncation on system sizes up to $L=64$, calculated the binding energy of p flipped spins [expressed

as $h_{\rm sat}(p)/h_{\rm sat}(p=1)]$[9] and displayed it in the upper panel of Fig. 2.5. A surprising series of stable bound states up to $p = 8$ is obtained, which are successively smaller in their J_2 extent, suggesting that $J_2 = 1/4$ is an accumulation point of $p \to \infty$ bound states. We now proceed to a comparison of the stability domain of the bound states to those predicted by locking rule Eq. (2.9) applied to the *zero field* structure factor. We fit a power law $q_{\rm max}(J_2) \propto (J_2 - 1/4)^\gamma$ (with $\gamma \approx 0.29$) to the finite size transition points, as shown by the bold black line in the lower panel of Fig. 2.5. This fitted line is used to construct the boundaries, giving rise to the lower color bar. The agreement between the transition boundaries in the upper and lower panels is excellent (apart from the $p = 2$ to $p = 3$ transition). It is striking that we are able to reproduce the domain of stability of bound states of magnons at the saturation magnetization, based solely on the spin structure factor obtained at zero field. This constitutes strong evidence for an approximate validity of locking rule Eq. (2.9) and the presence of a locking mechanism which pins the multipolar correlations to π at larger m as opposed to incommensurate transverse spin correlations for lower m. The transition from $p = 2$ to $p = 3$ is somewhat shifted compared to the prediction, and we attribute this discrepancy to the formation of a peculiar incommensurate $p = 2$ bound state [45; 58], leading to a collapse of the kinetic energy of the $p = 2$ bound state.

We furthermore stress that in the multipolar Luttinger liquid phase, our results predict a soft mode at the Fermi wave vector $(\pi/p)(1-m/m_{\rm sat})$ of the Luttinger liquid. A prominent property of Luttinger liquids is that they have soft modes at multiples of their Fermi wave vector, the *Oshikawa-Yamanaka-Affleck* (OYA) theorem (see Appendix B) stating the existence of a soft mode at momentum $\pi(1 - m/m_{\rm sat})$ is thus fulfilled. In the vector chiral phase however, it is unclear to us how this OYA soft mode appears. Fig. 2.6 illustrates these soft modes in the ($p = 2$)- and ($p = 3$)-multipolar phases (left and right panel respectively) in the energy spectra for different system sizes for $J_2 = 0.4$ (case $p = 2$) and $J_2 = 0.32$ (case $p = 3$) at half-saturation $m/m_{\rm sat} = 1/2$. Soft modes at momenta multiple of $(\pi/2)(1 - 1/2) = \pi/4$ (case $p = 2$) and $(\pi/3)(1 - 1/2) = \pi/6$ (case $p = 3$) are visible (dashed magenta lines), they are peaked downwards in the spectrum. These "reversed peaks" approach the zero excitation energy when increasing the system size.

[9] The quantity $h_{\rm sat}(p)$ is defined as $h_{\rm sat}(p) := [E_{\rm GS}(S_z = L/2) - E_{\rm GS}(S_z = L/2 - p)]/p$ where $E_{\rm GS}(S_z)$ is the ground state energy in the S_z magnetization sector. $h_{\rm sat}(p)$ has the units of a magnetic field and quantifies how energetically favorable it is to destabilize the ferromagnetic phase (as the field is decreased) by flipping p spins. Note that $h_{\rm sat}(p)/h_{\rm sat}(1) > 1\,\forall p \geq 2$ means that it is never favorable for the system to go directly from the ferromagnetic phase to a phase characterized by $\Delta S_z = 1$ steps (like the vector chiral one).

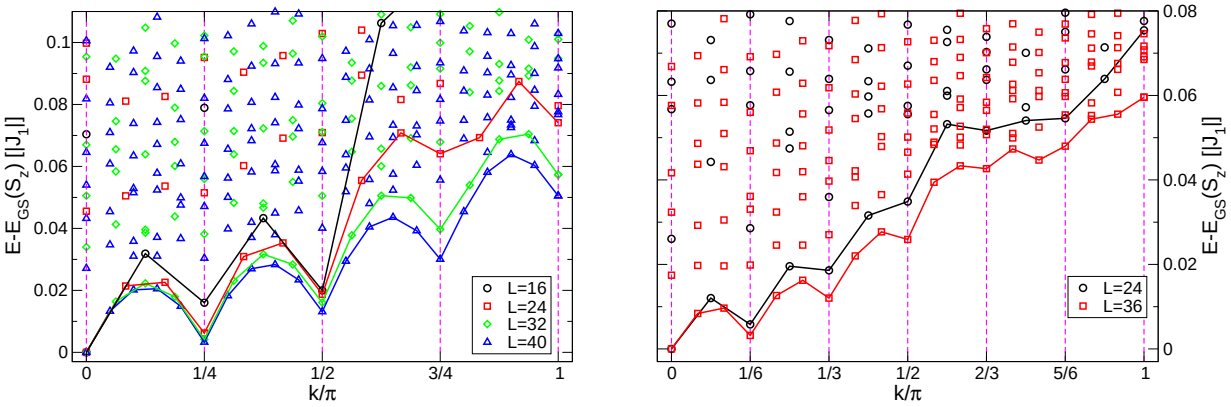

Figure 2.6: (Left) excitation energy spectra (the ground state energy of the magnetization sector is subtracted) of different chain lengths L for $J_2 = 0.4$ at $m/m_{\mathrm{sat}} = 1/2$. The system is in the $(p = 2)$-multipolar phase. For every L, the lowest energy levels of every momentum sector are joined together by solid lines, revealing that the spectra are peaked downwards at momenta multiple of $\pi/4$ (dashed magenta lines). These "reversed peaks" approach the zero excitation energy as L increases, making the soft modes well visible. (Right) the same in the case of the $(p = 3)$-multipolar phase for $J_2 = 0.32$ at $m/m_{\mathrm{sat}} = 1/2$. The soft modes lie at momenta multiple of $\pi/6$. Notice that finite size effects prevent the reversed peak at $k = 5\pi/6$ from showing up, even for the largest system $L = 36$.

2.5 A new approach to previously discovered multipolar phases

The idea that spin-multipolar phases can result from instabilities of spiral ordering is rather appealing, and not limited to 1D. It sheds new light on previously discovered spin-multipolar phases in two-dimensional spin-1/2 quantum magnets in a magnetic field. For instance, for the Heisenberg model on the square lattice with ferromagnetic nearest neighbor couplings, antiferromagnetic next-nearest neighbor couplings, and ring exchange in a magnetic field, it has been shown by Shannon, Momoi, and Sindzingre [19] that a bond quadrupolar phase exists close to the ferromagnetic state. The bond quadrupolar order is explained by a condensation of two-magnon bound states from the ferromagnetic side. Our results provide a complementary view as a destabilization of the neighboring antiferromagnetic striped collinear phase with momentum $(\pi, 0)$, see Fig. 2.7: in the striped collinear phase [panel (a)], the direction of the magnetic moments (i.e. the expectation value of S^z) is horizontally staggered and vertically uniform [panel (b)], this results in negative (red) bond quadrupolar expectation values for horizontal bonds and positive (black) bond quadrupolar expectation values for vertical bonds [panel (c)]. Once the quadrupolar phase

is entered [panel (c)→panel (d)], one observes that bond quadrupolar expectation values are indeed negative for horizontal bonds and positive for vertical ones [panel (d)]: the $(\pi, 0)$-spiral [panel (a)] has been destabilized towards the quadrupolar phase [panel (e)]. A similar process occurs in the multiple-spin exchange model on the triangular lattice, where an octupolar phase is surrounded by both a ferromagnetic and a canted antiferromagnetic spiral phase [20].

2.6 Conclusion

We have established the phase diagram of the frustrated ferromagnetic spin-1/2 Heisenberg chain in a uniform magnetic field. A vector chirally ordered phase, metamagnetic behavior and a sequence of spin multipolar Luttinger liquid phases up to hexadecupolar order have been identified. We have shown that the peculiar valence bond state at the Lifshitz point $J_2 = 1/4$ can be regarded as the quantum analog of the classical spiral ground state, in which multipolar correlations naturally occur. We have argued that above a certain magnetic field, spiral ordering is destabilized by quantum fluctuations via a locking mechanism, giving rise to higher order multipolar spin correlations. This point of view is consistent with existing phase diagrams exhibiting such phases. It might therefore be used to predict multipolar phases in models with some form of spiral ordering. It is an open question whether these fluctuation driven multipolar phases and the locking mechanism also appear for spins $S > 1/2$.

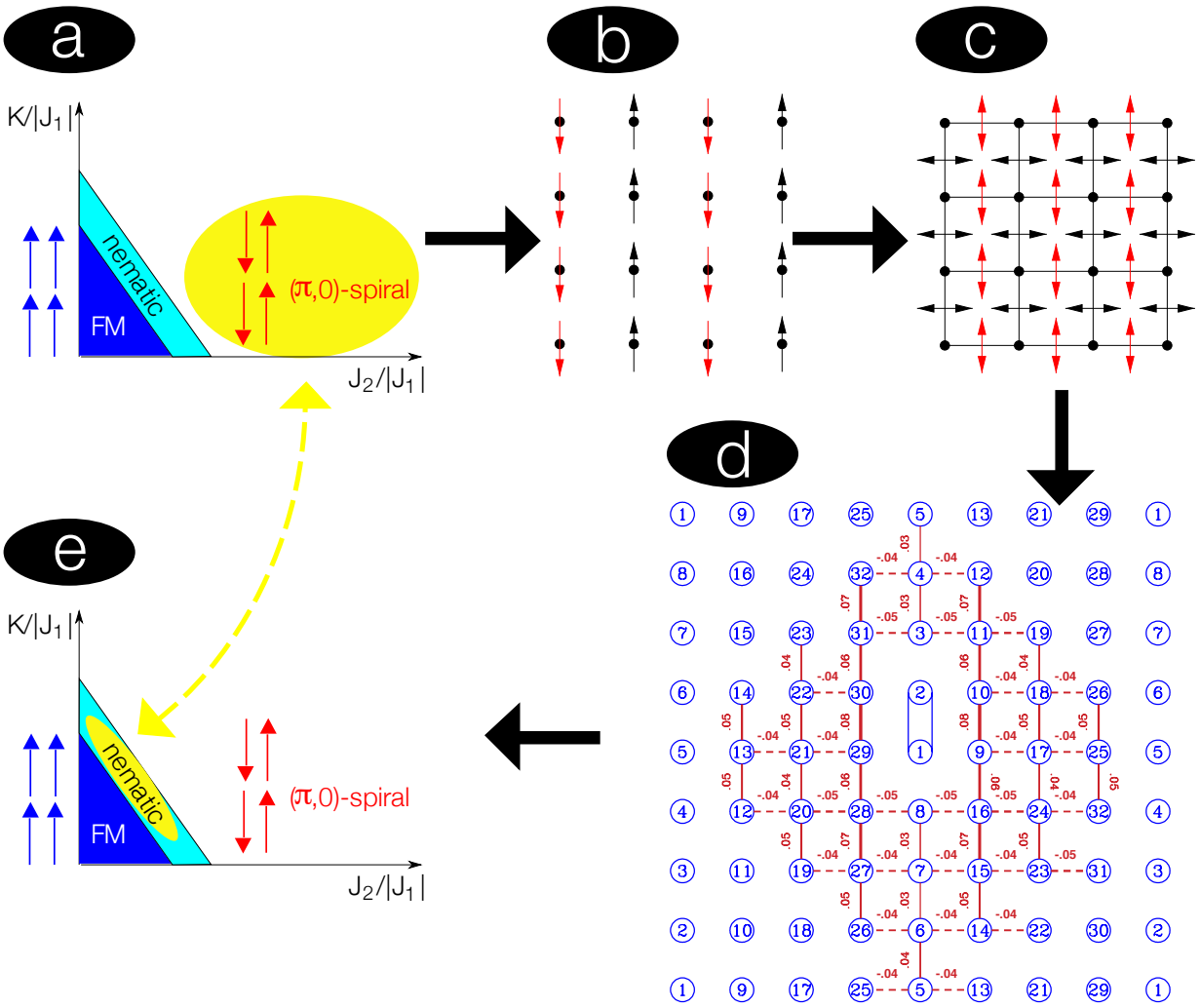

Figure 2.7: Illustration of the process we point out to drive the $(\pi, 0)$ spiral towards the quadrupolar (or n-type nematic) phase in the $J_1 < 0$, $J_2 > 0$ Heisenberg model on the square lattice with ring exchange K in a magnetic field. In the magnetically ordered $(\pi, 0)$ spiral state on the square lattice [panel (a)], the spins are arranged in collinear stripes [panel (b)]. The bond quadrupolar expectation values in this spiral state are shown in panel (c), where the black and red colors denote positive and negative expectation values (uniform d-wave configuration). Quadrupolar correlations become dominant as the quadrupolar phase is entered, exhibiting the bond quadrupolar correlation pattern shown in panel (d), with the same uniform d-wave configuration. The quadrupolar phase [panel (e)] is reached, the magnetic spin ordering is lost.

CHAPTER 3

The correlation density matrix (CDM) tool for extracting dominant correlations

3.1 Introduction

The nature of a state of a strongly interacting quantum many-body system in general – of a quantum spin system in particular – is governed by its dominant correlations. In some models, the type of dominant correlations we are likely to encounter is intuitive and can sometimes be easily foreseen. In bosonic systems for instance, one straightforwardly understands why the Mott insulating phase is stabilized in the Bose-Hubbard model at commensurate filling when the hopping term is small [59][1]. Regarding spin systems, typical phases of quantum dimer models naturally tend to be valence bond crystals [8] (even though topological order can appear as well [60; 61]). The type of Néel phases that are realized in non-frustrated, or weakly frustrated models (with weak quantum fluctuations) is also generally easy to guess. With the aid of a simple sketch, it is for instance natural to suspect that at zero temperature the $\mathbf{q} = 0$ Néel order is stabilized in the Heisenberg J_1–J_2

[1] This model was indeed originally introduced in order to describe the superfluid to insulator phase transition in ^{4}He, but is generally applicable to any system of interacting bosons on a lattice.

($J_1 = J_2 > 0$) model on the kagomé lattice [62], or that the Heisenberg J_1–J_2 ($J_1, J_2 > 0$) model on the square lattice sustains order with wave vectors (π, π) and $(0, \pi)/(\pi, 0)$ respectively "well below" and "well above" the point of maximal frustration $J_2/J_1 = 1/2$ [3]. On the other hand if the frustration is high, or if the coordination number of the lattice is particularly low (resulting in large quantum fluctuations), the guess of relevant order parameters is a challenging task most of the time, even if it is sometimes possible by comparison with similar models, or using theoretical arguments [13; 18–21; 49; 63]. Highly frustrated magnets are good candidates for displaying exotic – thus unexpected – phases, which renders the choice of relevant operators very difficult and subtle.

In some cases, one does not have any a priori knowledge about the correlations which may dominate in a quantum system. In order to circumvent this problem, the idea of extracting those dominant correlations between any two disjoint blocks by singular value decomposing the correlation density matrix (CDM) between these blocks has been put forward a couple of years ago [25; 64]. This process is unbiased – the relevant correlators are yielded by the method itself – and does thus not require any a priori knowledge of the system. Any phase will be detected, however exotic it may be.

This chapter is devoted to the presentation of the features and the mathematical properties of this novel method, which is then illustrated using some concrete examples. We first introduce it within a technical framework and generalize it at finite temperature. All the details are given about how to extract the dominant correlations between two arbitrarily selected disjoint blocks. Some consequences of lattice or state symmetries are investigated and illustrated by examples. The link between the CDM and the mutual information – which is a well known quantity in quantum information theory [65] – is addressed, and the states providing the maximal correlation between the two blocks (of various sizes) are identified. Finally, the method is applied for illustrative purposes on the J_1–J_2 model on a spin-1/2 chain at zero and finite temperature, and on its 2D analog on a square lattice at zero temperature. In this latter case, the poorly understood regime around the maximal frustration point $J_2/J_1 = 1/2$ is investigated as well.

3.2 The correlation density matrix object

We start with the definition of the correlation density matrix object which can be computed in any pure state of a system as well as in mixed thermal states. The properties and features of this tool are then given in a next step. We finally explain how to – and why – singular value decompose it in order to extract the dominant correlations.

3.2.1 Definition & properties of the correlation density matrix

Let a quantum many-body system be formed by two disjoint blocks A and B, and by their environment E, as shown in Fig. 3.1. Consider some state $|\psi\rangle$ (not necessarily the ground state) of this system whose dominant correlations we ignore. The reduced density matrices

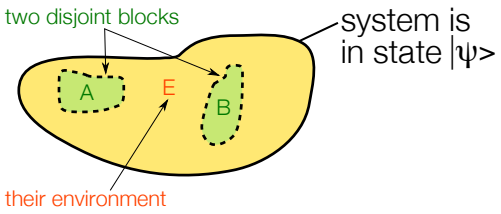

Figure 3.1: (Color online) The two disjoint blocks A and B and their environment E form a many-body system, which is in the pure state $|\psi\rangle$.

of blocks A, B and of the superblock $A \cup B$ are constructed by forming the density matrix of the global system $|\psi\rangle\langle\psi|$ and tracing out the irrelevant degrees of freedom

$$\begin{aligned} \rho_A &:= \mathrm{Tr}_{B\cup E}|\psi\rangle\langle\psi| \\ \rho_B &:= \mathrm{Tr}_{A\cup E}|\psi\rangle\langle\psi| \\ \rho_{A\cup B} &:= \mathrm{Tr}_E|\psi\rangle\langle\psi|. \end{aligned} \tag{3.1}$$

The correlation density matrix (CDM) between A and B is defined as

$$\rho^c_{AB} := \rho_{A\cup B} - \rho_A \otimes \rho_B. \tag{3.2}$$

If the two blocks are completely uncorrelated, we then have $\rho_{A\cup B} = \rho_A \otimes \rho_B$ and thus $\rho^c_{AB} = 0$. ρ^c_{AB} captures all informations about how block A is correlated to B and vice versa (it is symmetric in A and B). Indeed, in the same way that the density matrix $\rho_{A\cup B}$ allows to compute the correlation between any pair of operators O_A and O_B acting within A and B

$$\langle O_A O_B\rangle = \mathrm{Tr}_{(A\cup B)}\left[\rho_{A\cup B} O_A O_B\right],$$

the CDM yields the corresponding *connected* correlation (see Appendix D for a detailed proof)

$$\langle O_A O_B\rangle - \langle O_A\rangle\langle O_B\rangle = \mathrm{Tr}_{(A\cup B)}\left[\rho^c_{AB} O_A O_B\right]. \tag{3.3}$$

In particular if $O_A = \mathbb{1}_A$ and $O_B = \mathbb{1}_B$ we have

$$\langle \mathbb{1}_A \mathbb{1}_B\rangle - \langle \mathbb{1}_A\rangle\langle \mathbb{1}_B\rangle = 0 = \mathrm{Tr}_{(A\cup B)}\rho^c_{AB},$$

ρ^c_{AB} must therefore be traceless.

This formalism can also be adapted for the investigation of the finite temperature physics of a quantum model. In this case, the density matrices Eq. (3.1) have to be replaced by thermal density matrices of (mixed) thermal states

$$\rho_A(\beta) := \frac{1}{Z}\sum_n e^{-\beta E_n}\rho_A^{(n)}$$
$$\rho_B(\beta) := \frac{1}{Z}\sum_n e^{-\beta E_n}\rho_B^{(n)}$$
$$\rho_{A\cup B}(\beta) := \frac{1}{Z}\sum_n e^{-\beta E_n}\rho_{A\cup B}^{(n)},$$

in Eq. (3.2). The sums run over the entire spectrum of the whole quantum many-body system, $\beta := 1/(k_B T)$ is the inverse temperature, $\rho_A^{(n)}$, $\rho_B^{(n)}$, and $\rho_{A\cup B}^{(n)}$ are the density matrices computed in the eigenstate of energy E_n, and $Z := \sum_n e^{-\beta E_n}$. The thermal CDM is then given by

$$\rho_{AB}^c(\beta) := \rho_{A\cup B}(\beta) - \rho_A(\beta)\otimes\rho_B(\beta)$$

and can be singular value decomposed following the same procedure as for the zero temperature case.

Notation: from now on, ρ_{AB}^c can refer as well to the finite temperature case $\rho_{AB}^c(\beta)$ as to the zero temperature one $\rho_{AB}^c = \rho_{AB}^c(\beta = \infty)$.

3.2.2 Singular value decomposition of the correlation density matrix: technical details

Once the CDM between the two selected disjoint blocks A and B is known, the purpose is to extract the dominant correlations between A and B from this matrix. Each index of the $\dim_{\mathcal{H}}(A)\dim_{\mathcal{H}}(B)\times\dim_{\mathcal{H}}(A)\dim_{\mathcal{H}}(B)$[2] matrix ρ_{AB}^c refers to basis elements of block A and to basis elements of block B at once. The first step if we want informations about how A is correlated to B, is to transform ρ_{AB}^c into a new $\dim_{\mathcal{H}}^2(A)\times\dim_{\mathcal{H}}^2(B)$ matrix – say K – whose first index refers to basis elements of block A only, and whose second index refers to basis elements of block B only.

Indices without prime symbol refer to block A, those with a prime symbol refer to block B, and commas separate the two indices of a matrix. Underlined indices that are not

[2] $\dim_{\mathcal{H}}(*)$ denotes the dimensionality of the Hilbert subspace which spans block $*$ (and not the number of sites inside $*$).

separated by a comma must be considered as fused indices. We introduce the operators $\widetilde{X}_{\underline{ij}}$ and $\widetilde{Y}_{\underline{i'j'}}$ – acting within A and B respectively – with the matrix elements

$$\langle k|\widetilde{X}_{\underline{ij}}|l\rangle = \delta_{i,k}\delta_{j,l} \quad \text{and} \quad \langle k'|\widetilde{Y}_{\underline{i'j'}}|l'\rangle = \delta_{i',k'}\delta_{j',l'},$$

$\widetilde{X}_{\underline{ij}}$ are $\dim_{\mathcal{H}}(A)\times\dim_{\mathcal{H}}(A)$-matrices and $\widetilde{Y}_{\underline{i'j'}}$ are $\dim_{\mathcal{H}}(B)\times\dim_{\mathcal{H}}(B)$-matrices. It is then easy to realize that the CDM can be written as

$$\rho^c_{AB} = \sum_{i,j=1}^{\dim_{\mathcal{H}}(A)} \sum_{i',j'=1}^{\dim_{\mathcal{H}}(B)} K_{\underline{ij},\underline{i'j'}} \widetilde{X}_{\underline{ij}} \otimes \widetilde{Y}_{\underline{i'j'}} \tag{3.4}$$

provided that elements of ρ^c_{AB} are related to those of K as

$$(\rho^c_{AB})_{\underline{kk'},\underline{ll'}} = K_{\underline{kl},\underline{k'l'}}.$$

Thus, ρ^c_{AB} and K have the same matrix elements, which are just ordered differently: the first index of K refers to basis elements of block A and the second one to those of block B. Unlike ρ^c_{AB}, K is generally not square unless $\dim_{\mathcal{H}}(A) = \dim_{\mathcal{H}}(B)$.

The idea is now to perform a (numerical) singular value decomposition (SVD) of K, i.e. to write it in the form

$$K = U\Sigma V^\dagger, \tag{3.5}$$

where $\Sigma = \mathrm{diag}(\sigma_1^{AB}, \sigma_2^{AB}, \cdots, \sigma_{D^2}^{AB})$ is a $\dim^2_{\mathcal{H}}(A) \times \dim^2_{\mathcal{H}}(B)$ diagonal matrix containing the non-negative singular values (SVs) sorted in decreasing order $\sigma_1 \geq \sigma_2 \geq \sigma_3 \geq \ldots \geq \sigma_{D^2} \geq 0$, and $D^2 := \min\{\dim^2_{\mathcal{H}}(A), \dim^2_{\mathcal{H}}(B)\}$. U is a unitary $\dim^2_{\mathcal{H}}(A) \times \dim^2_{\mathcal{H}}(A)$ matrix, and V is a unitary $\dim^2_{\mathcal{H}}(B) \times \dim^2_{\mathcal{H}}(B)$ matrix. By plugging Eq. (3.5) into Eq. (3.4) we get

$$\rho^c_{AB} = \sum_{i=1}^{D^2} \sigma_i^{AB} X_i^{(A)} \otimes Y_i^{(B)\dagger}, \tag{3.6}$$

where we have introduced the operators

$$X_i^{(A)} := \sum_{k,l=1}^{\dim_{\mathcal{H}}(A)} U_{\underline{kl},i} \widetilde{X}_{\underline{kl}} \quad \text{and} \quad Y_j^{(B)\dagger} := \sum_{k',l'=1}^{\dim_{\mathcal{H}}(B)} V^\dagger_{j,\underline{k'l'}} \widetilde{Y}_{\underline{k'l'}}$$

($i = 1, \cdots, \dim^2_{\mathcal{H}}(A)$ and $j = 1, \cdots, \dim^2_{\mathcal{H}}(B)$) which act within A and B respectively, and are orthonormalized with respect to the Frobenius norm (follows from unitarity of U and V)

$$\mathrm{Tr}\left(X_i^{(A)} X_j^{(A)\dagger}\right) = \delta_{i,j} \qquad \text{and} \qquad \mathrm{Tr}\left(Y_i^{(B)} Y_j^{(B)\dagger}\right) = \delta_{i,j}. \tag{3.7}$$

Remark: from now on, index "AB" of σ_i^{AB} will be dropped any time this omission does not confuse the reader.

Eq. (3.6) is of central importance: one can check that the SVs "quantify" the strength of the connected correlations between the X and the Y operators since

$$\langle X_i^{\dagger(A)} Y_j^{(B)} \rangle - \langle X_i^{\dagger(A)} \rangle \langle Y_j^{(B)} \rangle = \delta_{i,j}\, \sigma_i \tag{3.8}$$

(this relation is derived using the property Eq. (3.3) and the decomposition Eq. (3.6) of the CDM, as well as the orthogonality relation Eq. (3.7)), in that sense, the decomposition Eq. (3.6) allows to identify the strongest correlations (corresponding to the highest SVs) without requiring any a priori knowledge about the quantum state under study. The dominant correlation is therefore given by

$$\langle X_1^{\dagger(A)} Y_1^{(B)} \rangle - \langle X_1^{\dagger(A)} \rangle \langle Y_1^{(B)} \rangle = \sigma_1 \geq 0.$$

Note that the signs and the phases are absorbed in the definition of $X_1^{(A)}$ and $Y_1^{(B)}$ ($\sigma_i \geq 0\ \forall i$).

Once the decomposition Eq. (3.6) is numerically performed, the resulting operators $X_i^{(A)}$ and $Y_i^{(B)\dagger}$ are well defined (up to some phase factor), and determined in an unbiased way by the SVD. In order to understand their physical meaning it is however often useful to decompose them in a complete basis given by physically meaningful operators. Bases of the spaces spanned by the operators acting on two and three spins $S = 1/2$ are given in Appendix E.

3.3 Upper and lower bounds on singular values

3.3.1 Upper bound on total and on individual correlations

For a given configuration of blocks A and B, the sum of the squared SVs resulting from the SVD provides a natural measure of the total correlation between A and B. This sum is proven in Ref. [25] to have as upper bound

$$\sum_{i=1}^{D^2} \sigma_i^2 = \| \rho_{AB}^c \|_F^2 \leq 1 - 1/D^2, \tag{3.9}$$

it is thus not an extensive quantity in the size of A and B. The equality between the sum of the squared SVs and the squared Frobenius norm of the CDM $\| \rho_{AB}^c \|_F^2 := \mathrm{Tr}(\rho_{AB}^c\, \rho_{AB}^{c\dagger})$ can

be shown easily. The upper bound Eq. (3.9) is reached in the case of maximally correlated blocks, such kinds of block configurations are identified and discussed in Section 3.5.

We do not have any analytical result for an upper bound on every individual SV. We have performed a numerical simulation of 71.700.000 CDMs between two blocks A and B, each containing one spin-1/2, see the right panel of Fig. 3.4 in Section 3.5. It turns out that the largest SV we have simulated was 0.4954. Furthermore for two blocks containing one site, the largest SV of the state identified in Section 3.5 that reaches the bound Eq. (3.9) is indeed 1/2. This is therefore the largest value of SV we have observed so far, and it seems that $\sigma_i \leq 1/2 \ \forall i$ is an upper bound on the individual SVs, but this is only a hypothesis and should be considered with care.

3.3.2 Lower bound on the highest singular value of enlarged blocks

Let A and B be two disjoint blocks with the same size (i.e. number of sites) in a spin-S system, and let the highest SV corresponding to this configuration be σ_1^{AB}. If A and B are

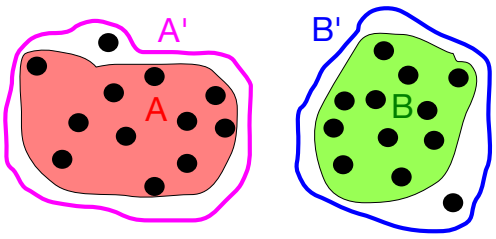

Figure 3.2: Two disjoint blocks A and B enclosing the same number of spin-S sites are each enlarged by one site, resulting in A' and B'. The dominant singular value between A and B yields the lower bound Eq. (3.10) for the dominant singular value between A' and B'.

both enlarged by one site to A' and B' (such that A' and B' are still disjoint) – as depicted in Fig. 3.2 – then the previously largest SV σ_1^{AB} enters a lower bound for the new one $\sigma_1^{A'B'}$

$$\sigma_1^{A'B'} \geq \frac{\sigma_1^{AB}}{2S+1}, \tag{3.10}$$

as proven in Appendix D. It is of course intuitive that any correlation – the dominant one as well – between A and B can still be measured between A' and B'. The $1/(2S+1)$ factor in the right term of Eq. (3.10) is due to the fact that the dominant correlator between A and B has to be Frobenius-renormalized to 1 when going to the enlarged blocks.

3.4 Symmetries

The consequences of two kinds of symmetries that can arise when performing the CDM analysis are discussed here. We shall firstly consider the particular case of two blocks at maximal distance, each of which consisting of two neighboring sites on a closed spin-1/2 chain (with an even number of sites) and we shall see that if the state under study is $SU(2)$-symmetric, the operators $X_i^{(A)}$ and $Y_i^{(B)}$ resulting from the SVD have special properties which simplify the CDM analysis in this case. We shall secondly consider the intrinsic symmetries of a state disregarding the configuration of the blocks. Those latter symmetries have consequences on the degeneracies of the SVs.

3.4.1 Correlations between two blocks at maximal distance on a closed spin chain

We have empirically observed that if blocks A and B are such that they enclose two sites each, and such that they are arranged at maximal distance one from another on a closed spin-1/2 chain with an even number of sites, as depicted in Fig. 3.3, then provided that the

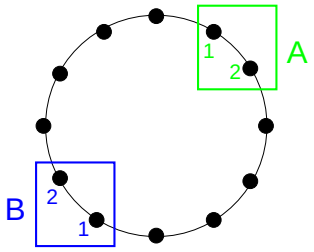

Figure 3.3: Closed spin chain with 12 sites. Blocks A and B have two neighboring sites and are at maximal distance.

system is in a $SU(2)$-symmetric state, any of the operators $X_i^{(A)}$ and $Y_i^{(B)}$ resulting from the SVD gets a contribution from only *one single element* of the following set of operators

$$\left\{\frac{1}{2}\mathbb{1}_{kl},\ \frac{2}{\sqrt{3}}(\mathbf{S}_k\cdot\mathbf{S}_l),\ \frac{1}{\sqrt{2}}(\mathbf{S}_k+\mathbf{S}_l),\ \frac{1}{\sqrt{2}}(\mathbf{S}_k-\mathbf{S}_l),\ \sqrt{2}\mathbf{S}_k\times\mathbf{S}_l,\ \mathbf{Q}_{kl}\right\}, \tag{3.11}$$

which is a Frobenius-orthonormalized basis for the space of operators acting on two spin-1/2 sites (here k and l). The contribution from more than one element of this operator set in any of the $X_i^{(A)}$'s or $Y_i^{(B)}$'s is forbidden. The meaning of the operators in the set Eq. (3.11) is clear, except for the last one which is a quadrupolar object defined in Eq. (E.1), Appendix E. It is symmetric under the $k \leftrightarrow l$ exchange. Basis Eq. (3.11) has two singlet

operators (with one component), three triplet operators (with three components), and one quintet operator (with five components).

3.4.2 Intrinsic symmetries of the state

The symmetry properties of the quantum state which is investigated have repercussions on the triples (σ_i, X_i, Y_i) that result from a SVD, in particular on the degeneracies of the SVs. Consider two blocks A and B in a spin-S system, which enclose the same number n of sites. These $2n$ spins-S live in the space

$$\underbrace{(S \otimes S \otimes \cdots \otimes S)}_{n \text{ terms}} \otimes \underbrace{(S \otimes S \otimes \cdots \otimes S)}_{n \text{ terms}}. \tag{3.12}$$

Case of a $SU(2)$-symmetric state – We treat here the case of rotationally invariant states, i.e. $SU(2)$-symmetric states. Singlet ($S_{\text{tot}} = 0$) eigenstates or mixed thermal states (with a contribution from the full spectrum and thus all the spin multiplets) of rotationally invariant Heisenberg hamiltonians for instance have this property.

It is very useful to classify all the possible operators acting within A or B into different sets such that operators belonging to the same set can be mapped one onto another by a $SU(2)$ rotation operation. The number of sets and their size is obtained by determining the irreducible representations of the $SU(2)$ group of operations acting within the space Eq. (3.12). This is done by performing a Clebsch-Gordan decomposition of Eq. (3.12), i.e. by writing this space in terms of a direct sum of individual subspaces that are globally invariant under $SU(2)$ operations. Such a subspace with spin j corresponds to a set of $2j+1$ operators which only differ by $SU(2)$ operations. It is a rank-j tensor with $2j+1$ components that can be written as

$$\Delta j^z = -j, -j+1, -j+2, \cdots, j$$

operators[3], where a Δj^z-operator is defined such that if applied to an eigenstate of S^z_{tot} with $S^z_{\text{tot}} = j^z$, it returns a new eigenstate of S^z_{tot} with $S^z_{\text{tot}} = j^z + \Delta j^z$.

In the case of a $SU(2)$-symmetric state, the $2j+1$ components within every spin-j subspace have the same correlation functions, and a spin-j subspace thus results in a $2j+1$ degenerate SV whose associated X and Y operators have a well defined spin-j, i.e. decompose onto basis operators of Table E.1 or E.2 (Appendix E) having a fixed number of

[3]The operators we have intuitively determined (i.e. without using the formula Eq. (C.2) of Appendix C) in Tables E.1 and E.2 of Appendix E are not necessarily Δj^z-operators. This would nevertheless be the case if they were derived using Eq. (C.2), as it is the case for the quadrupolar $\mathbf{Q}_{kl}$ operator in Table E.1 [see Eq. (E.1)], and for the quadrupolar $\mathbf{Q}_{klm}(i)$ and the octupolar $\mathbf{Se}_{klm}$ operators in Table E.2 [Eq. (E.2)].

components $2j+1$.

Case of a $U(1)$-symmetric state – We treat here the case of states which are invariant under rotations about the z-axis. This is for instance the case for eigenstates of Heisenberg hamiltonians that were originally rotationally invariant, but to which a magnetic field (pointing in the z-direction in the spin space) Zeeman term has been added. Such a hamiltonian conserves $S^z_{\rm tot}$, and its eigenstates are invariant under rotations in the xy-plane.

The $2j+1$ components of a spin-j subspace do no longer have the same correlation functions. Instead, only those with the same $|\Delta j^z|$ do, due to the $U(1)$ in-plane symmetry. Hence, degeneracies in the SV spectrum can be derived by first performing the Clebsch-Gordan decomposition of Eq. (3.12) and then considering that every spin-j sector gives

- $j+\frac{1}{2}$ SVs which are 2-fold degenerate

if j is half-integer, and

- j SVs which are 2-fold degenerate ($|\Delta j^z|\neq 0$ components)
- 1 SV which is non-degenerate ($|\Delta j^z|=0$ component)

if j is integer.

In contrast to the $SU(2)$-symmetric case, the X and Y operators associated to a given SV are here $|\Delta j^z|$-operators, i.e. decompose onto $|\Delta j^z|$-components of basis operators that do not necessarily have the same spin, for instance a given SV may simultaneously decompose onto $\frac{1}{\sqrt{2}}(S^x_k \pm S^x_l)$, $\frac{1}{\sqrt{2}}(S^y_k \pm S^y_l)$, and $Q^{(\pm 1)}_{kl} = \mp(S^\pm_k S^z_l + S^z_k S^\pm_l)$ of Table E.1 (Appendix E), since all of them are $|\Delta j^z|=1$.

The diagram below shows pictorially the evolution of the SV degeneracies if the $SU(2)$ symmetry is broken down to $U(1)$ if both A and B enclose 2 sites (spins-1/2). Every filled circle • is a SV, there are $D^2 = \min\{\dim^2_{\mathcal{H}}(A), \dim^2_{\mathcal{H}}(B)\} = (2^2)^2 = 16$ SVs.

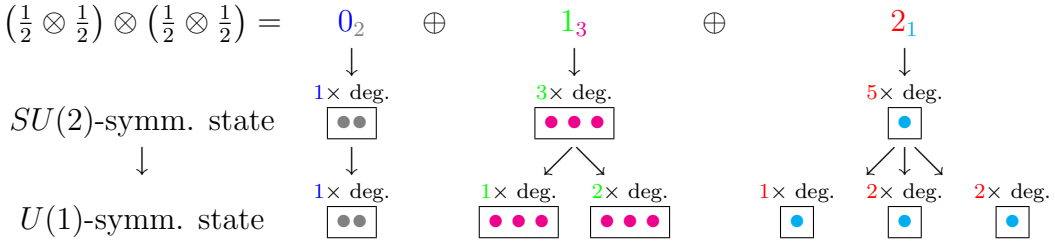

The notation j_m means that the subspace of spin j occurs m times in the Clebsch-Gordan

decomposition.

Illustration with blocks of two sites in a spin-1/2 system – Let us illustrate how state symmetries can be exploited in the particular case of two blocks A and B containing two sites each, in a spin-1/2 system. The Clebsch-Gordan decomposition of Eq. (3.12) in this case is given in the above picture, i.e. there are 2 singlet $j = 0$ subspaces, 3 triplet $j = 1$ subspaces, and one quintet $j = 2$ subspace.

Case of a $SU(2)$-invariant state – In the case of a $SU(2)$-invariant state, every $j = 0$ subspace gives one non-degenerate SV, every $j = 1$ subspace gives one 3-fold degenerate SV, and every $j = 2$ subspace gives one 5-fold degenerate SV. If the multiplicities are taken into account, we have

- two non-degenerate SVs,
- three 3-fold degenerate SVs,
- one 5-fold degenerate SV.

The number of SVs thus matches the dimensionality ($2^4 = 16$) of the space spanned by four spins-1/2. Regarding the basis Table E.1 of Appendix E, the X and Y operators associated to the non-degenerate SVs can simultaneously decompose onto $\frac{1}{2}\mathbb{1}_{kl}$ and $\frac{2}{\sqrt{3}}(\mathbf{S}_k \cdot \mathbf{S}_l)$ (singlet operators), the X and Y operators associated to the 3-fold degenerate SVs can simultaneously decompose onto $\frac{1}{\sqrt{2}}(\mathbf{S}_k + \mathbf{S}_l)$, $\frac{1}{\sqrt{2}}(\mathbf{S}_k - \mathbf{S}_l)$, and $\sqrt{2}\mathbf{S}_k \times \mathbf{S}_l$ (triplet operators), and the X and Y operators associated to the 5-fold degenerate SV decompose onto $\mathbf{Q}_{kl}$ (quintet operator).

Case of a $U(1)$-invariant state – If the state under study is $U(1)$-invariant, every $j = 0$ subspace gives one non-degenerate SV, every $j = 1$ subspace gives one 2-fold degenerate SV and one non-degenerate SV, and every $j = 2$ subspace gives two 2-fold degenerate SVs and one non-degenerate SV. If the multiplicities are taken into account, we have

- six non-degenerate SVs,
- five 2-fold degenerate SVs.

Thus a total of 16 SVs, as before. The non-degenerate SVs can get simultaneous contributions from $|\Delta j^z| = 0$ operators only, i.e. $\frac{1}{2}\mathbb{1}_{kl}$, $\frac{2}{\sqrt{3}}(\mathbf{S}_k \cdot \mathbf{S}_l)$, $\frac{1}{\sqrt{2}}(S^z_k \pm S^z_l)$, $\sqrt{2}[\mathbf{S}_k \times \mathbf{S}_l]^z$, and $Q^{(3)}_{kl}$. The 2-fold degenerate SVs can either get simultaneous contributions from $|\Delta j^z| = 1$ operators, i.e. $\frac{1}{\sqrt{2}}(S^x_k \pm S^x_l)$, $\frac{1}{\sqrt{2}}(S^y_k \pm S^y_l)$, $\sqrt{2}[\mathbf{S}_k \times \mathbf{S}_l]^x$, $\sqrt{2}[\mathbf{S}_k \times \mathbf{S}_l]^y$, $Q^{(2)}_{kl}$, and $Q^{(4)}_{kl}$; or from $|\Delta j^z| = 2$ operators, i.e. $Q^{(1)}_{kl}$ and $Q^{(5)}_{kl}$.

3.5 Correlation density matrix vs mutual information

Consider two disjoint blocks A and B enclosing the same number N of spins-S. Within our framework, it is natural to quantify the total correlation between A and B by the squared Frobenius norm (SFN) of their CDM (which is actually given by the sum of the squared SVs)

$$\| \rho^c_{AB} \|^2_F = \sum_{i=1}^{D^2} \sigma_i^2. \tag{3.13}$$

Another quantity has been introduced in quantum information theory in order to measure the total correlation between the two blocks, namely the *mutual information* [65] (MI)[4]

$$\mathrm{MI}(A,B) := S(A) + S(B) - S(A \cup B),$$

where $S(\mathcal{B}) := -\mathrm{Tr}(\rho_{\mathcal{B}} \ln \rho_{\mathcal{B}})$ is the *von Neumann entropy* of block $\mathcal{B}$, quantifying the entanglement of this block with its environment. $S(\mathcal{B})$ ranges from 0 if $\mathcal{B}$ is disentangled to its environment, up to $N_{\mathcal{B}} \ln(2S+1)$ – where $N_{\mathcal{B}}$ is the number of spins-S inside $\mathcal{B}$ – if the entanglement is maximal.

Both the SFN and the MI vanish if blocks A and B are uncorrelated. In the other hand if A and B are maximally correlated one to another, each of these two correlation measures does reach its upper bound (refer to Eq. (3.9) for SFN)

$$\| \rho^c_{AB} \|^2_F \leq 1 - 1/D^2, \tag{3.14}$$

$$\mathrm{MI}(A,B) \leq 2N \ln(2S+1) = 2 \ln D. \tag{3.15}$$

In a first approach, we identify the states for which the upper bounds Eqs. (3.14) and (3.15) are reached, we shall in a next step study how SFN and MI are related one to another. Let

$$\{|1\rangle_A, |2\rangle_A, \cdots, |\dim_{\mathcal{H}}(A)\rangle_A\} \qquad \text{and} \qquad \{|1\rangle_B, |2\rangle_B, \cdots, |\dim_{\mathcal{H}}(B)\rangle_B\}$$

be orthonormalized bases of A and B respectively ($\dim_{\mathcal{H}}(A) = \dim_{\mathcal{H}}(B) = (2S+1)^N$). It turns out that the maximal correlation between the two blocks is realized by the state

$$|\text{max. corr.}(N)\rangle := \frac{1}{\sqrt{(2S+1)^N}} \sum_{i=1}^{(2S+1)^N} |i\rangle_A |i\rangle_B \otimes |\text{env}\rangle, \tag{3.16}$$

as intuitively expected, where $|\text{env}\rangle$ is the arbitrary (normalized) configuration of the environment of $A \cup B$.

[4]The quantity we define as "mutual information" is sometimes also called "correlation entropy".

It is straightforward to realize that the state Eq. (3.16) reaches the bound Eq. (3.15): $S(A)$ and $S(B)$ are both maximal and equal to $N\ln(2S+1)$, while $S(A\cup B)$ vanishes since $A\cup B$ is uncorrelated to its environment. Regarding the way how bound Eq. (3.14) is reached, it can be shown that apart from the SV which is identically zero[5], the remaining D^2-1 SVs are the same and have the value $1/D$ resulting in a squared Frobenius norm $(D^2-1)(1/D^2) = 1-1/D^2 = 1-1/(2S+1)^{2N}$.

Coordinates representing the state Eq. (3.16) in the "SFN vs MI" plane for cases $N = 1,2,3,4$ and spins $S = 1/2$ are shown in the left panel of Fig. 3.4 (brown filled circles). It

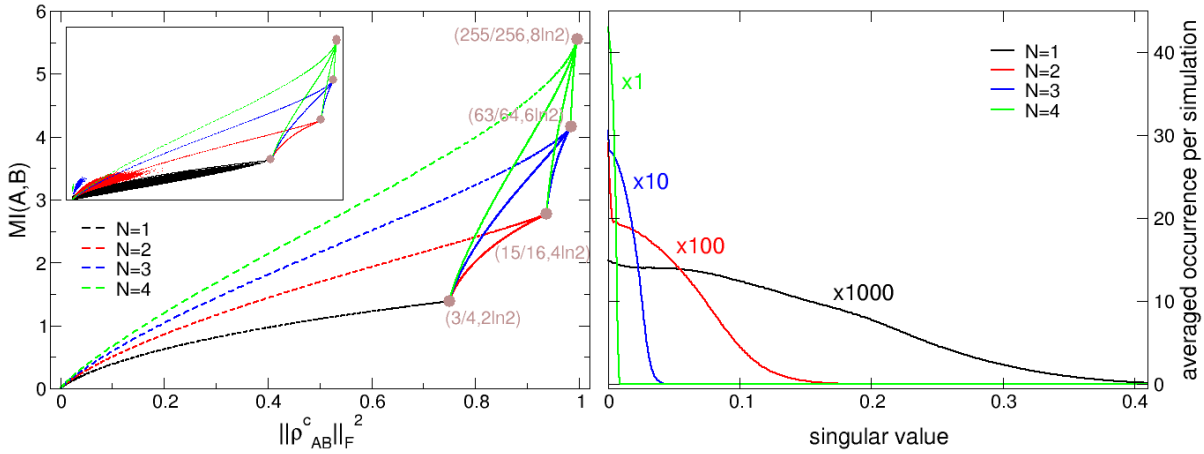

Figure 3.4: (Left) *Mutual information* (MI) vs *squared Frobenius norm* (SFN) for selected paths joining selected states of particular interest. Brown filled circles correspond to the maximally correlated state Eq. (3.16) for various sizes of blocks. The color of the curves is a function of the number of enclosed spins-1/2 inside the blocks. The inset shows the (SFN,MI)-coordinates of uniformly distributed random correlation density matrices (71.700.000 simulations for $N = 1$, 3.080.000 simulations for $N = 2$, 132.800 simulations for $N = 3$, 10.360 simulations for $N = 4$). (Right) Frequencies of occurrence of the singular values corresponding to the correlations density matrices that have been randomly generated in the left panel (i.e. the number of occurrence has been divided by the number of simulations). The colors have the same meaning as in the left panel. For the sake of clarity, the frequencies of occurrence have been rescaled: they are multiplied by 1000 for $N = 1$, by 100 for $N = 2$, and by 10 for $N = 3$. Singular values are peaked at small values for large blocks, and spread over a larger range of values for small blocks.

turns out that the brown filled circle corresponding to the maximal correlation for $N = 1$ i.e. $(3/4, 2\ln 2)$ is also reachable for blocks with $N = 2, 3$ and 4 sites, although it is not a

[5]Any configuration of blocks has a vanishing singular value corresponding to the connected correlation between identity operators, which cannot be different from zero, whatever A and B.

point of maximal correlation for those values of N. Similarly, the brown filled circle corresponding to maximal correlation for $N = 2$ i.e. $(15/16, 4\ln 2)$ is also reachable for blocks with $N = 3$ and 4 sites; and the brown filled circle corresponding to maximal correlation for $N = 3$ i.e. $(63/64, 6\ln 2)$ is also reachable for blocks with $N = 4$ sites.

Hence, for a fixed number N of sites inside A and B, it is a general fact that – whatever the value of $n \leq N$ – the brown filled circle $(1 - 1/(2S+1)^{2n}, 2n\ln(2S+1))$ in the left panel of Fig. 3.4 is realized by the state

$$|n\rangle := \frac{1}{\sqrt{(2S+1)^n}} \sum_{i=1}^{(2S+1)^n} |i\rangle_A |i\rangle_B \otimes |\text{env}\rangle, \quad n \leq N,$$

corresponding to Eq. (3.16) with the sum truncated to the $(2S+1)^{n\,\text{th}}$ term. Note that the origin $(0,0)$ (A and B are uncorrelated) is reached for the state $|n = 0\rangle$, and that if $n = N$ we get $|n = N\rangle = |\text{max. corr.}(N)\rangle$ [Eq. (3.16)] and the correlation is maximal.

In order to visualize how the regions attached to the different values of N look like in the left panel of Fig. 3.4, the curve corresponding to states

$$\alpha^2 |n = 0\rangle + (1 - \alpha^2)|\text{max. corr.}(N)\rangle \quad \text{for } \alpha \in [0, 1]$$

i.e. joining the minimally correlated state to the maximally correlated one, is drawn (dashed lines) for $N = 1$ (black), $N = 2$ (red), $N = 3$ (blue), and $N = 4$ (green). Curves corresponding to states

$$\alpha^2 |n = 1\rangle + (1 - \alpha^2)|\text{max. corr.}(N)\rangle \quad \text{for } \alpha \in [0, 1]$$

for $N = 2$ (red), $N = 3$ (blue), and $N = 4$ (green), to states

$$\alpha^2 |n = 2\rangle + (1 - \alpha^2)|\text{max. corr.}(N)\rangle \quad \text{for } \alpha \in [0, 1]$$

for $N = 3$ (blue) and $N = 4$ (green), and to states

$$\alpha^2 |n = 3\rangle + (1 - \alpha^2)|\text{max. corr.}(N)\rangle \quad \text{for } \alpha \in [0, 1]$$

for $N = 4$ (green) are shown as well (solid lines).

The four dashed curves joining $|n = 0\rangle$ to $|\text{max. corr.}(N)\rangle$ in the left panel of Fig. 3.4 might be naively interpreted as upper bounds on the MI as a function of the SFN for $N = 1, 2, 3$, and 4. We have numerically simulated random CDMs (see inset in the left panel of Fig. 3.4) from uniformly distributed density matrices, and shown that this is not the case: at small SFNs the MIs are higher than these dashed curves, this is at least clearly

visible for the red, blue, and green regions. These randomly simulated CDMs also show on the one hand that MI is correlated to SFN (the higher one of them, the higher the other), and on the other hand that there is a propensity for every color to lie in the lower left part of the "SFN vs MI" plane, i.e. far away from the brown filled circles. The regions close to the brown filled circles (where the correlation between A and B is particularly high) presumably correspond to atypical states that have a small measure in the whole space of the physical states.

Frequencies of occurrence of the SVs corresponding to the CDMs we have generated in the left panel of Fig. 3.4 are shown in its right panel. For small blocks, the frequencies have been vertically rescaled for the sake of legibility. It appears from that figure that the occurrence of the SVs are peaked at very small values for large blocks (for $N = 4$, no SV larger than ~ 0.01 was obtained), whereas they are spread over a much larger range of values for small blocks (for $N = 1$, SVs beyond ~ 0.4 were generated); this is indeed due to the very low probability of generating atypical states.

3.6 Applications of the method for illustrative purposes

3.6.1 Heisenberg J_1–J_2 spin-1/2 antiferromagnetic chain

We use the CDM method for investigating a well understood model: the spin-1/2 chain with antiferromagnetic (AF) $J_1 > 0$ and $J_2 > 0$ interactions between nearest and next nearest neighbors (nn and nnn) respectively. Its hamiltonian reads

$$H = J_1 \sum_i \mathbf{S}_i \cdot \mathbf{S}_{i+1} + J_2 \sum_i \mathbf{S}_i \cdot \mathbf{S}_{i+2} \tag{3.17}$$

where $\mathbf{S}_i$ is a spin-1/2 operator at site i.

The idea is – in a first step – to show that the method allows to recover the (known) phase diagram of hamiltonian Eq. (3.17) at zero temperature with a high precision; in a next step the CDM tool will be used for revealing its dominant correlations at finite temperature. In all cases, the states are computed using Exact Diagonalization (ED).

At zero temperature

The AF J_1–J_2 chain is known to undergo a phase transition as J_2/J_1 crosses 0.241167 [66] from a critical to a dimerized gapped phase. It is known to be two-fold degenerate at $J_2/J_1 = 1/2$ [67] (Majumdar-Ghosh point), with a ground state consisting of a superimposition of two dimerized states. Furthermore, spin correlations exhibit an incommensurate

behavior for $J_2/J_1 > 1/2$, and the dimerization (dimer-dimer correlations) is found to be maximal at $J_2/J_1 = 0.5781$ [68].

We compute the ground state of a chain of length $L = 30$ sites with periodic boundary conditions, and perform a SVD of the CDM between two blocks – each of which containing two nn sites – at maximal distance. This configuration is the one we chose for the examples in Section 3.4 (we are in the situation of Fig. 3.3), hence the X_i and Y_i operators associated to every resulting SV only differ by a phase factor, and have a well defined parity under the site-exchange within each block. Moreover since the ground state is a singlet (i.e. $SU(2)$-symmetric) there are only 6 independent SVs. As explained in Section 3.4, every SV decomposes onto a *single* element of the basis Eq. (3.11) in this case. These SVs are shown in the left panel of Fig. 3.5 for $J_2/J_1 \in [0, 2]$. The SV decomposing onto $\frac{2}{\sqrt{3}}(\mathbf{S}_k \cdot \mathbf{S}_l)$ is denoted by *dimerization* and non-degenerate, the SV decomposing onto $\frac{1}{\sqrt{2}}(\mathbf{S}_k + \mathbf{S}_l)$ is denoted by *F correlations* and 3-fold degenerate, the SV decomposing onto $\frac{1}{\sqrt{2}}(\mathbf{S}_k - \mathbf{S}_l)$ is denoted by *AF correlations* and 3-fold degenerate, the SV decomposing onto $\sqrt{2}\mathbf{S}_k \times \mathbf{S}_l$ is denoted by *twist* and 3-fold degenerate, and the SV decomposing onto the quadrupolar operator $\mathbf{Q}_{kl}$ is denoted by *quadrupolar correlations* and 5-fold degenerate.

As expected, for small J_2/J_1 AF spin correlations dominate. As J_2/J_1 is increased, it is surpassed by the SV corresponding to the dimerization, which reaches its maximum at $J_2/J_1 = 0.577$. At large J_2/J_1 AF spin correlations dominate again, but several others also grow in value.

The higher (lower) right panel of Fig. 3.5 shows the $J_{2,R}/J_1$ ($J_{2,L}/J_1$) value above (below) which the dimer SV no longer dominates, as a function of the system size ($L = 8, 12, 16, ..., 32$). As we can see:

- $J_{2,R}/J_1$ diverges with L, being well described by an exponential fit $J_{2,R}/J_1 \approx a_0 + a_1 \exp(a_2 L)$, indicating that in the thermodynamic limit, the model is dimerized up to $J_2/J_1 = \infty$.

- $J_{2,L}/J_1$ exhibits a quite different behavior: it is well fitted by a polynomial function $J_{2,L}/J_1 \approx a_0 + a_1/L + a_2/L^2$ converging to $a_0 = 0.249$ in the thermodynamic limit.

Our CDM approach thus predicts a system that is dimerized in the $J_2/J_1 \in [0.249, \infty[$ regime, which agrees well with $[0.241167, \infty[$. The method has therefore succeeded in providing a surprisingly accurate phase diagram of the AF J_1–J_2 chain at zero temperature.

At finite temperature

We now switch to the study of the J_1–J_2 spin-1/2 AF chain at finite temperature. We perform a full diagonalization of hamiltonian Eq. (3.17) on systems ranging from $L = 6$

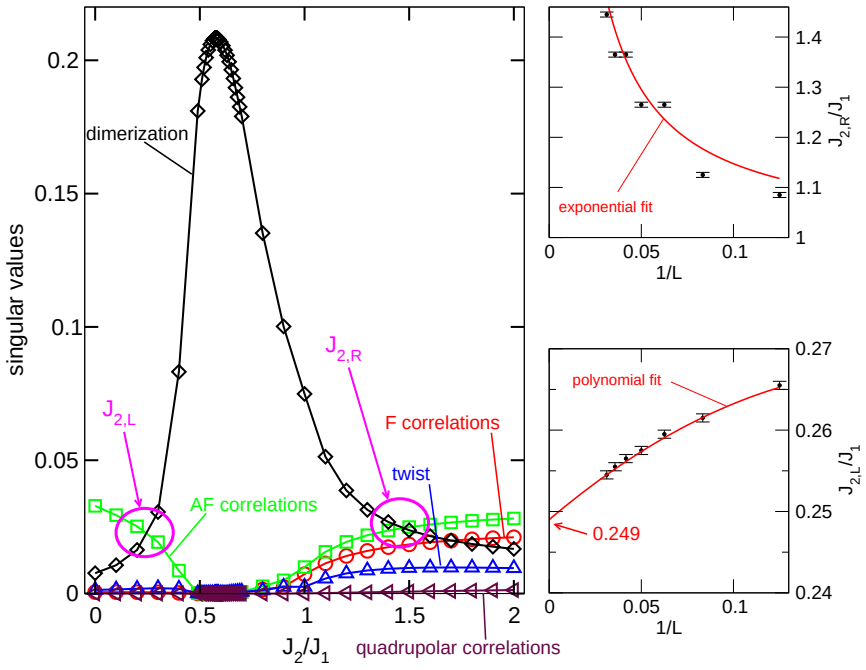

Figure 3.5: (Left) The 6 independent singular values for blocks at maximal distance containing two nn sites on the chain $L = 30$ (periodic boundary conditions) obtained by Exact Diagonalization. (Right, top) Extrapolation of the J_2/J_1 value above which the dimer singular value no longer dominates, with sizes $L = 8, 12, 16, ..., 32$. The extrapolated value diverges as $L \to \infty$. (Right, bottom) Extrapolation of the J_2/J_1 value below which the dimer singular value no longer dominates, with sizes $L = 8, 12, 16, ..., 32$. The extrapolated value goes to 0.249 as $L \to \infty$. Error bars on the J_2/J_1 values of the right panels are due to the discreteness of the J_2/J_1 space for the numerical simulations.

up to $L = 14$ using the LAPACK library. We stress that a diagonalization of the full spectrum can be performed beyond $L = 14$, but we do not intend to provide a deep study of the finite temperature properties of the J_1–J_2 spin-1/2 AF chain here. Our results are presented for illustrative purposes only.

We consider here the same block configuration as in the zero temperature case. Even if each individual state contributing to the thermal CDM is generally not a singlet, the $SU(2)$ symmetry is recovered in the thermal CDM, since the entire spectrum does contribute. The SVD thus yields only 6 independent SVs (including the identically zero one), as in the zero temperature case.

The squared Frobenius norm (SFN) Eq. (3.13) – which, we recall, can be seen as a bound on the total correlation between A and B – is shown as a function of J_2/J_1 and of the temperature T in Fig. 3.6 for systems $L = 6, 8, 10, 12, 14$. The J_2/J_1 parameter is extended

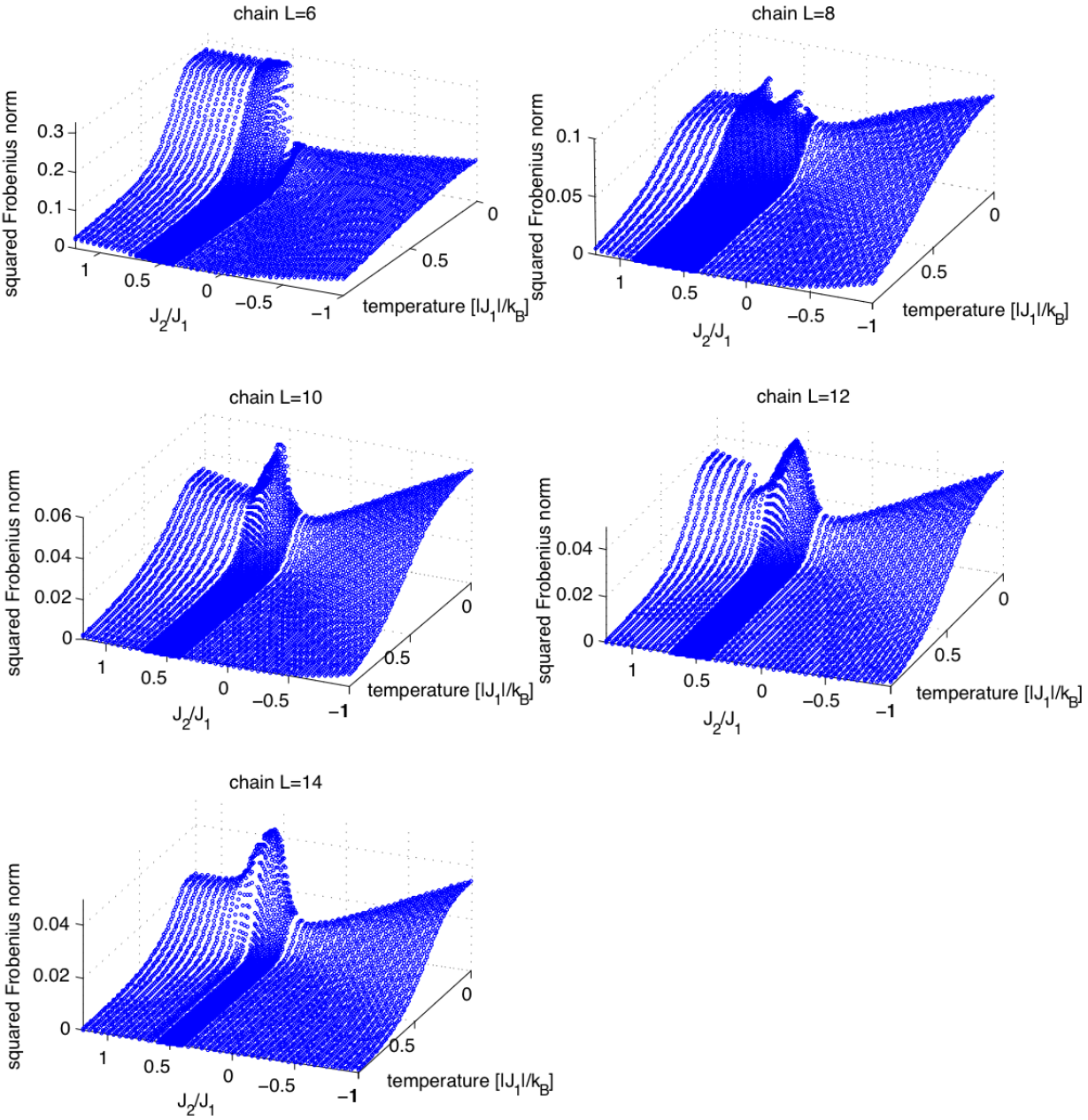

Figure 3.6: Squared Frobenius norm Eq. (3.13) as a function of J_2/J_1 and of the temperature T for $L = 6, 8, 10, 12, 14$. T ranges from 0 up to J_1/k_B, and the J_2/J_1 parameter is extended to the $J_2 < 0$ side in this figure for the sake of completeness and ranges from -1 up to 1.2.

to the $J_2 < 0$ side in that figure for the sake of completeness (J_1 is kept positive), but we focus our investigations on the $J_2 > 0$ side. The SFN exhibits a monotonic decrease with the temperature. Furthermore, as the size L increases, it develops a peak at low temperature around $J_2/J_1 \sim 0.6$ that is roughly the maximally dimerized point at zero temperature.

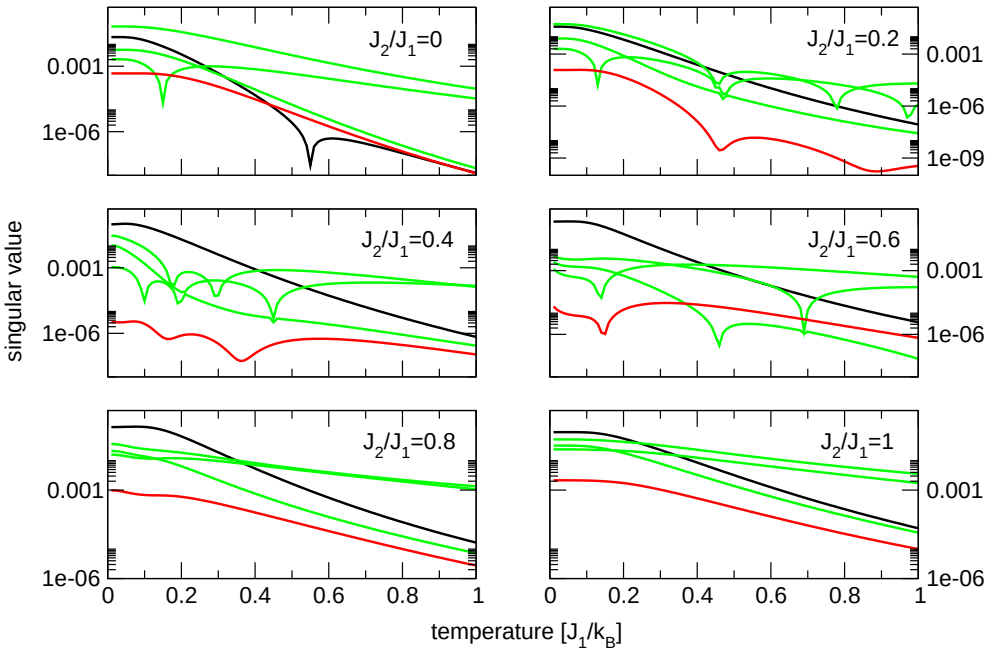

Figure 3.7: The 5 non-zero independent singular values in a chain $L = 14$ for various values of the J_2/J_1 parameter. The non-degenerate singular value is in black, the three 3-fold degenerate singular values are in green, and the 5-fold degenerate singular value is in red.

The individual evolution of the 5 non-zero independent SVs with the temperature is shown in Fig. 3.7 for $L = 14$ for various values of the J_2/J_1 parameter. The color of the different SVs is a function of their degeneracy. There are one non-degenerate SV (black), three 3-fold degenerate SVs (green), and one 5-fold degenerate SV (red), as it should be in the case of a SU(2)-invariance. The low temperature behavior of the SVs resembles the zero temperature one: the non-degenerate (decomposing onto the dimer operator) black SV is dominant for $J_2/J_1 = 0.4$, 0.6, 0.8, and 1, and it is surpassed by a green 3-fold degenerate SV at lower $J_2/J_1 = 0$ and 0.2 values. At higher temperatures however, the behavior changes: there is a crossover around $T \sim 0.4J_1/k_B$ [6] above which a 3-fold degenerate green

[6] As J_2 becomes comparable to J_1, the crossover occurs below $T \sim 0.4J_1/k_B$ in Fig. 3.7. This is an artifact due to the fact that the size $L = 14$ is not multiple of 4, and thus not well adapted for describing

SV is dominant whatever the value of J_2/J_1. For any value of the J_2/J_1 parameter and any temperature the 5-fold degenerate red SV remains very weak, indicating that correlations between quadrupolar objects are not important in that model.

By now varying the distance separating the blocks, each SV exhibits an exponential decay with the distance for fixed temperature[7]. We have extracted the correlation length ξ [8] of each of the 5 independent SVs by performing least squares fits of them over all distances separating the blocks, going from the minimal one up to one step before the maximal distance (since correlations are overestimated at maximal distance in closed systems) in systems $L = 12$ and $L = 14$. These correlation lengths are shown as a function of the temperature for the black non-degenerate (dimer) SV, the largest among the green 3-fold degenerate SVs, and the red 5-fold degenerate SV in Fig. 3.8 for $J_2/J_1 = 0$, 0.4, 0.6, and 1. The little peaks in red curves are finite-size effect, they are thus not representative of the $L = \infty$ physics[9].

Low temperature behavior of Fig. 3.8 – Notice that ξ is ill-defined for a correlator which is long-ranged or critical at $T = 0$. At $J_2/J_1 = 0$ (critical phase at zero temperature), a 3-fold degenerate green SV has the largest correlation length, which is nevertheless of a comparable order of magnitude to the correlation length of the black SV, namely a couple of lattice spacings. As the J_2/J_1 parameter enters the regime for which the model is dimerized at zero temperature ($J_2/J_1 >\sim 0.24$), the correlation length of the black (dimer) SV becomes larger and larger: it is ~ 10 lattice spacings at $J_2/J_1 = 0.4$, and even ~ 100 lattice spacings[10] close the point of maximal dimerization (which is so at zero temperature) $J_2/J_1 \sim 0.6$. If J_2/J_1 is increased further, the correlation length of the black SV decreases – remaining the largest one – and becomes a couple of lattice spacings again at $J_2/J_1 = 1$.

High temperature behavior of Fig. 3.8 – The crossover around $T \sim 0.4J_1/k_B$ which has been pointed out from Fig. 3.7 also appears in Fig. 3.8: above this temperature, a green SV has the largest correlation length, whatever the J_2/J_1 parameter. As

the physics in the regime of large J_2/J_1. We have checked that for $L = 8$ and 12, the crossover still occurs at $T \sim 0.4J_1/k_B$ for $J_2/J_1 = 1$.

[7] If the distance separating the blocks is no longer maximal, the SVs do no longer decompose onto one single element of basis Eq. (3.11).

[8] The correlation length of an exponentially decaying SV $\sigma(r)$ is the constant ξ such that $\sigma(r) \propto e^{-r/\xi}$.

[9] Peaks in red curves of Fig. 3.8 are finite-size effects due to the fact that the red SV does sometimes exhibit slight local increases with the distance in our finite systems, which is clearly not physical and not representative of the thermodynamic limit.

[10] There is no doubt that our approach yields much more accurate values of ξ at high temperature where the length scale of ξ is a couple of lattice spacings, than for $T \searrow 0$ where ξ may become quite large (it is even infinitely large at $T = 0$ for long-ranged or critical SVs), thus difficult to extract from a $L = 14$ chain.

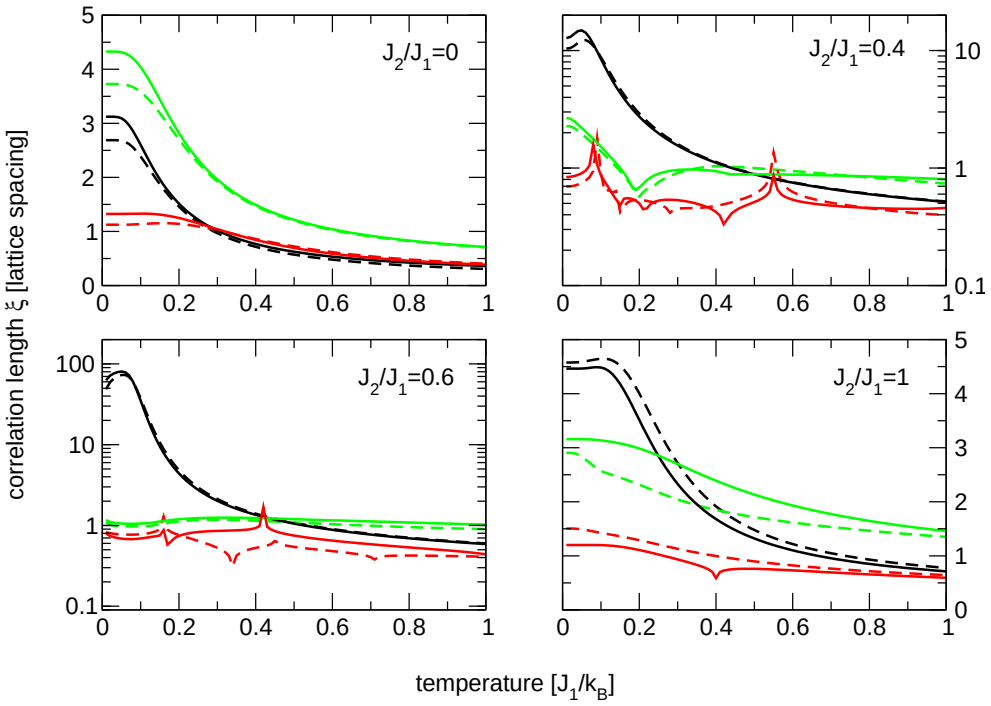

Figure 3.8: Correlation lengths of the non-degenerate singular value (black), the largest among the three 3-fold degenerate singular values (green), and the 5-fold degenerate singular value (red) for 4 different J_2/J_1 parameters as a function of the temperature. The dashed (solid) line refers to length $L = 12$ ($L = 14$).

argued above, $L = 12$ suits better than $L = 14$ for describing the large-J_2/J_1 physics, this explains why the crossover point decreases from $T \sim 0.4J_1/k_B$ at $J_2/J_1 = 0.6$ down to $T \sim 0.25J_1/k_B$ at $J_2/J_1 = 1$ for $L = 14$ whereas it is still $T \sim 0.4J_1/k_B$ at $J_2/J_1 = 1$ for $L = 12$.

Finally, the correlation length of the red 5-fold degenerate SV (that decomposes onto the quadrupolar operator) is low whatever the temperature and the value of the J_2/J_1 parameter: about one lattice spacing.

3.6.2 Heisenberg J_1–J_2 spin-1/2 antiferromagnet on the square lattice

We use here the CDM tool for investigating the dominant correlations at zero temperature in the 2D analog of the J_1–J_2 chain, namely the J_1–J_2 ($J_1, J_2 > 0$) antiferromagnet on a

square lattice. The hamiltonian is thus still given by Eq. (3.17), and ground states are still computed by ED with periodic boundary conditions. The interest of performing CDM investigations of this 2D system does not only reside in illustrative purposes, it is actually enhanced by the fact that – in contrast to its 1D analog – the nature of the ground state of this model is not understood around the phase of maximal frustration $J_2/J_1 = 1/2$.

The ground state of the 2D version of hamiltonian Eq. (3.17) is known to be a spin liquid in the intermediate phase $J_{c_1} < J_2/J_1 < J_{c_2}$ [3] with $J_{c_1} \approx 0.4$ and $J_{c_2} \approx 0.6$, whereas it has Néel magnetic long-range order (LRO) with the propagation wave vector (π, π) in the $J_2/J_1 < J_{c_1}$ regime, and collinear magnetic LRO with the propagation wave vectors $(\pi, 0)$ and $(0, \pi)$ for $J_2/J_1 > J_{c_2}$. It is commonly believed that the ground state in the intermediate disordered phase is a valence bond crystal (VBC), but the nature of this VBC (plaquette or columnar) is still under debate [69–74].

We have performed a SVD for extracting the dominant correlations between horizontal and vertical blocks consisting of two nn sites in the ground state of the square 6×6-site sample on the square lattice for the parameters $J_2/J_1 = 0.3$, 0.55, and 1 (corresponding to each of the three phases). For each of these three J_2/J_1 values, the left column of Fig. 3.9 shows the spin correlation patterns (the reference site is black, and blue/red sites indicate positive/negative correlations), while the middle and the right columns respectively show the $X_1^{(A)}$'s and $Y_1^{(B)}$'s associated to the largest SV σ_1.

Description of the SVD figure – In the middle and the right columns of Fig. 3.9, block A is fixed and shown in black[11], while block B is let free to move. Symbols (and their size) show the contribution of the basis operators Eq. (3.11) to the $X_1^{(A)}$'s and $Y_1^{(B)}$'s, the significance of the symbols is given in Table 3.1. Symbols associated to a horizontal or vertical block built on two nn sites are aligned on the straight line joining those sites. Fig. 3.9 shows that for each of the three values of the J_2/J_1 parameter, the only contribution to the highest SV is from the ferromagnetic (F) (triangle up), the antiferromagnetic (AF) (triangle down), and the dimer (circle) operators. Signs of the contributions (blue/red symbols mean positive/negative contribution) are only given for the dimer operator, since it is even under the $k \leftrightarrow l$ exchange (see Table 3.1) and does not contribute together with other operators. For a given configuration of blocks, the AF operator can contribute together with the F one in the highest SV, and since the AF operator is odd under the $k \leftrightarrow l$ exchange and we do not arrange the sites in an ordered way, it would not make any sense to give the signs of the contributions for those operators.

We furthermore stress that hamiltonian Eq. (3.17) is rotationally invariant, and that its ground states are singlets (as in the 1D case). Thus according to Section 3.4, there are

[11] The sample has the translations and the rotations by $\pi/2$ as symmetries. It is thus possible to fix block A with an arbitrary orientation.

$\frac{2}{\sqrt{3}}(\mathbf{S}_k \cdot \mathbf{S}_l)$	$\frac{1}{\sqrt{2}}(\mathbf{S}_k + \mathbf{S}_l)$	$\frac{1}{\sqrt{2}}(\mathbf{S}_k - \mathbf{S}_l)$
◯	△	▽

Table 3.1: One-to-one correspondence between symbols appearing in the singular value decomposition Fig. 3.9 and elements of the orthonormalized basis Eq. (3.11).

only 6 independent SVs for each configuration of blocks: for every non-singlet operator of basis Eq. (3.11), all the components contribute with the same weight.

Interpretation of the results – Spin correlations exhibit the expected structures: they are long-ranged and staggered in both direction for $J_2/J_1 = 0.3$ in accordance with the magnetic (π, π) ordering, they are short-ranged in the disordered phase $J_2/J_1 = 0.55$, and they correspond to the superimposition of two correlation patterns for $J_2/J_1 = 1$, the first one being staggered in one direction, the second one in the other direction (superimposition of $(\pi, 0)$ and $(0, \pi)$ orderings). Notice that in the disordered phase $J_2/J_1 = 0.55$, the spin correlations do not decay isotropically around the black reference site. Instead, they are much stronger and are staggered along the shortest loops joining one black reference site to its closest images (in the horizontal and vertical directions) than in the other directions. The consequences of this "loop effect" will be discussed in Chapter 4, where the spin correlation patterns of the kagomé antiferromagnet are studied.

The $X_1^{(A)}$'s and $Y_1^{(B)}$'s associated to the highest SV only consist of F and AF operators (triangles up and down) in the two ordered phases $J_2/J_1 = 0.3$ and 1, which is indeed what is expected for magnetically ordered states. Although F and AF correlations are also dominant for certain configurations of blocks in the disordered ground state ($J_2/J_1 = 0.55$), most of them turn out to be dominated by dimer correlations (circles) – see the columns highlighted in light green in Fig. 3.9 – which is in agreement with the fact that dimerization is believed to be the relevant instability for that value of the J_2/J_1 parameter.

3.7 Conclusion

We have introduced a method which allows to extract the dominant correlations between two disjoint blocks in a strongly interacting system in an unbiased way. It consists of performing a singular value decomposition of the correlation density matrix between those blocks. We have derived the properties of this method and investigated the consequences of some lattice and state symmetries. The relation with mutual information has been discussed in details, and the maximally correlated states have been identified.

In a second step, we have applied the method to the J_1–J_2 Heisenberg antiferromagnetic

spin-1/2 chain for illustration. Its phase diagram at zero temperature has been recovered with a good precision, and a crossover from the dimerized phase to a phase with dominant spin correlations has been revealed at finite temperature. The 2D analog of this model, i.e. the J_1–J_2 Heisenberg model on the square lattice has been investigated as well, at zero temperature. In its region of maximal frustration, dimerization is pointed out as the relevant instability, as expected.

This method has thus proven itself to be a useful tool for revealing the nature of strongly interacting systems (at zero or finite temperature) and should be considered as a serious alternative to other numerical methods for sheding light on the physics of models that are yet not completely understood.

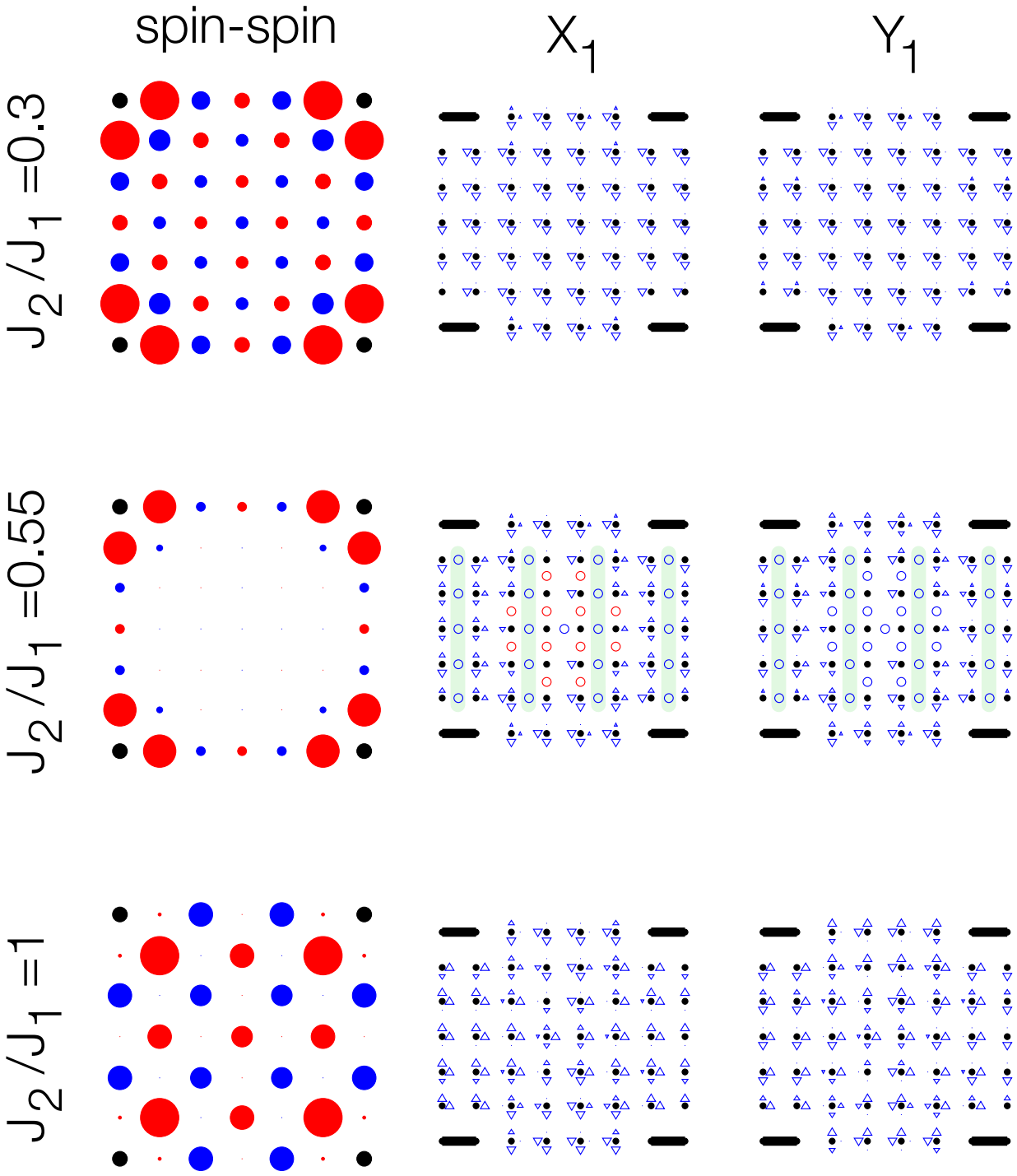

Figure 3.9: Spin-1/2 J_1–J_2 Heisenberg model on the square lattice (square 6×6-site sample) for parameters $J_2/J_1 = 0.3$, 0.55, and 1, corresponding to each of the three phases of this model. (Left column) spin correlations: the reference site is black, and blue/red sites mean positive/negative correlations. (Middle and right columns) decomposition of the $X_1^{(A)}$'s and $Y_1^{(B)}$'s – associated to the highest singular values – in the basis Eq. (3.11). Horizontal and vertical blocks with two nn sites are considered. Block A is fixed (black), while block B is let free to move. Symbols associated to a given block built on two nn sites are aligned on the straight line joining those sites, and defined in Table 3.1.

CHAPTER 4

Antiferromagnetic spin-1/2 Heisenberg model on the kagomé lattice

4.1 Introduction

The kagomé lattice – whose name originates from a japanese basket – is depicted in Fig. 4.1. It is a non-Bravais 2D lattice of corner-sharing triangles, or a "triangular lattice of triangles". The spin-1/2 kagomé antiferromagnet (KAF) is defined by the hamiltonian

$$H = J \sum_{\langle i,j \rangle} \mathbf{S}_i \cdot \mathbf{S}_j \tag{4.1}$$

where $\mathbf{S}_i$ is a spin-1/2 operator at site i, and $J > 0$ is an antiferromagnetic coupling constant. The sum runs over all the pairs of nearest neighboring sites on the kagomé lattice.

Let us first discuss the classical version of hamiltonian Eq. (4.1). While the continuous degeneracy of this model on the triangular lattice is only the trivial global one, classical ground states of the kagomé structure have a local continuous degeneracy. They are obtained whenever the sum of the three spins around each elementary triangle is zero. Two

typical ground state structures are generally considered, namely the $\mathbf{q} = 0$ type 120° spin alignment and the $\sqrt{3} \times \sqrt{3}$ type 120° spin alignment, both are shown in Fig. 4.1 and are distinguishable one from the other via the vectorial chirality, which is defined as

$$\kappa = \frac{2}{3\sqrt{3}} \left(\mathbf{S_1} \times \mathbf{S_2} + \mathbf{S_2} \times \mathbf{S_3} + \mathbf{S_3} \times \mathbf{S_1} \right),$$

where $\mathbf{S_1}$, $\mathbf{S_2}$, and $\mathbf{S_3}$ are spins on the corners of an elementary triangle. As spins are numbered clockwise around the triangle, the chirality is +1 when the spins rotate clockwise by 120° steps, and is −1 when the spins rotate counterclockwise by 120° steps. The $\mathbf{q} = 0$ type configuration is composed of triangles having either a chirality of +1 or −1, while the $\sqrt{3} \times \sqrt{3}$ type configuration contains both chiralities, as shown in Fig. 4.1. If thermal

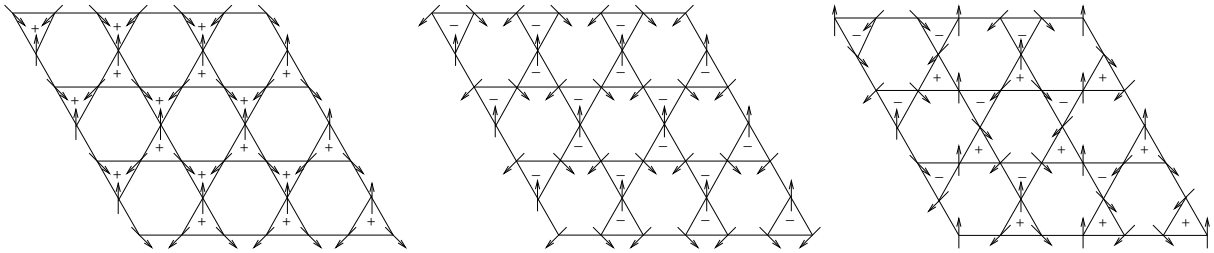

Figure 4.1: Three classical states on the kagomé lattice: (left) $\mathbf{q} = 0$ type with +1 chirality, (middle) $\mathbf{q} = 0$ type with −1 chirality, and (right) $\sqrt{3} \times \sqrt{3}$ type. Plus and minus signs indicate the chirality of spins on the elementary triangles.

fluctuations are incorporated to the classical hamiltonian Eq. (4.1), the model develops an octupolar order parameter [75], selecting coplanar spin configurations of the $\sqrt{3} \times \sqrt{3}$ type [76–78] (right panel of Fig. 4.1).

We now turn to the quantum version of hamiltonian Eq. (4.1) which sustains a large part of mystery, despite twenty years of theoretical investigations [63; 79–98]. The spin-1/2 KAF is the 2D model which offers the largest stabilization due to quantum fluctuations: the energy per spin in the quantum model is ~ 1.74 times as large as the energy per spin in the classical one, this ratio is higher than in any other 2D magnet. The low coordination number and low spin value of the spin-1/2 KAF both favor quantum fluctuations and work against spin ordering. While hamiltonian Eq. (4.1) on the triangular lattice (coordination number 6) has long-ranged spin correlations [99; 100], the KAF (coordination number 4) seems to be a spin liquid [63; 79–85]. Spectra of spin-1/2 KAF samples exhibit an unconventional behavior: a continuum of singlet excitations has been revealed just above the ground state [80; 85] and somewhat clarified [89; 90], but the mechanism responsible for this high density of singlet states is not completely understood yet. A physical consequence of this exceptional density of low-lying singlets can be observed in the specific heat: at low

temperature the specific heat of this spin system is unusually large, with a double peak structure [101–105], insensitive to relatively large magnetic fields [81] (singlet states are non-magnetic). Regarding the spin gap, the issue is still under debate. Many theoretical studies [79–84] (including a DMRG study of this 2D model [84]) have concluded to a small spin gap of the order of $\sim J/20$, but the scenario of a gapless spin liquid has been put forward recently [87; 88]. The nature of the ground state (and of the low-lying singlet excitations) is also unclear. C. Lhuillier *et al.* [4] have classified the spin-1/2 KAF as a special type of short-range resonating valence bond spin liquid (superposition of an exponential number of valence bond configurations that are roughly equally favorable, leading to a continuum of singlet states that are adjacent to the ground state), but the scenario of a valence bond crystal (VBC) is about to be considered as the most relevant one nowadays [92–98; 106–108]. The near criticality of the model as well as its location at a first order phase transition between two VBCs [108] also contribute to these conflicting theoretical results, and to the difficulty of selecting the VBC that could possibly be relevant.

From the experimental side it has long been – and is still – a challenge to synthesize materials that have both the good value of spin $S = 1/2$, and whose structure is close to the kagomé. Some materials, like the jarosites $AM_3(\mathrm{OH})_6(\mathrm{SO}_4)_2$ [109] for instance have the magnetic $M =\mathrm{Cr}^{3+}$ or Fe^{3+} ions on a perfect kagomé lattice, but with spins $S > 1/2$ ($A =$ K, Rb, Na, or NH_4 are located between the kagomé planes). Other have $S = 1/2$ but with a non-perfect kagomé structure, such as the magnetic Cu^{2+} ions in the volborthite[1] $\mathrm{Cu_3V_2O_7(OH)_2{\cdot}2H_2O}$ [111]. A third class of materials such as $\mathrm{SrCr_{9p}Ga_{12-9p}O_{19}}$[2] (quasi-2D insulator with the magnetoplumbite structure, where 2/3 of the Cr^{3+} ($S = 3/2$) ions lie in kagomé planes) and $\mathrm{Ba_2Sn_2ZnGa_{10-7p}Cr_{7p}O_{22}}$ were hampered by disorder or strong third direction interaction or many factors combined. Moreover, additional Dzyaloshinskii-Moriya (DM) interactions are present in these compounds due to the spin-orbit coupling. The herbertsmithite $\mathrm{ZnCu_3(OH)_6Cl_2}$ [113] has $S = 1/2$ and structurally perfect kagomé planes, but has been found to have impurities (about 6% of the Cu^{2+} are replaced by Zn^{2+} within the kagomé planes) [114; 115], DM interactions (of about $D = 0.08J$ magnitude) [116–118], as well as anisotropies [119]. It is the $x = 1$ end compound of the Zn-paratacamite family $\mathrm{Zn}_x\mathrm{Cu}_{4-x}(\mathrm{OH})_6\mathrm{Cl}_2$ ($0 \leq x \leq 1$) [120], whose crystal symmetry is monoclinic ($P2_1/n$) for $x < 0.33$ resulting in a distorted kagomé lattice. Around $x = 0.33$, the crystal symmetry increases to rhombohedral ($R\bar{3}m$) and the Cu triangular plaquettes become equilateral. For $0.33 \leq x \leq 1$ due to a more favorable electrostatic environment,

[1] From DFT calculation results, the authors of the recent paper Ref. [110] actually claim that a coupled spin chain model with orbital order provides a better description of the volborthite $\mathrm{Cu_3V_2O_7(OH)_2{\cdot}2H_2O}$ than the kagomé model does.

[2] The theoretically expected very small field dependence in the specific heat has been experimentally confirmed by measurements on $\mathrm{SrCr_{9p}Ga_{12-9p}O_{19}}$ [112] (notice that this compound has $S > 1/2$). Its specific heat around 5 K has an extremely low sensitivity to magnetic fields up to 10 T.

Cu^{2+} is expected to preferentially occupy the distorted octahedral kagomé sites only. When $x = 1$ the $S = 1/2$ ions should therefore form structurally perfect kagomé layers that are themselves well separated by diamagnetic Zn^{2+}. The crystal structure of the compound with 33% Zn occupancy is shown in Fig. 4.2.

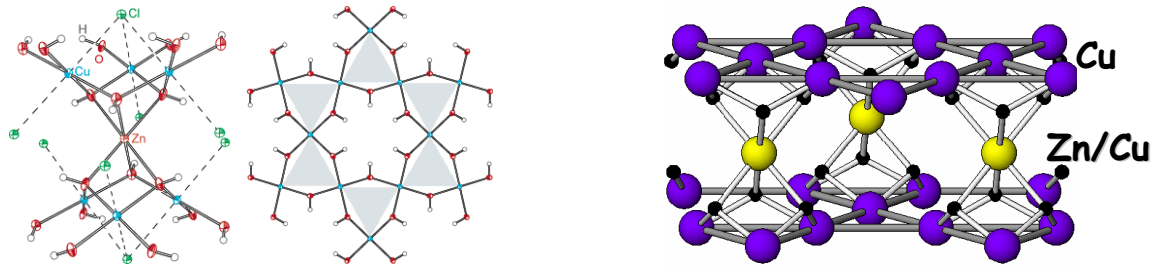

Figure 4.2: Structure of Zn-paratacamite $Zn_{0.33}Cu_{3.67}(OH)_6Cl_2$ (identical as the structure of the herbertsmithite) from Ref. [113]. (Left) Spatial structure. (Right) Simple sketch of the structure where Zn and Cu sites only have been represented. The violet Cu triangular plaquettes are equilateral for $x \geq 0.33$.

Almost all the experiments with the imperfect kagomé compounds we have listed have concluded to a gapless spin liquid [111; 114; 115; 121–126], including for the herbertsmithite in which the impurities do presumably not have significant consequences on its magnetic behavior[3]. Recently, the organometallic hybrid compound Cu(1,3-benzenedicarboxylate) with structurally perfect $S = 1/2$ copper kagomé planes separated by pure organic linkers has been synthesized [30], and spin resonance confirms [128] that it can serve as a model kagomé compound, but no experimental data are available yet for this new compound.

The first section of this chapter is devoted to the application of the tool which was introduced in the previous Chapter 3 – allowing to extract the dominant correlations in a spin system – to the spin-1/2 KAF. We study correlations between blocks of 1, 2, 3, and 6 sites and we show that at large distance, correlations of the dimer type dominate in most of its lowest-lying states; the scenario of a valence bond crystal (VBC) is therefore of primary importance. It is then more deeply investigated in the second section, were the compatibility between the symmetries of the low-lying singlet states of the spin-1/2 KAF and those of some VBCs (proposed in the literature or ad hoc) is analyzed. Finally, an analysis of the entanglement entropy of various kinds of blocks is performed in the

[3]Ref. [127] studies the magnetic properties of the new series of compounds $Mg_xCu_{4-x}(OH)_6Cl_2$ which are isostructural with paratacamite. They have less than 3% impurities (i.e. Cu^{2+} replaced by Mg^{2+} within the kagomé planes) – thus about twice as less as in the herbertsmithite – and are also disordered within the kagomé planes. The disorder in materials with this structure type is therefore not due to impurities, but indeed to the high spin frustration within the kagomé planes.

third section. Blocks realizing the minimal entropies are identified, and the question of the scaling law governing entanglement entropies is addressed.

4.2 The samples and their characteristics

Our ED studies are performed on the seven samples depicted in Fig. 4.3. They have 12, 18 (2x), 24 (2x), 30, and 36 sites and are referred to as s12, $s18_1$, $s18_2$, $s24_1$, $s24_2$, s30, and s36[4] respectively. Notice that we study two samples with 18 and 24 sites which are topologically different one from another. A particular attention is paid to sample s36 which

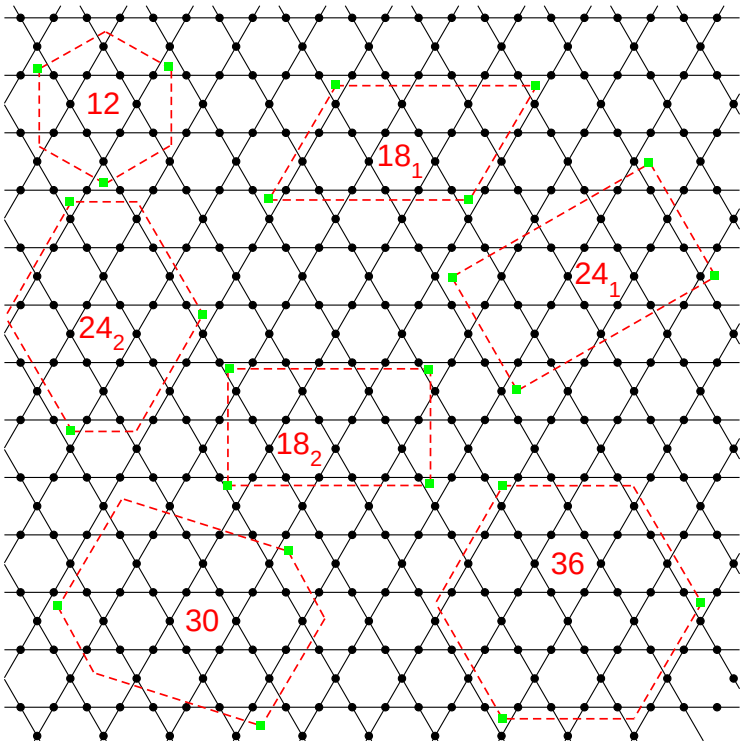

Figure 4.3: Unit cells of samples s12, $s18_1$, $s18_2$, $s24_1$, $s24_2$, s30, and s36 we use for performing Exact Diagonalization. Periodic boundary conditions are chosen. The light green squares illustrate how every sample are repeated in space.

is interesting in two respects: firstly it is the largest size one can reach performing ED, and

[4]It is also possible to construct a 36-site sample which is parallelogram-like and consists of 4×3 elementary triangles. Such a sample would nevertheless not have the symmetries of the infinite lattice, in contrast to s36.

secondly among the studies concluding that the low-energy physics of the spin-1/2 KAF is a VBC, many of them [92; 96–98; 107] point out a unit cell that is compatible with s36.

For every sample, the commensurate momenta within the hexagonal first Brillouin zone (BZ) are shown in Fig. 4.4. In each of the panels of Fig. 4.4, momenta that are related one

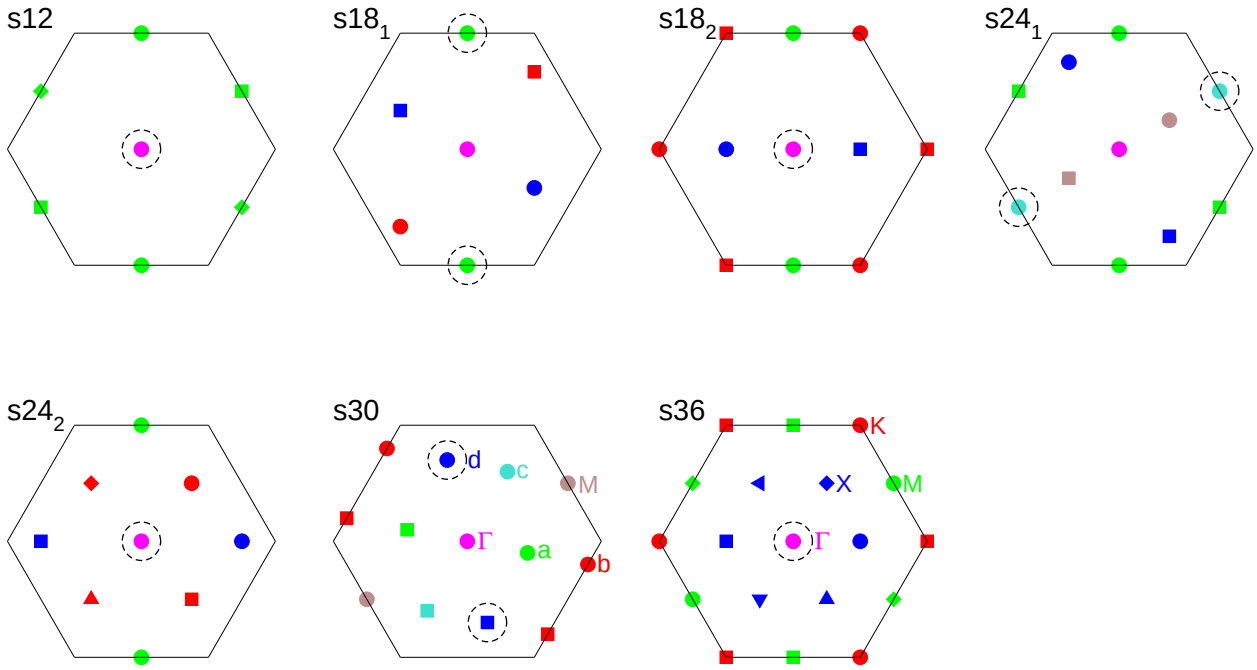

Figure 4.4: Commensurate momenta within the hexagonal first Brillouin zone (BZ) for every sample. Momenta which can be mapped one onto another by a symmetry of the BZ are shown with the same color. Among the momenta with the same color, those which are nonequivalent are shown with different symbols. Ground state momentum sectors are circled in black. s30 has a (twice) degenerate ground state. Only s12 and s36 have the full symmetry of the infinite lattice (C_{6v}).

to another by a symmetry of the BZ are shown with the same color. Among the momenta with the same color, those which are nonequivalent[5] are shown with different symbols. For every color, it is thus enough to numerically investigate in one momentum sector only. The ground state (GS) momentum sectors are circled in black in Fig. 4.4. The GS of

[5]Two momenta are said to be nonequivalent if they do not differ by a reciprocal vector of the (infinite) kagomé lattice.

a given sample is degenerate if it belongs to momentum sectors which can be mapped one onto another by a symmetry of the BZ, but are nonequivalent (momenta with the same color, but different symbols); or if it belongs to a representation of the little group of a momentum sector which is not one-dimensional[6] (refer to Appendix A for detailed explanations about the notion of "little group"). From those arguments, it turns out that only s30 has a (twice) degenerate GS, belonging to two nonequivalent momentum sectors. Although they are orthogonal one to another, the two GSs of s30 have symmetry related physical properties. We shall therefore refer to both of them at once as *the GS of s30*.

For illustration and further use, we display the singlet levels within the spin gap for samples s30 and s36 in Fig. 4.5. For the numerical investigation of sample s36, we use the full space group (including the point group, see Appendix A). The four nonequivalent momenta of s36 that are labelled and colored differently in Fig. 4.4 have the following little groups, each with its own irreducible representations (IRREPs): Γ has little group C_{6v}, M has little group C_{2v}, K has little group C_{3v}, and X has little group C_{1h}. We shall refer to some particular symmetry sector (or IRREP) of s36 using a tuple containing both the momentum and the point group symmetry in question, e.g. $[\Gamma, A_1]$ refers to the A_1 representation of the zero-momentum sector (trivial representation). If the momentum degeneracies are taken into account, we have counted 97 singlet states within the spin gap for sample s30, and 210 (in agreement with Ref. [91]) for s36. The lowest energy obtained for s36 by Ref. [98] with the MERA (Multi-scale Entanglement Renormalization Ansatz) variational wave function is shown in red in the right-hand side of Fig. 4.5: even if the relative error with the energy of the GS is small, s36 has 85 states below the lowest MERA energy.

The samples we consider for investigating the spin-1/2 KAF have their own topological characteristics that it is important to know in order to distinguish between a result which is really reflecting the physics of the thermodynamic limit, and an artifact due to topological finite size effects. Their magnetic and non-magnetic energy gaps as well as their GS energy per site strongly depend on how far from a 1D system they are. J.-B. Fouet *et al.* [7] have shown that the GS energy per site in the spin-1/2 Heisenberg model on the 2D checkerboard lattice is underestimated for quasi-1D samples. Regarding magnetic and non-magnetic energy gaps, they are overestimated in those samples. The left panel of Fig. 4.6 shows that this is also the case in the spin-1/2 KAF. The GS energy per site (top) and the energy gaps (bottom) are displayed as a function of the inverse size of every sample. In all cases, the dependence is roughly linear, and reasonably well described by the least-squares fits (dotted lines)[7]. Only sample $s24_1$ seems to behave differently and strongly deviates

[6]The little groups of the GS momentum sectors are C_{6v} (for s12), C_2 ($s18_1$), C_{2v} ($s18_2$), C_{2v} ($s24_1$), C_{2v} ($s24_2$), C_1 (s30), and C_{6v} (s36). These groups have only one-dimensional representations except C_{6v}, but the GSs of s12 and s36 are in the respective representations B_2 and A_1 of C_{6v}, which are one-dimensional.

[7]Notice that the non-magnetic energy gap – which is known to vanish in the thermodynamic limit – is

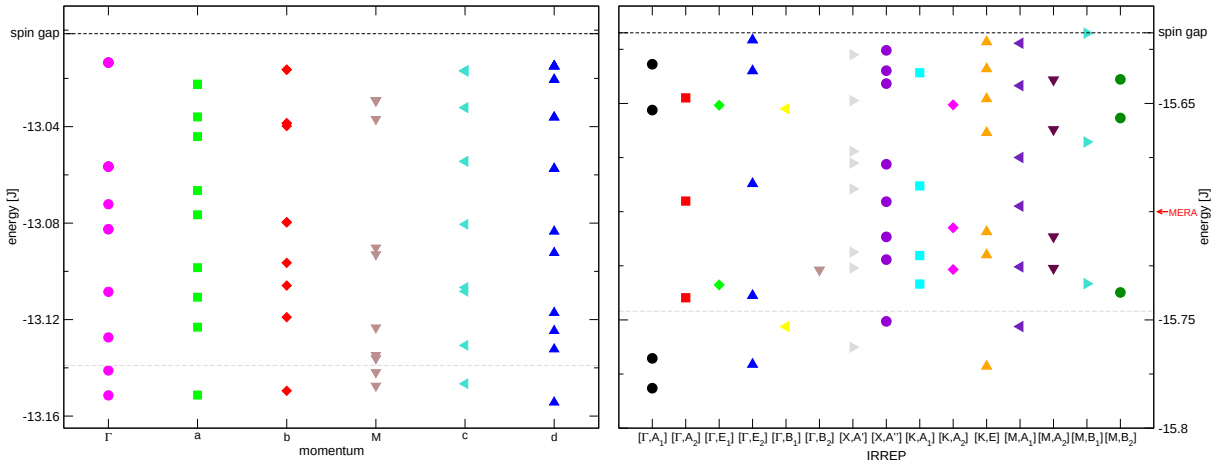

Figure 4.5: Singlet states within the spin gap arranged according to symmetry sectors in the spectra of samples s30 (left) and s36 (right). Momenta sectors are defined in Fig. 4.4. For both samples, the black dashed horizontal line denoted by "spin gap" shows the energy of the lowest triplet state, and the light gray dashed line separates the 8 lowest-lying states from the rest of the singlet spectrum. The lowest energy obtained for s36 by Ref. [98] with the MERA variational wave function is shown in red on the right hand side.

from these linear laws for the energy per site (it is well below the line) and the magnetic gap (it is well above the line). In order to understand in which respects $s24_1$ is particular, it is necessary to pay some attention to the cause of finite size effects in the samples, i.e. to *closed loops*. Closed loops are already present in the infinite lattice, the shortest of which has a length of 6 lattice spacings and is drawn along an elementary hexagon. The point is that in finite samples, periodic boundary conditions can artificially create closed loops that are shorter than 6 lattice spacings. Such loops will be "felt" by the system and will affect it.

On the kagomé lattice, one goes from any site to one of its four nearest neighbors (nn) by following one of these three directions (or their opposite): $\longrightarrow \equiv (1,0)$ (direction A), $\nearrow \equiv \left(1/2, \sqrt{3}/2\right)$ (direction B), or $\nwarrow \equiv \left(-1/2, \sqrt{3}/2\right)$ (direction C). Let us define by $\mathrm{LL}_X \leq 6$ ($X = A, B, C$) the Manhattan length[8] of the shortest closed loop starting in direction X (and then free to continue in any direction). LL_A, LL_B, and LL_C are given in Table 4.1 for every sample. Closed loops shortest than 6 lattice spacings are present in samples s12, $s18_1$, $s18_2$, and $s24_1$. In $s18_1$ and $s24_1$, the closed loops are shorter in one (preferred) direction (B and C respectively) than in the two others. It turns out that these

extrapolated to a negative value, which is not physical.

[8]The Manhattan length of a path is defined as the number of sites that are crossed when following it.

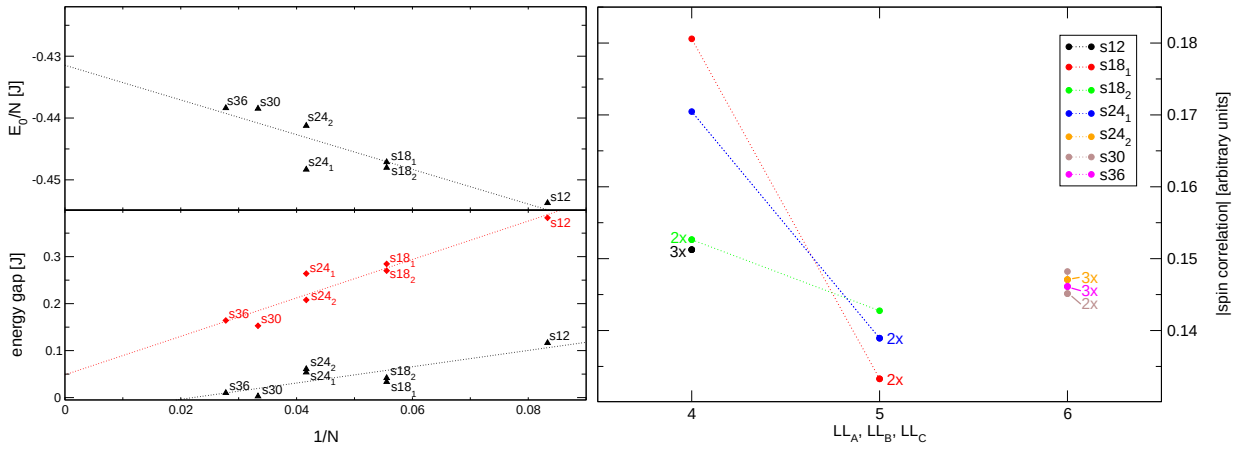

Figure 4.6: (Left) Energy per site, and magnetic (red) as well as non-magnetic (black) energy gaps as a function of the inverse size of the samples. (Right) Absolute value of spin correlations between two spins aligned along each possible direction A, B, and C for every sample as a function of the length of the shortest closed loop starting along those directions. Short loops favor strong spin correlations.

preferred directions have consequences on the structure of spin correlations and strongly affect them, whence the particular behavior of $s24_1$ we have pointed out when analyzing Fig. 4.6 (the particularity of $s18_1$ is less marked in that figure). Spin correlations between two nn spins that are aligned along direction X are shown as a function of LL_X in the right panel of Fig. 4.6 for $X = A, B, C$. It appears that the shortest the closed loop, the largest the strength of the correlation, i.e. *spin correlations are favored (stronger) along short closed loops*. Since the total energy Eq. (4.1) is given by the sum of the spin correlations between all nn spin pairs, one easily understand why the GS energy per site

sample	LL_A	LL_B	LL_C
s12	4	4	4
$s18_1$	5	4	5
$s18_2$	5	4	4
$s24_1$	5	5	4
$s24_2$	6	6	6
s30	6	6	6
s36	6	6	6

Table 4.1: LL_X $(X = A, B, C)$ distances for every sample.

is underestimated in small samples, or in samples with a preferred direction like $s24_1$.

4.3 Investigation of the lowest-lying states by means of the CDM tool

This section is devoted to the correlation density matrix (CDM) analysis of the spin-1/2 KAF. The nature of dominant correlations between blocks of 2 nn sites, blocks of 3 sites arranged on elementary triangles, and blocks of 6 sites arranged on elementary hexagons are investigated in its low-lying states. A particular attention is paid to spin correlations as well. Finally, the CDM analysis is performed on a small system at finite temperature for illustrative purposes.

4.3.1 Blocks with one site

The CDM analysis of correlations between blocks of one site actually amounts to analyzing spin correlations, which are well known to decrease quite fast in the spin-1/2 KAF [63; 79]. We wish to show here that their structure is nevertheless very sensitive to closed loops in the various samples we consider, i.e. depend on the topology of those samples.

Spin correlations are shown in Fig. 4.7 in the ground states of the seven samples under study[9]. Reference sites are black, and blue/red sites denote positive/negative correlations, their widths are proportional to the strength of the correlations. For samples s12 and s36 which have the symmetries of the infinite lattice, all the independent spin correlations can be shown in one panel (it is enough to fix the reference site on one single arbitrary vertex of a selected elementary triangle). For samples $s18_1$, $s18_2$, $s24_1$, and $s24_2$ that have mirror reflections and a π-rotation as symmetries it is necessary to consider the reference site on two different vertices of a selected elementary triangle in order to generate all the independent correlations[10], two panels are thus drawn. Regarding s30, there is only the π-rotation symmetry, therefore each of the three vertices of a selected elementary triangle have to be successively chosen as reference site in order to generate all the independent correlations. Notice that we have strongly zoomed in on the colored sites for revealing the structures in Fig. 4.7. Correlations between nn sites are dropped for the sake of clarity.

On every sample, the system gains energy by allowing spin correlations to be noticeably stronger along paths going from one black reference site to its closest image (i.e. to another black site) than elsewhere, see for illustration the green path in the panel corresponding

[9]The closed loop effects we shall describe occur in a similar way in the low-lying states.

[10]Sample $s18_1$ has no mirror reflection as symmetry, but due to "hidden" topological symmetries it is enough to consider two reference sites in order to generate all the independent spin correlations.

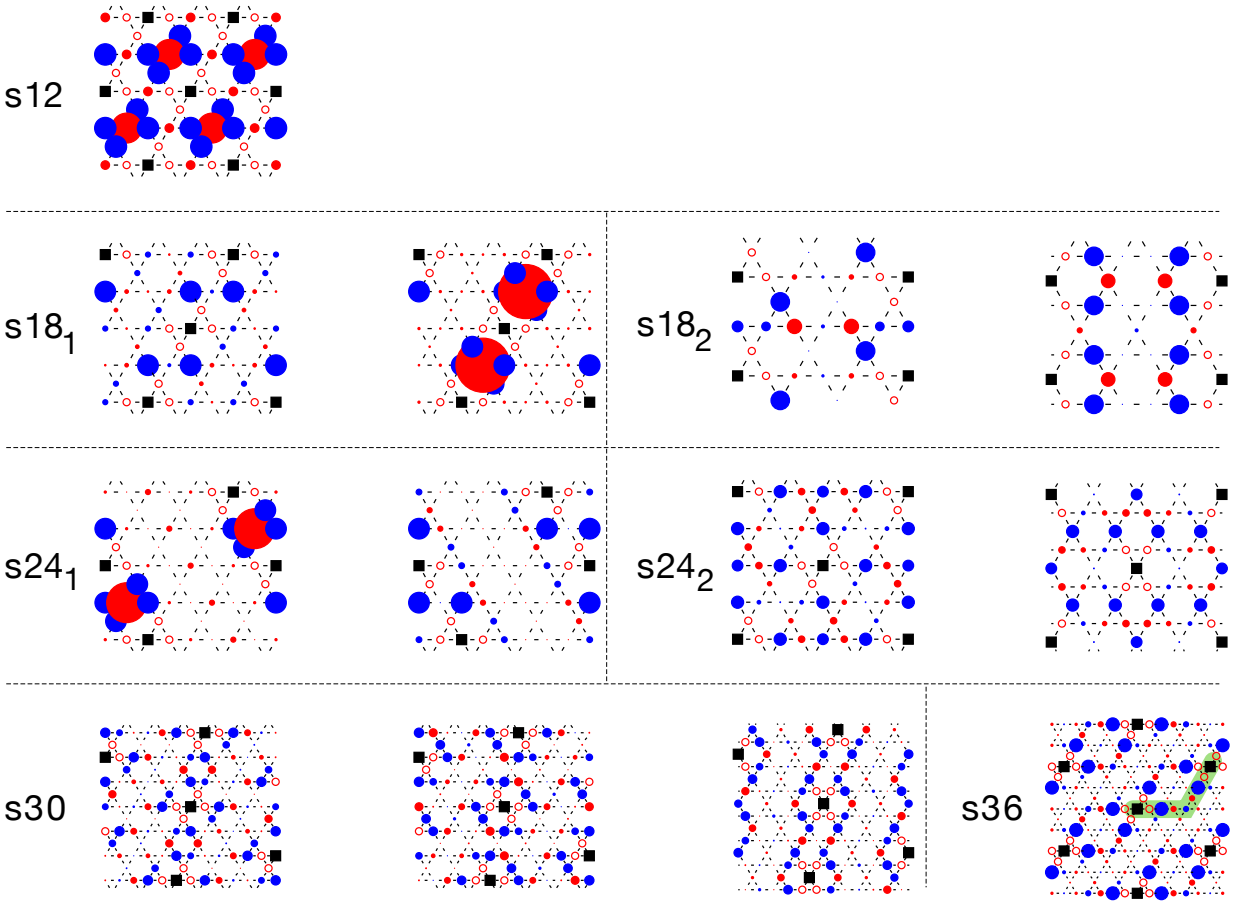

Figure 4.7: Spin correlations in the ground state of every sample. For s12 and s36, only one panel is necessary for showing all the independent correlations, while for s18$_1$, s18$_2$, s24$_1$, and s24$_2$ two panels are necessary, and for s30 three panels are necessary. The reference site is black, and blue/red sites denote positive/negative correlations, their diameter is proportional to the strength of the correlation. Correlations between nearest neighboring sites are skipped (empty circles with fixed width) for the sake of clarity.

to s36 (right panel on the bottom of Fig. 4.7). Spin correlations furthermore exhibit a propensity to be staggered along these favored paths. They are biased by closed loops, which have important consequences, even in the largest sample s36. Notice that the phenomenon – which has already been pointed out in Fig. 4.6 (right panel) of the previous section – is also visible in the spin correlations of the disordered $J_2/J_1 = 0.55$ phase of the spin-1/2 Heisenberg model on the square lattice Fig. 3.9: in the middle left panel of that figure, the spin correlations do not decrease isotropically from a reference black site:

they are strong and staggered along the horizontal and vertical directions (shortest loops between two black sites), and decrease much faster along diagonals.

From this spin correlations study, we draw the conclusion that the measurement of physical quantities on finite size samples are somewhat biased by their topology as well and should be considered with care. The phenomenon must nevertheless not be exaggerated: we recall that spin correlation in Fig. 4.7 have been zoomed substantially in order to make these structures visible. One could nevertheless imagine that – due to closed loop effects – the VBC which could be realized in the thermodynamic limit would not be selected in a finite size sample even though the sample would have the size of the unit cell of the crystal and would be commensurate with it. This could for instance explain why the MERA variational wave function used in Ref. [98] does not converge towards the 36-site unit cell VBC by Marston & Zeng Ref. [92] on the s36 topology, while it does in the infinite lattice.

4.3.2 Blocks with two sites

We compute here the SV spectrum for all possible configurations where both blocks are built on nn spin pairs. As hamiltonian Eq. (4.1) has the $SU(2)$ symmetry and we study singlet states, only 6 SVs among 16 are independent for every configuration of blocks, according to Subsection 3.4.2. One of the two singlet SVs – corresponding to correlations between identity operators – is always zero.

The study is restricted to the eight lowest-lying states (without taking their degeneracy into account) of the two largest samples s30 and s36. They are separated from the highest states by a dashed gray line in the energy spectra of s30 and s36, Fig. 4.5 in Section 4.2. The SV spectra of s30 and s36 are displayed in Fig. 4.8, the panels are arranged from the left to the right and from the top to the bottom in the order of increasing energy. The translational invariance due to periodic boundary conditions allows to fix one of the blocks successively on each of the three edges of an arbitrarily chosen elementary triangle for performing the SVD (the three edges are directed differently). For s36, the number of edges that must be taken into account among the three possible ones for generating all the independent CDMs depends on the symmetry properties of the IRREP we consider. All the IRREPs of sector Γ for instance have the rotation by $2\pi/6$ as symmetry, allowing to map every edge onto the two others. In these IRREPs, it is thus enough to consider the fixed block on one arbitrary edge only; which is also the case in the IRREPs of sector K. IRREPs of sector M have rotations by $\pi/2$ and two reflections as symmetries, and the only symmetry of sector X is one reflection. In these cases, two edges can be mapped one onto another, but cannot be mapped onto the third one: it is necessary to consider the fixed block on two edges in order to generate all the independent CDMs.

The base 10 logarithm of the SVs is represented in Fig. 4.8 as a function of the Man-

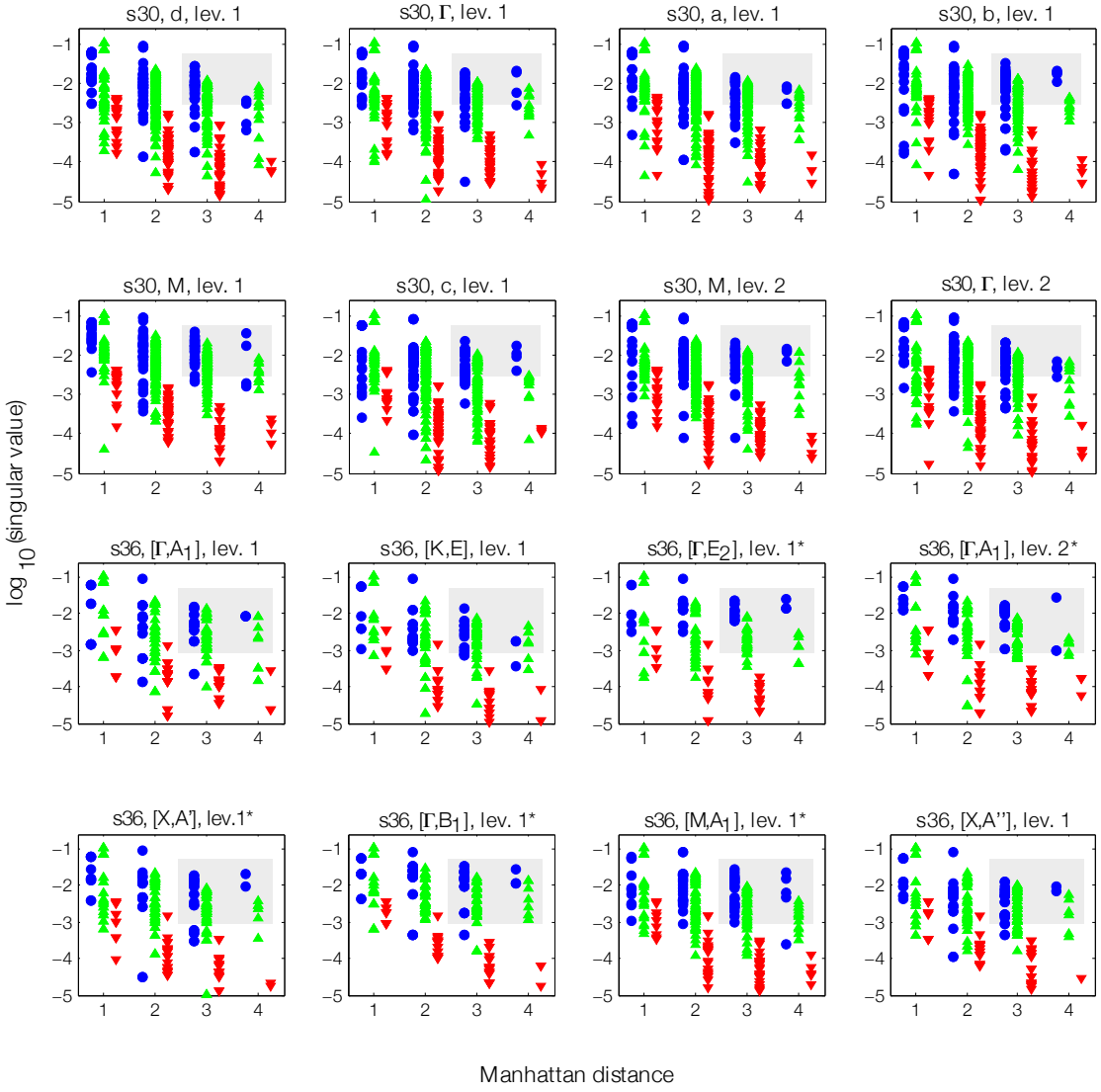

Figure 4.8: The base 10 logarithm of the singular values is shown as a function of the Manhattan distance between the blocks for all possible configurations of blocks built on nn spin pairs for the 8 lowest-lying states of s30 and s36. Only integer Manhattan distances appear, but the symbols are horizontally shifted regarding their color for the sake of clarity. Blue symbols (circles) represent singular values that decompose onto the singlet operator ($\mathbf{S}_k \cdot \mathbf{S}_l$), green symbols (triangles up) represent singular values that decompose onto triplet operators ($\mathbf{S}_k + \mathbf{S}_l$, $\mathbf{S}_k - \mathbf{S}_l$, and $\mathbf{S}_k \times \mathbf{S}_l$), and red symbols (triangles down) represent singular values that decompose onto the quintet operator ($\mathbf{Q}_{kl}$). Gray squares show the large distance-large SV domains of particular interest.

hattan distance between the two blocks[11]. The color of the SVs is function of the spin of the basis operator Eq. (3.11) they decompose onto. Operators with different spins are forbidden to contribute to the same SV. Blue symbols (circles) denote singlet SVs (i.e. the only possible contribution is from $\mathbf{S}_k \cdot \mathbf{S}_l$), green symbols (triangles up) denote triplet SVs (i.e. possible contributions from $\mathbf{S}_k + \mathbf{S}_l$, $\mathbf{S}_k - \mathbf{S}_l$, and $\mathbf{S}_k \times \mathbf{S}_l$), and red symbols (triangles down) denote quintet SVs (i.e. the only possible contribution is from $\mathbf{Q}_{kl}$). The panels in Fig. 4.8 all share a common property: red symbols (triangles down) lie on the lower part, indicating that correlations between quadrupolar objects are irrelevant for describing the low-energy physics of the spin-1/2 KAF. The competition is between blue and green SVs. The large distance-large SV domains (see gray squares in Fig. 4.8) are of particular interest. In those domains, all panels together, either blue (circles) and green (triangles up) symbols have the same order of magnitude, or blue (circles) symbols are dominant. Fig. 4.8 is thus of central importance: it reveals that even if they are weak in the ground states of s30 and s36, correlations of the form

$$\langle (\mathbf{S}_k \cdot \mathbf{S}_l)(\mathbf{S}_{k'} \cdot \mathbf{S}_{l'}) \rangle - \langle \mathbf{S}_k \cdot \mathbf{S}_l \rangle \langle \mathbf{S}_{k'} \cdot \mathbf{S}_{l'} \rangle \text{ where } (k,l),(k',l') \text{ are nn} \tag{4.2}$$

appear to dominate in some of their low-lying states which hence seem to be dimerized (the fact that correlations Eq. (4.2) are very strong in certain states will be shown in Section 4.4). This sustains the common belief that a VBC is a good candidate for describing the low-energy physics of the spin-1/2 KAF [92; 93; 95]. Furthermore, the smallness of the red SVs tells us that quadrupolar, or n-type nematic correlations are quite weak. The difference in behavior between a non-dimerized and a dimerized state is also shown in Fig. 4.9, which displays the squared Frobenius norm Eq. (3.13) of the correlation density matrices in the ground state of s36 (left panel) and in the first state of IRREP $[\Gamma, B_1]$ (right panel), which is dimerized. The ground state is short-ranged in 2-body correlators, which is obviously not the case for the first state of $[\Gamma, B_1]$. For illustration, Fig. 4.10 compares the SV spectra of these two states when a next nearest neighbor interaction $J_2 = J$ has been added in the ground state in order to stabilize the $\mathbf{q} = 0$ Néel order[12] [62]. While in the first state of $[\Gamma, B_1]$ the largest green SVs decrease with the distance and are of the order of $\sim 10^{-2}$ at maximal distance, they are roughly constant ($\sim 10^{-1}$) in the ground state with stabilized $\mathbf{q} = 0$ order. The largest blue SVs are moreover not too much affected by the distance in the dimerized state (roughly $10^{-1.5}$), while they are decreasing in the Néel ordered state ($< 10^{-2}$ at maximal distance). Regarding the red SVs, they fall off very fast in the

[11]The Manhattan distance between two blocks is defined as the minimal number of bonds a path going from one block to the other has to cross.

[12]We just stress the fact that in contrast to Fig. 4.7, we do not zoom in on spin correlations in Fig. 4.10, and correlations between nn spins are not hidden; spin correlations in both figures must therefore not be compared one to another, the scales are different.

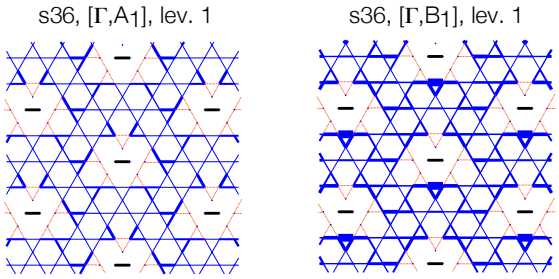

Figure 4.9: Squared Frobenius norm Eq. (3.13) in the ground state (left panel) of sample s36, and in the first state of IRREP $[\Gamma, B_1]$ (right panel). The black bond is the reference block. Squared norms corresponding to blocks in the vicinity of the black block are skipped (such blocks are shown in red) for the sake of clarity. The second state does have strong correlations between operators acting on 2 sites (2-body operators) while the first one does not.

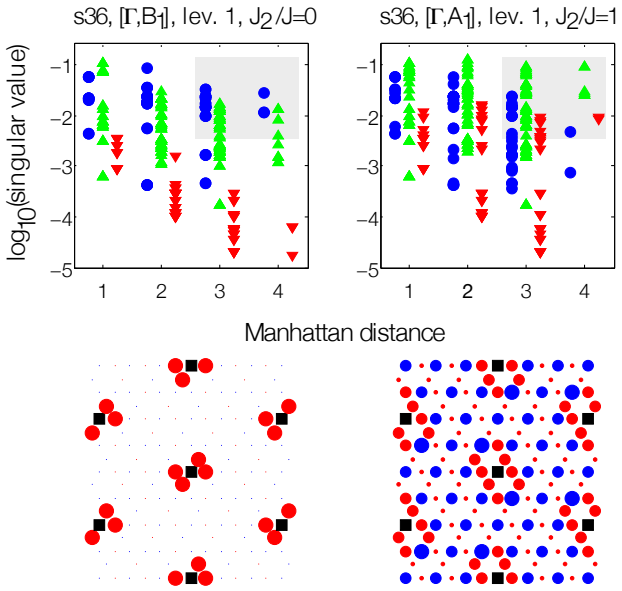

Figure 4.10: SV spectra (top) and spin correlations (bottom) in sample s36 in the first level of $[\Gamma, B_1]$ (left column), and in the first level of $[\Gamma, A_1]$ with an additional $J_2 = J$ interaction stabilizing $\mathbf{q} = 0$ Néel order (right column). In the first case, the state is dimerized (i.e. dimer correlation survive the distance) and the blue singlet SVs dominate in the large distance-large SV domain (gray square). In the latter case, the state has Néel order and the green SVs dominate in the large distance-large SV domain. None of the spectra in Fig. 4.8 resembles this Néel ordered one. Notice that the proportionality factor between spin correlations and widths is not the same as in Fig. 4.7, both figures cannot be compared one to another.

dimerized state and stay around $\sim 10^{-2}$ in the ordered state. It is presumably artificially "high" in this latter case due to the Néel order, but is not a relevant order parameter in a Néel ordered state. Notice that the SV spectrum of the ordered state resembles none of the spectra of Fig. 4.8.

An interesting fact should finally be stressed: short closed loops were shown in Subsection 4.3.1 to favor strong and staggered spin correlations; they actually also favor strong and staggered dimer correlations as illustrated in Fig. 4.11, which shows the X_1 and Y_1 operators related to the largest SV in the ground state of samples s36 and $s24_1$ for all block configurations. Symbols are defined as in Fig. 3.9 and Table 3.1 of Chapter 3, i.e. positive/negative contributions of dimer operators are denoted by blue/red circles. In Table 4.1 in Section 4.2, sample $s24_1$ was shown to have a particularly short loop along direction $\nwarrow$, whereas the three directions of s36 are equivalent. This is indeed visible in Fig. 4.11: staggered dimer correlations dominate along direction $\nwarrow$ in sample $s24_1$ (see light green lines) while they only dominate at large distance in s36 (see light green spot). Notice that the ground state of s36 is in IRREP $[\Gamma, A_1]$ which has the symmetries of the infinite lattice, we would thus get identical patterns for s36 if the black reference bond would have been directed differently.

4.3.3 Blocks with three sites

The choice of blocks consisting of triangles is natural on the kagomé lattice, which is a "triangular lattice of triangles". In the same spirit as what was done with blocks containing two nn sites, we show here the results of the CDM analysis of correlations between two disjoint blocks built on elementary triangles. A Frobenius-orthonormalized complete basis – consisting of operators with more obvious physical meanings – of the space spanned by the operators acting on three spins $S = 1/2$ is given in Appendix E. There are five singlet operators, nine triplet operators, five quintet operators, and one septuplet operator. In singlet states, the number of independent SVs is limited to 20 among 64 for a given configuration of blocks, accordingly to part 3.4.2 of Section 3.4. One of the five singlet SVs – corresponding to correlations between identity operators – is always zero.

The results are illustrated in Fig. 4.12 for the eight lowest-lying states of s30 and s36. Colors of the SVs again depend on the spin of the basis operator they decompose onto. In the spectrum Fig. 4.12, blue symbols (circles) denote singlet SVs (i.e. possible contributions from singlet operators only), green symbols (triangles up) denote triplet SVs (possible contributions from triplet operators), red symbols (triangles down) denote quintet SVs (possible contributions from quintet operators), and cyan symbols (squares) denote septuplet SVs (possible contributions from septuplet operators).

Red quintet (triangles down) and cyan septuplet (squares) SVs are quite small. The

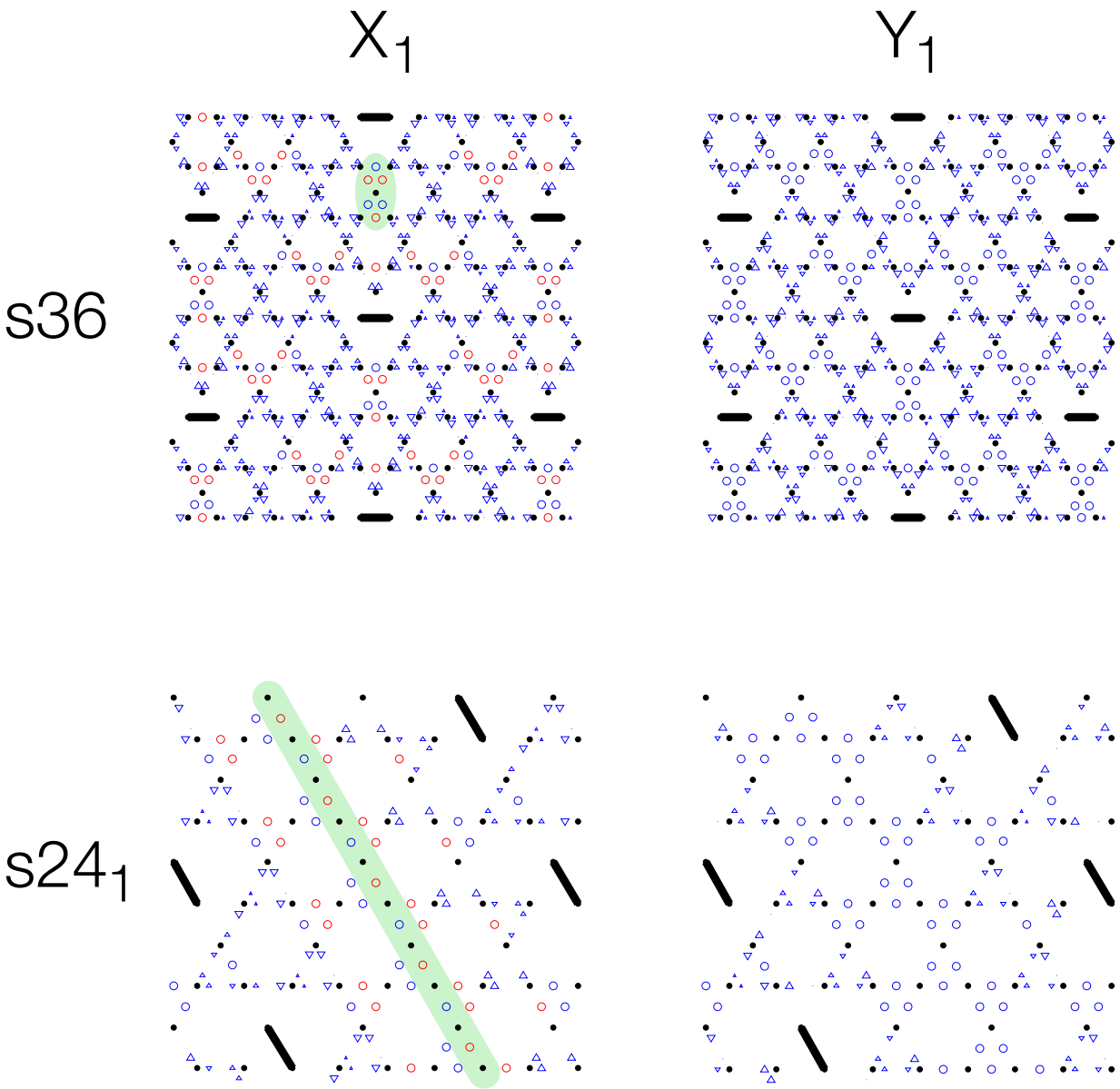

Figure 4.11: X_1 and Y_1 operators related to the largest SV in the ground state of samples s36 and $s24_1$. Symbols are defined as in Fig. 3.9 and Table 3.1 of Chapter 3, i.e. positive/negative contributions of dimer operators are denoted by blue/red circles. Staggered dimer correlations are favored along the shortest loop direction $\nwarrow$ in $s24_1$ (see Table 4.1 in Section 4.2), while they only dominate at large distance in s36, which has no "preferred direction" in terms of loop lengths.

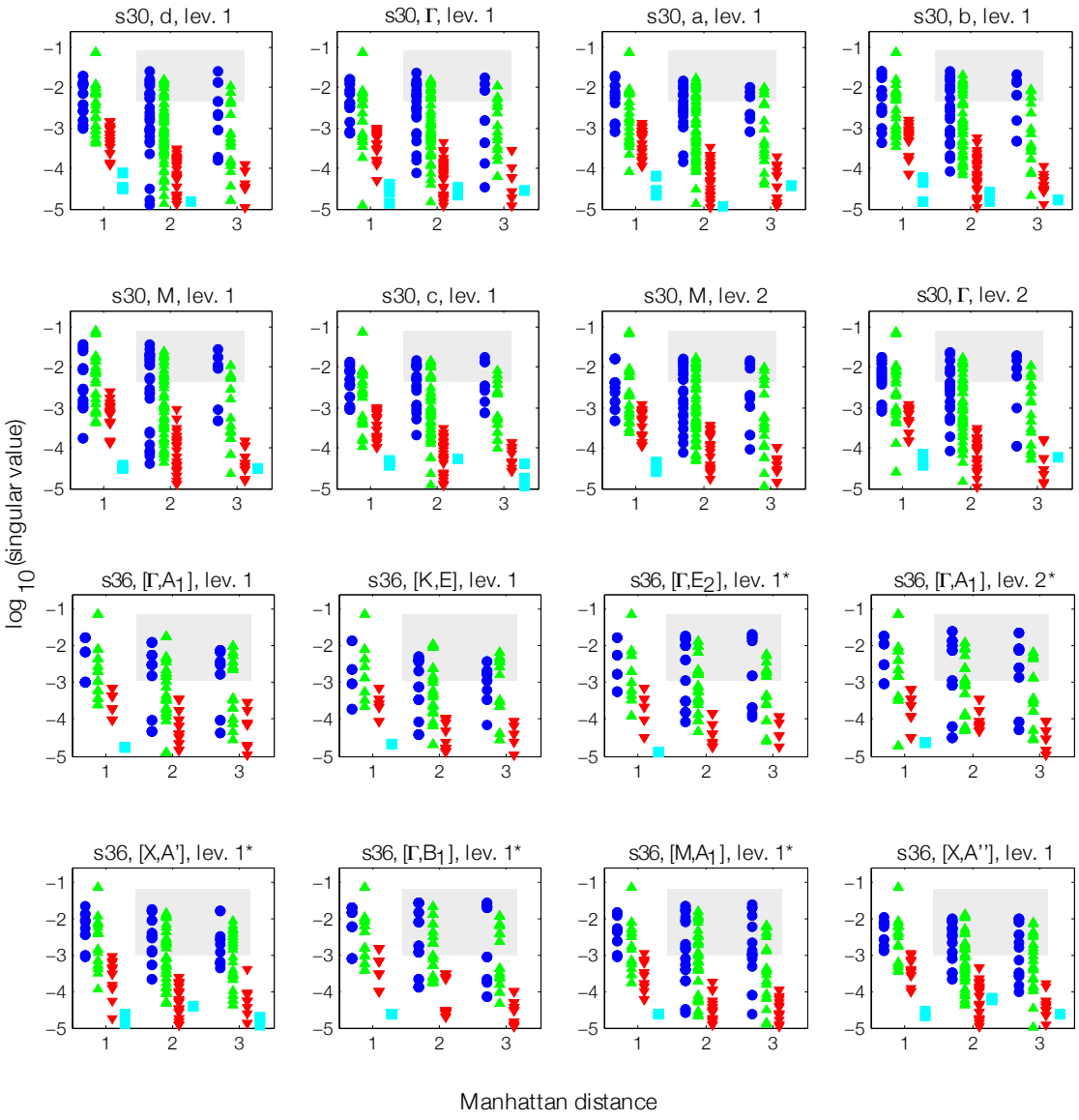

Figure 4.12: Analog of Fig. 4.8 for all possible configurations of blocks built on elementary triangles. Singular values smaller than 10^{-5} are not shown for the sake of clarity. Blue symbols (circles) represent singular values that decompose onto the singlet operator, green symbols (triangles up) represent singular values that decompose onto triplet operators, red symbols (triangles down) represent singular values that decompose onto quintet operators, and cyan symbols (squares) represent singular values that decompose onto the septuplet operator. Gray squares show the large distance-large SV domains of particular interest.

gray square on Fig. 4.12 shows that the competition is again between blue singlet (circles) and green triplet (triangles up) SVs in the large distance-large SV domain. Note that unlike in the previous analysis with 2-site blocks, blue singlet (circles) SVs can get contributions from more than one type of operator (there are 5 singlet operators). It turns out that in each of the eight lowest-lying states of s30 and s36 which are studied in Fig. 4.12, the main contribution (squared overlap > 0.97 for s30 and > 0.99 for s36 all states together) in the highest blue SV at maximal distance is from operators

$$\frac{1}{3}\left[\left(\mathbf{S}_k \cdot \mathbf{S}_l e^{i\frac{2\pi}{3}} + \mathbf{S}_k \cdot \mathbf{S}_m e^{-i\frac{2\pi}{3}} + \mathbf{S}_l \cdot \mathbf{S}_m\right) \pm h.c.\right]. \tag{4.3}$$

In particular, the contribution from the scalar chirality operator $\frac{2}{\sqrt{3}}\mathbf{S}_k \cdot (\mathbf{S}_l \times \mathbf{S}_m)$ is low (< 0.03 for s30 and < 0.001 for s36 all states together). The sharp decrease of this correlator was already pointed out in Ref. [80]. The emergence of dominating correlations of type Eq. (4.3) – which is the 3-site analog of Eq. (4.2) – again favors the VBC scenario.

Fig. 4.13 displays the squared Frobenius norm for the same two states as it was done in Fig. 4.9 for blocks with two sites. One notices that the message which was provided by Fig. 4.9 is somewhat buried in too many details in Fig. 4.13: particularly strong correlations in 2-body operators are much more difficult to detect in Fig. 4.13 than in Fig. 4.9 because of the "noise" that is due to the addition of one site. In Fig. 4.13, the squared Frobenius norms are slightly larger in the first state of $[\Gamma, B_1]$ than in the the ground state, but decrease quite fast in both cases.

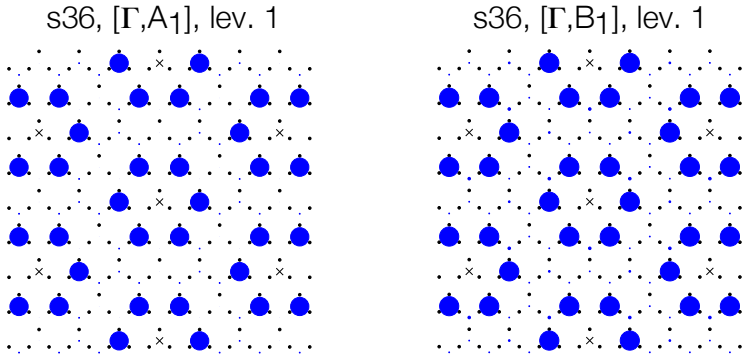

Figure 4.13: Squared Frobenius norm Eq. (3.13) in the ground state (left panel) of sample s36, and in the first state of IRREP $[\Gamma, B_1]$ (right panel). The reference elementary triangle is marked by a cross $\times$.

4.3.4 Blocks on hexagons

Another natural choice for constructing blocks on the kagomé lattice is to choose elementary hexagons (blocks with 6 sites). Unfortunately this study is hampered by the fact that there are only a few possibilities of constructing two disjoint hexagonal blocks on the small samples we study. CDM computations on hexagonal blocks have been performed in the ground state of samples $s18_2$ (1 way of constructing the two disjoint blocks), $s24_1$ (2 ways), $s24_2$ (1 way), and s30 (3 ways, 2 of which are nonequivalent), and the resulting SV spectra are shown in Fig. 4.14. There is no way of constructing two disjoint hexagonal blocks on s12 and $s18_1$. In Fig. 4.14, we only distinguish between singlet and nonsinglet SVs. It appears that for every configuration of blocks, the dominant SVs are singlet ones.

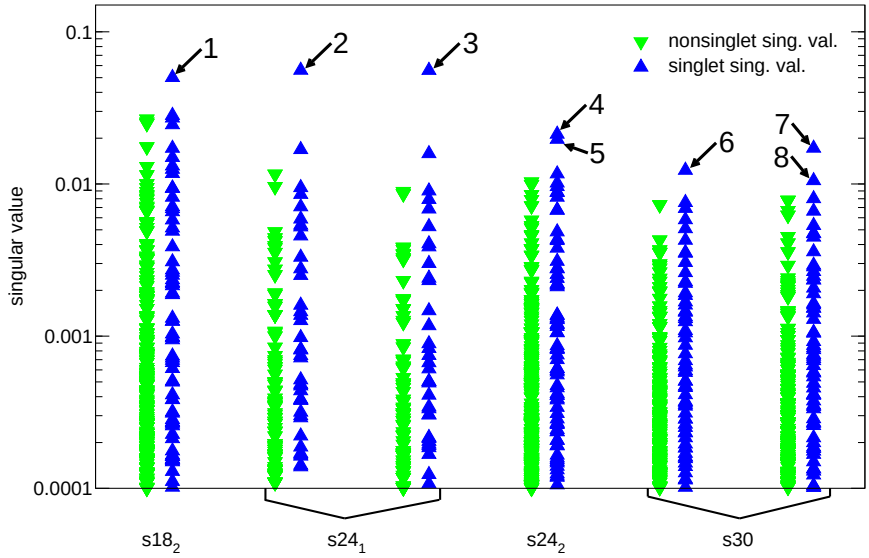

Figure 4.14: Singular values for blocks built on elementary hexagons in the ground states of $s18_2$, $s24_1$, $s24_2$, and s30. There are 1/2/1/3 ways of constructing disjoint hexagons on samples $s18_2$/$s24_1$ /$s24_2$/s30 respectively. Among the three ways of constructing them on s30, only two are nonequivalent. In every case, singlet singular values are shown in blue (triangles up) on the right hand side and nonsinglet ones are shown in green (triangles down) on the left hand side; singlet singular values are always dominant.

The number of operators in the different spin spaces is determined by computing the Clebsch-Gordan decomposition

$$\left(\frac{1}{2}\otimes\frac{1}{2}\otimes\frac{1}{2}\otimes\frac{1}{2}\otimes\frac{1}{2}\otimes\frac{1}{2}\right)\otimes\left(\frac{1}{2}\otimes\frac{1}{2}\otimes\frac{1}{2}\otimes\frac{1}{2}\otimes\frac{1}{2}\otimes\frac{1}{2}\right)$$
$$= 0_{132}\oplus 1_{297}\oplus 2_{275}\oplus 3_{154}\oplus 4_{54}\oplus 5_{11}\oplus 6_1. \qquad (4.4)$$

The construction of a complete basis of physical meaningful singlet operators looks to be a cumbersome task: 132 operators have to be found. Instead of constructing the entire set of singlet basis operators, we aim to investigate to which extent products of $(\mathbf{S}\cdot\mathbf{S})$ operators i.e. elements of the set

$$\begin{aligned}&\{(\mathbf{S}_k\cdot\mathbf{S}_l)\mathbb{1}\!\!\mathrm{I}_{mnpq}|k<l\}\cup\\&\{(\mathbf{S}_k\cdot\mathbf{S}_l)(\mathbf{S}_m\cdot\mathbf{S}_n)\mathbb{1}\!\!\mathrm{I}_{pq}|k<l,m<n,\text{ and }k<m\}\cup\\&\{(\mathbf{S}_k\cdot\mathbf{S}_l)(\mathbf{S}_m\cdot\mathbf{S}_n)(\mathbf{S}_p\cdot\mathbf{S}_q)|k<l,m<n,p<q,\text{ and }k<m<p\}\end{aligned}\tag{4.5}$$

contribute to the dominant singlet SVs that are numbered in Fig. 4.14. The set Eq. (4.5) has 75 elements, each of which is even under the time reversal operation $t\mapsto -t$ (resulting in $\mathbf{S}_i\mapsto-\mathbf{S}_i\ \forall i$). Singlet basis operators that are odd under this operation are thus not included in this set. Once the elements of Eq. (4.5) have been orthonormalized w.r. to the Frobenius scalar product $\left(\widehat{O}\middle|\widehat{O}'\right)_F:=\mathrm{Tr}\left(\widehat{O}\widehat{O}'^{\dagger}\right)$, we have computed for each of the 8 singlet SVs (blue, triangles up) that are numbered in Fig. 4.14 the sum of the squared overlaps between the operators resulting from the SVD[13], and the elements of this orthonormalized set. This sum turns out to be 1 for arrows 1 to 5 (samples $\mathrm{s18}_2$, $\mathrm{s24}_1$, and $\mathrm{s24}_2$) and >0.94 for arrows 6 to 8 (sample s30), although $(\mathbf{S}\cdot\mathbf{S})$-product operators represent only about one half of the total number of independent singlet operators acting within blocks with 6 sites.

This CDM study of correlations between elementary hexagons thus points out two interesting facts: on the one hand dominant SVs are singlet ones, as it was the case for the study of correlations between blocks with 2 and 3 sites; on the other hand the major contribution to these dominant singlet SVs is from products of dimer-like $(\mathbf{S}\cdot\mathbf{S})$ operators, that are even under the time reversal operation. These facts agree with the VBC scenario and support the idea that dimer correlations (or at least correlations between singlet operators) are the most relevant for describing the low-energy physics of the spin-1/2 KAF.

4.3.5 Illustration of the CDM method at finite temperature

As we already stressed in Section 3.6 while analyzing the spin-1/2 J_1–J_2 chain at finite temperature, the $SU(2)$ symmetry is restored in the thermal CDM, which has a contribution from the entire energy spectrum. The number of independent SVs for a given configuration of blocks is therefore the same as in the zero temperature case.

Fig. 4.15 shows the evolution of the 5 independent nonzero SVs with the temperature T for one particular configuration of two disjoint blocks (made of two nn sites) at maximal

[13]These sums of squared overlaps are actually identical for the $\widehat{X}$ and $\widehat{Y}$ operators.

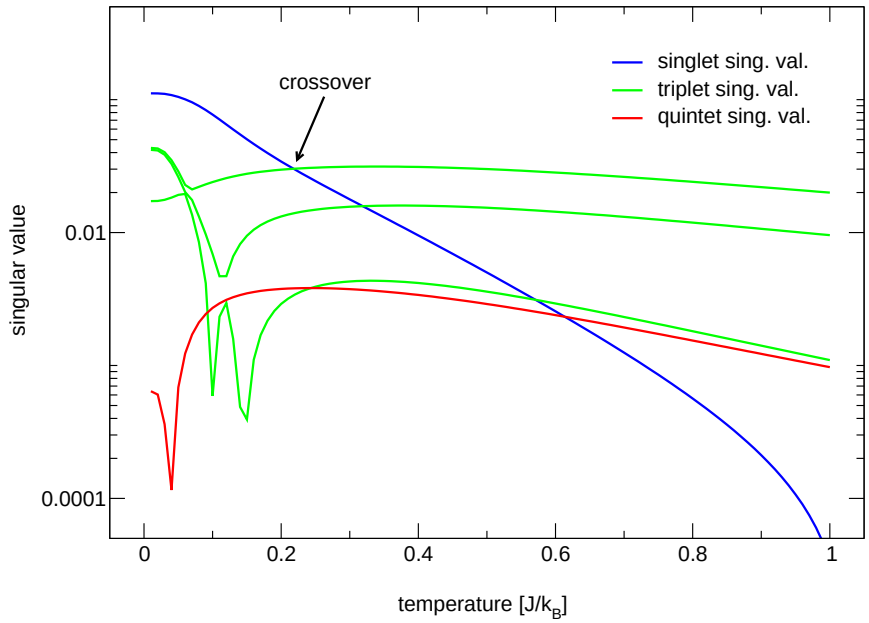

Figure 4.15: Evolution of the five nonzero independent singular values for two disjoint blocks built on nn sites in sample s12 as a function of the temperature, which ranges from 0 up to J/k_B. Colors are defined as in Fig. 4.8. This is a particular case where the two blocks are at maximal Manhattan distance. There are 4 ways of constructing two such blocks at maximal distance, but the qualitative behavior of the singular values is the same in the other 3 cases i.e. the blue singlet singular value is much more sensitive to the temperature increase than the green triplet ones.

Manhattan distance on sample s12. There are 4 ways of constructing such blocks at maximal distance, but the qualitative behavior of the SVs is the same for all of them: the blue singlet (dimer) SV dominates at low temperature – in agreement with the results we have put forward from the zero temperature study – and falls off exponentially fast as the temperature is increased, whereas green triplet SVs are roughly insensitive to the temperature. A crossover occurs at $T \sim 0.2J/k_B$ (see arrow in Fig. 4.15), and a triplet SV becomes dominant above this temperature. Notice that whatever the temperature, the red quintet SV is quite weak and exhibits a peculiar behavior at very low temperature: as T goes from 0 up to $0.1J/k_B$ it is first sharply decreasing, and then sharply increasing. For $T > 0.1J/k_B$, the quintet SV is – like the triplet ones – roughly insensitive to the temperature. We stress that ED of the full energy spectrum can be performed for spin-1/2 systems containing much more than 12 sites. Hence, Fig. 4.15 should not be considered as a deep study of the finite temperature properties of the spin-1/2 KAF, but rather as an illustration of the CDM method at finite temperature.

With the CDM method – which can be used to investigate systems at arbitrarily low

temperature – we have pointed out here the interesting fact that the physics of the spin-1/2 KAF at the (albeit very low) temperature $T \sim J/k_B$ is not representative of its zero-temperature physics: a crossover occurs in between. Temperatures as low as the order of the coupling constant which are now numerically accessible in the spin-1/2 KAF using the recently developed *nested cluster algorithm* [129] (and in other models using the *loop cluster algorithm*[14]) are therefore still too high in order to get a picture of the physics at zero temperature, one should actually go down to temperatures below one fifth of the coupling constant for that purpose.

4.3.6 Conclusion

To conclude, the unbiased analyzes of correlations between blocks of 2 nearest-neighboring sites, 3 sites built on elementary triangles, and 6 sites built on elementary hexagons we have performed reveal dominant correlations of the dimer type in some of the lowest-lying singlet states in the spectrum of the spin-1/2 KAF. This result provides strong arguments for thinking that the low-energy physics of this model may be described by a valence bond crystal (VBC). Furthermore, a phenomenon which was already pointed out while studying spin correlations on the square lattice in Subsection 3.6.2 also occurs in the case of the kagomé: the samples we have considered minimize their energy by allowing very strong and staggered spin correlations along their shortest closed loops. Even in the largest 36-site sample we study, spin correlations are biased by closed loops. The 36-site sample should therefore not be expected to mimic the thermodynamic limit, it might be that some details of the spin-1/2 KAF are not captured by this sample due to its finite nature.

[14]In the early nineties, the *loop cluster algorithm* [130; 131] had been invented to investigate physical observables in various models at very low temperature, motivated by experimental data. It is fully ergodic, and autocorrelation times are drastically reduced compared to the quantum Monte-Carlo algorithm – especially at low temperature – leading to smaller statistical errors of observables. The loop cluster algorithm has been used in the past to successfully study some models in temperature ranges which were not accessible with other methods [132–136]. The *nested cluster algorithm* has been constructed 15 years later to tackle the cases for which the sign problem is particularly hampering.

4.4 Dimer correlations and valence bond crystals (VBCs) in the 36-site sample

4.4.1 Dimer correlations in the lowest-lying states

Although dimer correlations (DCs) Eq. (4.2) fall off fast in the ground state of the spin-1/2 KAF [79], our CDM studies of Section 4.3 have concluded that DCs dominate in some of its low-lying singlet states. We report here for the first time DC measurements in states of the entire singlet spectrum of sample s36 within the spin gap, and emphasize that it is indeed true that some of these singlet states have very large DCs which are insensitive to the distance and exhibit some periodic structures, i.e. are *dimerized*. The DCs in two such states (namely the first state in IRREP $[\Gamma, B_1]$ and the second one in $[M, A_2]$) are compared to those in the ground state in Fig. 4.16 for illustration. The fixed reference bond

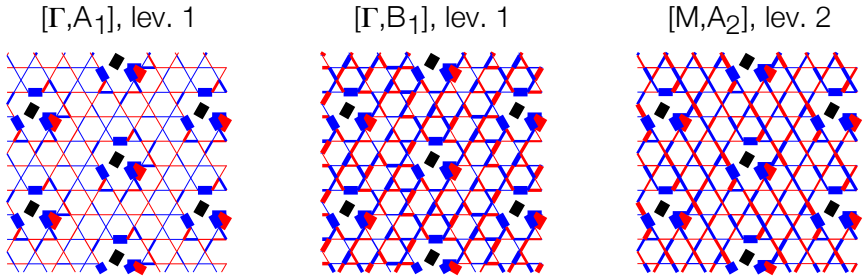

Figure 4.16: Dimer correlations Eq. (4.2) in the first level of IRREP $[\Gamma, A_1]$ (ground state) are quite weak compared to those in both the first level of $[\Gamma, B_1]$ and the second level of $[M, A_2]$. The black bond is taken as fixed reference bond. The width of colored bonds is proportional to the strength of the correlation, and their color indicates the sign of the correlation (blue/red bonds denote positive/negative correlations).

is black. Blue and red bonds denote positive and negative DCs respectively, their width is proportional to the strength of the correlation. It is clearly visible that DCs behave differently in the ground state and in the two excited states: in the ground state, they are large in the vicinity of the black reference bond only and become very weak beyond a distance of 1–2 lattice spacings whereas in the excited states, they are roughly insensitive to the distance. Furthermore, DCs exhibit interesting structures in the two excited states in Fig. 4.16: they are staggered with a period of one lattice spacing along every direction in the first level of $[\Gamma, B_1]$, and with a period of 2 lattice spacings along directions $\nearrow$ and $\nwarrow$ in the second level of $[M, A_2]$. These two properties (strong dimer correlations plus structure) in a correlation pattern typically originate from a VBC.

In order to quantify the importance DCs play in every state of the spectrum Fig. 4.5 of

s36, we introduce the *mean dimer-dimer correlation* (MDDC) defined as ("ref. b." denotes the reference black bond and "prob. b." the blue/red bond which probes the system)

$$\text{MDDC} := \max_{\text{ref. b.}} \sum_{\text{prob. b.}\notin\mathcal{N}(\text{ref. b.})} \left|\langle(\mathbf{S}_i\cdot\mathbf{S}_j)_{i,j\in\text{ref. b.}}(\mathbf{S}_k\cdot\mathbf{S}_l)_{k,l\in\text{prob. b.}}\rangle - \langle\mathbf{S}_i\cdot\mathbf{S}_j\rangle_{i,j\in\text{ref. b.}}\langle\mathbf{S}_k\cdot\mathbf{S}_l\rangle_{k,l\in\text{prob. b.}}\right| /60 \tag{4.6}$$

where the sum runs over all the probing bonds except in the "neighborhood" $\mathcal{N}$(ref. b.) of the reference bond, where DCs are large whatever the state. The sum runs over 60 elements, whence the /60 term. Each of the three directions $\longrightarrow$, $\nearrow$, and $\nwarrow$ could be chosen as reference bond (the fact that they are equivalent or not depends on the IRREP we consider). The $\max_{\text{ref. b.}}$ term in Eq. (4.6) ensures the selection of the direction providing a maximal mean dimer correlation. The "neighborhood" of a reference bond is pictorially defined in Fig. 4.17.

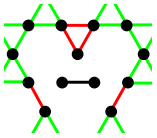

Figure 4.17: The neighborhood $\mathcal{N}$(ref. b.) of the black reference bond is depicted in red. Any other type of reference bond can be mapped onto this one by applying operations of the space group of the kagomé lattice. Green bonds do not belong to $\mathcal{N}$(ref. b.) and thus do come into play in the sum Eq. (4.6).

The MDDC Eq. (4.6) of every state in the singlet spectrum Fig. 4.5 of sample s36 within the spin gap is displayed on the top of Fig. 4.18: the width of the circles representing each state is proportional to its MDDC. MDDC values range from MDDC = 0.002 for the fourth state of IRREP $[\Gamma, E_2]$ (state "0") with the weakest overall DCs, up to MDDC = 0.012 for the first state of IRREP $[\Gamma, B_1]$ (state "4") with the largest overall DCs, the MDDC thus fluctuates a lot from one singlet state to the other. The 12 states with MDDC > 0.0075 are circled and numbered on the top of Fig. 4.18, and their DCs are compared with those in the fourth state of IRREP $[\Gamma, E_2]$ (with the weakest MDDC) in the different panels of Fig. 4.18. These 12 circled states with large MDDCs do not exhibit any decrease in the DCs with distance. Moreover some of them exhibit periodic structures, as stressed while commenting Fig. 4.16. Those whose SV spectra have been analyzed in Figs. 4.8 (CDM analysis of correlations between blocks of 2 sites) and 4.12 (CDM analysis of correlations between blocks of 3 sites) are identified by an asterisk "$*$" in these figures. There is obviously a large overlap between states with large overall DCs and states dominated by blue (circles) singlet SVs in Figs. 4.8 and 4.12.

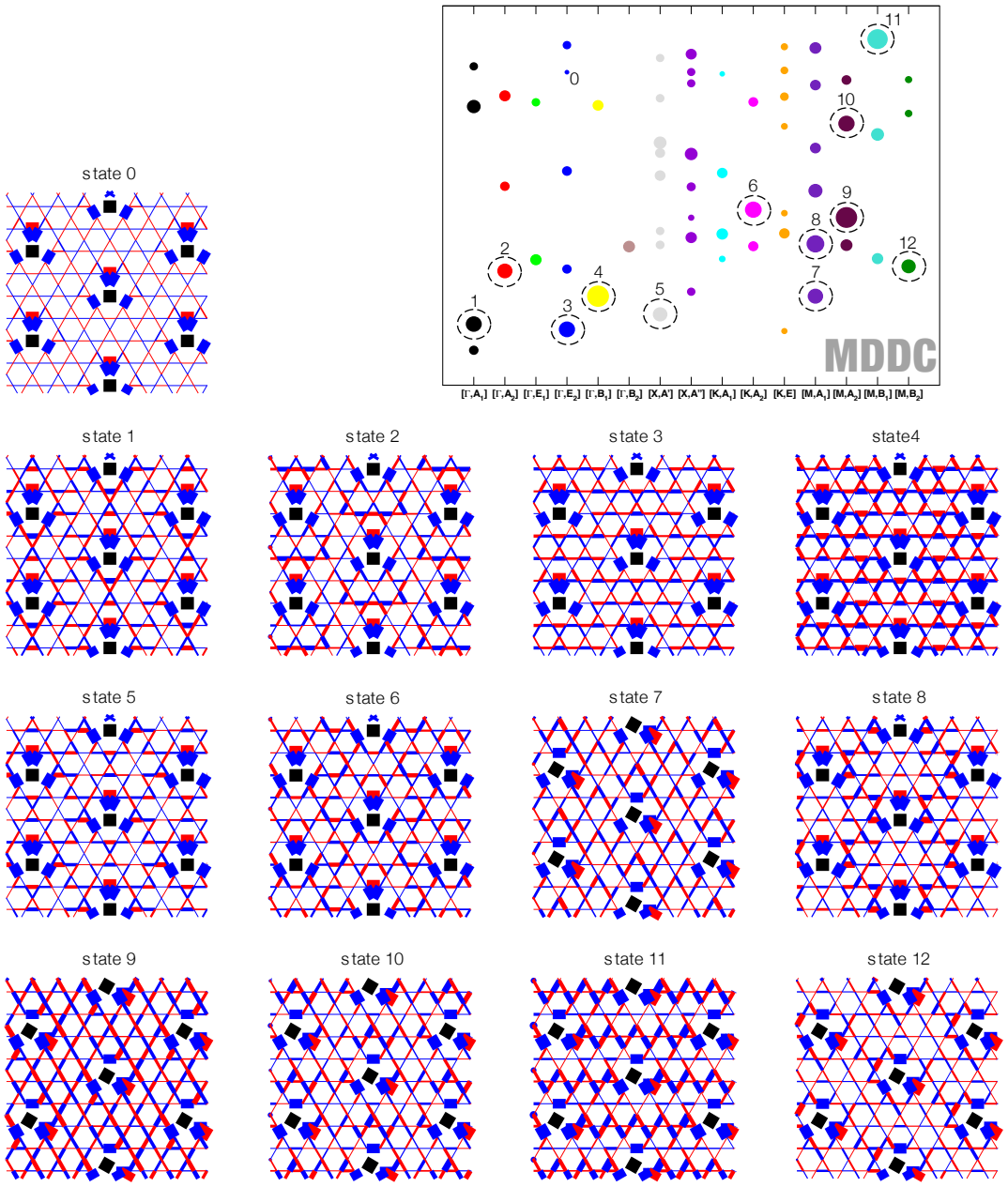

Figure 4.18: Comparison of the dimer correlations in the state 0 (MDDC = 0.002), with the dimer correlations in the states 1–12 (MDDC > 0.0075). The black reference bond has the direction which is selected in the definition of MDDC [Eq. (4.6)]. The correlation patterns are represented as in Fig. 4.16.

4.4.2 Analysis of the relevance of several VBCs

As well the CDM studies as the analysis of DCs in the low-lying states put forward the idea that the low-energy physics of the spin-1/2 KAF is governed by a VBC. In this Subsection we analyze the compatibility of the ED results on the largest sample s36 with several kinds of VBCs (allowing certain closed loops to resonate), all of them are commensurate with the s36 topology.

The different VBCs and their properties

The different VBCs whose relevance we investigate are depicted in Fig. 4.19. Closed loops (paths) with alternatively arranged dimers can be conjugated (all the dimers are shifted by one lattice spacing along the loop, the direction of every dimer being unchanged) or can resonate (superimposition between the initial and the conjugated loop), they are depicted in color and highlighted by dotted lines. In contrast, fixed dimers are black. Notice that we have also considered some crystals containing dimer bonds longer than one lattice spacing, we do not restrict ourselves to paths joining nn sites.

We pointed out in Sections 4.3.1 and 4.3.2 respectively that spin and dimer correlations are strong and staggered along short closed loops. This fact thus motivates us to analyze – in addition to well known crystals that have been proposed in the literature – ad hoc crystals with dimers alternatively arranged on closed loops[15].

The VBCs we investigate are listed below; their configurations are denoted by $[c_n]^{\alpha}_{\beta}$, where $n = 1, 2, ..., 9$ refers to the type of VBC given in Fig. 4.19, α indicates the (colored) closed loops that are conjugated or that resonate. If a loop is allowed to resonate, β indicates the parity of the resonance. Colored loops can be conjugated (c), can resonate with even (e) or with odd (o) parity, or can be frozen in the configuration depicted in Fig. 4.19 (–).

- **VBC**$_1$ was proposed by Marston & Zeng in Ref. [92]. It consists of a honeycomb structure of perfect hexagons (H_1 and H_2) (hexagons are closed loops of length 6) surrounding a pinwheel (P) (closed loop of length 12). We have considered its configurations below.

[15]Note that closed loops crossing the whole sample get an infinite length in the thermodynamic limit and thus we do not have any argument favoring crystals with this kind of loops in that limit, their relevance is probed in the context of the description of the low-energy physics of sample s36 only.

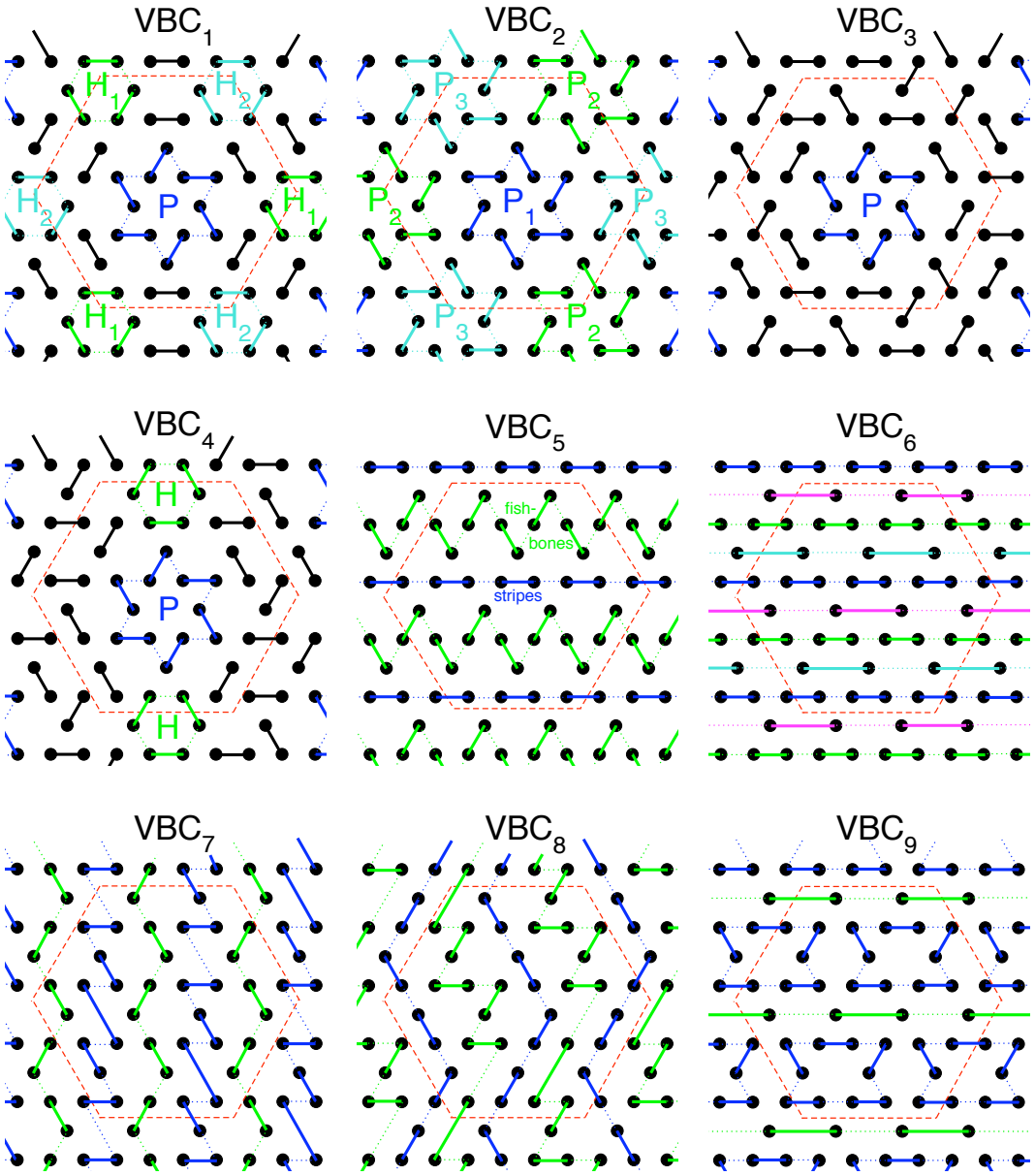

Figure 4.19: The VBCs whose relevance we analyze. All of them are commensurate with the topology of s36. The hexagonal unit cell of the s36 sample is displayed in dashed red in every panel. Dimers are denoted by solid lines joining two sites (that are not necessarily nearest-neighbors). Black dimers are fixed while colored ones can be conjugated or can resonate along the closed loops represented by dotted lines.

	$[c_1]$	$[c_1]^{H_2}$	$[c_1]_e^{H_{12}}$	$[c_1]_o^{H_{12}}$	$[c_1]_e^{P}$	$[c_1]_o^{P}$	$[c_1]_{ee}^{H_{12}P}$	$[c_1]_{eo}^{H_{12}P}$	$[c_1]_{oe}^{H_{12}P}$	$[c_1]_{oo}^{H_{12}P}$
H_1	–	–	e	o	–	–	e	e	o	e
H_2	–	c	e	o	–	–	e	e	o	e
P	–	–	–	–	e	o	e	o	e	e

- **VBC**$_2$ was proposed by Syromyatnikov & Maleyev in Ref. [93]. It consists of three pinwheels (P_1, P_2, and P_3). We have considered its configurations below.

	$[c_2]$	$[c_2]^{P_2}$	$[c_2]_e^{P_{123}}$	$[c_2]_o^{P_{123}}$
P_1	–	–	e	o
P_2	–	c	e	o
P_3	–	–	e	o

- **VBC**$_3$ consists of one pinwheel (P) surrounded by fixed black dimers. We have considered its configurations below.

	$[c_3]$	$[c_3]_e^{P}$	$[c_3]_o^{P}$
P	–	e	o

- **VBC**$_4$ consists of one pinwheel (P) and one perfect hexagon (H) surrounded by fixed black dimers. We have considered its configurations below.

	$[c_4]$	$[c_4]_e^{H}$	$[c_4]_o^{H}$	$[c_4]_e^{P}$	$[c_4]_o^{P}$	$[c_4]_{ee}^{HP}$	$[c_4]_{eo}^{HP}$	$[c_4]_{oe}^{HP}$	$[c_4]_{oo}^{HP}$
H	–	e	o	–	–	e	e	o	o
P	–	–	–	e	o	e	o	e	o

- **VBC**$_5$ consists of stripes (s) and "fishbones" (f). We have considered its configurations below.

	$[c_5]$	$[c_5]^f_e$	$[c_5]^f_o$	$[c_5]^s_e$	$[c_5]^s_o$	$[c_5]^{fs}_{ee}$	$[c_5]^{fs}_{eo}$	$[c_5]^{fs}_{oe}$	$[c_5]^{fs}_{oo}$
stripes	–	e	o	–	–	e	e	o	o
fishbones	–	–	–	e	o	e	o	e	o

- **VBC**$_6$ consists of dimers arranged along four horizontal lines: the blue (b) and the green (g) lines cross nn sites while the turquoise (t) and the magenta (m) lines cross sites that are not nn. We have considered its configurations below.

	$[c_6]$	$[c_6]^{bg}_{ee}$	$[c_6]^{bg}_{oe}$	$[c_6]^{bg}_{oo}$	$[c_6]^{tm}_{ee}$	$[c_6]^{tm}_{oe}$	$[c_6]^{tm}_{oo}$	$[c_6]^{bgtm}_{eeee}$	$[c_6]^{bgtm}_{ooee}$	$[c_6]^{bgtm}_{eeoo}$	$[c_6]^{bgtm}_{oooo}$
b	–	e	o	o	–	–	–	e	o	e	o
g	–	e	e	o	–	–	–	e	o	e	o
t	–	–	–	–	e	o	o	e	e	o	o
m	–	–	–	–	e	e	o	e	e	o	o

- **VBC**$_7$ and **VBC**$_8$ consist of green (g) and blue (b) closed loops that cross the sample, while **VBC**$_9$ consists of blue (b) closed loops of length 10 that are sandwiched between green (g) stripes made of dimers joining sites which are not nn. We have considered the configurations below ($n = 7, 8, 9$).

	$[c_n]$	$[c_n]^g_e$	$[c_n]^g_o$	$[c_n]^b_e$	$[c_n]^b_o$	$[c_n]^{gb}_{ee}$	$[c_n]^{gb}_{oe}$	$[c_n]^{gb}_{eo}$	$[c_n]^{gb}_{oo}$
g	–	e	o	–	–	e	o	e	o
b	–	–	–	e	o	e	e	o	o

Each of the VBCs we have selected has its own symmetry properties, and therefore its own set of symmetry sectors with which it is compatible. How does a given VBC decompose onto the different IRREPs that are considered in the energy spectrum of s36 Fig. 4.5? The basic idea is explained in details in Ref. [137].

Let $|\psi\rangle$ be the wavefunction representing some configuration $[c_n]^\alpha_\beta$ of VBC$_n$, and $\mathcal{G}$ the symmetry space group of hamiltonian Eq. (4.1) on the topology of sample s36[16]. Since $|\psi\rangle$ is a *broken symmetry state*, there exists, by definition, at least one group element $g \in \mathcal{G}$ under which $|\psi\rangle$ is not invariant: $|\langle\psi|g|\psi\rangle| < 1$. Hence, the linear space V generated by all the states $V := \{g|\psi\rangle \mid g \in \mathcal{G}\}$ has a dimension $d > 1$, and defines a (non-trivial) linear representation Γ of $\mathcal{G}$. Because any $g \in \mathcal{G}$ commutes with the hamiltonian, all the states of

[16] $\mathcal{G}$ has $|\mathcal{G}| = 144$ elements given by (the 12 point group operations of C_{6v})$\times$(the $36/3 = 12$ translations).

V are degenerate. The multiplicities n_α in the decomposition of Γ onto the IRREPs $\{\gamma_\alpha\}_\alpha$ of $\mathcal{G}$: $\Gamma = \bigoplus_\alpha n_\alpha \gamma_\alpha$ may be obtained from the character representation formula

$$n_\alpha = \frac{1}{|\mathcal{G}|} \sum_{g\in\mathcal{G}} \chi_\alpha^*(g) \sum_{|i\rangle} \langle i|g|i\rangle, \tag{4.7}$$

where $\chi_\alpha(g) := \mathrm{Tr}[\gamma_\alpha(g)]$ is the character of γ_α for the group element g, and the states $|i\rangle$ form an orthonormal basis of the manifold V. These multiplicities can also be written as $n_\alpha = \sum_{|i\rangle} ||\Pi_\alpha|i\rangle||^2$, where

$$\Pi_\alpha := \frac{1}{\sqrt{|\mathcal{G}|}} \sum_{g\in\mathcal{G}} \chi_\alpha(g) g^{-1} \tag{4.8}$$

is the projector onto the subspace which transforms according to γ_α. Therefore, $n_\alpha > 0$ if and only if a broken symmetry state has a non-zero projection onto sector α. Multiplicities $\{n_\alpha\}_\alpha$ *only* depend on the symmetry properties of V, and the sum of the multiplicities over all IRREPs multiplied by the dimensionalities of the IRREPs in question must match the number of degenerate configurations

$$\sum_\alpha n_\alpha \dim(\gamma_\alpha) = |V|. \tag{4.9}$$

In the case of sample s36 we have $|V| \leq |\mathcal{G}| = 144$, and the maximal degeneracy 144 is reached for a minimally symmetric configuration (actually without any symmetry).

Since we have only investigated the 4 independent momenta sectors Γ, X, K, and M of s36 (see definitions in the BZ Fig. 4.4), the multiplicities we compute from Eq. (4.7) must be multiplied by the number of momentum sectors that are degenerate with each of these four sectors (same color, but different symbols in Fig. 4.4). A set of degenerate momentum sectors is called a *star*, we shall therefore speak of multiplicities of IRREPs in the *stars of momentum sectors* Γ, X, K, and M instead of speaking of multiplicities of IRREPs in the momentum sectors Γ, X, K, and M themselves. Momentum Γ is alone on its star, while star X has 6 momenta, star K has 2 momenta, and star M has 3 momenta. Multiplicities of the IRREPs in the stars of the momentum sectors Γ, X, K, and M are given in Tables 4.2 and 4.3 for all configurations of the VBCs of Fig. 4.19. Some of the configurations we consider here were already decomposed onto symmetry sectors in Table 1 of Ref. [137], our results agree with theirs whenever the comparison is feasible. The degeneracy Eq. (4.9) of every configuration is given in the rightmost column of these tables, it is computed using

$$\dim(\gamma_\alpha) = \begin{cases} 2 & \text{if } \gamma_\alpha = [\text{star } \Gamma, E_1],\ [\text{star } \Gamma, E_2],\ \text{or } [\text{star } K, E], \\ 1 & \text{otherwise.} \end{cases}$$

	star Γ						star X		star K			star M				
	A_1	A_2	B_1	B_2	E_1	E_2	A'	A''	A_1	A_2	E	A_1	A_2	B_1	B_2	$\lvert V\rvert$
$[c_1]$	1	1	1	1	0	0	12	12	4	4	0	3	3	3	3	48
$[c_1]^{H_2}/[c_1]^{H_{12}}_{e/o}$	1	1	0	0	0	0	6	6	2	2	0	3	3	0	0	24
$[c_1]^{P}_{e}$	1	0	0	1	0	0	6	6	2	2	0	3	0	3	0	24
$[c_1]^{P}_{o}$	0	1	1	0	0	0	6	6	2	2	0	0	3	0	3	24
$[c_1]^{H_{12}P}_{ee/oe}$	1	0	0	0	0	0	6	0	2	0	0	3	0	0	0	12
$[c_1]^{H_{12}P}_{eo/oo}$	0	1	0	0	0	0	0	6	0	2	0	0	3	0	0	12
$[c_2]$	1	1	0	0	0	0	0	0	0	0	0	3	3	0	0	8
$[c_2]^{P_2}$	1	1	0	0	0	0	6	6	2	2	0	3	3	0	0	24
$[c_2]^{P_{123}}_{e}$	1	0	0	0	0	0	0	0	0	0	0	3	0	0	0	4
$[c_2]^{P_{123}}_{o}$	0	1	0	0	0	0	0	0	0	0	0	0	3	0	0	4
$[c_3]$	1	1	1	1	2	2	36	36	4	4	8	9	9	9	9	144
$[c_3]^{P}_{e}$	1	0	0	1	1	1	18	18	2	2	4	6	3	6	3	72
$[c_3]^{P}_{o}$	0	1	1	0	1	1	18	18	2	2	4	3	6	3	6	72
$[c_4]_{\text{all}}$	1	1	1	1	2	2	36	36	4	4	8	9	9	9	9	144
$[c_5]$	1	1	1	1	2	2	0	0	0	0	0	3	3	3	3	24
$[c_5]^{f}_{e}$	1	0	0	1	1	1	0	0	0	0	0	3	0	3	0	12
$[c_5]^{f}_{o}$	0	1	1	0	1	1	0	0	0	0	0	0	3	0	3	12
$[c_5]^{s}_{e}$	1	0	1	0	1	1	0	0	0	0	0	0	3	3	0	12
$[c_5]^{s}_{o}$	0	1	0	1	1	1	0	0	0	0	0	3	0	0	3	12
$[c_5]^{fs}_{ee}$	1	0	0	0	0	1	0	0	0	0	0	0	0	3	0	6
$[c_5]^{fs}_{eo}$	0	0	0	1	1	0	0	0	0	0	0	3	0	0	0	6
$[c_5]^{fs}_{oe}$	0	0	1	0	1	0	0	0	0	0	0	0	3	0	0	6
$[c_5]^{fs}_{oo}$	0	1	0	0	0	1	0	0	0	0	0	0	0	0	3	6

Table 4.2: Multiplicities of the different IRREPs in the stars of momentum sectors Γ, X, K, and M for VBC_1 to VBC_5. The rightmost column yields the degeneracy Eq. (4.9) of every configuration. All the configurations of VBC_4 we have considered decompose identically.

Since the system has a finite size, the different sectors with $n_\alpha > 0$ will not be exactly degenerate, but for a large enough system they should become the lowest eigenstates of the spectrum. This actually does not occur for any of the VBC configurations we study. For instance taking into account the above described degeneracies (within each momentum star), the 8 symbols below the dashed gray line in the energy spectrum of s36 Fig. 4.5 (right panel) actually correspond to 24 states: 2 in $[\Gamma, A_1]$, 1 in $[\Gamma, B_1]$, 2 in $[\Gamma, E_2]$, 6

	star Γ						star X		star K			star M				
	A_1	A_2	B_1	B_2	E_1	E_2	A'	A''	A_1	A_2	E	A_1	A_2	B_1	B_2	$\lvert V\rvert$
$[c_6]$	1	1	1	1	2	2	0	0	0	0	0	3	3	3	3	24
$[c_6]^{bg}_{ee/oo}$	1	1	0	0	0	2	0	0	0	0	0	3	3	0	0	12
$[c_6]^{bg}_{oe}$	0	0	1	1	2	0	0	0	0	0	0	6	6	3	3	24
$[c_6]^{tm}_{ee}$	1	0	0	1	1	1	0	0	0	0	0	0	0	0	0	6
$[c_6]^{tm}_{oe}$	0	0	0	0	0	0	0	0	0	0	0	3	3	3	3	12
$[c_6]^{tm}_{oo}$	0	1	1	0	1	1	0	0	0	0	0	0	0	0	0	6
$[c_6]^{bgtm}_{eeee/ooee}$	1	0	0	0	0	1	0	0	0	0	0	0	0	0	0	3
$[c_6]^{bgtm}_{eeoo/oooo}$	0	1	0	0	0	1	0	0	0	0	0	0	0	0	0	3
$[c_7]$	1	1	1	1	2	2	12	12	4	4	8	3	3	3	3	72
$[c_7]^{g}_{e/o}$	1	1	0	0	0	2	6	6	2	2	4	3	3	0	0	36
$[c_7]^{b}_{e/o}$	1	1	1	1	2	2	0	0	4	4	8	0	0	0	0	36
$[c_7]^{gb}_{ee/oe/eo/oo}$	1	1	0	0	0	2	0	0	2	2	4	0	0	0	0	18
$[c_8]/[c_8]^{g}_{e/o}/[c_8]^{b}_{e/o}$	1	1	1	1	2	2	12	12	4	4	8	3	3	3	3	72
$[c_8]^{gb}_{ee/oe/eo/oo}$	1	1	0	0	0	2	6	6	2	2	4	0	0	3	3	36
$[c_9]$	1	1	1	1	2	2	0	0	0	0	0	9	9	9	9	48
$[c_9]^{g}_{e}$	0	1	1	0	1	1	0	0	0	0	0	3	6	3	6	24
$[c_9]^{g}_{o}$	1	0	0	1	1	1	0	0	0	0	0	6	3	6	3	24
$[c_9]^{b}_{e}$	0	0	1	1	2	0	0	0	0	0	0	0	0	9	9	24
$[c_9]^{b}_{o}$	1	1	0	0	0	2	0	0	0	0	0	9	9	0	0	24
$[c_9]^{gb}_{ee}$	0	0	1	0	1	0	0	0	0	0	0	0	0	3	6	12
$[c_9]^{gb}_{oe}$	0	0	0	1	1	0	0	0	0	0	0	0	0	6	3	12
$[c_9]^{gb}_{eo}$	0	1	0	0	0	1	0	0	0	0	0	3	6	0	0	12
$[c_9]^{gb}_{oo}$	1	0	0	0	0	1	0	0	0	0	0	6	3	0	0	12

Table 4.3: Multiplicities of the different IRREPs in the stars of momentum sectors Γ, X, K, and M for VBC_6 to VBC_9. The rightmost column yields the degeneracy Eq. (4.9) of every configuration.

in $[X, A']$, 6 in $[X, A'']$, 4 in $[K, E]$, and 3 in $[M, A_1]$[17]. This does not match any of the configurations of Tables 4.2 or 4.3. If only the 4 lowest symbols in the energy spectrum Fig. 4.5 corresponding to 8 states (2 in $[\Gamma, A_1]$, 2 in $[\Gamma, E_2]$, and 4 in $[K, E]$) are considered,

[17]Every symbol appearing at $[\Gamma, E_2]$ or $[K, E]$ in Fig. 4.5 corresponds to 2 degenerate states since these IRREPs are two-dimensional, and can be split into 2 one-dimensional IRREPs as shown in Fig. A.5 of Appendix A.

there is again no crystal configuration that decomposes onto the relevant IRREPs. As we shall see, some the VBC configurations we have studied nevertheless provide a good description of the structures of DCs in some of the low-lying states of s36 that have large overall DCs (i.e. large MDDCs).

Dimer correlations in the VBCs compared to exact ones

We shall see that although they are unable to completely explain the low-energy physics of sample s36, some of the VBCs in Fig. 4.19 nevertheless allow to recover the main structures in certain of its DC patterns.

The VBC states belonging to every IRREP (with a multiplicity $n_\alpha > 0$) are determined using the projector Eq. (4.8). We deal with one-dimensional IRREPs only since two-dimensional ones are split into two degenerate one-dimensional IRREPs, as illustrated in Fig. A.5 of Appendix A. These projected states consist of superimpositions of various dimer patterns, DCs are computed in each of them using the simplification

$$\langle(\mathbf{S}_i \cdot \mathbf{S}_j)(\mathbf{S}_k \cdot \mathbf{S}_l)\rangle = \begin{cases} (-3/4)^2 & \text{if both spin pairs } (i,j) \text{ and } (k,l) \text{ form dimers} \\ 0 & \text{otherwise} \end{cases}$$
$$\text{and } \langle(\mathbf{S}_i \cdot \mathbf{S}_j)\rangle = (3/4)f,\ f = 1/4 \tag{4.10}$$

and are then averaged over all of them. Here, f is the fraction of nn spin pairs that form dimers. This simplification amounts to neglecting the overlap between distinct dimer configurations.

Once for a given VBC configuration the DCs have been computed in every relevant IRREP, the idea is to probe its relevance by counting the proportion of DCs – among the strong ones – whose signs are correctly reproduced by the VBC configuration in question. Such a comparison is performed in Table 4.4: for each of the states that are circled in the spectrum on the top of Fig. 4.18 and labelled from 1 up to 12 (i.e. with MDDC> 0.0075), the signs of the exact DCs are compared to those from the VBCs (for every configuration) only if the absolute value of both of them are > 0.005. Table 4.4 has three columns per state: the middle one gives the number of DCs that are taken into account for the comparison, among them the number of DCs with the good sign is given in the left column, and the right column gives the percentage of correlations with the good sign (i.e. left column divided by the middle one). For a fixed reference block containing two sites, there are 65 ways of constructing the second block, assuming that both of them are made of nn spin pairs. Since the comparison in Table 4.4 is performed by considering the three possible directions for the reference block[18], the maximal number of correlations which are taken into account for the comparisons (middle columns) is $3 \times 65 = 195$.

[18]In the IRREPs with multiplicity $n_\alpha > 1$, it is possible to construct more than one state. Those

state label in Fig. 4.18	$[\Gamma, A_1]$, 2			$[\Gamma, A_2]$, 1			$[\Gamma, E_2]$, 1			$[\Gamma, B_1]$, 1			$[X, A']$, 1			$[K, A_2]$, 2			$[M, A_1]$, 1			$[M, A_1]$, 2			$[M, A_2]$, 2			$[M, A_2]$, 3			$[M, B_1]$, 3			$[M, B_2]$, 1		
	1			2			3			4			5			6			7			8			9			10			11			12		
$[c_1]$	63	123	51	123	123	100	–	–	–	57	129	44	55	107	51	108	141	77	50	86	58	59	105	56	67	113	59	59	107	55	59	123	48	59	105	56
$[c_1]^{H_2}$	63	147	43	147	147	100	–	–	–	–	–	–	55	107	51	135	141	96	62	102	61	75	129	58	83	137	61	61	119	51	–	–	–	–	–	–
$[c_1]^{H_{12}}_{e/o}$	51	105	49	123	123	100	–	–	–	–	–	–	41	79	52	93	105	89	46	78	59	55	95	58	59	101	58	53	101	52	–	–	–	–	–	–
$[c_1]^{P}_{e}$	63	123	51	–	–	–	–	–	–	–	–	–	47	91	52	93	117	79	50	86	58	59	105	56	–	–	–	–	–	–	59	123	48	–	–	–
$[c_1]^{P}_{o}$	–	–	–	123	123	100	–	–	–	57	129	44	47	91	52	93	117	79	–	–	–	–	–	–	67	113	59	59	107	55	–	–	–	59	105	56
$[c_1]^{H_{12}P}_{ee/oe}$	51	105	49	–	–	–	–	–	–	–	–	–	41	79	52	–	–	–	46	78	59	55	95	58	–	–	–	–	–	–	–	–	–	–	–	–
$[c_1]^{H_{12}P}_{eo/oo}$	–	–	–	123	123	100	–	–	–	–	–	–	–	–	–	93	105	89	–	–	–	–	–	–	59	101	58	53	101	52	–	–	–	–	–	–
$[c_2]$	129	147	88	87	147	59	–	–	–	–	–	–	–	–	–	–	–	–	88	102	86	109	129	84	115	137	84	81	119	68	–	–	–	–	–	–
$[c_2]^{P_2}$	48	147	33	78	147	53	–	–	–	–	–	–	64	107	60	96	141	68	48	102	47	54	129	42	64	137	47	56	119	47	–	–	–	–	–	–
$[c_2]^{P_{123}}_{e}$	48	69	70	–	–	–	–	–	–	–	–	–	–	–	–	–	–	–	44	60	73	50	71	70	–	–	–	–	–	–	–	–	–	–	–	–
$[c_2]^{P_{123}}_{o}$	–	–	–	42	63	67	–	–	–	–	–	–	–	–	–	–	–	–	–	–	–	–	–	–	56	77	73	34	57	60	–	–	–	–	–	–
$[c_3]$	63	123	51	72	102	71	21	81	26	57	129	44	55	107	51	51	84	61	50	86	58	59	105	56	67	113	59	59	107	55	49	111	44	51	93	55
$[c_3]^{P}$	72	102	71	–	–	–	21	96	22	–	–	–	44	81	54	51	90	57	48	70	69	43	79	54	69	89	78	45	81	56	43	93	46	41	83	49
$[c_3]^{P}_{e}$	–	–	–	72	102	71	21	96	22	21	96	22	44	81	54	51	90	57	48	70	69	43	79	54	69	89	78	45	81	56	43	93	46	41	83	49
$[c_3]^{P}_{o}$	–	–	–	42	63	67	–	–	–	–	–	–	–	–	–	–	–	–	–	–	–	–	–	–	56	77	73	34	57	60	–	–	–	–	–	–
$[c_4]$	57	57	100	57	63	90	39	87	45	27	69	39	60	91	66	21	45	47	44	82	54	103	109	94	57	109	52	45	107	42	67	135	50	43	97	44
$[c_4]^{H}_{e/o}$	69	75	92	69	75	92	51	105	49	39	93	42	65	95	68	45	84	54	32	56	57	95	99	96	45	75	60	29	77	38	43	101	43	29	77	38
$[c_4]^{P}_{e/o}$	54	54	100	60	60	100	45	96	47	21	66	32	46	91	51	45	60	75	34	62	55	63	81	78	49	83	59	33	77	43	47	99	47	43	77	56
$[c_4]^{HP}_{ee/eo/oe/oo}$	54	66	82	72	72	100	36	84	43	27	72	38	44	81	54	57	66	86	30	50	60	57	69	83	45	67	67	21	57	37	31	75	41	37	63	59
$[c_5]$	57	147	39	63	147	43	117	141	83	129	153	84	–	–	–	–	–	–	67	102	66	51	129	40	89	137	65	101	119	85	143	151	95	61	121	50
$[c_5]^{f}$	57	147	39	–	–	–	129	141	91	–	–	–	–	–	–	–	–	–	67	102	66	51	129	40	–	–	–	–	–	–	143	151	95	–	–	–
$[c_5]^{f}_{g}$	–	–	–	63	147	43	129	141	91	129	153	84	–	–	–	–	–	–	–	–	–	–	–	–	89	137	65	101	119	85	–	–	–	61	121	50
$[c_5]^{}_{e}$	57	147	39	–	–	–	129	141	91	129	153	84	–	–	–	–	–	–	–	–	–	–	–	–	89	137	65	101	119	85	143	151	95	–	–	–
$[c_5]^{}_{s}$	–	–	–	63	147	43	129	141	91	–	–	–	–	–	–	–	–	–	67	102	66	51	129	40	–	–	–	–	–	–	–	–	–	61	121	50
$[c_5]^{fs}_{ee}$	57	147	39	–	–	–	129	141	91	–	–	–	–	–	–	–	–	–	–	–	–	–	–	–	–	–	–	–	–	143	151	95	–	–	–
$[c_5]^{fs}_{eo}$	–	–	–	–	–	–	–	–	–	–	–	–	–	–	–	–	–	–	67	102	66	51	129	40	–	–	–	–	–	–	–	–	–	–	–	–
$[c_5]^{fs}_{oe}$	–	–	–	–	–	–	–	–	–	129	153	84	–	–	–	–	–	–	–	–	–	–	–	–	89	137	65	101	119	85	–	–	–	–	–	–
$[c_5]^{fs}_{oo}$	–	–	–	63	147	43	129	141	91	–	–	–	–	–	–	–	–	–	–	–	–	–	–	–	–	–	–	–	–	–	–	–	61	121	50
$[c_6]$	57	147	39	57	147	39	105	141	74	105	153	69	–	–	–	–	–	–	34	76	45	12	38	32	40	86	47	40	74	54	40	60	67	38	56	68
$[c_6]^{bg}_{ee}/[c_6]^{bg}_{oo}$	63	147	43	63	147	43	87	141	62	–	–	–	–	–	–	–	–	–	34	76	45	16	38	42	40	86	47	34	74	46	–	–	–	–	–	–
$[c_6]^{bg}_{oe}$	–	–	–	–	–	–	–	–	–	87	153	57	–	–	–	–	–	–	0	0	–	2	7	29	0	5	0	3	3	100	34	60	57	32	56	57
$[c_6]^{tm}_{ee}$	57	147	39	–	–	–	105	141	74	–	–	–	–	–	–	–	–	–	–	–	–	–	–	–	–	–	–	–	–	–	–	–	–	–	–
$[c_6]^{tm}_{oe}$	–	–	–	–	–	–	–	–	–	–	–	–	–	–	–	–	–	–	34	76	45	12	38	32	40	86	47	40	74	54	40	60	67	38	56	68
$[c_6]^{tm}_{oo}$	–	–	–	57	147	39	105	141	74	105	153	69	–	–	–	–	–	–	–	–	–	–	–	–	–	–	–	–	–	–	–	–	–	–	–	–
$[c_6]^{bgtm}_{eeee/ooee}$	63	147	43	–	–	–	87	141	62	–	–	–	–	–	–	–	–	–	–	–	–	–	–	–	–	–	–	–	–	–	–	–	–	–	–
$[c_6]^{bgtm}_{eeoo/oooo}$	–	–	–	63	147	43	87	141	62	–	–	–	–	–	–	–	–	–	–	–	–	–	–	–	–	–	–	–	–	–	–	–	–	–	–
$[c_7]$	51	108	47	51	120	43	45	99	45	57	114	50	42	107	39	45	120	38	51	98	52	39	113	35	83	129	64	69	119	58	71	139	51	33	117	28
$[c_7]^{g}_{e}/[c_7]^{g}_{o}$	51	99	52	51	111	46	42	102	41	–	–	–	41	103	40	54	117	46	53	98	54	43	105	41	83	125	66	65	115	57	–	–	–	–	–	–
$[c_7]^{b}_{e}$	60	147	41	39	108	36	78	141	55	45	102	44	–	–	–	51	120	43	–	–	–	–	–	–	–	–	–	–	–	–	–	–	–	–	–	–
$[c_7]^{b}_{o}$	51	108	47	39	108	36	48	105	46	45	102	44	–	–	–	51	120	43	–	–	–	–	–	–	–	–	–	–	–	–	–	–	–	–	–	–
$[c_7]^{gb}_{ee/oe/eo/oo}$	51	102	50	39	102	38	45	105	43	–	–	–	–	–	–	45	108	42	–	–	–	–	–	–	–	–	–	–	–	–	–	–	–	–	–	–
$[c_8]$	36	66	55	12	54	22	27	57	47	36	66	55	49	107	46	21	63	33	63	94	67	37	93	40	85	125	68	79	103	77	91	115	79	27	101	27
$[c_8]^{g}_{e}/[c_8]^{g}_{o}$	51	93	55	15	69	22	51	69	74	63	99	64	63	105	60	36	90	40	47	90	52	41	95	43	67	115	58	67	93	72	93	109	85	45	95	47
$[c_8]^{b}_{e}/[c_8]^{b}_{o}$	48	117	41	36	117	31	66	78	85	93	123	76	32	74	43	36	84	43	57	92	62	41	113	36	85	123	69	87	105	83	123	127	97	57	107	53
$[c_8]^{gb}_{ee/oe/eo/oo}$	48	105	46	12	93	13	39	57	68	–	–	–	51	97	53	21	81	26	–	–	–	–	–	–	–	–	–	–	–	–	109	123	89	49	105	47
$[c_9]$	57	135	42	57	135	42	129	129	100	129	141	91	–	–	–	–	–	–	49	102	48	67	129	52	53	137	39	77	119	65	99	151	66	53	121	44
$[c_9]^{g}$	–	–	–	57	135	42	63	63	100	69	69	100	–	–	–	–	–	–	50	92	54	38	80	48	13	41	32	33	43	77	114	151	75	84	121	69
$[c_9]^{g}_{o}$	57	135	42	–	–	–	129	129	100	–	–	–	–	–	–	–	–	–	55	102	54	58	129	45	64	137	47	84	119	71	114	151	75	84	121	69
$[c_9]^{b}_{e}/[c_9]^{gb}_{ee}$	–	–	–	–	–	–	–	–	–	57	78	73	–	–	–	–	–	–	–	–	–	–	–	–	–	–	–	–	–	49	69	71	43	69	62
$[c_9]^{b}_{o}$	54	82	66	42	66	64	51	60	85	–	–	–	–	–	–	–	–	–	40	60	67	35	57	61	43	73	59	43	63	68	–	–	–	–	–	–
$[c_9]^{gb}_{oe}$	–	–	–	–	–	–	–	–	–	–	–	–	–	–	–	–	–	–	–	–	–	–	–	–	–	–	–	–	–	–	49	69	71	43	69	62
$[c_9]^{gb}_{eo}$	–	–	–	42	66	64	51	60	85	–	–	–	–	–	–	–	–	–	40	60	67	35	57	61	43	73	59	43	63	68	–	–	–	–	–	–
$[c_9]^{gb}_{oo}$	54	84	64	–	–	–	51	60	85	–	–	–	–	–	–	–	–	–	40	60	67	35	57	61	43	73	59	43	63	68	–	–	–	–	–	–

Table 4.4: Relevance of every VBC configuration for describing the 12 states that are circled in the spectrum on the top of Fig. 4.18. Only the dimer correlations (exact and in the VBC) stronger than 0.005 are taken into account for the comparison, their number is given in the middle column for every state. The left column gives the number of times the signs agree, and the right column gives the proportion [%] of good signs (green if larger than 75%, and in red otherwise).

states may differ one from another (and exhibit different correlation patterns) or not. However, since the comparison is performed with the reference bond taking all the three possible directions, the result given in Table 4.4 is the same for all of them.

Even if no VBC configuration does exhibit a perfect agreement with the dimerized low-lying states of sample s36, some of them allow to recover the signs of their strongest dimer correlations with a high precision[19]. We wish to emphasize that VBC_5 – which consists of dimer bonds joining nn sites and arranged on closed loops crossing the s36 sample – provides a particularly good description of the dimer correlations in several states of s36. For illustration purposes, the dimer correlations in some of the states of s36 are pictorially compared to correlations in several non-resonating VBC configurations in Fig. 4.20. The main structures which are highlighted in green are shared by both of them.

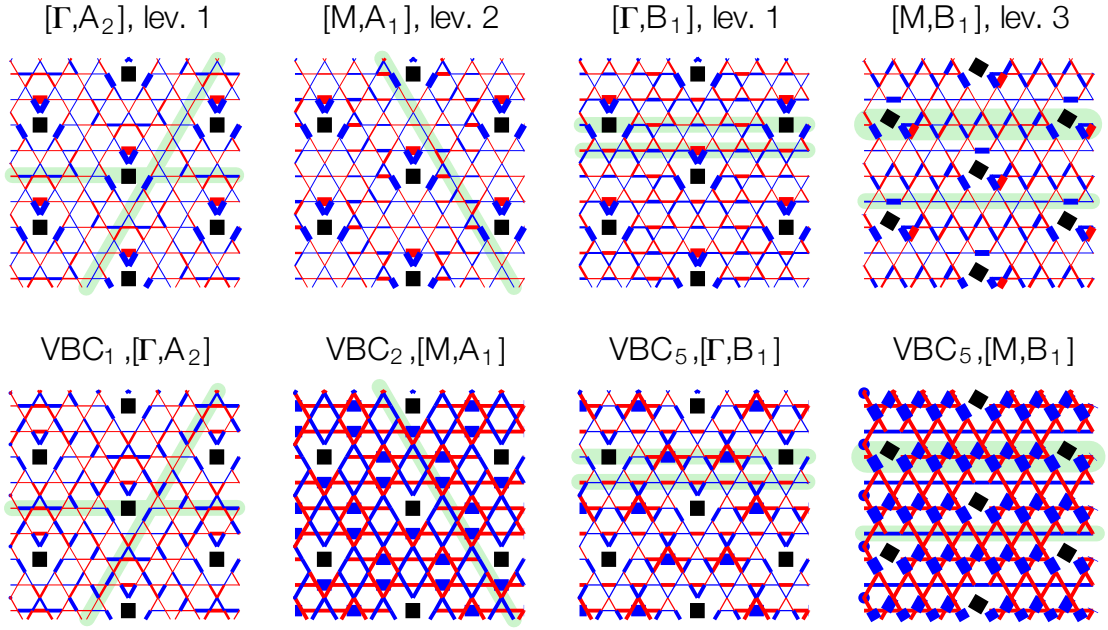

Figure 4.20: Dimer correlations in some of the dimerized states of s36 (top) are compared to those in the non-resonating configurations of several VBCs (bottom). The main structures (highlighted in green) are shared by both of them.

Due to the particular role of closed loops that we have pointed out in this Chapter, a natural question arise: is there a link between the relevance of a crystal configuration for describing the dimer correlations of s36, and the number of closed nn dimer loops[20] (CnnDLs) of a specific length this crystal contains[21]? In other words, does a "good" crystal

[19] In some cases, Table 4.4 gives an agreement of 100%. We however stress that if the comparison had been systematically performed over all the 195 bonds (instead of being restricted to correlations stronger than 0.005), none of the crystal configurations would have permitted to correctly recover 100% of the signs.

[20] We call *closed nn dimer loop* any closed path joining nn sites only, and consisting of an alternation of dimers and absence of dimers between those nn sites.

[21] In Ref. [90], it is shown that states consisting of dimers joining nn sites capture the main properties

require a maximal number of CnnDLs of a specific length? In order to answer this question, we shall examine the relevance of the non-resonating configurations of the crystals with dimers between nn sites only (i.e. $[c_1]$, $[c_1]^{H_2}$, $[c_2]$, $[c_2]^{P_2}$, $[c_3]$, $[c_4]$, and $[c_5]$) as a function of the number of CnnDLs of lengths of 6, 8, 10, and 12 lattice spacings they contain. We distinguish between the CnnDLs of type I that go from the starting site back to itself, and the CnnDLs of type II that go from the starting site to one of its images (belonging to a copy of the sample the starting site belongs to). This distinction can be important since CnnDLs of type II are suppressed in the infinite system. Table 4.5 gives the number of loops of the different lengths and of both types in all the crystal configurations we have listed above. The next step is to quantify the relevance of a crystal configuration with a *relevance*

type/length	I/6	I/8	I/10	I/12	II/6	II/8	II/10	II/12
$[c_1]$	2	24	6	47	0	3	19	29
$[c_1]^{H_2}$	3	17	6	63	0	0	22	37
$[c_2]$	0	14	0	100	0	0	0	83
$[c_2]^{P_2}$	0	14	0	101	0	0	0	83
$[c_3]$	0	27	4	33	0	2	14	35
$[c_4]$	2	18	8	67	0	0	20	48
$[c_5]$	0	27	10	44	0	0	15	60

Table 4.5: Number of closed dimer loops of type I and II and of length of 6, 8, 10, and 12 lattice spacings in the non-resonating configurations of the crystals containing dimers between nn sites only.

parameter. For that purpose, we define the relevance $\mathrm{Rel}([c_i],\tau)$ of some configuration $[c_i]$ as the deviation from one-half of the proportion of connected dimer correlations Eq. (4.2) having the good sign in the circled states of the spectrum on the top of Fig. 4.18, among the correlations stronger than some fixed threshold τ

$$\mathrm{Rel}([c_i],\tau) := \frac{1}{N}\sum_s \Bigg| \sum_{\langle k,l\rangle}\sum_{\langle k',l'\rangle} \Theta\left[|C_s(k,l,k',l')|-\tau\right]\Theta\left[\left|C_{[c_i]}(k,l,k',l')\right|-\tau\right] \left\{\Theta\left[C_s(k,l,k',l')C_{[c_i]}(k,l,k',l')\right]-1/2\right\}\Bigg|, \tag{4.11}$$

of the ground state of the spin-1/2 KAF, it makes thus sense to pay a special attention to dimer bonds joining nn sites only.

where s runs over those N circled states in the spectrum on the top of Fig. 4.18 belonging to IRREPs that contribute to the VBC configuration $[c_i]$ ($N \leq 12$ since there are 12 circled states), $C_s(k,l,k',l')$ is the connected dimer correlation Eq. (4.2) in the circled state s, $C_{[c_i]}(k,l,k',l')$ is the connected dimer correlation computed with the approximation Eq. (4.10) in the crystal configuration $[c_i]$, and Θ is the Heaviside step function

$$\Theta(x) := \begin{cases} 1 & \text{if } x > 0 \\ 0 & \text{if } x \leq 0 \end{cases}, \qquad x \in \mathbb{R}.$$

The relevances $\mathrm{Rel}([c_i], \tau = 0.005)$ and $\mathrm{Rel}([c_i], \tau = 0)$ are shown in Fig. 4.21 as a function of the total number of CnnDLs (i.e. CnnDLs of type I and II) for every non-resonating VBC configuration with nn dimers. Loops of length 6 are referred to with green symbols, loops of length 8 are referred to with red symbols, loops of length 10 are referred to with blue symbols, and loops of length 12 are referred to with black symbols; the number of loops is rescaled in the first three cases for the sake of clarity. The different symbols correspond to different crystal configurations.

It is difficult to draw a final conclusion from Fig. 4.21. One can nevertheless see that – provided that the relevance is large enough, i.e. above the black colored region – both relevances $\mathrm{Rel}([c_i], \tau = 0.005)$ and $\mathrm{Rel}([c_i], \tau = 0)$ exhibit a propensity to increase with the number of CnnDLs of length of 12 lattice spacings (black dashed lines), but we did not find any VBC configuration with a particularly high number of such CnnDLs that could allow us to verify this hypothesis. Notice furthermore that $\mathrm{Rel}([c_i], \tau = 0.005)$ and $\mathrm{Rel}([c_i], \tau = 0)$ behave quite similarly: the signal is not stronger or significantly different if correlations weaker than 0.005 are discarded.

4.4.3 Conclusion

Motivated by the results from Section 4.3, in which dominant correlations of the dimer type have been pointed out, we have identified those lowest-lying singlet states of the 36-site sample of the spin-1/2 KAF which have strong dimer correlations, and probed the relevance of various VBC configurations for describing the low-energy physics of that model (including the famous VBC by Marston & Zeng, and the one by Syromyatnikov & Maleyev). Wherever the cut-off is put in the spectrum of the 36-site sample, the set of IRREPs corresponding to the lowest-lying states of this sample does match none of the sets of IRREPs that are compatible with any of the crystal configurations we have studied; this may be due to the influence of closed loops – we pointed out in the part 4.3.1 of Section 4.3 – which is strong even in the 36-site sample. Some of the VBCs nevertheless provide a good description of the spatial patterns of dimer correlations in those lowest-lying states having large overall dimer correlations (i.e. dimerized), revealing that several VBC prototypes are

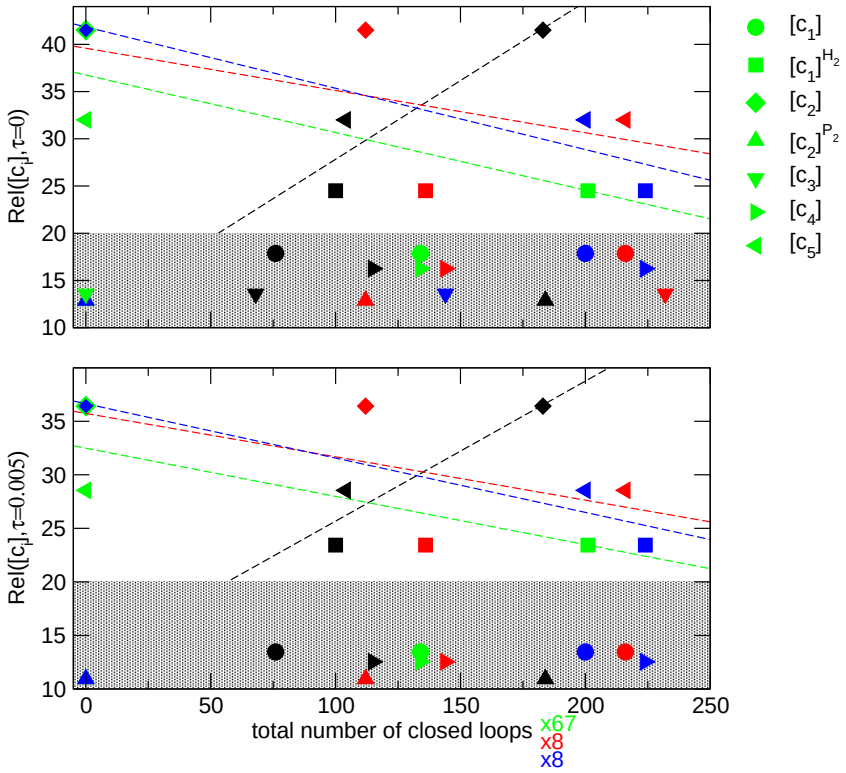

Figure 4.21: Relevances $\mathrm{Rel}([c_i], \tau = 0.005)$ (bottom) and $\mathrm{Rel}([c_i], \tau = 0)$ (top) for every non-resonating VBC configuration with nn dimers as a function of total number of closed dimer loops, for loops of length of 6 (green), 8 (red), 10 (blue), and 12 (black) lattice spacings. Notice that the number of loops of lengths 6, 8, and 10 is rescaled (multiplied by 67, 8, and 8 respectively) for the sake of clarity. The dashed lines are least squares fits performed by discarding the symbols inside the black region, which correspond to low relevance. Symbols in the region Rel < 10 are not displayed.

still competing on the largest available sample. It seems moreover – but remains at a quite speculative stage – that the higher the number of closed dimer loops long by 12 lattice spacings in a VBC configuration, the higher its relevance.

Note that it remains an open question to understand why in certain IRREPs of the 36-site sample – for instance $[\Gamma, A_1]$ or $[M, A_2]$ – the lowest state does not have strong dimer correlations while higher ones (within the same IRREP) do. If a VBC was stabilized, we would actually expect a strong signal in the *lowest* among the low-lying states of the compatible IRREPs.

4.5 Entanglement entropy

This section is devoted to the investigation of the low-energy physics of the spin-1/2 KAF by probing a fundamental property of quantum states: *entanglement* (see Ref. [138] for a detailed introduction). This quite intriguing trait of quantum mechanics is the essence of correlations in quantum many-body states. Entanglement is also a key concept in quantum information theory [139], and the problem of measuring and quantifying it is a field of research of its own; in this section, we shall quantify the entanglement between a block and its environment using the so-called *von Neumann entanglement entropy*. Studies of entanglement entropy have enjoyed a great interest since many years [140–143], which is benefitting from both the new perspectives of quantum information theory, and the realization of their efficiency for describing quantum phase transitions, especially in low dimensional quantum systems (see Refs. [143; 144] and references therein).

Entropy is a concept originally coming from thermodynamics, and applied across information theory, mathematics, and various fields of physics, including condensed matter physics. The entanglement between one block and its complement – say A and $\bar{A}$ – can be measured by the Von Neumann entropy of block A, defined by

$$S(A) := -\mathrm{Tr}(\rho_A \ln \rho_A),$$

where ρ_A is the reduced density matrix of block A. $S(A)$ is identical to $S(\bar{A})$, and ranges from 0 if A is uncorrelated to its environment, to $N \ln(2S{+}1)$ (N being the number of spin-S sites enclosed in A) if the entanglement is maximal. In the case of spins $S = 1/2$, the upper bound on the block entropy per site is thus $\ln 2$. Computation of block entropies in some given quantum state provide important informations about its nature: a significantly high entropy means that the block is strongly correlated (and thus entangled) to its environment, whereas a low entropy indicates that the state in question is close to a tensor product between the block and its environment, i.e. has a large overlap with the set $A \otimes \bar{A}$. A simple illustration of two maximally entangled spins-1/2 is for instance provided by the singlet state

$$(|\uparrow \otimes \downarrow\rangle - |\downarrow \otimes \uparrow\rangle)/\sqrt{2}.$$

In contrast, the two spins in the triplet state

$$|\uparrow \otimes \uparrow\rangle$$

are uncorrelated.

Often, one is rather interested in the *scaling* of the entanglement entropy when the considered block grows in size. For quantum chains for instance, the scaling of entanglement reflects to a large extent the critical behavior of the quantum many-body system: critical

spin chains are known to have entanglement entropy that diverges logarithmically in the block size [143; 145–147] with an universal coefficient proportional to the central charge c of the associated conformal field theory. The von Neumann entropy $S(A)$ of a block A enclosing L sites in a chain of N sites with periodic boundary conditions is [148–150]

$$S(A) = \frac{c}{3} \ln \left[\frac{N}{\pi} \sin \frac{\pi(L/a)}{N} \right] + b \overset{N\to\infty}{\longrightarrow} \frac{c}{3} \ln(L/a) + b \qquad D = 1 \tag{4.12}$$

where a is the lattice spacing and b is a non-universal constant. Away from the critical point, the entanglement entropy saturates to a finite value $S_{\text{sat}}(A)$ which is related to the logarithm of the correlation length ξ as [143]

$$S_{\text{sat}}(A) = \frac{c}{3} \ln(\xi/a) + b' \qquad D = 1.$$

There are logarithmic violations of the law Eq. (4.12) in critical 1D systems and some higher dimensional fermionic systems. The specific manner with which the area law is violated is tied to certain universal properties of the phase or critical point. In some cases, important informations about the phase can be revealed by studying the correction to the area law, for example this is the case for topologically ordered phases [151; 152].

The natural question arising now is how does the entropy scale in higher dimensions? The scaling of entanglement entropy was in fact formerly studied in the context of quantum field theory and black hole physics. There, the systems have typical dimensionalities $D > 1$. There are however only a few results on the behavior of entanglement entropy above one spatial dimension [153–158]. One might be tempted to think that the entropy of a distinguished block in a $D > 1$ system will possess an extensive character in the volume of the block. Such a behavior – referred to as a *volume scaling* – is generally observed for thermal states. Instead typical ground states fulfill an *area law*[22]: if a quantum state has a finite correlation length, then the entropy of a given block in the system is proportional to the area of the common boundary between the block and its environment (see Ref. [159] for some rigorous results, and Ref. [160] for a complete review). In a system of dimensionality $D > 1$, the von Neumann entropy $S(A)$ of a block A having a boundary of area $\mathcal{A}$ obeys the area law

$$S(A) = C \frac{\mathcal{A}}{a^{D-1}} + b'' \qquad D > 1. \tag{4.13}$$

In the law Eq. (4.13), the proportionality coefficient C is sensitive to the lattice spacing a, and is therefore non-universal. So, in contrast to the 1D case Eq. (4.12), the leading term in Eq. (4.13) for the entanglement entropy in higher dimensions cannot be used to characterize various critical points.

[22]Note that the 1D result Eq. (4.12) is also an area law (the area of some block in 1D does not depend on its length) to which a logarithmic correction has been added. The consequence of this correction is that entanglement pervades the system at any distance, not staying just at the point-like borders of the block.

4.5.1 Block entropies in the low-energy states

Block entropies in the ground state

We study here the entropy of various kinds of blocks with sizes ranging from 2 up to 5 sites in the ground state of the samples we consider, and identify the configurations of blocks exhibiting the lowest entropies. This identification work is important since – as explained above – blocks with a particularly low entropy can be seen as the "elementary bricks" that "build up" the state.

Fig. 4.22 shows block entropies for all possible blocks containing 2 (upper left panel), 3 (upper right panel), 4 (lower left panel), and 5 (lower right panel) sites in samples as large as possible (numerically tractable). Colors of the symbols indicate the number of nn spin pairs among each possible pairing of sites one can imagine within the blocks. Orange/black/red/green/blue/magenta/brown symbols indicate that there are respectively 0/1/2/3/4/5/6 nn spin pairs. Apart from some exceptions we shall discuss further which are due to the finite nature of the samples, symbols with the same color collapse onto a same "pile" showing that the entropy of a given block is essentially a function of the number of nn spin pairs within it, and is nearly independent on the distance between the sites as soon as they are not nn. This is at least clear for the largest samples $s24_2$, s30, and s36. Moreover, the piles of some given color are aligned at a similar entropy value all panels together, and for orange symbols – corresponding to blocks without any nn spin pair – the entropy per site is close to its upper bound $\ln 2$. This leads to the conclusion that as long as two spins are not nn, they are very weakly correlated; and that the correlation length in the system is quite small, less or of the order of one lattice spacing.

In the paragraphs below, we identify the blocks realizing the lowest entropies; their configurations in space are depicted in turquoise in Fig. 4.22. The peculiarities related to the topology of every sample – in particular the consequences of closed loops on the entropy – are discussed as well.

Blocks with** 2 **sites – Consider the upper left panel in Fig. 4.22. The two sites forming the blocks do either be nn (black symbols) or do not (orange symbols). In the case of blocks built on two nn sites – i.e. bond-shaped blocks – the direction the bonds point in is indicated in the panel (turquoise double arrows). Referring to Table 4.1 of Section 4.2, one notices that the entropies are particularly low for blocks pointing in the direction of short closed loops. Spins within such blocks tend to align antiferromagnetically, being roughly insensitive to the configuration of other spins outside the block, and thus weakly correlated to the exterior. This fact is strongly marked for samples $s18_1$ and $s24_1$ which have *only one* "preferred" direction. We have also identified the lowest orange symbols for those two samples $s18_1$ and $s24_1$, since they exhibit a particularly low entropy. It turns out

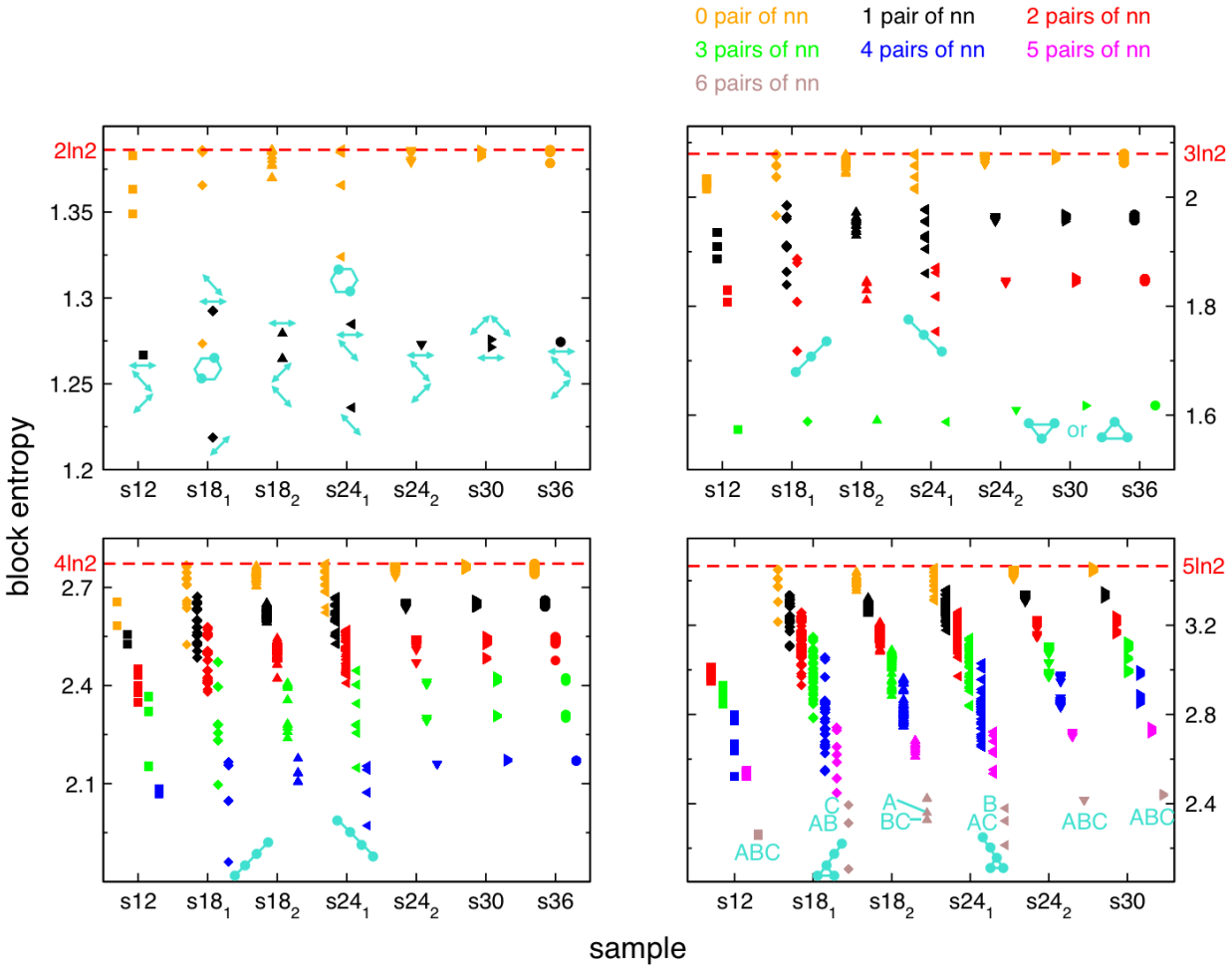

Figure 4.22: Block entropies in the ground state for all possible blocks containing 2 (upper left panel), 3 (upper right panel), 4 (lower left panel), and 5 (lower right panel) sites. Colors of the symbols indicate the number of nn spin pairs among each possible pairing of sites within the blocks (orange/black/red/green/blue/magenta/brown symbols indicate 0/1/2/3/4/5/6 nn spin pairs). The red dashed lines show the upper bound on the entropy in each panel. The configurations of particular interest which exhibit a low entropy are depicted in turquoise beside the points they are attached to. In the upper right panel, turquoise elementary triangles pointing upwards or downwards are attached to the entire set of green points. Blocks corresponding to the capital turquoise letters in the lower right panel are defined in Fig. 4.23. It is not possible to build blocks of 5 sites with 0 or 1 pair of nn sites in s12.

that in both cases, the two sites forming them are located at two opposite corners of an elementary hexagon (see turquoise draw in the panel). They form a "superbond" (whose

length is larger than one lattice spacing) that still points in the direction of the shortest closed loop. We see therefore that the peculiar topologies of $s18_1$ and $s24_1$ have strong consequences on the block entropies: in those samples, the entropy does not only depend on the number of nn pairs within the blocks, but the way the blocks are directed is important as well. Aligning a block in the direction of the (unique) shortest loop significantly lowers its entropy.

Blocks with** 3 **sites – Consider the upper right panel in Fig. 4.22. The lowest entropies are realized for blocks represented by green symbols and is roughly independent on the sample under study. Such blocks correspond to upwards and downwards directed elementary triangles. Regarding the lowest red symbols on the other hand, they are significantly low in entropy for samples $s18_1$ and $s24_1$, and roughly constant for the other samples. As expected from the above arguments, the blocks with low entropies for $s18_1$ and $s24_1$ consist of three sites that are aligned along the direction of the shortest closed loop (depicted in turquoise).

Blocks with** 4 **sites – Consider the lower left panel in Fig. 4.22. The lowest blue symbols representing blocks with minimal entropy are particularly low for $s18_1$ and $s24_1$, and roughly at the same height for the other blocks. As shown in turquoise in the panel, they correspond to blocks containing four sites that are aligned along the direction of the shortest closed loop in these two samples.

Blocks with** 5 **sites – Consider the lower right panel in Fig. 4.22. If topological effects do not (or do only weakly) bias the result, blocks corresponding to the lowest entropies are butterflies directed in each of the three possible directions which are defined in Fig. 4.23. This is the case for s12, $s24_2$, and s30.

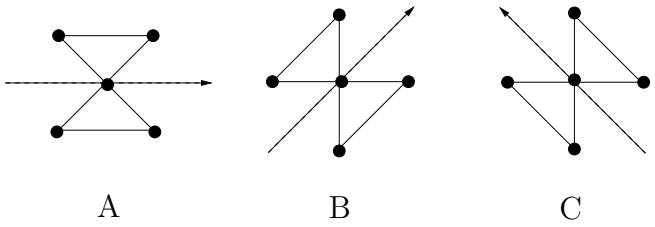

Figure 4.23: Blocks of 5 sites with the highest number of nn spin pairs (6 pairs, brown symbols in Fig. 4.22). They consist of butterfiles that point in the three possible directions.

If one direction is preferred – like in $s18_1$ or $s24_1$ – the ideal block minimizing the entropy would consist of five sites that are aligned along this preferred direction. However, since the topologies of these two samples do allow the alignment of a maximum of four sites along the preferred direction ↗ (for $s18_1$) or ↖ (for $s24_1$), the last site has to be chosen in another direction, as depicted in turquoise in the panel. Furthermore, the three butterflies in Fig. 4.23 are no longer equally favored.

Comparison with ordered systems – It is interesting to compare the block entropy results in the ground state of the spin-1/2 KAF with those in ordered systems, like the ground state of the spin-1/2 J_1–J_2 model on the square lattice (which has the same coordination number 4 as the kagomé lattice) – its phase diagram is given in the beginning of Subsection 3.6.2 – or the spin-1/2 KAF with an additional $J_2/J_1 = 1$ interaction stabilizing the $\mathbf{q} = 0$ Néel order [62]. Block entropies in these systems are shown in Fig. 4.24.

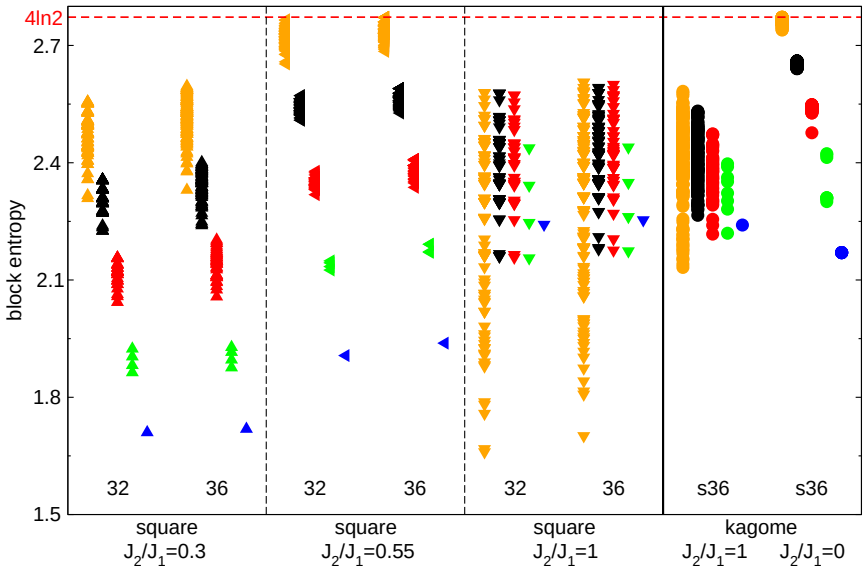

Figure 4.24: Block entropies for all possible blocks containing 4 sites in the ground state of the J_1–J_2 model on the square lattice (samples of 32 and 36 sites with diamond-shaped and 6×6-square unit cells respectively) for $J_2/J_1 = 0.3$, $J_2/J_1 = 0.55$, and $J_2/J_1 = 1$ (the three rightmost panels), and in the ground state of the J_1–J_2 model on s36 with $J_2/J_1 = 1$ ($\mathbf{q} = 0$ Néel order) and $J_2/J_1 = 0$ ("regular" Heisenberg model) (leftmost panels). The dashed red line shows the location of the upper bound $4 \ln 2$ on the entropy for blocks with four spins-1/2. The colors are defined as in Fig. 4.22.

In the case of the square lattice, each of the three phases has its own entropy behavior:

in the (π, π) Néel ordered phase ($J_2/J_1 = 0.3$), the entropy is roughly a function of the number of nn spin pairs within the blocks, and the upper bound $4 \ln 2$ is not reached for blocks without nn spin pairs (orange symbols). The behavior is similar in the disordered phase ($J_2/J_1 = 0.55$), but the piles are narrower for every color, and the entropies are shifted upwards such that orange symbols do reach the upper bound, as expected in a phase without order. As in the (π, π) Néel ordered phase, the orange symbols do not reach the upper bound in the collinear ordered phase ($J_2/J_1 = 1$); the behavior is nevertheless quite different: correlations are strong between nnn spins (instead of nn spins in the (π, π) phase), resulting in the extent of orange symbols down to very low entropy values, and the entropy is no longer a function of the number of nn spin pairs within the blocks. This is easily understood by taking a look at the spin correlation pattern (see for instance Fig. 3.9 in Section 3.6). The behavior of the KAF with stabilized $\mathbf{q} = 0$ order is similar.

Regarding the "regular" $J_2/J_1 = 0$ KAF we study, it behaves like the J_1–J_2 model on the square lattice in its disordered phase: the entropy is a function of the number of nn spin pairs within the blocks, and the upper bound is reached by some of the orange symbols (blocks without nn spins). This comparison therefore sustains the fact that the KAF is disordered (and potentially a VBC).

Block entropies in the low-lying states

Once the behavior of block entropies in the ground state is understood and the blocks corresponding to the lowest entropies are identified, it is interesting to investigate whether a similar behavior is recovered in the low-lying excited states of the spin-1/2 KAF. The study of the evolution of entropies when going from the ground state to an excited one is of great interest: as illustrated in Fig. 4.24 with the J_1–J_2 model on the square lattice, the overall behavior of the block entropies strongly depends on the type of ordering which is realized. Similar block entropies would mean that the two states would have the same "amount of disorder". In contrast, if the excited state was more disordered than the ground state, it would have higher block entropies. The left panel of Fig. 4.25 shows block entropies in the ground state of all samples, but the two largest ones. Entropies are computed for all possible blocks containing 3 sites one can build in those samples. Colors of the symbols are defined as in Fig. 4.22. The right panel of Fig. 4.25 displays the same informations as the left one for the five lowest-lying states belonging to the momentum sector of the ground state for sample s30, and for the states of s36 in IRREPS $[\Gamma, A_1]$, $[\Gamma, A_2]$, $[\Gamma, B_1]$, and $[\Gamma, B_2]$ (arbitrary choice) which are within the spin gap.

We put forward the interesting fact that for s30 as well as for s36, block entropies in the lowest-lying states have roughly the same values as in the ground state for all kinds of blocks. This result agrees with the conclusion we drew in Section 4.4 that some of the lowest-lying states of the spin-1/2 KAF are dimerized while others (like the ground state)

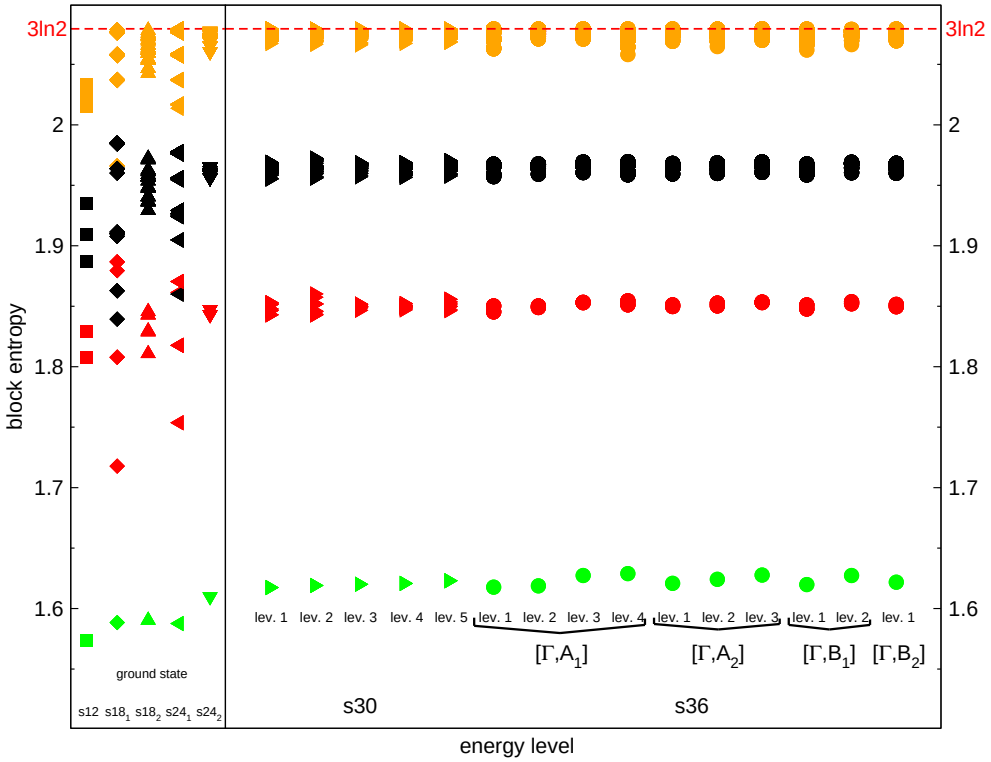

Figure 4.25: Block entropies for all possible blocks containing 3 sites in the ground state of s12, $s18_1$, $s18_2$, $s24_1$, and $s24_2$, and in some low-lying states of s30 (in the momentum sector of the ground state) and s36 (in IRREPS $[\Gamma, A_1]$, $[\Gamma, A_2]$, $[\Gamma, B_1]$, and $[\Gamma, B_2]$). The dashed red line shows the location of the upper bound $3 \ln 2$ on the entropy for blocks with three spins-1/2. Colors of the symbols are defined as in Fig. 4.22.

are completely disordered (spin liquids with dimer correlations falling quite fast): in both cases, the correlation between non-nn spins must be very weak. In that sense, the VBC scenario is compatible with Fig. 4.25.

Notice that the size effects are visible mostly in the left panel of Fig. 4.25, i.e. for samples smaller than s30, for which the strength of the correlation between non-nn spins is noticeable due to the smallness of those samples (in s12, the orange symbols are well below the red upper bound). As the size of the sample increases, the green, red, black, and orange piles become more and more narrow and "converge" to the piles of s36. The piles we get for s36 are thus representative of the thermodynamic limit, and it is a general property that the low-lying states of our model have a quite short correlation length.

Evolution of block entropies with the temperature

The lowest-lying excited states of the spin-1/2 KAF are shown above to roughly have the same block entropies as the ground state. The natural question that now arises is what happens at finite temperature, i.e. in thermal states[23]? Block entanglement entropy at finite temperature was introduced in Ref. [161] (where it is called *thermal entanglement*) in 2001 for the study of the 1D isotropic Heisenberg model. Entanglement entropy should not be confused with the entropy due to the lack of knowledge about the microstates of the system[24] (which – in contrast to entanglement entropy – vanishes at zero temperature).

Fig. 4.26 shows the evolution of the block entropies with the temperature T (the colors are defined as in Fig. 4.22) on sample s12. T ranges from 0 up to J/k_B. Notice that at $T = J/k_B$, states up to excitation energy J get a nonnegligible Boltzmann weight. This is well beyond the excitation energy of the states whose block entropies we have displayed in Fig. 4.25, the highest of which being the 4^{th} excited state of IRREP $[\Gamma, A_1]$ of sample s36 with the excitation energy $\sim 0.15J \ll 1J$ (see spectrum Fig. 4.5, right-hand side).

The four panels in Fig. 4.26 resemble one another: the curves are flat just above $T = 0$, and exhibit a sharp increase between $T = 0.02J/k_B$ and $0.1J/k_B$. There is an inflection point around $T = 0.1J/k_B$, and the curves increase much more slowly beyond it. Note that some of the orange curves even exhibit a slight local maximum around $T = 0.1J/k_B$. At large temperature, all curves approach the upper bound (dashed red lines).

Physically, an increasing entropy is related to an increasing number of disordered states having a nonnegligible Boltzmann weight. Thus, the more dense the spectrum (i.e. the higher the specific heat), the faster the entropy increase. It is thus not surprising if the specific heat Fig. 4.27 does sharply increase in the same region $T \in [0.02, 0.1]J/k_B$ as the block entropies do. The specific heat of the spin-1/2 KAF is well known to exhibit a double peak structure at low temperature [81; 101; 102; 104; 162], which is insensitive to large magnetic fields [81] (i.e. is the result of a large density of non-magnetic singlet states). These two peaks lie at $T \approx 0.1J/k_B$ and $T \approx 0.7J/k_B$ in the case of sample s12, see Fig. 4.27. The $T \approx 0.1J/k_B$ peak is roughly located at the inflection point of the block entropies, whereas the $T \approx 0.7J/k_B$ one is not foreseeable from Fig. 4.26. Hence, the high density of states responsible for the peak at $T \approx 0.7J/k_B$ do not significantly increase the disorder that was already existing below the $T = 0.7J/k_B$ point: there is a huge amount of disordered states with excitation energies well below $T = 0.7J/k_B$ that presumably partly

[23]Thermal states are mixed states with contributions from the entire spectrum, given by the Boltzmann weights.

[24]In statistical mechanics, the entropy quantifies the amount of uncertainty which remains about a system, after its observable macroscopic quantities (such as temperature, pressure and volume) have been taken into account. For a given set of macroscopic variables, the entropy measures the degree to which the probability of the system is spread out over different possible microstates.

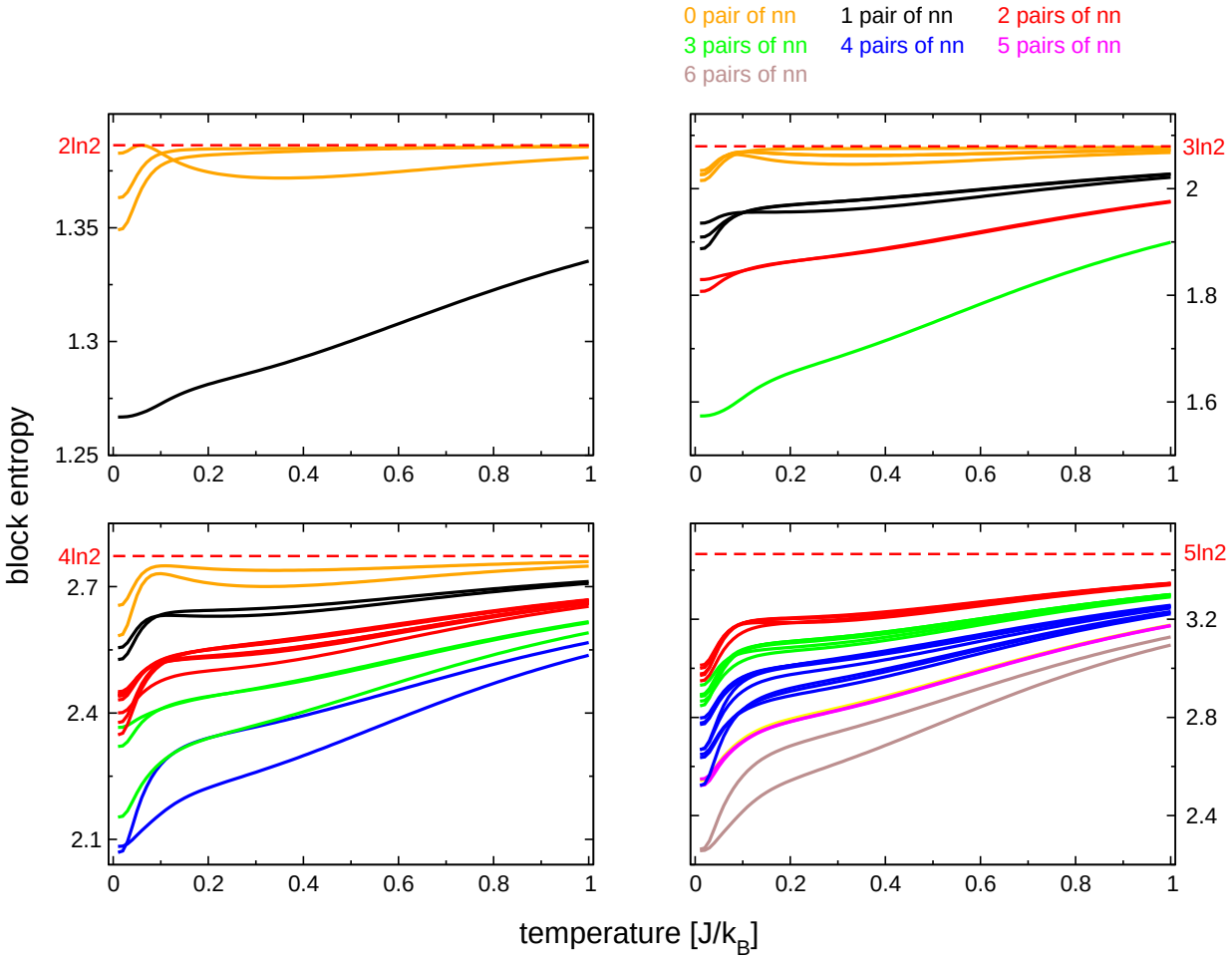

Figure 4.26: Evolution of the Von Neumann block entropies with the temperature for sample s12 for all possible blocks with 2 sites (upper left panel), 3 sites (upper right panel), 4 sites (lower left panel), and 5 sites (lower left panel).

"screen" the effect of the disordered states with higher excitation energies.

4.5.2 Scaling of block entropies: relevance of the area law

We aim here to verify the area law Eq. (4.13) governing the scaling of the entanglement entropy in systems with dimensionality $D > 1$. The area of the boundary of a given block is defined as the number of interactions connecting sites inside the block to the exterior. On the kagomé topology, a block with N sites and P pairs of nn sites has $4N-2P$ outgoing interactions (each spin interacts with four nearest neighbors).

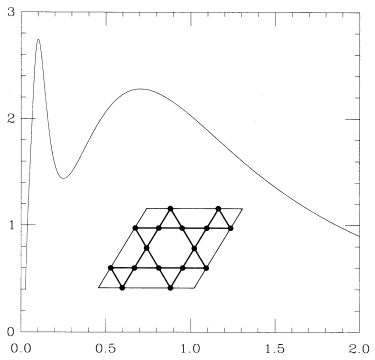

Figure 4.27: Specific heat as a function of the temperature for sample s12, from Ref. [101].

We have computed block entropies in the ground state for all possible blocks with 3 and 4 sites on samples $s24_2$, s30, and s36, for all possible blocks with 5 sites on samples $s24_2$ and s30, and for all possible blocks with 6, 7, and 8 sites on the sample $s24_2$. These entropies are shown in Fig. 4.28 as a function of the area of the blocks; the area law is obviously well verified. Data from the different samples are roughly superimposed. We stress that we are close to the ideal case where the amount of entropy that is gained by a fixed increase in area is independent on the block itself, since the slopes of the black, red, green, blue, magenta, and turquoise dashed straight lines are very similar one to another. The area law holds if the typical dimensions of the blocks are (much) larger than the correlation length of the system. Two kinds of blocks are therefore slightly off since they do not fulfill this requirement: the blocks with the smallest areas on the one hand, and blocks consisting of several "subblocks", one (or some) of which having a very small area. Those blocks with 4 sites (red) at area 10 which are below the red dashed line do for instance belong to this latter category. They are actually made of 3 sites forming a perfect elementary triangle, plus one isolated site. This isolated site is indeed the "subblock" whose size is of the order of the correlation length (roughly one lattice spacing), whence the disagreement with the area law. The fact that blocks with typical dimensions of 2 or 3 lattice spacings fulfill the area law indeed shows that one lattice spacing is probably a good estimate for the correlation length in this model. A further necessary requirement for the area law to hold is that the blocks are much smaller (in term of number of enclosed sites) than the sample they are built on. This is less and less true as the size of the blocks becomes larger and larger.

Let us pay some attention to the configurations with maximal areas for every size of blocks (i.e. for every color). These blocks do not contain any nn spin pair and thus have area $4N$. Sites inside them are therefore minimally correlated (and maximally correlated to the environment of the block). When enlarging one of these blocks by one site (such

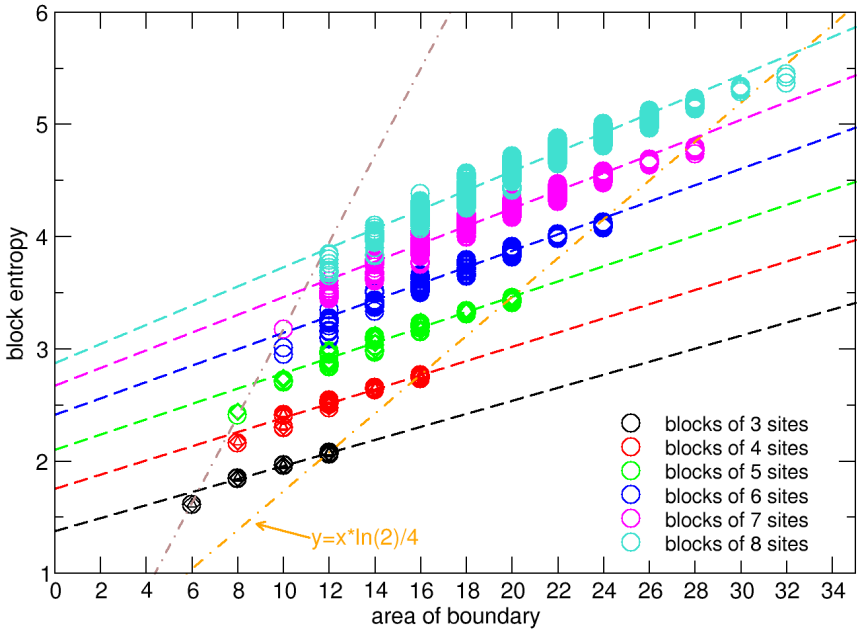

Figure 4.28: Block entropies vs areas in the ground state for all blocks containing 3 and 4 sites on $s24_2$ ($\circ$), s30 ($\diamond$), and s36 ($\triangle$), all blocks containing 5 sites on $s24_2$ and s30, and all blocks containing 6, 7, and 8 sites on $s24_2$. Dashed black, red, green, blue, magenta, and turquoise straight lines are guide to the eye highlighting the linear dependence. The brown dashed-dotted straight line shows the entropy evolution for minimally entangled blocks through the black, green, and magenta symbols at minimal areas. The orange dashed-dotted line has equation $y = x \cdot \frac{\ln 2}{4}$ and is in good agreement with the entropies of maximally entangled blocks (meaning a contribution to the entropy of $\ln 2$ per site).

that the new block still has a maximal area), the gain in entropy is consequently $\sim \ln 2$, i.e. the entropy of one single independent spin $S = 1/2$. This is confirmed by the fact that their symbols in Fig. 4.28 are roughly onto the $y = x \cdot \frac{\ln 2}{4}$ dashed-dotted orange straight line that represents the extreme case of blocks containing uncorrelated sites.

We now switch to configurations with minimal areas, i.e. with area $N + 3$ for blocks having an odd number of sites and $N+4$ for those having an even number of sites. Symbols representing blocks of 3, 5 and 7 sites are roughly aligned (brown dashed-dotted straight line in Fig. 4.28) but they are not aligned with symbols representing blocks with even number of sites (4, 6, and 8), which are thus discarded for drawing the brown line[25]. Its slope ~ 0.39 yields the gain in entropy per additional site[26] (such that the new block still

[25]The slope would nevertheless be similar if only even blocks were considered.
[26]Actually, it is half the entropy the block gains when two sites are added.

has a minimal area), which is roughly $\frac{\ln 2}{0.39} \approx 1.8$ times as less as the gain in entropy per additional site for blocks with maximal entropies.

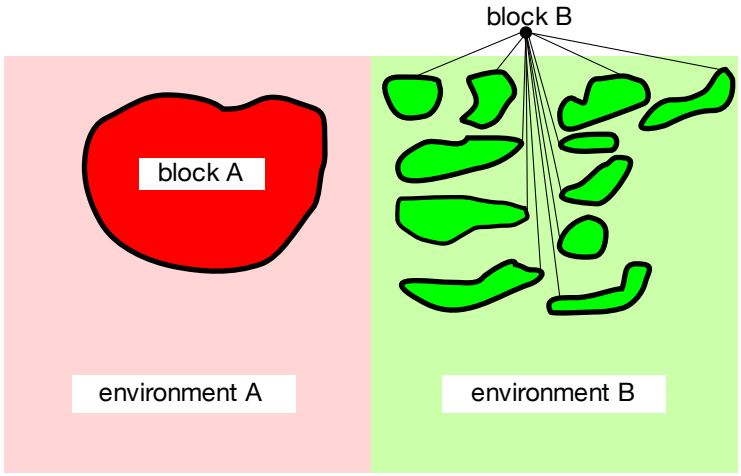

Block A

- area is small
- sites inside the block are weakly correlated to the exterior, i.e. entanglement with the environment of the block is small
- hence block entropy is small
- sites inside the block are "strongly" correlated between them

Block B

- area is large
- sites inside the block are strongly correlated to the exterior, i.e. entanglement with the environment of the block is large
- hence block entropy is large
- sites inside the block are separated by "large" distances and thus are nearly uncorrelated

Figure 4.29: Case of the spin-1/2 kagomé antiferromagnet. The volumes (i.e. number of sites) of blocks A and B are identical but the area of block B is much larger than that of block A, which amounts to a stronger entanglement with the environment and thus a larger block entropy.

A conceptually good picture of the structure of blocks with small and large entropies is provided by Fig. 4.29: blocks with small entropies look basically like one single compact block (small area), whereas those with large entropies are composed by a lot of small subblocks[27] (large area). In the extreme case, blocks with maximal entropies consist of

[27] By "a lot of small subblocks", we mean that two sites belonging to two different subblocks are not nn.

subblocks containing one site each. It is always possible to enlarge them by adding one isolated site – resulting in a gain in entropy of $\sim \ln 2 = 0.69315$ – for recovering a new block with maximal entropy. Regarding blocks with minimal entropies, it is physically not possible to enlarge them by one (or more) site in such a way that an increase in entropy is avoided. The enlargement of blocks with minimal entropies to larger blocks with minimal entropies is necessarily accompanied by an increase in the entropy – by 0.39 as seen above – which is the minimal amount of entropy (i.e. minimal entanglement with the environment) a block is obligated to gain as one site is added to it.

4.5.3 Conclusion

We have identified the blocks associated to the lowest entropies for various sample topologies, and shown that in the low-lying singlet states of the spin-1/2 kagomé antiferromagnet, block entropies essentially depend on the number of pairs of nearest-neighboring sites within the block in question (revealing a correlation length of the order of one lattice spacing), and neither depend on the energy of the state which is investigated, nor on the sample. These results support the VBC scenario that was initially put forward in Section 4.3 and more deeply investigated in Section 4.4. Moreover, the consequences of closed loops that were revealed in Section 4.3 also bias block entropy calculations, that turn out to be strongly dependent on the topology of the sample which is studied. Performing simulations on blocks containing up to 8 sites, we have shown that entanglement entropy in the spin-1/2 kagomé antiferromagnet scales with the area of the blocks, i.e. the "area law" is fulfilled. We have also discussed the way the entropy evolves with the temperature, and with the size of minimally and maximally entangled blocks.

CHAPTER 5

Conclusion & outlook

In this thesis, we have investigated two spin-1/2 Heisenberg models – namely the ferromagnetic frustrated chain in a magnetic field and the kagomé antiferromagnet – by means of a novel approach, which consists of extracting the dominant correlations between two disjoint blocks in a quantum many-body system from the *correlation density matrix* (CDM) between those blocks. The states were obtained by exact diagonalization as well as by the density matrix renormalization group algorithm. The CDM approach was recently introduced by Cheong and Henley [25]; it is non-biased and does not require any a priori knowledge of the system. We have developed a mathematical framework for utilizing this method, and derived several of its mathematical properties and features, in particular the consequences of symmetries are discussed. We have also identified the states providing the maximal correlation between the two blocks, and studied how *correlations* and *entanglement* are related one to another. For illustrative purposes, the CDM method is applied to simple models whose physics is already understood, at zero as well as at finite temperature.

Our study of the ferromagnetic frustrated spin-1/2 Heisenberg chain in a magnetic field has revealed a vector chiral phase breaking the parity symmetry at low field and a sequence of spin multipolar Luttinger liquid phases at higher field. This latter phase exhibits a crossover: it is dominated by spin density wave correlations at intermediate field, and by multipolar correlations close to the saturation field. Not content with solving the phase diagram of this model, we have also clarified the underlying mechanism responsible for the presence of the chiral and the multipolar phases: it turns out that both of them result from

the destabilization by quantum fluctuations of a spiral state, which is the classical ground state in the absence of magnetic field. We have moreover shown that the type of multipolar phase which is realized in the different coupling parameter regimes is predictable from the zero field physics. It was well known that a spiral phase may destabilize towards a vector chiral phase, but the idea that it may be responsible for the emergence of multipolar phases has never been put forward yet, although it is compatible with several phase diagram that have already been reported, showing a multipolar phase in the neighborhood of a spiral state. The discovery of this mechanism is crucial since it will permit to possibly predict the stabilization of multipolar phases in other models which have a spiral-like phase in a certain regime, but whose phase diagram is not completely understood yet.

Regarding the kagomé antiferromagnet, we have identified the *closed loop effect* which is responsible for the structure of the spin correlations in the ground state of the different samples we have studied, and we have shown that finite size effects due to closed loops are strong, even in the largest samples. CDM analyses of the dominant correlations between blocks of 2,3, and 6 sites have pointed out the scenario of a *valence bond crystal* (VBC) to be the most credible candidate for governing the low-energy physics of this highly frustrated model. The comparison of the dimer correlations in the lowest-lying states of its spectrum with the dimer correlations in different kinds of VBCs has shown a good agreement in several cases; we have mentioned the fact that the lack of a perfect agreement might be indeed due to the finite size effects. We have finally studied the entanglement entropy of blocks of various sizes in the ground state of the kagomé antiferromagnet, and identified the blocks corresponding to the lowest entropies, being those which are minimally entangled to their environment. Paying some attention to block entropies in the lowest-lying states as well, we have seen that on the one hand – as expected – two sites are nearly disentangled one to another as long as they are not nearest neighbors, and on the other hand the entropy of any kind of block is roughly independent on the energy of the state which is investigated, which agrees with the VBC scenario at low-energy. Furthermore, we have checked that the ground state of the kagomé antiferromagnet fulfills the *area law*.

It should be stressed that the CDM approach this thesis is focused on is very promising, among other things because it is not restricted to spins-1/2 – some higher-spin systems can be studied as well – and it is moreover not restricted to spin systems themselves. This systematic CDM method allows to tackle all kinds of quantum many-body systems one is likely to encounter in condensed matter physics. In his seminal paper introducing the method [25], C.L. Henley illustrates it with the study of a toy model of spinless fermions on a two-leg ladder. In another paper [163], Münder and collaborators show how this method can be used for studying a class of spinless extended Hubbard model for fermions. There is therefore no doubt that this novel approach is a significant progress in the field of

computational methods applied to condensed matter physics.

APPENDIX A

Numerical diagonalization techniques

A.1 Exact Diagonalization (ED)

Different kinds of Exact Diagonalization (ED) algorithms are existing, each with its particularities [Lanczos (C. Lanczos, 1950) [172], "modified Lanczos" (E. Gagliano et al., 1986) [173], Davidson (E.R. Davidson, 1975) [174], LAPACK libraries for full diagonalizations (in ALPS)]. The Lanczos and the Davidson methods build up a small set of basis vectors, and minimize the energy within the basis. The reduced set of basis vectors is systematically expanded until convergence is reached. They are efficient at finding a few extremal eigenvalues and eigenstates of a large sparse hamiltonian matrix H. The Davidson method utilizes the diagonal elements of H in an attempt to generate an improved reduced basis. Consequently, if the hamiltonian is at all dominated by its diagonal elements, the Davidson method will probably converge more quickly than the Lanczos method (on which we shall focus in this section).

ED algorithms become really powerful only when the Hilbert space is divided into several symmetry sectors, and the spectrum is computed separately in each of them. We therefore first give a detailed introduction on how to exploit translational and point group symmetries in Bravais lattices in the subsections below, and then introduce the Lanczos algorithm in the last part of this section.

A.1.1 Why use symmetries for performing ED?

The models we study in condensed matter physics consist of interacting quantum magnetic moments (spins) that are regularly arranged on a lattice. Numerical investigations can only be performed on *finite samples* of the lattice, which we wish to be as large as possible in order to describe our macroscopic world as precisely as possible. Since the study of large samples is hampered by the dimensionality of the total Hilbert space (dimensionality $(2S+1)^N$ for a sample with N spins-S, increasing exponentially fast with N), symmetries have to be taken into account in order to divide this total Hilbert space into subspaces which are globally invariant under the action of the hamiltonian we investigate.

If the hamiltonian has periodic boundary conditions for instance, translational invariance can be exploited. If the sample has some reflectional or rotational symmetries – called *point group* symmetries – the translationally invariant subspaces can themselves be further divided into smaller subspaces[1]. The numerical investigation of "reasonably large" samples then becomes possible.

A.1.2 Translational symmetries

If the hamiltonian has periodic boundary conditions – thus translational invariance – the total Hilbert space can be decomposed into subspaces, each of which having an additional quantum number called *momentum*, and usually denoted by the vector $\mathbf{k}$. A state belonging to the subspace of momentum $\mathbf{k}$ is such that – if translated by a lattice vector $\mathbf{R}$ – it is multiplied by the phase factor $e^{i\mathbf{k}\cdot\mathbf{R}}$. Hence, a projector onto the subspace of momentum $\mathbf{k}$ is given by

$$\Pi_{\mathbf{k}} = \frac{1}{\sqrt{|\mathcal{T}|}} \sum_{\mathbf{R}\in\mathcal{T}} e^{-i\mathbf{k}\cdot\mathbf{R}} T_{\mathbf{R}} \tag{A.1}$$

where the sum runs over the entire group $\mathcal{T}$ of translation operations, and the operator $T_{\mathbf{R}}$ translates a state by the lattice vector $\mathbf{R}$.

The momenta are generally chosen inside the first Brillouin zone[2] (BZ) in the reciprocal space (which is the unit cell of the reciprocal lattice). In the thermodynamic limit of an infinite sample, the whole continuum of momenta inside the BZ is allowed, but in the case of finite samples, only a finite number of them – equal to the number of sites in the sample[3] – are allowed. They are derived from the primitive vectors spanning the superlattice in the direct space[4]. Let us consider various kinds of samples on the square lattice as examples.

[1] (point group symmetries)×(translational symmetries)=space group symmetries

[2] We shall argue further why the choice of the Wigner-Seitz cell as BZ suits particularly well.

[3] Or equal to the number of sites in the sample, divided by the number of sites in the unit cell in the case of a non-Bravais lattice (e.g. the kagomé lattice, that has a unit cell of three sites).

[4] The superlattice in the direct space is the "lattice of samples", i.e. the sample itself is taken as unit

Sample of 4 sites on the square lattice

We consider here the square lattice with a sample containing 4 sites, as shown in Fig. A.1. The BZ in the reciprocal space can be chosen to be $[0, 2\pi] \times [0, 2\pi]$, and the 4 different

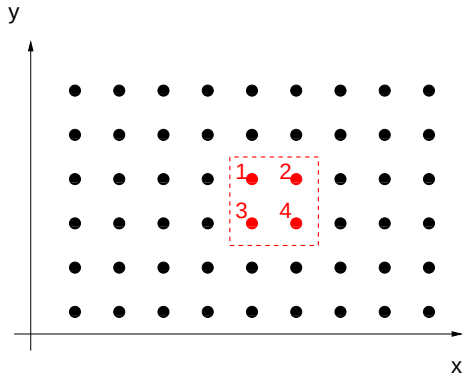

Figure A.1: Sample of 4 sites on the square lattice.

allowed momenta are

$\mathbf{k}_1 = (0,0) \equiv (2\pi,0) \equiv (0,2\pi) \equiv (2\pi,2\pi)$; $\mathbf{k}_2 = (\pi,0) \equiv (\pi,2\pi)$; $\mathbf{k}_3 = (0,\pi) \equiv (2\pi,\pi)$; and $\mathbf{k}_4 = (\pi,\pi)$.

The translation operations of the sample are the following ones (4 operations as the sample contains 4 sites): identity ($\mathcal{E}$), translation by one site along x (T_x), translation by one site along y (T_y), and the combination of both ($T_y T_X$).

Each allowed momentum $\mathbf{k}$ is also a representation $\Gamma_\mathbf{k}$ of the group $\mathcal{T} = \{\mathcal{E}, T_x, T_y, T_y T_X\}$. The characters of these (one-dimensional) representations are the multiplicative phase factors acquired under the action of symmetry operations. They are given in Table A.1.

$\Gamma_\mathbf{k}$	$\mathcal{E}$	T_x	T_y	$T_y T_x$
$\mathbf{k}_1 = (0,0)$	1	1	1	1
$\mathbf{k}_2 = (\pi,0)$	1	-1	1	-1
$\mathbf{k}_3 = (0,\pi)$	1	1	-1	-1
$\mathbf{k}_4 = (\pi,\pi)$	1	-1	-1	1

Table A.1: Characters corresponding to the translation symmetries.

cell.

The states belonging to every momentum sector can be derived by construction using the projector Eq. (A.1). If the sample in Fig. A.1 has for instance a spin-1/2 at each site, the 16 states in the total Hilbert space are shared as follows (apart from the normalization factor):

$\mathbf{k}_1 = (0,0)$ sector (7 states):
$\{|\uparrow\uparrow\uparrow\uparrow\rangle, |\uparrow\uparrow\uparrow\downarrow\rangle + |\uparrow\uparrow\downarrow\uparrow\rangle + |\uparrow\downarrow\uparrow\uparrow\rangle + |\downarrow\uparrow\uparrow\uparrow\rangle, |\uparrow\uparrow\downarrow\downarrow\rangle + |\downarrow\downarrow\uparrow\uparrow\rangle, |\uparrow\downarrow\uparrow\downarrow\rangle + |\downarrow\uparrow\downarrow\uparrow\rangle,$
$|\uparrow\downarrow\downarrow\uparrow\rangle + |\downarrow\uparrow\uparrow\downarrow\rangle, |\downarrow\downarrow\downarrow\uparrow\rangle + |\downarrow\downarrow\uparrow\downarrow\rangle + |\downarrow\uparrow\downarrow\downarrow\rangle + |\uparrow\downarrow\downarrow\downarrow\rangle, |\downarrow\downarrow\downarrow\downarrow\rangle\}$

$\mathbf{k}_2 = (\pi,0)$ sector (3 states):
$\{|\uparrow\uparrow\uparrow\downarrow\rangle - |\uparrow\uparrow\downarrow\uparrow\rangle + |\uparrow\downarrow\uparrow\uparrow\rangle - |\downarrow\uparrow\uparrow\uparrow\rangle, |\uparrow\downarrow\uparrow\downarrow\rangle - |\downarrow\uparrow\downarrow\uparrow\rangle,$
$|\downarrow\downarrow\downarrow\uparrow\rangle - |\downarrow\downarrow\uparrow\downarrow\rangle + |\downarrow\uparrow\downarrow\downarrow\rangle - |\uparrow\downarrow\downarrow\downarrow\rangle\}$

$\mathbf{k}_3 = (0,\pi)$ sector (3 states):
$\{|\uparrow\uparrow\uparrow\downarrow\rangle + |\uparrow\uparrow\downarrow\uparrow\rangle - |\uparrow\downarrow\uparrow\uparrow\rangle - |\downarrow\uparrow\uparrow\uparrow\rangle, |\uparrow\uparrow\downarrow\downarrow\rangle - |\downarrow\downarrow\uparrow\uparrow\rangle,$
$|\downarrow\downarrow\downarrow\uparrow\rangle + |\downarrow\downarrow\uparrow\downarrow\rangle - |\downarrow\uparrow\downarrow\downarrow\rangle - |\uparrow\downarrow\downarrow\downarrow\rangle\}$

$\mathbf{k}_4 = (\pi,\pi)$ sector (3 states):
$\{|\uparrow\uparrow\uparrow\downarrow\rangle - |\uparrow\uparrow\downarrow\uparrow\rangle - |\uparrow\downarrow\uparrow\uparrow\rangle + |\downarrow\uparrow\uparrow\uparrow\rangle, |\uparrow\downarrow\downarrow\uparrow\rangle - |\downarrow\uparrow\uparrow\downarrow\rangle,$
$|\downarrow\downarrow\downarrow\uparrow\rangle - |\downarrow\downarrow\uparrow\downarrow\rangle - |\downarrow\uparrow\downarrow\downarrow\rangle + |\uparrow\downarrow\downarrow\downarrow\rangle\}$.

The total Hilbert space is thus divided into 4 subspaces.

Sample of 5 sites on the square lattice

We consider the same lattice as above (the BZ is thus identical), and a sample with 5 sites as depicted in Fig. A.2. In contrast to the sample of 4 sites, it is not obvious here to guess which $\mathbf{k}$ vectors are allowed. One has to derive them from the primitive vectors which span the superlattice (i.e which translate the sample onto one of its copies)

$$\mathbf{a}_1 = (2,1), \qquad \mathbf{a}_2 = (-1,2).$$

A third z-coordinate is artificially added in this 2D system by redefining

$$\mathbf{a}_1 = (2,1,0), \qquad \mathbf{a}_2 = (-1,2,0), \qquad \mathbf{a}_3 = (0,0,1),$$

whose corresponding primitive vectors in the reciprocal space are

$$\mathbf{a}_1^* = 2\pi\frac{\mathbf{a}_2 \times \mathbf{a}_3}{\mathbf{a}_1 \cdot (\mathbf{a}_2 \times \mathbf{a}_3)} = \frac{2\pi}{5}(2,1,0), \qquad \mathbf{a}_2^* = 2\pi\frac{\mathbf{a}_3 \times \mathbf{a}_1}{\mathbf{a}_1 \cdot (\mathbf{a}_2 \times \mathbf{a}_3)} = \frac{2\pi}{5}(-1,2,0),$$

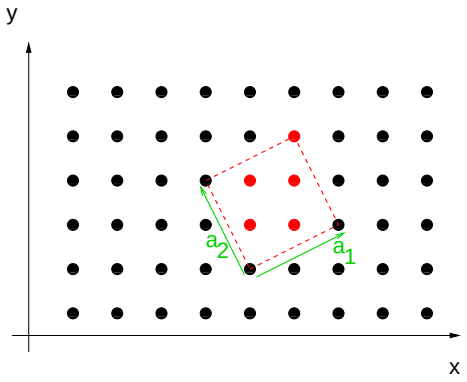

Figure A.2: Sample of 5 sites on the square lattice. The primitive vectors $\mathbf{a}_1$ and $\mathbf{a}_2$ span the superlattice.

which yields, after removing the artificial z-coordinate

$$\mathbf{a}_1^* = \frac{2\pi}{5}(2,1), \qquad \mathbf{a}_2^* = \frac{2\pi}{5}(-1,2).$$

One finds the 5 allowed $\mathbf{k}$ vectors by adding/subtracting $\mathbf{a}_1^*$ and $\mathbf{a}_2^*$ in all possible ways

$$\mathbf{k}_1 = (0,0), \qquad \mathbf{k}_2 = \mathbf{a}_1^* = \left(\frac{4\pi}{5}, \frac{2\pi}{5}\right), \qquad \mathbf{k}_3 = \mathbf{a}_2^* = \left(-\frac{2\pi}{5}, \frac{4\pi}{5}\right)$$
$$\mathbf{k}_4 = \mathbf{a}_1^* + \mathbf{a}_2^* = \left(\frac{2\pi}{5}, \frac{6\pi}{5}\right) \equiv \left(\frac{2\pi}{5}, -\frac{4\pi}{5}\right), \qquad \mathbf{k}_5 = \mathbf{a}_1^* - \mathbf{a}_2^* = \left(\frac{6\pi}{5}, -\frac{2\pi}{5}\right) \equiv \left(-\frac{4\pi}{5}, -\frac{2\pi}{5}\right).$$

Two momenta $\mathbf{k}$ and $\mathbf{k}'$ are equivalent (i.e. have identical projectors $\Pi_{\mathbf{k}} = \Pi_{\mathbf{k}'}$, Eq. (A.1)) if they differ by (a multiple of) $(2\pi, 0)$ or $(0, 2\pi)$[5].

The translation operations that act on the sample and their characters for every representation $\Gamma_{\mathbf{k}}$ are given in Table A.2 (5 translations since the sample has 5 sites). The total Hilbert space is thus divided into 5 subspaces.

A.1.3 Point group symmetries

Only translational symmetries have been used up to now. It is possible to further reduce the representations of the translational symmetries group by taking into account the point group operations, i.e. *rotational* as well as *reflectional* symmetries. In concrete terms, each sector will be described by the good quantum number $\mathbf{k}$ and an additional good quantum

[5]They are derived from the primitive vectors of the lattice $(1,0)$ and $(0,1)$ in the direct space, not by those of the superlattice $\mathbf{a}_1$ and $\mathbf{a}_2$.

$\Gamma_{\mathbf{k}}$	$\mathcal{E}$	T_x	T_y	T_x^2	T_yT_x
$\mathbf{k}_1 = (0,0)$	1	1	1	1	1
$\mathbf{k}_2 = (\frac{4\pi}{5}, \frac{2\pi}{5})$	1	$e^{i\frac{4\pi}{5}}$	$e^{i\frac{2\pi}{5}}$	$e^{i\frac{8\pi}{5}}$	$e^{i\frac{6\pi}{5}}$
$\mathbf{k}_3 = (-\frac{2\pi}{5}, \frac{4\pi}{5})$	1	$e^{-i\frac{2\pi}{5}}$	$e^{i\frac{4\pi}{5}}$	$e^{-i\frac{4\pi}{5}}$	$e^{i\frac{2\pi}{5}}$
$\mathbf{k}_4 = (\frac{2\pi}{5}, -\frac{4\pi}{5})$	1	$e^{i\frac{2\pi}{5}}$	$e^{-i\frac{4\pi}{5}}$	$e^{i\frac{4\pi}{5}}$	$e^{-i\frac{2\pi}{5}}$
$\mathbf{k}_5 = (-\frac{4\pi}{5}, -\frac{2\pi}{5})$	1	$e^{-i\frac{4\pi}{5}}$	$e^{-i\frac{2\pi}{5}}$	$e^{-i\frac{8\pi}{5}}$	$e^{-i\frac{6\pi}{5}}$

Table A.2: Characters corresponding to the translation symmetries.

number that we shall call M. Globally invariant subspaces are therefore labelled by the pair [$\mathbf{k}$,M] which denotes an irreducible representation (IRREP) of the spatial symmetries group. For a given momentum $\mathbf{k}$, those operations in the point group of the Bravais lattice that leave $\mathbf{k}$ invariant (fixed) in the reciprocal space build the so-called *little group* $G_{\mathbf{k}}$ *of* $\mathbf{k}$, whose representations correspond to M. We can understand at this stage why the Wigner-Seitz cell suits particularly well as BZ: an important property of the Wigner-Seitz BZ cell is that it has the same point group symmetries as the sample in the direct space, which simplifies the task. We give below a concrete example with a sample of 12 sites on the kagomé lattice.

Sample of 12 sites on the kagomé lattice

The sample we consider is displayed in Fig. A.3 (left). In order to perform Exact Diagonalization (ED), all IRREPs and characters must be determined. The kagomé lattice is not a Bravais lattice. Its underlying Bravais lattice is the triangular lattice, with a triangular unit cell (of 3 sites). The first step consists in determining the allowed momentum values by considering the sample of $12/3 = 4$ sites on the triangular Bravais lattice shown in Fig. A.4.

From the primitive vectors $\mathbf{a}_1$, $\mathbf{a}_2$ of the lattice, and $\mathbf{b}_1$, $\mathbf{b}_2$ of the superlattice in the direct space (see Fig. A.4), one derives the corresponding primitive vectors in the reciprocal space

$$\mathbf{a}_1^* = \frac{2\pi}{\sqrt{3}}\left(\sqrt{3}, -1\right), \quad \mathbf{a}_2^* = \frac{2\pi}{\sqrt{3}}\left(0, 2\right), \quad \mathbf{b}_1^* = \pi\left(1, -1/\sqrt{3}\right), \quad \mathbf{b}_2^* = \pi\left(0, 2/\sqrt{3}\right).$$

The 4 allowed $\mathbf{k}$ vectors are found by adding/subtracting the $\mathbf{b}_1^*$ and $\mathbf{b}_2^*$ vectors, and are given by

$$\mathbf{k}_1 = (0,0), \quad \mathbf{k}_2 = \left(0, 2\pi/\sqrt{3}\right), \quad \mathbf{k}_3 = \left(\pi, \pi/\sqrt{3}\right), \quad \mathbf{k}_4 = \left(\pi, -\pi/\sqrt{3}\right),$$

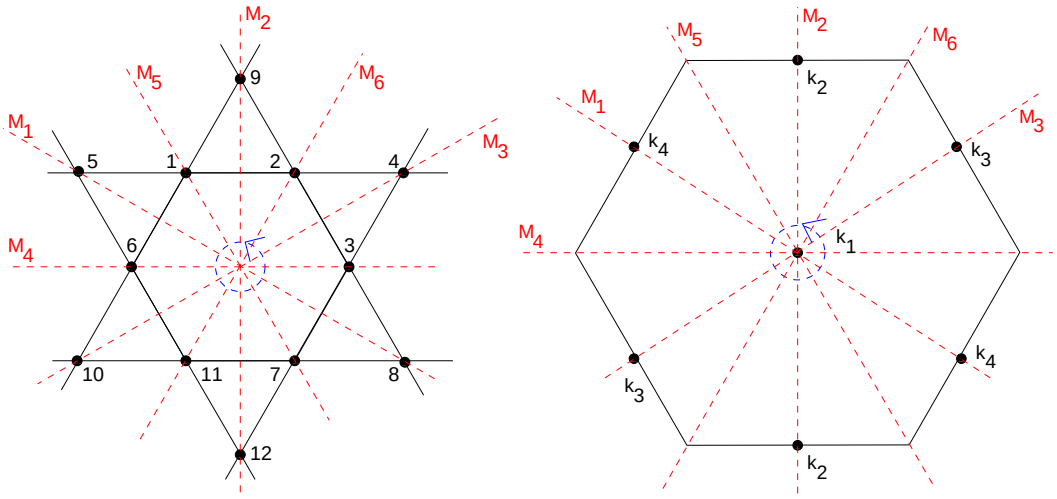

Figure A.3: (Left) Sample of 5 sites on the square lattice. The 6 reflectional mirror symmetries are shown in red, and the center of the 5 rotations is shown in blue. (Right) Allowed $\mathbf{k}$ points in the first Brillouin zone. Note that the $\mathbf{k}_2$, the $\mathbf{k}_3$, and the $\mathbf{k}_4$ sectors will display identical energy spectra, as they can be recovered one from another by a point group symmetry.

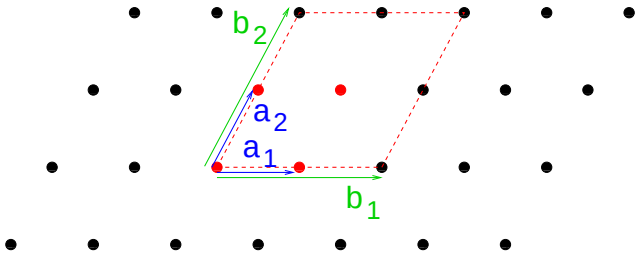

Figure A.4: Triangular lattice with the primitive vectors $\mathbf{a}_1 = (1, 0)$ and $\mathbf{a}_2 = \left(1/2, \sqrt{3}/2\right)$, and those of the superlattice $\mathbf{b}_1 = (2, 0)$ and $\mathbf{b}_2 = \left(1, \sqrt{3}\right)$. The sample – shown in red – has 4 (=12/3) sites.

they are represented in Fig. A.3 (right). Two momenta that differ by a multiple of $\mathbf{a}_1^*$ or $\mathbf{a}_2^*$ are equivalent. Note that the Brillouin zone (Fig. A.3, right) has the same point group symmetries as the sample in the direct space (Fig. A.3, left), namely the symmetry group of the hexagon.

The translational symmetries of the triangular lattice Fig. A.4 are $\{\mathcal{E}, T_{\mathbf{a}_1}, T_{\mathbf{a}_2}, T_{\mathbf{a}_2} T_{\mathbf{a}_1}\}$, where the $T_{\mathbf{a}_1}$ and $T_{\mathbf{a}_2}$ operators translate a state by $\mathbf{a}_1$ and $\mathbf{a}_2$ respectively. These operations amount to permuting the sites as shown in Table A.3. The corresponding characters are shown in Table A.4, we recall that for translations, representations are given by the allowed momenta values.

initially ($\mathcal{E}$)	1	2	3	4	5	6	7	8	9	10	11	12
$T_{\mathbf{a}_1}$	4	5	6	1	2	3	10	11	12	7	8	9
$T_{\mathbf{a}_2}$	10	11	12	7	8	9	4	5	6	1	2	3
$T_{\mathbf{a}_2}T_{\mathbf{a}_1}$	7	8	9	10	11	12	1	2	3	4	5	6

Table A.3: Action of the translation operations.

	$\mathcal{E}$	$T_{\mathbf{a}_1}$	$T_{\mathbf{a}_2}$	$T_{\mathbf{a}_2}T_{\mathbf{a}_1}$
$\mathbf{k}_1$	1	$e^{i\mathbf{a}_1\cdot\mathbf{k}_1}$	$e^{i\mathbf{a}_2\cdot\mathbf{k}_1}$	$e^{i(\mathbf{a}_1+\mathbf{a}_2)\cdot\mathbf{k}_1}$
$\mathbf{k}_2$	1	$e^{i\mathbf{a}_1\cdot\mathbf{k}_2}$	$e^{i\mathbf{a}_2\cdot\mathbf{k}_2}$	$e^{i(\mathbf{a}_1+\mathbf{a}_2)\cdot\mathbf{k}_2}$
$\mathbf{k}_3$	1	$e^{i\mathbf{a}_1\cdot\mathbf{k}_3}$	$e^{i\mathbf{a}_2\cdot\mathbf{k}_3}$	$e^{i(\mathbf{a}_1+\mathbf{a}_2)\cdot\mathbf{k}_3}$
$\mathbf{k}_4$	1	$e^{i\mathbf{a}_1\cdot\mathbf{k}_4}$	$e^{i\mathbf{a}_2\cdot\mathbf{k}_4}$	$e^{i(\mathbf{a}_1+\mathbf{a}_2)\cdot\mathbf{k}_4}$

$\Longrightarrow$

	$\mathcal{E}$	$T_{\mathbf{a}_1}$	$T_{\mathbf{a}_2}$	$T_{\mathbf{a}_2}T_{\mathbf{a}_1}$
$\mathbf{k}_1$	1	1	1	1
$\mathbf{k}_2$	1	1	-1	-1
$\mathbf{k}_3$	1	-1	-1	1
$\mathbf{k}_4$	1	-1	1	-1

Table A.4: Characters corresponding to the translation symmetries.

Let us now move on with the point group (i.e. rotations and reflections) of the sample. The 6 reflectional (mirror) symmetries are shown in Fig. A.3 (red) as M_1, M_2, M_3, M_4, M_5, and M_6. They permute the initial combination of sites as shown in Table A.5. In addition

initially	1	2	3	4	5	6	7	8	9	10	11	12
M_1	6	11	7	12	5	1	3	8	10	9	2	4
M_2	2	1	6	5	4	3	11	10	9	8	7	12
M_3	7	3	2	4	12	11	1	9	8	10	6	5
M_4	11	7	3	8	10	6	2	4	12	5	1	9
M_5	1	6	11	6	9	2	7	12	5	4	3	8
M_6	3	2	1	9	8	7	6	5	4	12	11	10

Table A.5: Action of the reflection operations.

to the reflections, the sample in Fig. A.3 has also 5 rotational symmetries whose center of rotation is shown in blue. We define the rotation operation R_i such that it rotates the sites by an angle $\frac{2\pi}{6}\cdot i$ in the counterclockwise direction ($i = 1, 2, \cdots, 5$). The action of R_1 is for instance given in Table A.6, and then $R_2 = R_1^2$, $R_3 = R_1^3$, $R_4 = R_1^4$, $R_5 = R_1^5$. Taking into account the identity operation $\mathcal{E}$ as symmetry as well, the point group of this sample is therefore C_{6v} (symmetry group of the hexagon)

$$\text{point group} = C_{6v} = \{M_1, M_2, M_3, M_4, M_5, M_6, R_1, R_2, R_3, R_4, R_5, \mathcal{E}\}.$$

initially	1	2	3	4	5	6	7	8	9	10	11	12
R_1	2	3	7	8	9	1	11	12	4	5	6	10

Table A.6: Action of the rotation operation R_1.

The little group of the allowed momenta – i.e. those among the point group operations leaving these momenta invariant – is

$$\begin{aligned}
\mathcal{G}_{\mathbf{k}_1} &= \{M_1, M_2, M_3, M_4, M_5, M_6, R_1, R_2, R_3, R_4, R_5, \mathcal{E}\} = C_{6v} \\
\mathcal{G}_{\mathbf{k}_2} &= \{M_2, M_4, R_3, \mathcal{E}\} = C_{2v} \\
\mathcal{G}_{\mathbf{k}_3} &= \{M_3, M_5, R_3, \mathcal{E}\} = C_{2v} \\
\mathcal{G}_{\mathbf{k}_4} &= \{M_1, M_6, R_3, \mathcal{E}\} = C_{2v}
\end{aligned}$$

Thus, only the zero-momentum sector has the full C_{6v} group as little group. For other momenta sectors, the little group is C_{2v}, which is a subgroup of C_{6v}. Once the little groups are found, one refers to a book on group theory for finding the characters.

For $\mathbf{k}_1$

The little group C_{6v} divides into 6 classes[6], namely

$$\begin{aligned}
3\sigma_v &= \{M_1, M_2, M_3\} \\
3\sigma_d &= \{M_4, M_5, M_6\} \\
2C_6 &= \{R_1, R_5\} \\
2C_3 &= \{R_2, R_4\} \\
C_2 &= \{R_3\} \\
E &= \{\mathcal{E}\}
\end{aligned}$$

with the characters in Table A.7, where the Γ_i denote the different representations. The last two representations have dimension 2. In order to perform ED, it is requested to deal with one-dimensional representations only. For circumventing this problem, both Γ_5 and Γ_6 can actually be split into two one-dimensional representations by reducing the considered symmetry group from C_{6v} down to C_6 (i.e. by discarding the reflectional symmetries). The characters of C_6 are given in Table A.8.

[6]Elements A and B in a group belong to the same class if there exists an element R in this group such that $A = R^{-1}BR$.

	E	C_2	$2C_3$	$2C_6$	$3\sigma_d$	$3\sigma_v$
Γ_1	1	1	1	1	1	1
Γ_2	1	1	1	1	-1	-1
Γ_3	1	-1	1	-1	-1	1
Γ_4	1	-1	1	-1	1	-1
Γ_5	2	-2	-1	1	0	0
Γ_6	2	2	-1	-1	0	0

Table A.7: Characters of the C_{6v} group.

	E	C_6	C_3	C_2	C_3^2	C_6^5
$\Gamma_{1'}$	1	1	1	1	1	1
$\Gamma_{2'}$	1	-1	1	-1	1	-1
$\Gamma_{3'}$	1	ω	ω^2	ω^3	ω^4	ω^5
$\Gamma_{4'}$	1	ω^5	ω^4	ω^3	ω^2	ω
$\Gamma_{5'}$	1	ω^2	ω^4	ω	ω^2	ω^4
$\Gamma_{6'}$	1	ω^4	ω^2	ω	ω^4	ω^2

$\omega := e^{i\frac{2\pi}{6}}$

Table A.8: Characters of the C_6 group.

Fig. A.5 illustrates how C_6 and C_{6v} are related one to another. $\Gamma_{1'}$ splits into Γ_1 and Γ_2, and $\Gamma_{2'}$ splits into Γ_3 and Γ_4 (in both cases characters are identical for the classes E, C_2, C_3 and C_6 that are shared by both C_6 and C_{6v}, and additional characters are considered for the reflections).

Reciprocally, if the reflections are additionally assumed in the C_6 group[7] (which is actually the case, even though they have been put aside for a while, these reflections do exist), representations $\Gamma_{3'}$ and $\Gamma_{4'}$, as well as $\Gamma_{5'}$ and $\Gamma_{6'}$ of C_6 as identical. By summing the elements of $\Gamma_{3'}$ and $\Gamma_{4'}$, we recover Γ_5, and by summing those of $\Gamma_{5'}$ and $\Gamma_{6'}$, we recover Γ_6. Therefore as depicted in Fig. A.5, the two-dimensional representation Γ_5 can be replaced by the one-dimensional representations $\Gamma_{3'}$ and $\Gamma_{4'}$ (which will have the same spectrum due to the reflectional symmetries) for investigations, and Γ_6 can be replaced by $\Gamma_{5'}$ and $\Gamma_{6'}$ (with the same spectrum again).

For investigating the $\mathbf{k}_1$ momentum sector, ED must thus be performed in IRREPs $[\mathbf{k}_1, \Gamma_1]$, $[\mathbf{k}_1, \Gamma_2]$, $[\mathbf{k}_1, \Gamma_3]$, $[\mathbf{k}_1, \Gamma_4]$, $[\mathbf{k}_1, \Gamma_{3'}]$, and $[\mathbf{k}_1, \Gamma_{5'}]$: 6 subspaces have to be considered.

Individual characters arising from translational operations (always 1 in the case of $\mathbf{k}_1$) and from point group operations are multiplied one with another to give the resulting char-

[7] This amounts to assuming the existence of the $\mathbf{k} \to -\mathbf{k}$ (or $\omega \to \omega^*$) symmetry.

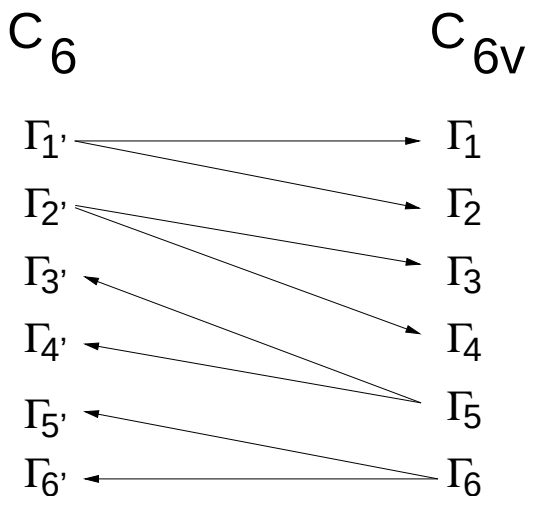

Figure A.5: Relations between the representations of the C_6 group and those of the C_{6v} group.

acter of the resulting space group operation. The character of $[\mathbf{k}_1, \Gamma_3]$ w.r. to operation $T_{\mathbf{a}_1} R_2$ for instance is $1 \cdot 1 = 1$ (refer to Tables A.4 and A.7).

For $\mathbf{k}_2$, $\mathbf{k}_3$, and $\mathbf{k}_4$

The little group (C_{2v}) of those momenta has 4 classes

$$\sigma_v = \{M_2\}$$
$$\sigma_{v'} = \{M_4\}$$
$$C_2 = \{R_3\}$$
$$E = \{\mathcal{E}\}$$

with the characters given in Table A.9. Since all the representations of C_{2v} have dimension

	σ_v	$\sigma_{v'}$	C_2	E
Γ_1	1	1	1	1
Γ_2	1	-1	-1	1
Γ_3	1	1	-1	-1
Γ_4	1	-1	1	-1

Table A.9: Characters of the C_{2v} group.

1, characters in Table A.9 can directly be used for performing ED.

The energy spectra of these last 3 momenta sectors are degenerate (the momenta can be mapped one onto another with rotation operations), it is therefore enough to investigate for instance the $\mathbf{k}_2$ sector only. ED must hence be performed in the IRREPs $[\mathbf{k}_2, \Gamma_1]$, $[\mathbf{k}_2, \Gamma_2]$, $[\mathbf{k}_2, \Gamma_3]$, and $[\mathbf{k}_2, \Gamma_4]$.

Individual characters arising from translational operations and from point group operations are multiplied one with another to give the resulting character of the resulting space group operation. The character of $[\mathbf{k}_2, \Gamma_3]$ w.r. to operation $T_{\mathbf{a}_2} M_4$ for instance is $(-1) \cdot 1 = -1$ (refer to Tables A.4 and A.9).

A.1.4 Concluding discussion on symmetries

Once the characters of every IRREP are determined for every symmetry operation, one constructs a basis made of "Bloch states" in the spirit of Eq. (A.1) for every globally invariant subspace (IRREP). The hamiltonian under study thus has to be diagonalized in every individual subspace, which is a much easier numerical task than performing the diagonalization in the total Hilbert space.

A.1.5 The Lanczos algorithm

(C. Lanczos, 1950 [172])

The Lanczos algorithm consists of starting from an initial random vector $|\psi_1\rangle$[8], and iteratively building an orthonormal basis $\{|\psi_1\rangle, |\psi_2\rangle, |\psi_3\rangle, ...\}$ (spanning the so-called Krylov subspace) of the Hilbert space in which H is tridiagonal. This new basis is recursively determined by the relations

$$\begin{aligned} \alpha_n &:= \langle \psi_n | H | \psi_n \rangle \\ \beta_n &:= \langle \psi_n | H | \psi_{n-1} \rangle \\ \beta_{n+1} |\psi_{n+1}\rangle &:= H|\psi_n\rangle - \alpha_n |\psi_n\rangle - \beta_n |\psi_{n-1}\rangle \qquad \text{for } n = 1, 2, 3, ..., \end{aligned}$$

where $|\psi_0\rangle := \mathbf{0}$. After the n^{th} step, the projection H_n of H onto the subspace spanned by the basis vectors $\{|\psi_1\rangle, |\psi_2\rangle, |\psi_3\rangle, ..., |\psi_n\rangle\}$ is given by the (real and symmetric) tridiagonal

[8] This initial random vector must be chosen inside the symmetry sector that is investigated.

matrix

$$H_n = \begin{pmatrix} \alpha_1 & \beta_2 & 0 & \dots & 0 \\ \beta_2 & \alpha_2 & \beta_3 & \ddots & \vdots \\ 0 & \beta_3 & \alpha_3 & \ddots & 0 \\ \vdots & \ddots & \ddots & \ddots & \beta_n \\ 0 & \dots & 0 & \beta_n & \alpha_n \end{pmatrix}$$

that is numerically much more efficiently diagonalized than a general matrix. Note that at the n^{th} step, only the non-zero matrix elements of H_n as well as the three vectors $|\psi_{n-1}\rangle$, $|\psi_n\rangle$, and $|\psi_{n+1}\rangle$ need to be stored.

The spectrum of the growing tridiagonal matrix H_n progressively converges to the spectrum of H, but the interest of this method resides in the fact that the extremal eigenvalues converge first. In particular, the lowest eigenvalue of the tridiagonal matrices H_n converges exponentially fast to the true ground state energy. The two first eigenvalues of a matrix of size 10^6 are typically obtained with the machine accuracy in about only 100 iterations. Notice that the accumulation of rounding errors can produce spurious eigenvalues of the tridiagonal matrices.

With the present day limits one can compute in the absence of magnetic field ($S^z_{\text{tot}} = 0$) low-energy spectra of spin-1/2 2D systems containing typically about forty spins using the space group symmetries. For that purpose, numerical diagonalizations have to be performed within subspaces spanned by about 2 billion basis states (a higher number of basis states can be taken into account if the symmetries are not used). Of course in elevated magnetization sectors ($S^z_{\text{tot}} \lesssim N/2$, where N is the total number of spins) much larger samples become numerically tractable. Note that its size is not the only criterion coming into play for selecting a sample, one must also take care that the selected sample is indeed commensurate with the momentum sector(s) one wishes to investigate. Whether this is the case or not is also influenced by the choice of the type of closed boundary conditions (periodic, twisted).

A.2 Density matrix renormalization group (DMRG)

(S.R. White, 1992 [175])

DMRG is a numerical technique for finding accurate approximations to the ground state and low-lying states of strongly interacting quantum lattice systems. Since its inception by S.R. White in 1992, DMRG has quickly achieved the status of a highly reliable, precise, and versatile numerical method in the field. It is remarkable in the accuracy that can be achieved for one-dimensional systems with open boundary conditions. For example, the

ground state energy of the spin-1 antiferromagnetic Heisenberg chain on lattices of hundreds of sites can be calculated to an accuracy of order 10^{-12} with a modest amount of computational effort [176].

In order to understand DMRG, it is useful to first introduce the *Wilson renormalization group* (RG) procedure [177]. Consider a one-dimensional quantum lattice model, and isolate a portion of the system containing L sites. Here, L is chosen to be small enough so that the corresponding hamiltonian H_L can be diagonalized exactly. The Wilson RG procedure then proceeds as follows:

1. Diagonalize H_L numerically, obtaining the m lowest eigenvalues (discard the largest ones) and eigenvectors.

2. Transform H_L and other operators in the "block" of length L to a new basis consisting of the m lowest eigenvectors of H_L, i.e. form $\bar{H}_L := O_L^\dagger H_L O_L$, $\bar{A}_L := O_L^\dagger A_L O_L$, etc..., where the columns of O_L contain the m lowest eigenvectors of H_L, and A_L is an arbitrary operator in the block. Note that $\bar{H}_L$ is a diagonal $m \times m$-matrix.

3. Add a site to $\bar{H}_L$ to form H_{L+1}. In order to do this, the interaction between the block of length L and the additional site added must be reconstructed.

4. Repeat starting with step 1, substituting H_{L+1} for H_L.

The scheme is depicted pictorially in Fig. A.6. Typically, the number of states m kept at

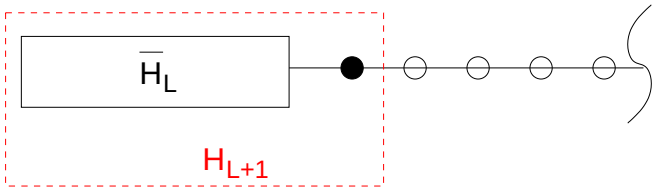

Figure A.6: Scheme of the Wilson numerical RG procedure.

each step is held constant, so the time and memory required for each diagonalization stays the same. The basic idea of this scheme is that only the low-energy eigenstates obtained for a system of size L will be important in making up the low-energy states of a system of size $L+1$. We do not want to go into details, but it turns out that because of problems due to the boundary conditions, the Wilson RG procedure breaks down for interacting quantum lattice systems[9].

[9]The Wilson RG procedure is on the other side very accurate for studying Kondo and Anderson impurity problems.

Tracing its roots to Wilson's RG, DMRG algorithms consider a *system block* of growing size, which is embedded in some *environment* mimicking the thermodynamic limit system. The system block and the environment block together form the so-called *superblock*, that has the total length of the chain investigated. In contrast to the Wilson RG procedure, the m states we use for projecting the growing hamiltonian matrix are no longer given by the lowest-lying eigenstates of the growing hamiltonian matrix itself, they instead correspond to the eigenstates of the reduced density matrix of the system block with the m highest eigenvalues (i.e. the m most "relevant" eigenstates)[10]. The environment block mimics the thermodynamic limit system in the sense that the reduced density matrix of the system block is obtained by first computing the density matrix of the entire superblock, and then tracing out the degrees of freedom of the environment. We shall call the superblock state used to form the reduced density matrix for the system block *target state*[11].

There are two classes of algorithms, depending on how the environment block is chosen to form the superblock: the *infinite system algorithm* (the size of the superblock – i.e. the chain size – progressively increases), and the *finite system algorithm* (the size of the superblock is held constant). Note that for a given system size L, the finite system algorithm almost always gives substantially more accurate results than the infinite system algorithm, and is therefore usually preferred unless there is a specific reason to go to the thermodynamic limit.

A.2.1 The infinite system algorithm

The infinite system algorithm is the most straightforward extension of the Wilson RG procedure described above (the system being diagonalized grows at each step) that incorporates the superblock concept. We build up the system block one site at a time, just as in the Wilson procedure, but must choose some sort of environment block. The simplest way of forming the environment block is to use a reflection of the system block (thus both have the same size l). The superblock configuration is shown in Fig. A.7. Here, $\bar{H}_l$ is the hamiltonian for the system block in the reduced basis, and the solid dots represent single sites. The right environment block $\bar{H}_l^R$ is formed by relabelling the sites in the system block $\bar{H}_l$ so that they are reflected onto the right part of the lattice. The size of the superblock is $L = 2l + 2$. The infinite system algorithm then proceeds as follows:

1. Form a superblock H_L^{super} containing L sites which is small enough to be exactly diagonalized.

[10]The sum of the discarded eigenvalues of the density matrix of the system block is called *discarded weight*. The smaller the discarded weight, the better the approximation.

[11]The target states may also consist of more than one state, but for simplicity we assume that only the ground state is targeted.

2. Diagonalize H_L^{super} numerically (for instance with the Lanczos or the Davidson algorithm), obtaining the targeted ground state $|\psi\rangle$.

3. Form the reduced density matrix ρ_{l+1} for the new system block from $|\psi\rangle$ by tracing out the degrees of freedom of the environment. Note that $l+1 = L/2$.

4. Diagonalize ρ_{l+1} with a dense matrix diagonalization routine to obtain the m eigenvectors with the largest eigenvalues.

5. Construct H_{l+1} and other operators in the new system block and transform them to the reduced density matrix eigenbasis using $\bar{H}_{l+1} := O_{l+1}^{\dagger} H_{l+1} O_{l+1}$, $\bar{A}_{l+1} := O_{l+1}^{\dagger} A_{l+1} O_{l+1}$, etc..., where the columns of O_{l+1} contain the m highest eigenvectors of ρ_{l+1}, and A_{l+1} in an operator in the system block.

6. $\bar{H}_{l+1}^{R}$ is given by the reflection of $\bar{H}_{l+1}$.

7. Construct H_{L+2}^{super} (corresponding to a superblock of size $L+2$) using $\bar{H}_{l+1}$, two single sites and $\bar{H}_{l+1}^{R}$.

8. Repeat starting with step 2, substituting H_{L+2}^{super} for H_L^{super}.

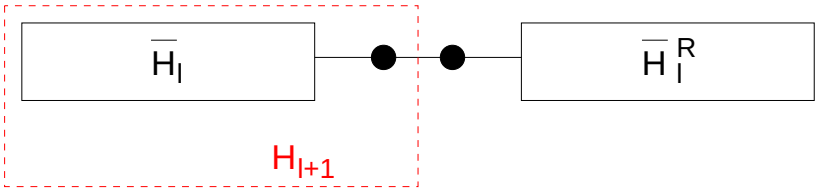

Figure A.7: The superblock configuration for the infinite system algorithm.

Note that the size of the superblock (i.e. the length of the chain we study) grows by two sites rather than one site at every step.

A.2.2 The finite system algorithm

The idea of the finite system algorithm is to stop the infinite system algorithm at some preselected superblock length L which is kept fixed, i.e. $L = l + l' + 2$ is fixed, (l and l' denote the respective size of each block, which are no longer identical in contrast to the infinite system algorithm). Instead of simultaneous growth of both blocks, growth of one block is accompanied by shrinkage of the other block. Reduced basis transformations are carried only for the growing block.

Suppose that we have run the infinite system algorithm until the superblock reaches size L, but have stored all the $\bar{H}_l$ (or $\bar{H}^R_{l'}$) for $l = l' = 1, ..., L/2 - 1$ as well as all the additional operators needed to connect the blocks at each step. We can then continue to build up the system block, but keep $L = l + l' + 2$ fixed by using the appropriate previously stored $\bar{H}^R_{l'}$. The finite system algorithm then proceeds as follows:

1. Carry out the infinite system algorithm until the superblock reaches size L, storing $\bar{H}_l$ and the operators needed to connect the blocks at each step.
2. Carry out steps 3 to 5 of the infinite system algorithm to obtain $\bar{H}_{l+1}$. Store it. Now $l \neq l'$.
3. Form a superblock of size L using $\bar{H}_{l+1}$, two single sites, and $\bar{H}^R_{l'-1}$. The superblock configuration is now given by Fig. A.8, where $l' = L - l - 2$.
4. Repeat steps 2 to 3 until $l = L - 3$ (i.e. l' has decreased down to 1). This is the *left to right* phase of the algorithm, with increasing l and decreasing l'.
5. Carry out steps 3 to 5 of the infinite system algorithm, reversing the roles of $\bar{H}_l$ and $\bar{H}^R_{l'}$, i.e. switch directions to build up the right block and obtain $\bar{H}^R_{l'+1}$. Store it.
6. Form a superblock of size L using $\bar{H}_{l-1}$, two single sites, and $\bar{H}^R_{l'+1}$.
7. Repeat steps 5 to 6 until $l = 1$ (i.e. l' has increased up to $L - 3$). This is the *right to left* phase of the algorithm, with decreasing l and increasing l'.
8. Repeat starting with step 2.

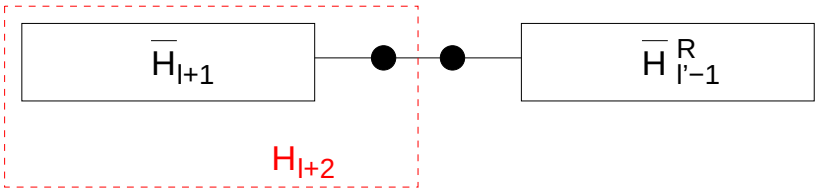

Figure A.8: The superblock configuration at step 3 of the procedure in the left to right phase of the finite system algorithm.

A useful analogy is to think of this procedure as being like running a zipper repeatedly from left to right and then right to left through a superblock that is always the same size. Each time the zipper changes direction, a new set of stored blocks is used as the environment block. In this way, the representations of the stored blocks are iteratively improved and the zipping can be repeated until convergence is reached. A complete shrinkage and growth sequence for both blocks is called a *sweep*.

APPENDIX B

Important theorems in condensed matter physics

B.1 Theorems stating the existence of gapless excitations

The more general theorem stating the existence of gapless modes is due to Goldstone in the early 1960s, and has applications in various fields of physics.

The first theorem focused on condensed matter physics is due to Lieb, Schultz, and Mattis in 1961, and predicts the existence of gapless excitations in 1D systems. It has been generalized by Oshikawa, Yamanaka and Affleck in 1997 for 1D systems in a magnetic field, and generalized again in 2004 to higher dimensional systems by Hastings.

The Goldstone theorem

(Goldstone, 1961 [164]; Lange, 1986 [165])

Consider a system of N spins, and the hamiltonian $H = \sum_{i,j} J_{ij} \mathbf{S}_i \cdot \mathbf{S}_j$ with short-range

interactions that obey

$$\lim_{N\to\infty} \frac{1}{N} \sum_{i,j} |J_{ij}||\mathbf{x}_i - \mathbf{x}_j|^2 < \infty$$

where $\mathbf{x}_i$ is the location of spin $\mathbf{S}_i$. If a continuous symmetry is broken and the spin structure factor diverges at some wave vector $\mathbf{q}$, then there exists a Goldstone mode whose energy vanishes at momentum $\mathbf{q}$.

The Lieb-Schultz-Mattis theorem

(Lieb, Schultz, and Mattis, 1961 [166]; generalized by Affleck and Lieb, 1986 [167])

An antiferromagnetic periodic chain of length L with half-odd integer spins ($S = 1/2, 3/2, \cdots$) in the unit cell either have gapless excitations (with energy $\mathcal{O}(1/L)$), or degenerate ground states which spontaneously break the translational invariance, in the thermodynamic limit.

The Oshikawa-Yamanaka-Affleck theorem

(Oshikawa, Yamanaka, and Affleck, 1997 [168])

Any hamiltonian of a spin-S chain of length L, including a magnetic field term, with short-range interactions, which is invariant under rotation about z-axis and either reflexion about a link or time reversal has at least one excited state with energy $\mathcal{O}(1/L)$ and momentum $2\pi(S - m)$, where $m := (1/L)\sum_{i=1}^{L} S_j^z$ is the magnetization per site. This statement does not hold for integer $S - m$.

The Hastings theorem

(Hastings, 2004 [169])

Consider a d-dimensional spin system with a half-odd integer spin in the unit cell, with finite range, $SU(2)$ invariant hamiltonian. Define the total number of unit cells in the lattice to be V. Let L be the (even) number of unit cells in one particular direction; this direction will be referred to as the length direction. Let the system be periodic and translationally invariant in the length direction. Let V/L^d be bounded by an arbitrary constant r. Define V/L to be the "width" of the system, and let this number be odd. Then if the ground state is unique, the gap to the first excited state behaves as $\mathcal{O}\left(\ln(L)/L\right)$, i.e. vanishes in the thermodynamic limit.

B.2 Other useful theorems

The Mermin-Wagner theorem – which prohibits a continuous symmetry to be spontaneously broken at zero temperature in 1D, and at finite temperature in 1D and 2D – is particularly important.

The Mermin-Wagner theorem

(Mermin and Wagner, 1966 [170])

Consider a system of N spins, and the hamiltonian $H(h) = \sum_{i,j} J_{ij}\mathbf{S}_i \cdot \mathbf{S}_j - hS^z_{\mathbf{q}}$ (including a magnetic field term) with short-range interactions that obey

$$\lim_{N\to\infty} \frac{1}{N} \sum_{i,j} |J_{ij}||\mathbf{x}_i - \mathbf{x}_j|^2 < \infty$$

where $\mathbf{x}_i$ is the location of spin $\mathbf{S}_i$, and $S^z_{\mathbf{q}} := \sum_i e^{i\mathbf{q}\cdot\mathbf{x}_i} S^z_i$ is the spin density wave in the z direction. There is then no spontaneously broken spin symmetry in 1D and 2D at finite temperature, and in 1D at zero temperature, i.e. in those cases we have

$$\lim_{h\searrow 0} \quad \lim_{N\to\infty} m_{\mathbf{q}}(h, N) = 0 \qquad \forall \mathbf{q},$$

where $m_{\mathbf{q}}(h, N) := \frac{\mathrm{Tr}\left[e^{-H(h)/(k_B T)}\left(S^z_{\mathbf{q}}/N\right)\right]}{\mathrm{Tr}\left[e^{-H(h)/(k_B T)}\right]}$ is the magnetization per site.

The Lieb-Mattis theorem

(Lieb and Mattis, 1962 [171])

Consider a Heisenberg hamiltonian $H = \sum_{i,j} J_{i,j}\mathbf{S}_i \cdot \mathbf{S}_j$ on a lattice which can be divided into sublattices A and B in such a way that for all sites $\{i(A)\}$ of sublattice A and $\{i(B)\}$ of sublattice B, there exists a constant $g^2 \geq 0$ such that

$$J_{i(A),j(A)} \leq g^2, \qquad J_{i(B),j(B)} \leq g^2, \qquad \text{and} \qquad J_{i(A),j(B)} \geq g^2,$$

$S_A := \sum_{i(A)} S_{i(A)}$ ($S_B := \sum_{i(B)} S_{i(B)}$) is the maximum possible spin value on sublattice A (B). Then if $E_{\mathrm{GS}}(S)$ denotes the lowest energy eigenvalue belonging to total spin sector S, we have

$$E_{\mathrm{GS}}(S+1) > E_{\mathrm{GS}}(S) \qquad \forall S \geq |S_A - S_B|,$$

meaning that the ground state of H belongs *at most* to total spin $S = |S_A - S_B|$, and

$$E_{\mathrm{GS}}(S) > E_{\mathrm{GS}}(|S_A - S_B|) \qquad \forall S < |S_A - S_B| \text{ if } g^2 = 0.$$

APPENDIX C

Classical vs quantum spin-multipolar correlations in the UDRVB state

In Subsection 2.3.2 of Chapter 2, a *qualitative* comparison was performed between the spin-multipolar correlations in the UDRVB state (which is the singlet ground state of the frustrated ferromagnetic spin-1/2 Heisenberg chain at the Lifshitz point $J_2/J_1 = -1/4$) and the spin-multipolar correlations in a classical spiral with propagation vector $q = 2\pi/L$. We learnt that the propagation vector of both types of correlations agree, among other things. This appendix is devoted to a more *quantitative* comparison.

Since the p-multipolar correlations in Fig. 2.4 are computed in singlet states (the UDRVB), they are identical for the $2p + 1$ components of the $SU(2)$ multipolar tensorial operator of rank p. The quantitative comparison we wish to perform here is hence valid only if classical correlations are computed between $SU(2)$ invariant objects. We shall therefore construct the classical analogues of the multipolar operators, and restore their $SU(2)$ invariance "on average" by deriving their $2p + 1$ components and contracting them together.

The $SU(2)$ p-multipolar tensorial operator acting on p sites is given by the tensorial operator of rank $Q = p$ acting on those p sites[1]. For $p = Q = 1$, one can check that the dipolar

[1]In the case of spins $S = 1/2$, p-multipolar order can only be detected via operators that act on p sites at least. This is no longer true for $S > 1/2$.

tensorial operator (with Frobenius-orthonormalized components) is

$$T_i(1,q) = (S_i^-, \sqrt{2}S_i^z, -S_i^+). \tag{C.1}$$

For $p = Q = 2, 3, 4, ...$, the tensorial multipolar operators can be derived iteratively using Eq. (C.1) and the formula

$$T(Q,q) \propto (-1)^{Q-q} \sum_{q_1=-Q_1}^{Q_1} \sum_{q_2=-Q_2}^{Q_2} T'(Q_1,q_1)T''(Q_2,q_2) \begin{pmatrix} Q_1 & Q_2 & Q \\ q_1 & q_2 & -q \end{pmatrix}, \tag{C.2}$$

(Wigner $3j$-symbols have been used) allowing to construct a tensor $T(Q,q)$ of rank Q ($q = -Q, -Q+1, \cdots, Q$) from two tensors $T'(Q_1,q_1)$ and $T''(Q_2,q_2)$ of respective ranks Q_1 and Q_2 ($q_1 = -Q_1, -Q_1+1, \cdots, Q_1$ and $q_2 = -Q_2, -Q_2+1, \cdots, Q_2$) as long as the triangular inequality $|Q_1 - Q_2| \leq Q \leq Q_1 + Q_2$ holds. The positive proportionality constant in Eq. (C.2) is chosen such that the $2Q+1$ components of T are Frobenius-orthonormalized[2]. Since multipolar operators whose correlations are shown in Fig. 2.4 are Frobenius-orthonormalized as well, a quantitative comparison is possible.

Using Eqs. (C.1) and (C.2), we derive the components of the quadrupolar operator

$$T_{i,j}(2,q) = \left(S_i^- S_j^-, S_i^- S_j^z + S_i^z S_j^-, -\frac{1}{\sqrt{6}}(S_i^- S_j^+ + S_i^+ S_j^- - 4S_i^z S_j^z), -S_i^+ S_j^z - S_i^z S_j^+, S_i^+ S_j^+ \right)$$

note that component q is a raising operator which changes S^z_{tot} by q. By contracting all components[3], substituting $S_l^\pm \to S_l^x \pm iS_l^y$ and replacing the quantum spins by a classical spiral

$$\mathbf{S}_l = S \begin{pmatrix} \cos(ql) \\ \sin(ql) \\ 0 \end{pmatrix}$$

(which amounts to Eq (2.5) with $\vartheta \to 0$, we do not consider the effect of a magnetic field in this particular case), we get for the dipolar and the quadrupolar correlators respectively

$$\frac{1}{3}\sum_{q=-1}^{1} T_1(1,q)T_{1+r}^\dagger(1,q) \to \frac{S^2}{3} \cdot 2\cos(qr),$$

[2]Components of a rank-p multipolar operator are Frobenius-orthonormalized if $\text{Tr}\left[T(Q,q)T^\dagger(Q,q')\right] = \delta_{q,q'}$.

[3]We contract the components of a rank-Q tensor by summing the correlators between each of its $2Q+1$ components, and dividing the result by $2Q+1$ in order to get an "averaged $SU(2)$ correlator" which can be compared to Fig. 2.4).

and

$$\frac{1}{5}\sum_{q=-2}^{2} T_{1,2}(2,q)T^{\dagger}_{1+r,2+r}(2,q) \rightarrow \frac{S^4}{5}\left[2\cos(2qr)+\frac{2}{3}\cos^2(q)\right].$$

Following the same way for the octupolar and hexadecupolar correlators, we find

$$\frac{1}{7}\sum_{q=-3}^{3} T_{1,2,3}(3,q)T^{\dagger}_{1+r,2+r,3+r}(3,q) \rightarrow \frac{S^6}{7}\left\{2\cos(3qr)+\frac{2}{15}\cos(qr)\left[1+2\cos(2q)\right]^2\right\}$$

$$\frac{1}{9}\sum_{q=-4}^{4} T_{1,2,3,4}(4,q)T^{\dagger}_{1+r,2+r,3+r,4+r}(4,q) \rightarrow \frac{S^8}{9}\left\{2\cos(4qr)+\frac{2}{7}\cos(2qr)\left[\cos(q)+\cos(3q)\right]^2 + \frac{2}{35}\left[1+\cos(2q)+\cos(4q)\right]\right\}.$$

Note that if p is even the p-multipolar correlator has only even harmonics in qr, while if p is odd it has only odd harmonics in qr. The first harmonic in every case is given in Eq. (2.7).

Replacing q by the propagation vector of spin correlations $q \rightarrow 2\pi/L$ [see Eq. (2.8)] and the spin by $S \rightarrow 1/2$, we have

For the **dipolar correlations**

$$\frac{1}{3}\sum_{q=-1}^{1} T_{1}(1,q)T^{\dagger}_{1+r}(1,q) \rightarrow \frac{1}{6}\cos\left(\frac{2\pi}{L}r\right), \tag{C.3}$$

for the **quadrupolar correlations**

$$\frac{1}{5}\sum_{q=-2}^{2} T_{1,2}(2,q)T^{\dagger}_{1+r,2+r}(2,q) \rightarrow \frac{1}{40}\cos\left(\frac{2\pi}{L}2r\right)+\frac{1}{120}\cos^2(q), \tag{C.4}$$

for the **octupolar correlations**

$$\frac{1}{7}\sum_{q=-3}^{3} T_{1,2,3}(3,q)T^{\dagger}_{1+r,2+r,3+r}(3,q) \rightarrow \frac{1}{224}\cos\left(\frac{2\pi}{L}3r\right)+\frac{1}{3360}\cos\left(\frac{2\pi}{L}r\right)\left[1+2\cos(2q)\right]^2, \tag{C.5}$$

and for the **hexadecupolar correlations**

$$\frac{1}{9}\sum_{q=-4}^{4} T_{1,2,3,4}(4,q)T^{\dagger}_{1+r,2+r,3+r,4+r}(4,q) \to \frac{1}{1152}\cos\left(\frac{2\pi}{L}4r\right) + \frac{1}{8064}\cos\left(\frac{2\pi}{L}2r\right)\left[\cos(q)+\cos(3q)\right]^2 + \frac{1}{40320}\left[1+\cos(2q)+\cos(4q)\right]. \quad \text{(C.6)}$$

Note that the above classical dipolar (spin) correlations Eq. (C.3) match the quantum ones Eq. (2.8) in the thermodynamic limit.

The quantitative comparison between spin-multipolar correlations of order $p = 1, 2, 3,$ and 4 [Eq. (2.3), Chapter 2] in the UDRVB state and their classical analogues [Eqs. (C.3), (C.4), (C.5), (C.6)] is performed in Fig. C.1 for various system sizes. We see that the agreement between the quantum correlations in the UDRVB state and those in the classical spiral is of course qualitatively good – as pointed out in Subsection 2.3.2 of Chapter 2 – but not only: the quantitative agreement is good as well. It is slightly less good at the local minima and maxima of the correlation curves in Fig. C.1 but notice that size effects are particularly strong at those points, which allows to guess that in the thermodynamic limit the quantum correlations will agree very well with the classical ones, and that remnants of the classical spiral are indeed still present in the quantum UDRVB state as pointed out in Subsection 2.3.2 of Chapter 2.

The agreement between classical and quantum multipolar correlations in large systems is particularly well illustrated by Fig. C.2, which shows the multipolar quantum correlations in the UDRVB state at maximal distance for the same system sizes as in Fig. C.1. Classical correlations are shown at $1/L = 0$ (thermodynamic limit). Classical and quantum p-multipolar correlations are rescaled – i.e. multiplied by a factor $1/S^{2p} = 2^{2p}$ [4] – along the y-direction in Fig. C.2. There is also a rescaling in the x-direction: the $1/L$ values of p-multipolar correlations are multiplied by p. We thus keep the same ratio between the wavelength of every multipolar correlator and the lattice spacing. Fig. C.2 exhibits a *data collapse*: with the rescaling we perform, the colored spots collapse onto a power law fit (solid black curve) $y \approx \mathcal{O}(x^{4.1})$. The agreement between the curve and the spots is excellent for $p = 1$ (black spots) and $p = 2$ (red spots), and fairly good for $p = 3$ (green spots) and $p = 4$ (blue spots).

[4] For a given system size, the $(p+1)$-multipolar correlation at maximal distance is roughly $2^2 = 4$ times as small as the p-multipolar correlation at maximal distance.

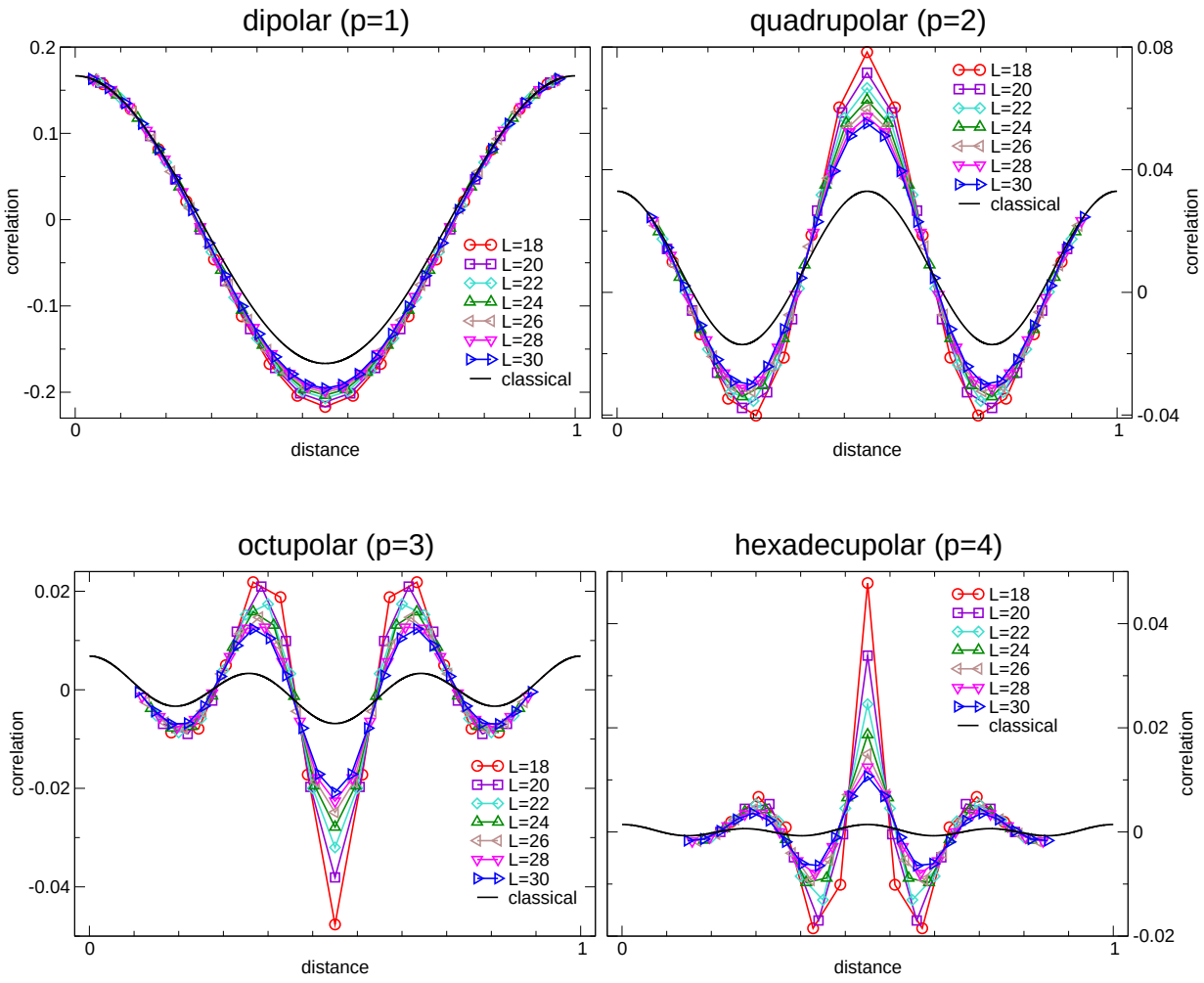

Figure C.1: The spin-multipolar correlations of order $p = 1, 2, 3$, and 4 [Eq. (2.3), Chapter 2] in the UDRVB state for system sizes ranging from $L = 18$ up to $L = 30$ (by ED, with periodic boundary conditions) are compared to the spin-multipolar correlations in a classical spiral with propagation vector $q = 2\pi/L$ [Eqs. (C.3), (C.4), (C.5), (C.6)]. The size of every system is normalized to one for the comparison.

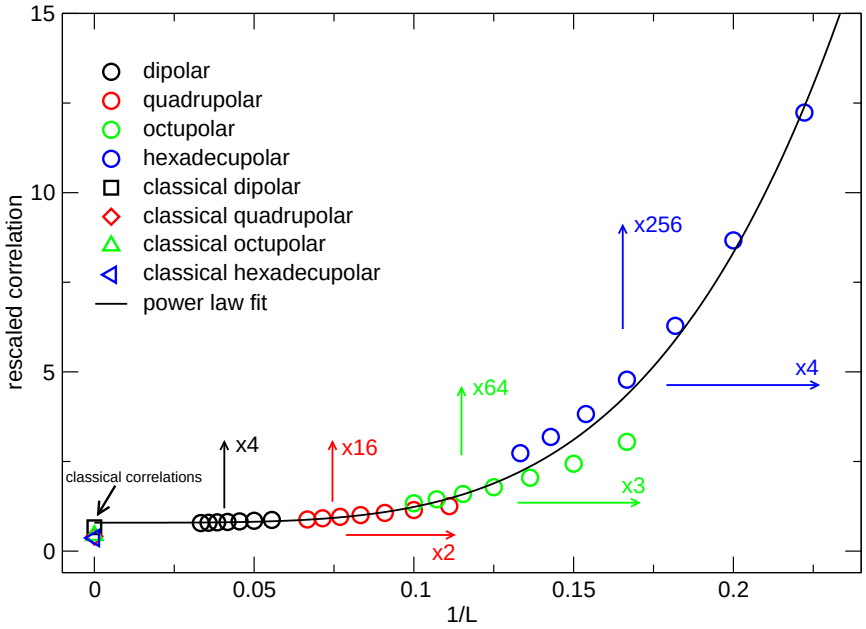

Figure C.2: The rescaled (by a factor 2^{2p}) p-multipolar correlations at maximal distance for various system sizes collapse onto a power law fit. The $1/L$ values are also rescaled – by a factor p – in order to keep the same ratio between the wavelength of every multipolar correlator and the lattice spacing. Classical correlations at maximal distance are shown at $1/L = 0$, they agree well with quantum correlations in large systems.

APPENDIX D

The correlation density matrix tool for extracting dominant correlations: proofs

For the sake of clarity, technical proofs have been skipped in Chapter 3. They are nevertheless important, and are therefore given in details in this appendix.

Proof of Eq. (3.3)

As in Subsection 3.2.2, we adopt for this proof the following convention: indices without prime symbol refer to block A, those with a prime symbol refer to block B, and commas separate the two indices of a matrix. Underlined indices that are not separated by a comma must be considered as fused indices. With the well known property of density matrices

$$\langle O_A O_B \rangle = \mathrm{Tr}_{(A\cup B)} \left[\rho_{A\cup B} O_A O_B \right]$$

and the individual averages (lower and upper bounds of summation indices are dropped for the sake of clarity, sums run from 1 up to $D^2 := \min\{\dim^2_{\mathcal{H}}(A), \dim^2_{\mathcal{H}}(B)\}$)

$$\begin{aligned}
\langle O_A\rangle\langle O_B\rangle &= \mathrm{Tr}_A\left[\rho_A O_A\right]\,\mathrm{Tr}_B\left[\rho_B O_B\right] = \mathrm{Tr}_{(A\cup B)}\left[\rho_{A\cup B} O_A \mathbb{1}_B\right]\,\mathrm{Tr}_{(A\cup B)}\left[\rho_{A\cup B}\mathbb{1}_A O_B\right] \\
&= \sum_{i,i',j,j'} \rho^{\underline{ii'},\underline{jj'}}_{A\cup B} O_A^{j,i} \underbrace{\mathbb{1}_B^{j',i'}}_{=\delta_{j',i'}} \sum_{\tilde{i},\tilde{i}',\tilde{j},\tilde{j}'} \rho^{\underline{\tilde{i}\tilde{i}'},\underline{\tilde{j}\tilde{j}'}}_{A\cup B} \underbrace{\mathbb{1}_A^{\tilde{j},\tilde{i}}}_{=\delta_{\tilde{j},\tilde{i}}} O_B^{\tilde{j}',\tilde{i}'} = \sum_{i,j,j'} \rho^{\underline{ij'},\underline{jj'}}_{A\cup B} O_A^{j,i} \sum_{\tilde{i}',\tilde{j},\tilde{j}'} \rho^{\underline{\tilde{j}\tilde{i}'},\underline{\tilde{j}\tilde{j}'}}_{A\cup B} O_B^{\tilde{j}',\tilde{i}'} \\
&= \sum_{i,j} \rho_A^{i,j} O_A^{j,i} \sum_{\tilde{i}',\tilde{j}'} \rho_B^{\tilde{i}',\tilde{j}'} O_B^{\tilde{j}',\tilde{i}'} = \sum_{i,j,\tilde{i}',\tilde{j}'} \rho_A^{i,j}\rho_B^{\tilde{i}',\tilde{j}'} O_A^{j,i} O_B^{\tilde{j}',\tilde{i}'} = \sum_{i,j,\tilde{i}',\tilde{j}'} [\rho_A\otimes\rho_B]^{\underline{i\tilde{i}'},\underline{j\tilde{j}'}} [O_A O_B]^{\underline{j\tilde{j}'},\underline{i\tilde{i}'}} \\
&= \sum_{i,\tilde{i}'} [\rho_A\otimes\rho_B O_A O_B]^{\underline{i\tilde{i}'},\underline{i\tilde{i}'}} = \mathrm{Tr}_{A\cup B}\left[\rho_A\otimes\rho_B O_A O_B\right],
\end{aligned}$$

we get Eq. (3.3)

$$\begin{aligned}
&\langle O_A O_B\rangle - \langle O_A\rangle\langle O_B\rangle = \mathrm{Tr}_{(A\cup B)}\left[\rho_{A\cup B} O_A O_B\right] - \mathrm{Tr}_{A\cup B}\left[\rho_A\otimes\rho_B O_A O_B\right] \\
&= \mathrm{Tr}_{(A\cup B)}\left\{\left[\rho_{A\cup B} - \rho_A\otimes\rho_B\right] O_A O_B\right\} = \mathrm{Tr}_{(A\cup B)}\left[\rho^c_{AB} O_A O_B\right].
\end{aligned}$$

∎

Proof of Eq. (3.10)

Let A and B be two disjoint blocks with the same size (number of sites) in a spin-S system, and let A' (B') consist of blocks A (B) plus one additional spin-S (each initial block is enlarged by one site), as shown in Fig. 3.2. Eq. (3.10) then states that the highest SV σ_1^{AB} of ρ^c_{AB} provides a lower bound for the highest SV $\sigma_1^{A'B'}$ of $\rho^c_{A'B'}$. Let us prove this statement. The SVD Eq. (3.6) of ρ^c_{AB} reads

$$\rho^c_{AB} = \sum_{i=1}^{D^2} \sigma_i^{AB} X_i^{(A)} Y_i^{(B)\dagger}.$$

where $D^2 := \min\{\dim^2_{\mathcal{H}}(A), \dim^2_{\mathcal{H}}(B)\}$. We define the extension $O^{(A')}$ and $O^{(B')}$ of the operators $X_1^{(A)}$ and $Y_1^{(B)}$ corresponding to the dominant SV σ_1^{AB} by

$$O^{(A')} := X_1^{(A)}\otimes\mathbb{1}_{A'\setminus A} \qquad \text{and} \qquad O^{(B')} := Y_1^{(B)}\otimes\mathbb{1}_{B'\setminus B}$$

where $A'\setminus A$ and $B'\setminus B$ contain the additional spins only. Eq. (3.8) yields the dominant correlation

$$\langle X_1^{(A)\dagger} Y_1^{(B)}\rangle - \langle X_1^{(A)\dagger}\rangle\langle Y_1^{(B)}\rangle = \sigma_1^{AB}$$

which must be unchanged w.r. to the extended operators

$$\langle O^{(A')\dagger} O^{(B')} \rangle - \langle O^{(A')\dagger} \rangle \langle O^{(B')} \rangle = \sigma_1^{AB}. \tag{D.1}$$

Neither $O^{(A')}$ nor $O^{(B')}$ are Frobenius-normalized, let us thus calculate the squared norm of $O^{(A')}$ (the reasoning is the same for the squared norm of $O^{(B')}$). We introduce an orthonormalized basis in block A

$$\{|a_1\rangle, |a_2\rangle, |a_3\rangle, \cdots |a_{\dim_{\mathcal{H}}(A)}\rangle\}.$$

In that basis, let us denote the $\dim_{\mathcal{H}}(A) \times \dim_{\mathcal{H}}(A)$ matrix of operator $X_1^{(A)}$ by

$$X_1^{(A)} \Leftrightarrow \left(\begin{array}{c} \square \end{array} \right).$$

We also introduce an orthonormalized basis in $A' \setminus A$ $[\dim_{\mathcal{H}}(A' \setminus A) = 2S+1)]$

$$\{|1\rangle, |2\rangle, |3\rangle, \cdots, |2S+1\rangle\}.$$

Then, the matrix of $O^{(A')}$ with respect to basis

$$\begin{array}{l} \{|a_1 \otimes 1\rangle, |a_2 \otimes 1\rangle, |a_3 \otimes 1\rangle, \cdots, |a_{\dim_{\mathcal{H}}(A)} \otimes 1\rangle, \\ |a_1 \otimes 2\rangle, |a_2 \otimes 2\rangle, |a_3 \otimes 2\rangle, \cdots, |a_{\dim_{\mathcal{H}}(A)} \otimes 2\rangle, \cdots, \\ |a_1 \otimes 2S+1\rangle, |a_2 \otimes 2S+1\rangle, |a_3 \otimes 2S+1\rangle, \cdots, \\ |a_{\dim_{\mathcal{H}}(A)} \otimes 2S+1\rangle\} \end{array}$$

will be $[\dim_{\mathcal{H}}(A) \cdot (2S+1)] \times [\dim_{\mathcal{H}}(A) \cdot (2S+1)]$ and will read

$$O^{(A')} = \left(\begin{array}{c|c|c|c} X_1^{(A)} & 0 & 0 & 0 \\ \hline 0 & X_1^{(A)} & 0 & 0 \\ \hline 0 & 0 & \ddots & 0 \\ \hline 0 & 0 & 0 & X_1^{(A)} \end{array} \right) \Leftrightarrow \left(\begin{array}{c|c|c|c} \square & 0 & 0 & 0 \\ \hline 0 & \square & 0 & 0 \\ \hline 0 & 0 & \ddots & 0 \\ \hline 0 & 0 & 0 & \square \end{array} \right).$$

This matrix has $2S+1$ blocks consisting of $X_1^{(A)}$. Hence,

$$\mathrm{Tr}\left(O^{(A')} O^{(A')\dagger} \right) = \mathrm{Tr}\left[\left(\begin{array}{c|c|c|c} \square\square^\dagger & 0 & 0 & 0 \\ \hline 0 & \square\square^\dagger & 0 & 0 \\ \hline 0 & 0 & \ddots & 0 \\ \hline 0 & 0 & 0 & \square\square^\dagger \end{array} \right) \right] = (2S+1) \cdot \mathrm{Tr}\left(X_1^{(A)} X_1^{(A)\dagger} \right) = 2S+1.$$

Both $O^{(A')}$ and $O^{(B')}$ have the squared Frobenius norm $2S+1$. Operators $\frac{1}{\sqrt{2S+1}}O^{(A')}$ and $\frac{1}{\sqrt{2S+1}}O^{(B')}$ are thus Frobenius-normalized, and there exists two sets of coefficients $\{c_i^{(A')}\}_i$ and $\{c_i^{(B')}\}_i$ with the constraints

$$\sum_{i=1}^{D'^2}\left|c_i^{(A')}\right|^2=1 \qquad \text{and} \qquad \sum_{i=1}^{D'^2}\left|c_i^{(B')}\right|^2=1$$

$[D'^2 := \dim^2_{\mathcal{H}}(A') = \dim^2_{\mathcal{H}}(B')]$ such that

$$\frac{1}{\sqrt{2S+1}}O^{(A')}=\sum_{i=1}^{D'^2}c_i^{(A')}\widetilde{X}_i^{(A')} \qquad \text{and} \qquad \frac{1}{\sqrt{2S+1}}O^{(B')}=\sum_{i=1}^{D'^2}c_i^{(B')}\widetilde{Y}_i^{(B')}, \tag{D.2}$$

where $\{\widetilde{X}_i^{(A')}\}_i$ and $\{\widetilde{Y}_i^{(B')}\}_i$ are the Frobenius-orthonormalized operators resulting from the SVD of the CDM between blocks A' and B'

$$\rho^c_{A'B'}=\sum_{i=1}^{D'^2}\sigma_i^{A'B'}\widetilde{X}_i^{(A')}\widetilde{Y}_i^{(B')\dagger}. \tag{D.3}$$

The fact that both blocks A' and B' have the same size (number of sites) ensures that the $\{\widetilde{X}_i^{(A')}\}_i$ and $\{\widetilde{Y}_i^{(B')}\}_i$ sets provide *complete* bases of the spaces of operators acting within A' and B' respectively – with $\min\{\dim^2_{\mathcal{H}}(A'),\dim^2_{\mathcal{H}}(B')\} = \dim^2_{\mathcal{H}}(A') = \dim^2_{\mathcal{H}}(B') = D'^2$ elements – and thus that decompositions Eq. (D.2) are possible. The connected correlator between $O^{(A')}$ and $O^{(B')}$ is

$$\begin{aligned}
&\left\langle\frac{1}{\sqrt{2S+1}}O^{(A')}\frac{1}{\sqrt{2S+1}}O^{(B')}\right\rangle-\left\langle\frac{1}{\sqrt{2S+1}}O^{(A')}\right\rangle\left\langle\frac{1}{\sqrt{2S+1}}O^{(B')}\right\rangle\\
&\overset{(3.3)}{=}\mathrm{Tr}\left(\rho^c_{A'B'}\frac{1}{2S+1}O^{(A')}O^{(B')}\right)\overset{(D.2)}{=}\mathrm{Tr}\left(\rho^c_{A'B'}\sum_{j,j'=1}^{D'^2}c_j^{(A')}c_{j'}^{(B')}\widetilde{X}_j^{(A')\dagger}\widetilde{Y}_{j'}^{(B')}\right)\\
&\overset{(D.3)}{=}\mathrm{Tr}\left(\sum_{i=1}^{D'^2}\sigma_i^{A'B'}\widetilde{X}_i^{(A')}\widetilde{Y}_i^{(B')\dagger}\sum_{j,j'=1}^{D'^2}c_j^{(A')}c_{j'}^{(B')}\widetilde{X}_j^{(A')\dagger}\widetilde{Y}_{j'}^{(B')}\right)\\
&=\sum_{i=1}^{D'^2}\sigma_i^{A'B'}\sum_{j,j'=1}^{D'^2}c_j^{(A')}c_{j'}^{(B')}\mathrm{Tr}\left(\widetilde{X}_i^{(A')}\widetilde{X}_j^{(A')\dagger}\right)\mathrm{Tr}\left(\widetilde{Y}_i^{(B')\dagger}\widetilde{Y}_{j'}^{(B')}\right)\overset{(3.7)}{=}\sum_{i=1}^{D'^2}\sigma_i^{A'B'}c_i^{(A')}c_i^{(B')}.
\end{aligned} \tag{D.4}$$

Finally, Eqs. (D.1) and (D.4) yield

$$\frac{\sigma_1^{AB}}{2S+1} = \sum_{i=1}^{D'^2} c_i^{(A')} c_i^{(B')} \sigma_i^{A'B'}.$$

The right term of the above equation is necessarily smaller than it would have been if the whole weight would have been given to the largest SV (i.e. $c_1^{(A')} = c_1^{(B')} = 1$ and $c_i^{(A')} = c_i^{(B')} = 0$ if $i > 1$), which can be written as

$$\frac{\sigma_1^{AB}}{2S+1} \leq \sigma_1^{A'B'}.$$

∎

APPENDIX E

Complete orthonormalized bases of operator spaces

The $X_i^{(A)}$'s and $Y_i^{(B)}$'s operators resulting from the singular value decomposition Eq. (3.6) in Chapter 3 can generally not be physically interpreted at first sight, and must be decomposed onto operators whose physical meaning is obvious. It is the aim of this appendix to provide complete orthonormalized[1] bases of the spaces spanned by the operators acting on two and three spins $S = 1/2$, and to explain how bases of operators acting in arbitrarily large blocks can be obtained.

E.1 Operators acting on two sites

Consider two blocks of two magnetic moments $S = 1/2$ which live in the space

$$\left(\frac{1}{2} \otimes \frac{1}{2}\right) \otimes \left(\frac{1}{2} \otimes \frac{1}{2}\right) = 0_2 \oplus 1_3 \oplus 2_1,$$

where the notation j_m means that the subspace of dimension $2j+1$ occurs m times in the Clebsch-Gordan decomposition. This space is thus the direct sum of two singlet subspaces

[1] With respect to the Frobenius scalar product $\left(\widehat{O}|\widehat{O'}\right)_F := \mathrm{Tr}\left(\widehat{O}\widehat{O'}^{\dagger}\right)$.

(providing two one-component operators), three triplet subspaces (providing three three-component operators), and one quintet subspace (providing one five-component operator). A complete orthonormalized basis of the space of operators acting on two spins-1/2 located at sites k and l is given in Table E.1. All of them can easily be guessed and understood,

operator	nb comp.	spin
$\frac{1}{2}\mathbb{1}_{kl}$	1	0
$\frac{2}{\sqrt{3}}\mathbf{S}_k \cdot \mathbf{S}_l$	1	0
$\frac{1}{\sqrt{2}}(\mathbf{S}_k + \mathbf{S}_l)$	3	1
$\frac{1}{\sqrt{2}}(\mathbf{S}_k - \mathbf{S}_l)$	3	1
$\sqrt{2}\mathbf{S}_k \times \mathbf{S}_l$	3	1
$\mathbf{Q}_{kl}$	5	2

Table E.1: Frobenius-orthonormalized basis of the space spanned by the operators acting on two spins $S = 1/2$ located at sites k and l.

apart from the quintet operator $\mathbf{Q}_{kl}$ (rank-2 tensor) whose components are derived using the formula Eq (C.2) of Appendix C: the two rank-1 tensors $T_k(1, q)$ and $T_l(1, q)$ of Eq. (C.1) are coupled into a rank-2 tensor $\mathbf{Q}_{kl}$ (quadrupolar object) which turns out to be given by

$$\mathbf{Q}_{kl} = \begin{pmatrix} S_k^- S_l^- \\ S_k^- S_l^z + S_k^z S_l^- \\ -\frac{1}{\sqrt{6}}(S_k^- S_l^+ + S_k^+ S_l^- - 4S_k^z S_l^z) \\ -S_k^+ S_l^z - S_k^z S_l^+ \\ S_k^+ S_l^+ \end{pmatrix}. \tag{E.1}$$

Note that $\mathbf{Q}_{kl}$ is symmetric under the $k \leftrightarrow l$ exchange.

E.2 Operators acting on three sites

Consider two blocks of three magnetic moments $S = 1/2$ which live in the space

$$\left(\frac{1}{2} \otimes \frac{1}{2} \otimes \frac{1}{2}\right) \otimes \left(\frac{1}{2} \otimes \frac{1}{2} \otimes \frac{1}{2}\right) = 0_5 \oplus 1_9 \oplus 2_5 \oplus 3_1,$$

that is the direct sum of five singlet subspaces (providing five one-component operators), nine triplet subspaces (providing nine three-component operators), five quintet subspaces (providing five five-component operators), and one septuplet subspace (providing one

seven-component operator). A complete orthonormalized basis of the space of operators acting on three spins-1/2 located at sites k, l, and m is given in Table E.2. The quintet $\mathbf{Q}_{klm}(i)$ and septuplet $\mathbf{Se}_{klm}$ operators are not explicitly given since they are complicated objects. For constructing them, one has to couple – using formula Eq. (C.2) – the rank-0 tensors $T_k(0,0)$, $T_l(0,0)$, and $T_m(0,0)$ defined by

$$T_i(0,0) = \frac{1}{\sqrt{2}} \mathbb{1}_i,$$

and the rank-1 tensors $T_k(1,q)$, $T_l(1,q)$, and $T_m(1,q)$ which were already defined in Eq. (C.1)

$$T_i(1,q) = (S_i^-, \sqrt{2}S_i^z, -S_i^+)$$

in all possible ways leading to a final rank-2 [for each of the $\mathbf{Q}_{klm}(i)$'s] or rank-3 [for $\mathbf{Se}_{klm}$] tensor.

Using the notation $(a_u \otimes b_v) \to c_{uv}$ for denoting a rank-a tensor acting in u that is coupled with a rank-b tensor acting in v into a rank-c tensor ($|a-b| \leq c \leq a+b$) acting in $u \cup v$ (u and v being ordered sets of sites), we have

$$\begin{aligned}
\mathbf{Q}_{klm}(1) \quad &\text{constructed by} \quad (1_k \otimes 1_l) \otimes 0_m \to 2_{kl} \otimes 0_m \to 2_{klm} \\
\mathbf{Q}_{klm}(2) \quad &\text{constructed by} \quad (0_k \otimes 1_l) \otimes 1_m \to 1_{kl} \otimes 1_m \to 2_{klm} \\
\mathbf{Q}_{klm}(3) \quad &\text{constructed by} \quad (1_k \otimes 0_l) \otimes 1_m \to 1_{kl} \otimes 1_m \to 2_{klm} \\
\mathbf{Q}_{klm}(4) \quad &\text{constructed by} \quad (1_k \otimes 1_l) \otimes 1_m \to 1_{kl} \otimes 1_m \to 2_{klm} \\
\mathbf{Q}_{klm}(5) \quad &\text{constructed by} \quad (1_k \otimes 1_l) \otimes 1_m \to 2_{kl} \otimes 1_m \to 2_{klm} \\
\mathbf{Se}_{klm} \quad &\text{constructed by} \quad (1_k \otimes 1_l) \otimes 1_m \to 2_{kl} \otimes 1_m \to 3_{klm}.
\end{aligned} \tag{E.2}$$

For spaces spanned by operators acting on a larger and larger number of sites, it becomes more and more difficult to intuitively guess some of the elements of an orthonormalized basis, and therefore particularly necessary to use a systematic method. Eqs. (C.2) and (C.1) provide a starting framework that allows to construct such orthonormalized bases for an arbitrarily large number of sites.

operator	nb comp.	spin
$\frac{1}{2\sqrt{2}}\mathbb{1}_{klm}$	1	0
$\frac{2}{\sqrt{3}}\mathbf{S}_k \cdot (\mathbf{S}_l \times \mathbf{S}_m)$	1	0
$\frac{\sqrt{2}}{3}(\mathbf{S}_k \cdot \mathbf{S}_l + \mathbf{S}_k \cdot \mathbf{S}_m + \mathbf{S}_l \cdot \mathbf{S}_m)$	1	0
$\frac{1}{3}[(\mathbf{S}_k \cdot \mathbf{S}_l e^{i\alpha} + \mathbf{S}_k \cdot \mathbf{S}_m e^{-i\alpha} + \mathbf{S}_l \cdot \mathbf{S}_m) + h.c.]$	1	0
$\frac{1}{3}[(\mathbf{S}_k \cdot \mathbf{S}_l e^{i\alpha} + \mathbf{S}_k \cdot \mathbf{S}_m e^{-i\alpha} + \mathbf{S}_l \cdot \mathbf{S}_m) - h.c.]$	1	0
$\frac{1}{\sqrt{6}}(\mathbf{S}_k + \mathbf{S}_l + \mathbf{S}_m)$	3	1
$\frac{1}{2\sqrt{3}}[(\mathbf{S}_k + \mathbf{S}_l e^{i\alpha} + \mathbf{S}_m e^{-i\alpha}) + h.c.]$	3	1
$\frac{1}{2\sqrt{3}}[(\mathbf{S}_k + \mathbf{S}_l e^{i\alpha} + \mathbf{S}_m e^{-i\alpha}) - h.c.]$	3	1
$\frac{1}{\sqrt{3}}(\mathbf{S}_k \times \mathbf{S}_l + \mathbf{S}_k \times \mathbf{S}_m + \mathbf{S}_l \times \mathbf{S}_m)$	3	1
$\frac{\sqrt{2}}{3}\{\mathbf{S}_k \times (\mathbf{S}_l \times \mathbf{S}_m) + \mathbf{S}_m \times (\mathbf{S}_k \times \mathbf{S}_l)e^{i\alpha} + \mathbf{S}_l \times (\mathbf{S}_m \times \mathbf{S}_k)e^{-i\alpha} + h.c.\}$	3	1
$\frac{\sqrt{2}}{3}\{\mathbf{S}_k \times (\mathbf{S}_l \times \mathbf{S}_m) + \mathbf{S}_m \times (\mathbf{S}_k \times \mathbf{S}_l)e^{i\alpha} + \mathbf{S}_l \times (\mathbf{S}_m \times \mathbf{S}_k)e^{-i\alpha} - h.c.\}$	3	1
$2\sqrt{\frac{2}{15}}[\mathbf{S}_k(\mathbf{S}_l \cdot \mathbf{S}_m) + \mathbf{S}_m(\mathbf{S}_k \cdot \mathbf{S}_l) + \mathbf{S}_l(\mathbf{S}_m \cdot \mathbf{S}_k)]$	3	1
$\sqrt{\frac{2}{3}}\{(\mathbf{S}_k(\mathbf{S}_l \cdot \mathbf{S}_m) + \mathbf{S}_m(\mathbf{S}_k \cdot \mathbf{S}_l)e^{i\alpha} + \mathbf{S}_l(\mathbf{S}_m \cdot \mathbf{S}_k)e^{-i\alpha}) + h.c.\}$	3	1
$\sqrt{\frac{2}{3}}\{(\mathbf{S}_k(\mathbf{S}_l \cdot \mathbf{S}_m) + \mathbf{S}_m(\mathbf{S}_k \cdot \mathbf{S}_l)e^{i\alpha} + \mathbf{S}_l(\mathbf{S}_m \cdot \mathbf{S}_k)e^{-i\alpha}) - h.c.\}$	3	1
$\mathbf{Q}_{klm}(1)$	5	2
$\mathbf{Q}_{klm}(2)$	5	2
$\mathbf{Q}_{klm}(3)$	5	2
$\mathbf{Q}_{klm}(4)$	5	2
$\mathbf{Q}_{klm}(5)$	5	2
$\mathbf{Se}_{klm}$	7	3

Table E.2: Frobenius-orthonormalized basis of the space spanned by the operators acting on three spins $S = 1/2$ located at sites k, l, and m. In the above Table, $\alpha := 2\pi/3$. Eq. (E.2) explains in details how to construct the spin-2 quintet and spin-3 septuplet operators.

APPENDIX F

Symmetry breaking in 2D spin-1/2 systems

The breaking of discrete or continuous symmetries generally leads to a degenerate ground state, whose degeneracy depends on "how much" the symmetry is broken. The consequences of the breaking of discrete (with a concrete application to the square lattice) and continuous symmetries are reviewed in the first part of this appendix. Its second part is devoted to explaining how the nature of a broken symmetry can be read in an energy spectrum. The origin of the Anderson tower of states emerging when continuous symmetries are broken is explained.

F.1 Breaking of discrete and continuous symmetries

The existence of a spontaneous symmetry breaking (SSB) at zero temperature in a model has direct consequences on its low-energy physics. Although the SSB only occurs in the thermodynamic limit, the signature of a SSB is often visible in "small" systems that are numerically tractable by Exact Diagonalization (ED), see Ref. [137] for a good overview.

F.1.1 Broken discrete symmetry: the example of a VBC

If a discrete symmetry is broken, the ground state has a finite degeneracy in the thermodynamic limit, with a finite gap to physical excitations. In a VBC phase for instance, the number of spatial symmetries which are broken by the realized VBC (i.e. its degeneracy) can generally be directly read in the spectrum, without computing any correlation function. The spontaneous symmetry breaking in the thermodynamic limit can be checked by verifying that the energy splitting between the quasi-degenerate ground states decays with the size of the sample.

Let us illustrate this point with the Heisenberg model on the checkerboard lattice which is depicted in Fig. F.1. Exact Diagonalization studies have shown [7] that in the

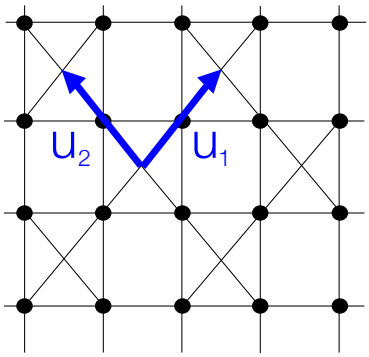

Figure F.1: Checkerboard lattice with the primitive vectors $\mathbf{u}_1$ and $\mathbf{u}_2$ of the corresponding Bravais lattice: spins are represented by black bullets, and all pairs of linked spins interact with the same strength.

thermodynamic limit the ground state of this model is two-fold degenerate with a finite gap to higher excitations. Four kinds of crystals are candidates as ground state, namely the columnar and staggered configurations of dimers (see Fig. F.2, first two panels), and two types of $S = 0$ four-spin plaquette crystals (Fig. F.2, last two panels). It turns out that while the columnar and the staggered configurations of dimers are both four-fold degenerate (translation by $\mathbf{U}_1$ and rotation by $\pi/2$), each of the plaquette configurations are only two-fold degenerate (translation by $\mathbf{U}_1$ only). It is thus clear that neither the columnar nor the staggered configuration of dimers suits for describing the ground state, the choice is restricted to one among the two plaquette configurations. Using symmetry arguments, Ref. [7] explains why the right plaquette configuration is finally the most favorable.

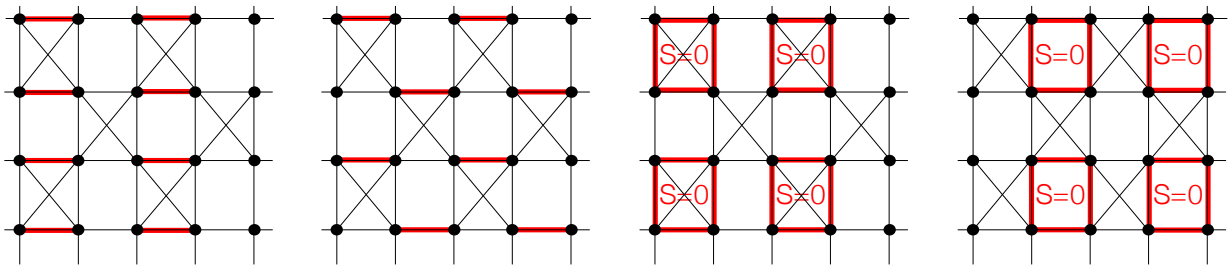

Figure F.2: The 4 candidates as ground state of the spin-1/2 checkerboard antiferromagnet: (from the left to the right) columnar and staggered configurations of dimers, and two kinds of $S = 0$ four-spin plaquette VBCs.

F.1.2 Broken continuous symmetry: Néel & nematic phases

Frustrated magnets exhibit a remarkably large variety of phases with broken continuous symmetries, like the semi-classical Néel phase, nematic phases, or much more complex structures with non-collinear and non-coplanar sublattice magnetizations, order-by-disorder effects,...

The structure of the spectrum is richer for continuous broken symmetries than for discrete ones. First, the existence of gapless Goldstone modes makes the distinction between *ground state* and *excitations* more subtle. Furthermore, since the ground state has an infinite degeneracy in the thermodynamic limit (one can perform infinitesimal rotations of the initial broken symmetry state), the number of quasi-degenerate ground states has to grow as a function of the system size.

F.2 Analysis of energy spectra

F.2.1 How to read an energy spectrum?

Spectra of finite samples and scaling laws governing them can reveal a lot about the nature of the phase that is realized in the thermodynamic limit: the study of the symmetries of the lowest-lying states provides informations about the nature of the symmetries that are spontaneously broken in the infinite system. Towers of quasi-degenerate states in every total spin-S sector which collapse onto the ground state as $\mathcal{O}(S(S+1)/N)$ (N is the size of the sample) are for instance the signature of the realization of a $SU(2)$ symmetry breaking phase (Néel ordered, nematic) in the thermodynamic limit (see the section below). In case of the realization of a VBC ground state, one expects the unit cell of the realized VBC to have the spatial symmetries of the lowest levels in the spectrum, and these latter to be clearly separated from higher energy levels. If *all* the spatial symmetry representations

have a low-lying level which is close to the ground state in energy, then no particular symmetry is preferred and this is a strong indication of the absence of long-range Néel order (there is no antiferromagnetic order parameter) and also a strong argument against a VBC phase, one probably deals with another kind of spin liquid in this case.

Ref. [85] shows for instance that those states in the spectrum of the 36-site sample on the spin-1/2 kagomé antiferromagnet which are compatible with the spatial symmetries of the $\sqrt{3} \times \sqrt{3}$ Néel order are quite high in energy, this kind of order must thus be ruled out in that model. Ref. [137] analyzes the compatibility between the spatial symmetries of the low-lying states in the spectrum of the 36-site sample on the spin-1/2 kagomé antiferromagnet with those of three types of VBC (namely the 36-sites VBC by Marston & Zeng [92], the 12-sites VBC by Syromyatnikov & Maleyev [93], and a third VBC by Budnik & Auerbach [95]). The conclusion they draw is that in the three cases, the compatibility is not clear: the crystallization would require a reshuffling of the low-energy spectrum.

F.2.2 Anderson tower of states in broken continuous symmetry phases

We arbitrarily focus our explanations on the mechanism breaking the $SU(2)$ symmetry in Néel ordered systems, but we wish to stress that the mechanism breaking $SU(2)$ in nematic ordered states is the same and that spectra exhibit similar tower structures in this latter case.

In a semi-classical Néel ordered phase, the lattice spontaneously breaks up into sublattices in which all spins point in the same direction (ferromagnetic sublattices). If we denote by N the (even) number of sites in the sample, by p the number of sublattices, and by Q the number of sites per sublattice in the sample ($N = pQ$), every ferromagnetic sublattice has total spin $Q \cdot \frac{1}{2} = Q/2$. The total spin value S of the entire system is determined by the coupling of these p spins $Q/2$, and can take any value between $S = 0$ and $S = N/2$. Indeed, the Néel state (realized in the thermodynamic limit) has a finite overlap on all total spin sectors between 0 and $N/2$[1].

The low-lying energy levels arising from the Néel order in each of these spin sectors are usually well separated from the first magnon excitations on the spectrum and thus easily recognizable, one refers to them as *Anderson tower of states* since Anderson has first reported their existence in his famous paper on spin-waves in antiferromagnets [178]. The energy $E(N, S, l)$ of the l^{th} level of the Anderson tower in the total spin-S sector of a sample of size N behaves as $E(N, S, l) = \mathcal{O}\left(\frac{S(S+1)}{N}\right)$. These states hence collapse onto the

[1]The weight of the different spin sectors nevertheless decreases with increasing S in a Néel state (which has no net magnetization in any direction).

ground state in the thermodynamic limit $N \to \infty$, breaking the $SU(2)$ symmetry (since different spin sectors do contribute) and giving rise to the Néel phase; one also call them QDJS for *quasi-degenerate joint states*. The tower structure offers a very efficient way to recognize systems with continuous broken symmetries, as it already shows up on very small systems since the energy gaps in the Anderson tower decay more quickly ($\sim 1/N$) than the finite-size corrections to the sublattice magnetization ($\sim 1/\sqrt{N}$).

The following 3 features of the QDJS are important:

- the finite-size scaling leading to a clear cut separation from the first inhomogeneous magnon excitations (the absence of separation between the scaling laws would sign a quantum critical behavior)

- the number of levels $E(N, S, l)$ in each S sector. For a given S and a given N, this number of levels is determined by the number p of ferromagnetic sublattices of the underlying Néel order. Collinear versus non-collinear Néel states can also be readily discriminated from their spectra. A collinear structure has a tower with exactly one level per value of S whereas the tower of a non-collinear system (with $q \geq 3$ sublattices) contains $2S + 1$ levels per total spin sector S

- the spatial symmetries of the levels $E(N, S, l)$: the number and nature of the space group irreducible representations that appear in each S subspace are uniquely determined by the geometrical symmetries of the Néel order.

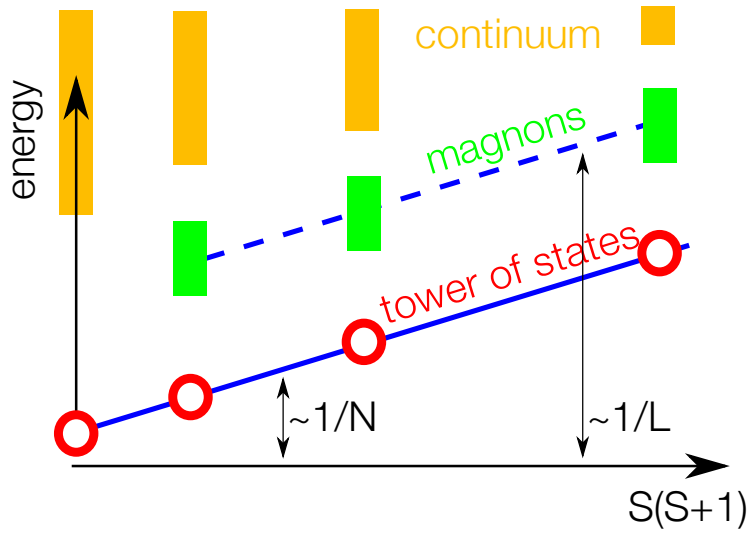

Figure F.3: Spectrum in the case of a broken $SU(2)$ phase: the Anderson tower of states collapses like the inverse number of sites in the sample N^{-1}, it is well distinct from the magnon excitations that collapse like the inverse typical length scale of the sample $L^{-1} = N^{-1/D}$ (D is the dimension). The number of QDJS in each total spin-S sector depends on the way $SU(2)$ is broken: $2S + 1$ distinct energy levels appear if the phase fully breaks $SU(2)$, whereas only one level appears if $SU(2)$ is broken down to $U(1)$ only.

Bibliography

[1] H. Bethe, Z. Phys. **71**, 205 (1931)

[2] W. Heisenberg, Z. Phys. **38**, 411 (1926);
P.A.M. Dirac, Proc. Roy. Soc. (London) **A112**, 661 (1926)

[3] E. Dagotto and A. Moreo, Phys. Rev. Lett. **63**, 2148 (1989);
H.J. Schulz and T.A.L. Ziman, Europhys. Lett. **18**, 355 (1992)

[4] C. Lhuillier and P. Sindzingre, *Spin-1/2 antiferromagnets in 2 dimensions*, arXiv:0212351;
C. Lhuillier and G. Misguich, *Frustrated quantum magnets*, arXiv:0109146;
C. Lhuillier, *Frustrated quantum magnets*, arXiv:0502464

[5] G. Misguich and C. Lhuillier, *Two-dimensional quantum antiferromagnets*, arXiv:0310405

[6] R. Coldea *et al.*, Phys. Rev. Lett. **86**, 5377 (2001)

[7] J.-B. Fouet *et al.*, Phys. Rev. B **67**, 054411 (2003)

[8] D.S. Rokhsar and S.A. Kivelson, Phys. Rev. Lett. **61**, 2376 (1988)

[9] P.W. Anderson, Mater. Res. Bull. **8**, 153 (1973);
P. Fazekas and P.W. Anderson, Philos. Mag. **30**, 432 (1974)

[10] A.F. Albuquerque and F. Alet, *Critical Correlations for Short-Range Valence-Bond Wavefunctions on the Square Lattice*, arXiv:1009.1307

[11] K.S.D. Beach, *Fractal valence bond loops in a long-range Heisenberg model at criticality*, arXiv:0707.0297

[12] X.G. Wen and Q. Niu, Phys. Rev. B **41**, 9377 (1990)

[13] G. Misguich *et al.*, Phys. Rev. B **60**, 1064 (1999)

[14] J.-B. Fouet, P. Sindzingre, and C. Lhuillier, Eur. Phys. J. B **20**, 241 (2001)

[15] X.G. Wen, F. Wilzcek, and A. Zee, Phys. Rev. B **39**, 11413 (1989)

[16] D.F. Schroeter *et al.*, Phys. Rev. Lett. **99**, 097202 (2007)

[17] A.F. Andreev and I.A. Grishchuk, Sov. Phys. JETP **60**, 267 (1984)

[18] A. Läuchli *et al.*, Phys. Rev. Lett. **95**, 137206 (2005)

[19] N. Shannon, T. Momoi, and P. Sindzingre, Phys. Rev. Lett. **96**, 027213 (2006)

[20] T. Momoi, P. Sindzingre, and N. Shannon, Phys. Rev. Lett. **97**, 257204 (2006)

[21] J. Sudan, A. Lüscher, and A.M. Läuchli, Phys. Rev. B **80**, 140402(R) (2009)

[22] G.V. Chester, Phys. Rev. A **2**, 256 (1970);
A.J. Leggett, Phys. Rev. Lett. **25**, 1543 (1970)

[23] E. Kim and M.H.W. Chan, Nature **427**, 225 (2004);
P.W. Anderson, W.F. Brinkman, and D.A. Huse, Science **310**, 1164 (2005);
M. Boninsegni, N. Prokof'ev, and B. Svistunov, Phys. Rev. Lett. **96**, 105301 (2006);
S. Sasaki *et al.*, Science **313**, 1098 (2006);
N. Prokof'ev, Adv. Phys. **56**, 381 (2007);
B. Hunt *et al.*, Science **324**, 632 (2009);
C. Cazorla *et al.*, New J. Phys. **11**, 013047 (2009)

[24] T. Giamarchi, C. Rüegg, and O. Tchernyshyov, Nature Physics **4**, 198 (2008)

[25] S.-A. Cheong, PhD thesis, *Many-body fermion density matrices*, Cornell University, May 2006;
S.-A. Cheong and C.L. Henley, Phys. Rev. B **79**, 212402 (2009)

[26] S. Furukawa, G. Misguich, and M. Oshikawa, Phys. Rev. Lett. **96**, 047211 (2006)

[27] M. Enderle *et al.*, Europhys. Lett. **70**, 237 (2005);
M. Enderle *et al.*, Phys. Rev. Lett. **104**, 237207 (2010)

[28] S.-L. Drechsler *et al.*, Phys. Rev. Lett. **98**, 077202 (2007)

[29] M. Hase *et al.*, Phys. Rev. B **70**, 104426 (2004)

[30] E.A. Nytko *et al.*, J. Am. Chem. Soc. **130**, 2922 (2008)

[31] J. Villain, J. Phys. Chem. Solids **11**, 303 (1959);
T.A. Kaplan, Phys. Rev. **116**, 888 (1959);
A. Yoshimori, J. Phys. Soc. Jpn. **14**, 807 (1959)

[32] I. Dzyaloshinskii, Sov. Phys. JETP **19**, 960 (1964);
T. Moriya, Phys. Rev. **120**, 91 (1960)

[33] A. Herpin and P. Meriel, Journal de Physique et le radium **22**, 337 (1961);
R. Plumier, C. R. Acad. Sc. **260**, 3348 (1965);
J.M. Hastings and L.M. Corliss, J. Phys. Chem. Solids **29**, 9 (1968);
V.J. Minkiewicz, D.E. Cox, and G. Shirane, Solid State Communications **8**, 1001 (1970);
I. Sosnowska, T. Peterlin-Neumaier, and E. Steichele, J. Phys. C: Solid State Phys. **15**, 4835 (1982)

[34] J. Villain, J. Phys. C: Solid State Phys. **10**, 4793 (1977)

[35] H. Kawamura, J. Phys.: Condens. Matter **10**, 4707 (1998)

[36] P. Chandra and P. Coleman, Phys. Rev. Lett. **66**, 100 (1991)

[37] F. Cinti *et al.*, Phys. Rev. Lett. **100**, 057203 (2008)

[38] S. Seki *et al.*, Phys. Rev. Lett. **100**, 127201 (2008)

[39] R.M. Hornreich, M. Luban, and S. Shtrikman, Phys. Rev. Lett. **35**, 1678 (1975)

[40] D.C. Cabra, A. Honecker, and P. Pujol, Eur. Phys. Jour. B **13**, 55 (2000)

[41] C. Itoi and S. Qin, Phys. Rev. B **63**, 224423 (2001)

[42] T. Hamada *et al.*, J. Phys. Soc. Jpn. **57**, 1891 (1988);
Y. Natsume *et al.*, J. Phys. Soc. Jpn. **58**, 3869 (1989)

[43] F. Heidrich-Meisner, A. Honecker, and T. Vekua, Phys. Rev. B **74**, 020403(R) (2006)

[44] T. Vekua *et al.*, Phys. Rev. B **76**, 174420 (2007)

[45] L. Kecke, T. Momoi, and A. Furusaki, Phys. Rev. B **76**, 060407(R) (2007)

[46] S.-L. Drechsler *et al.*, *Comment on "Two-spinon and four-spinon continuum in a frustrated ferromagnetic spin-1/2 chain" by M. Enderle et al*, arXiv:1006.5070

[47] T. Hikihara *et al.*, Phys. Rev. B **78**, 144404 (2008)

[48] A. Kolezhuk and T. Vekua, Phys. Rev. B **72**, 094424 (2005)

[49] I.P. McCulloch *et al.*, Phys. Rev. B **77**, 094404 (2008)

[50] K. Okunishi, J. Phys. Soc. Jpn. **77**, 114004 (2008)

[51] F. Heidrich-Meisner, I.P. McCulloch, and A.K. Kolezhuk, Phys. Rev. B **80**, 144417 (2009)

[52] M.E. Zhitomirsky and H. Tsunetsugu, *Magnon pairing in quantum spin nematic*, arXiv:1003.4096

[53] M. Sato, T. Momoi, and A. Furusaki, Phys. Rev. B **79**, 060406(R) (2009)

[54] M. Sato, T. Hikihara, and T. Momoi, *Field and temperature dependence of the NMR relaxation rate in the magnetic quadrupolar liquid phase of spin-1/2 frustrated ferromagnetic chains*, arXiv:1009.3206

[55] S. Nishimoto *et al.*, *Quasi-1d quantum helimagnets: The fate of multipolar phases*, arXiv:1005.5500

[56] L.E. Svistov *et al.*, *New high magnetic field phase of the frustrated $S = 1/2$ ferromagnetic chain $LiCuVO_4$*, arXiv:1005.5668

[57] R.W. Chhajlany *et al.*, Phys. Rev. A **75**, 032340 (2007)

[58] A.V. Chubukov, Phys. Rev. B **44**, 4693 (1991)

[59] M.P.A. Fisher *et al.*, Phys. Rev. B **40**, 546 (1989)

[60] R. Moessner and S.L. Sondhi, Phys. Rev. Lett. **86**, 1881 (2001)

[61] G. Misguich, D. Serban, and V. Pasquier, Phys. Rev. Lett. **89**, 137202 (2002)

[62] P. Lecheminant, PhD thesis, Université Pierre et Marie Curie, Paris, 1995

[63] J.T. Chalker and J.F.G. Eastmond, Phys. Rev. B **46**, 14201 (1992)

[64] J. Sudan and A.M. Läuchli, *The correlation density matrix tool for extracting dominant correlations: properties & applications*, in preparation

[65] V. Vedral, Rev. Mod. Phys. **74**, 197 (2002)

[66] S. Eggert, Phys. Rev. B **54**, 9612 (1996)

[67] C.K. Majumdar and D.K. Ghosh, J. Math. Phys. **10**, 1399 (1969)

[68] S.R. White and I. Affleck, Phys. Rev. B **54**, 9862 (1996)

[69] M.P. Gelfand, Phys. Rev. B **42**, 8206 (1990)

[70] R.R.P. Singh *et al.*, Phys. Rev. B **60**, 7278 (1990)

[71] M.E. Zhitomirsky and K. Ueda, Phys. Rev. B **54**, 9007 (1996)

[72] L. Capriotti and S. Sorella, Phys. Rev. Lett. **84**, 3173 (2000)

[73] O.P. Sushkov, J. Oitmaa, and Z. Weihong, Phys. Rev. B **63**, 104420 (2001)

[74] M. Mambrini *et al.*, Phys. Rev. B **74**, 144422 (2006)

[75] M.E. Zhitomirsky, Phys. Rev. B **78**, 094423 (2008)

[76] J.T. Chalker, P.C.W. Holdsworth, and E.F. Shender, Phys. Rev. Lett. **68**, 855 (1992)

[77] D.A. Huse and A.D. Rutenberg, Phys. Rev. B **45**, 7536 (1992)

[78] C.L. Henley, Phys. Rev. B **80**, 180401 (2009)

[79] P.W. Leung and V. Elser, Phys. Rev. B **47**, 5459 (1993)

[80] C. Waldtmann *et al.*, Eur. Phys. J. B **2**, 501 (1998)

[81] P. Sindzingre *et al.*, Phys. Rev. Lett. **84**, 2953 (2000)

[82] R.R.P. Singh and D.A. Huse, Phys. Rev. B **77**, 144415 (2008)

[83] Z. Hao and O. Tchernyshyov, Phys. Rev. Lett. **103**, 187203 (2009)

[84] H.C. Jiang *et al.*, Phys. Rev. Lett. **101**, 117203 (2008)

[85] P. Lecheminant *et al.*, Phys. Rev. B **56**, 2521 (1997)

[86] A.M. Läuchli and C. Lhuillier, *Dynamical Correlations of the Kagome $S = 1/2$ Heisenberg Quantum Antiferromagnet*, arXiv:0901.1065

[87] Y. Ran *et al.*, Phys. Rev. Lett. **98**, 117205 (2007)

[88] P. Sindzingre and C. Lhuillier, EPL **88**, 27009 (2009)

[89] F. Mila, Phys. Rev. Lett. **81**, 2356 (1998)

[90] M. Mambrini and F. Mila, Eur. Phys. J. B **17**, 651 (2000)

[91] C. Lhuillier, P. Sindzingre, and J.-B. Fouet, Can. J. Phys. **79**, 1525 (2001)

[92] J.B. Marston and C. Zeng, J. Appl. Phys. **69**, 5962 (1991)

[93] A.V. Syromyatnikov and S.V. Maleyev, Phys. Rev. B **66**, 132408 (2002)

[94] E.S. Sørensen, M.J. Lawler, and Y.B. Kim, Phys. Rev. B **79**, 174403 (2009)

[95] R. Budnik and A. Auerbach, Phys. Rev. Lett. **93**, 187205 (2004)

[96] P. Nikolic and T. Senthil, Phys. Rev. B **68**, 214415 (2003)

[97] R.R.P. Singh and D.A. Huse, Phys. Rev. B **76**, 180407(R) (2007)

[98] G. Evenbly and G. Vidal, Phys. Rev. Lett. **104**, 187203 (2010)

[99] B. Bernu *et al.*, Phys. Rev. B **50**, 10048 (1994)

[100] L. Capriotti, A.E. Trumper, and S. Sorella, Phys. Rev. Lett. **82**, 3899 (1999)

[101] V. Elser, Phys. Rev. Lett. **62**, 2405 (1989)

[102] C. Zeng and V. Elser, Phys. Rev. B **42**, 8436 (1990)

[103] N. Elstner and A.P. Young, Phys. Rev. B **50**, 6871 (1994)

[104] T. Nakamura and S. Miyashita, Phys. Rev. B **52**, 9174 (1995)

[105] P. Tomczak and J. Richter, Phys. Rev. B **54**, 9004 (1996)

[106] J. Sudan and A.M. Läuchli, *Correlation Density Matrix study of the $S = 1/2$ kagomé antiferromagnet: relevance of the valence bond crystal scenario*, in preparation

[107] D. Schwandt, M. Mambrini, and D. Poilblanc, Phys. Rev. B **81**, 214413 (2010)

[108] D. Poilblanc, M. Mambrini, and D. Schwandt, Phys. Rev. B **81**, 180402(R) (2010)

[109] A. Keren *et al.*, Phys. Rev. B **53**, 6451 (1996)

[110] O. Janson *et al.*, *Coupled frustrated quantum spin-1/2 chains with orbital order in volborthite $Cu_3V_2O_7(OH)_2 \cdot 2H_2O$*, arXiv:1004.2185

[111] A. Fukaya *et al.*, Phys. Rev. Lett. **91**, 207603 (2003)

[112] A.P. Ramirez, B. Hessen, and M. Winklemann, Phys. Rev. Lett. **84**, 2957 (2000)

[113] M.P. Shores *et al.*, J. Am. Chem. Soc. **127**, 13462 (2005)

[114] M.A. de Vries *et al.*, Phys. Rev. Lett. **100**, 157205 (2008)

[115] A. Olariu *et al.*, Phys. Rev. Lett. **100**, 087202 (2008)

[116] A. Zorko *et al.*, Phys. Rev. Lett. **101**, 026405 (2008)

[117] M. Rigol and R.R.P. Singh, Phys. Rev. Lett. **98**, 207204 (2007)

[118] M. Rigol and R.R.P. Singh, Phys. Rev. B **76**, 184403 (2007)

[119] O. Ofer and A. Keren, Phys. Rev. B **79**, 134424 (2009)

[120] P. Mendels and F. Bert, J. Phys. Soc. Jpn. **79**, 011001 (2010)

[121] O. Ofer *et al.*, *Ground state and excitation properties of the quantum kagomé system $ZnCu_3(OH)_6Cl_2$ investigated by local probes*, arXiv:0610540

[122] P. Mendels *et al.*, Phys. Rev. Lett. **98**, 077204 (2007)

[123] J.S. Helton *et al.*, Phys. Rev. Lett. **98**, 107204 (2007)

[124] Y. Okamoto *et al.*, J. Phys. Soc. Jpn. **78**, 033701 (2009)

[125] H. Yoshida *et al.*, J. Phys. Soc. Jpn. **78**, 043704 (2009)

[126] D. Wulferding *et al.*, *Interplay of thermal and quantum spin fluctuations on the kagome lattice*, arXiv:1005.4831

[127] S. Chu *et al.*, J. Am. Chem. Soc. **132**, 5570 (2010)

[128] L. Marcipar *et al.*, Phys. Rev. B **80**, 132402 (2009)

[129] M. Nyfeler *et al.*, Phys. Rev. Lett. **100**, 247206 (2008)

[130] H.G. Evertz, G. Lana, and M. Marcu, Phys. Rev. Lett. **70**, 875 (1993)

[131] U.-J. Wiese and H.-P. Ying, Z. Phys. B **93**, 147 (1994)

[132] B. Frischmuth, B. Ammon, and M. Troyer, Phys. Rev. B **54**, R3714 (1996)

[133] M. Troyer, H. Kontani, and K. Ueda, Phys. Rev. Lett. **76**, 3822 (1996)

[134] M. Greven, R.J. Birgeneau, and U.-J. Wiese, Phys. Rev. Lett. **77**, 1865 (1996)

[135] B.B. Beard *et al.*, Phys. Rev. Lett. **80**, 1742 (1998)

[136] M. Greven and R.J. Birgeneau, Phys. Rev. Lett. **81**, 1945 (1998)

[137] G. Misguich and P. Sindzingre, J. Phys.: Condens. Matter **19**, 145202 (2007); G. Misguich and P. Sindzingre, *Detecting spontaneous symmetry breaking in finite-size spectra of frustrated quantum antiferromagnets*, arXiv:0607764 (actually more recent than the publication itself: v3 was last revised in December 2008)

[138] L. Amico *et al.*, Rev. Mod. Phys. **80**, 517 (2008)

[139] M.A. Nielsen and I.L. Chuang, *Quantum Computation and Quantum Information*, Cambridge University Press, Cambridge, England, 2000

[140] K.M.R. Audenaert *et al.*, Phys. Rev. A **66**, 042327 (2002)

[141] T.J. Osborne and M.A. Nielsen, Phys. Rev. A **66**, 032110 (2002)

[142] A.L. Osterloh *et al.*, Nature (London) **416**, 608 (2002)

[143] G. Vidal *et al.*, Phys. Rev. Lett. **90**, 227902 (2003)

[144] T. Roscilde *et al.*, Phys. Rev. Lett. **94**, 147208 (2005)

[145] V.E. Korepin, Phys. Rev. Lett. **92**, 096402 (2004)

[146] G. Refael and J.E. Moore, Phys. Rev. Lett. **93**, 260602 (2004)

[147] J. Eisert and T.J. Osborne, Phys. Rev. Lett. **97**, 150404 (2006)

[148] C. Holzhey, F. Larsen, and F. Wilczek, Nucl. Phys. B **424**, 443 (1994)

[149] P. Calabrese and J. Cardy, J. Stat. Mech. P06002 (2004)

[150] P. Calabrese and J. Cardy, J. Phys. A: Math. Theor. **42**, 504005 (2009)

[151] A. Kitaev and J. Preskill, Phys. Rev. Lett. **96**, 110404 (2006)

[152] M. Levin and X.-G. Wen, Phys. Rev. Lett. **96**, 110405 (2006)

[153] S. Ryu and T. Takayanagi, Phys. Rev. Lett. **96**, 181602 (2006)

[154] E. Fradkin and J.E. Moore, Phys. Rev. Lett. **97**, 050404 (2006)

[155] M.A. Metlitski, C.A. Fuertes, and S. Sachdev, Phys. Rev. B **80**, 115122 (2009)

[156] B. Hsu *et al.*, Phys. Rev. B **79**, 115421 (2009)

[157] M. Cramer *et al.*, Phys. Rev. A **73**, 012309 (2006)

[158] M. Srednicki, Phys. Rev. Lett. **71**, 666 (1993)

[159] M.M. Wolf, F. Verstraete, M.B. Hastings, and J. Ignacio Cirac, Phys. Rev. Lett. **100**, 070502 (2008)

[160] J. Eisert, M. Cramer, and M.B. Plenio, Rev. Mod. Phys. **82**, 277 (2010)

[161] M.C. Arnesen, S. Bose, and V. Vedral, Phys. Rev. Lett. **87**, 017901 (2001)

[162] N. Eltsner and A.P. Young, Phys. Rev. B **50**, 6871 (1994)

[163] W. Münder *et al.*, *Correlation density matrices for 1-dimensional quantum chains based on the density matrix renormalization group*, arXiv:0910.0753

[164] J. Goldstone, Nuovo Cimento **19**, 154 (1961)

[165] R.V. Lange, Phys. Rev. **146**, 301 (1966)

[166] E.H. Lieb, T.D. Schultz, and D.C. Mattis, Ann. Phys. (N.Y.) **16**, 407 (1961)

[167] I. Affleck and E.H. Lieb, Lett. Math. Phys. **12**, 57 (1986)

[168] M. Oshikawa, M. Yamanaka, and I. Affleck, Phys. Rev. Lett. **78**, 1984 (1997)

[169] M.B. Hastings, Phys. Rev. B **69**, 104431 (2004)

[170] N.D. Mermin and H. Wagner, Phys. Rev. Lett. **17**, 1133 (1966)

[171] E. Lieb and D. Mattis, J. Math. Phys. **3**, 749 (1962)

[172] C. Lanczos, J. Res. Natl. Bur. Stand. **45**, 255 (1950)

[173] E.R. Gagliano *et al.*, Phys. Rev. B **34**, 1677 (1986)

[174] E.R. Davidson, J. Comput. Phys. **17**, 87 (1975)

[175] S.R. White, Phys. Rev. Lett. **69**, 2863 (1992)

[176] S.R. White and D. Huse, Phys. Rev. B **48**, 3844 (1993)

[177] K.G. Wilson, Rev. Mod. Phys. **47**, 773 (1975)

[178] P.W. Anderson, Phys. Rev. **86**, 694 (1952)

Curriculum Vitæ

Julien Sudan

EPFL SB IRRMA-GE
BSP 725
CH-1015 Lausanne
+41 (0)21 693 54 27
julien.sudan@a3.epfl.ch

born July 28, 1981
swiss citizen
married

Education

2006–2010	PhD candidate at *Institut de Recherche Numérique en Physique des Matériaux* (IRRMA), EPFL, Lausanne under the supervision of Prof. Frédéric Mila (EPFL) and Dr. Andreas Läuchli (MPI-PKS Dresden, Germany)
2004–2006	Master of Science in Physics under the supervision of Prof. Dionys Baeriswyl, University of Fribourg
2001–2004	Bachelor of Science in Physics University of Fribourg
1997–2001	Swiss Federal Baccalaureate, scientific orientation (C) Collège Sainte-Croix, Fribourg

Assistantship at EPFL

2009/2010	*Physique générale III*, by Prof. H. Rønnow
2009	*Mécanique quantique II*, by Prof. F. Mila
2008/2009	*Physique générale III*, by Prof. H. Rønnow
2008	*Physique numérique II*, by Prof. L. Villard and Dr. A. Läuchli
2007/2008	*Physique numérique I*, by Prof. L. Villard and Dr. A. Läuchli
2007	*Physique numérique II*, by Prof. L. Villard and Dr. A. Läuchli
2006/2007	*Physique numérique I*, by Prof. L. Villard and Dr. A. Läuchli

Schools & conferences

2010 – Workshop on *Emergence of New States of Matter in Magnetic Systems and Beyond*, ICTP, Trieste (I)
– Workshop *Novel Physics on the Kagome Network*, Orsay (F)
2009 – *Linking Nuclei, Molecules, and Condensed Matter: Computational Quantum Many-Body Approaches*, ECT*, Trento (I)
– *Strongly Correlated Systems meeting*, Geneva
– *Conference on frustration in condensed matter*, Lyon (F)
– *Swiss National Supercomputing Centre* meeting, Lucerne
2008 – *Highly Frustrated Magnetism* conference, University of Braunschweig (D)
– *International Summer School on Numerical Methods for Correlated Systems in Condensed Matter*, University of Sherbrooke, Canada
– *Swiss Physical Society (SPS)* meeting, Geneva
– Workshop *Magnetism in nanostructures and novel materials*, Max-Planck-Institute Stuttgart (D)
2007 – *Strongly Correlated Systems* meeting, EPFL
– Summer school & Workshop *Highly Frustrated Magnets and Strongly Correlated Systems: From Non-Perturbative Approaches to Experiments*, ICTP, Trieste (I)
– *Strongly Correlated Systems* meeting, Fribourg
– *Swiss Physical Society (SPS)* meeting, Zurich
– *Strongly Correlated Systems* meeting, Geneva
– Lecture *Introduction to the Quantum Hall Effects* by Prof. P. Lederer (Université de Paris Sud), EPFL

Presentations & posters

2010 – Poster at the *Emergence of New States of Matter in Magnetic Systems and Beyond* workshop, ICTP, Trieste (I)
– Poster at the *Novel Physics on the Kagome Network* workshop, Orsay (F)
2009 – Poster at the *Conference on frustration in condensed matter*, Lyon (F)
2008 – Presentation, Journal Club group meeting, EPFL
– Poster at the *Highly Frustrated Magnetism* conference, University of Braunschweig (D)
– Poster at the *Swiss Physical Society (SPS)* meeting, Geneva

2007 – Poster at the *Highly Frustrated Magnets and Strongly Correlated Systems: From Non-Perturbative Approaches to Experiments* workshop, ICTP, Trieste (I)
– Presentation at the *Swiss Physical Society (SPS)* meeting, Zurich
– Presentation, Journal Club group meeting, EPFL

Publications

- J. Sudan, A. Lüscher, and A.M. Läuchli, Phys. Rev. B **80**, 140402(R) (2009) *selected as "PRB Editor's suggestion"*
- A.M. Läuchli, J. Sudan, and A. Lüscher, J. Phys.: Conf. Ser. **145**, 012057 (2009)
- J. Sudan and A.M. Läuchli, *Correlation density matrix study of the $S = 1/2$ kagomé antiferromagnet: importance of valence bond crystal fluctuations*, in preparation
- J. Sudan and A.M. Läuchli, *The correlation density matrix tool for extracting dominant correlations: properties & applications*, in preparation
- J. Sudan and A.M. Läuchli, *Entropy studies of the spin-1/2 kagomé antiferromagnet*, in preparation